



**HAL**  
open science

# Additive manufacturing Processing and characterization of Fe-Si soft magnetic alloys

Shuohong Gao

► **To cite this version:**

Shuohong Gao. Additive manufacturing Processing and characterization of Fe-Si soft magnetic alloys. Other. Université Bourgogne Franche-Comté, 2021. English. NNT : 2021UBFCA015 . tel-03600459

**HAL Id: tel-03600459**

**<https://theses.hal.science/tel-03600459v1>**

Submitted on 7 Mar 2022

**HAL** is a multi-disciplinary open access archive for the deposit and dissemination of scientific research documents, whether they are published or not. The documents may come from teaching and research institutions in France or abroad, or from public or private research centers.

L'archive ouverte pluridisciplinaire **HAL**, est destinée au dépôt et à la diffusion de documents scientifiques de niveau recherche, publiés ou non, émanant des établissements d'enseignement et de recherche français ou étrangers, des laboratoires publics ou privés.



SPIM

Thèse de Doctorat



école doctorale sciences pour l'ingénieur et microtechniques

UNIVERSITÉ DE TECHNOLOGIE BELFORT-MONTBÉLIARD

**Additive manufacturing processing and  
characterization of Fe-Si soft magnetic alloys**

**Shuohong GAO**



**Université de technologie de Belfort-Montbéliard**  
**Ecole Doctorale Sciences physiques pour**  
**l'Ingénieur et Microtechniques**

**THESE**

Présentée pour obtenir le grade de  
Docteur de l'Université de Technologie de Belfort-Montbéliard en Sciences pour  
l'Ingénieur

**Additive manufacturing processing and characterization of Fe-Si  
soft magnetic alloys**

**Shuohong GAO**

**Defensed on December 09, 2021**

With the jury:

**Reporters**

Dr. Moataz ATTALLAH, Professor, School of Metallurgy & Materials, University of Birmingham, UK  
Dr. Salim-Mourad CHERIF, Professor, LSPM, University of Paris 13, France

**Examiners**

Dr. Riad BADJI, Research Director, CRTI, Research Center In Industrial Technologies, Algeria  
Dr. Xingchen YAN, Associate Professor, Institute of New Materials, Guangdong Academy of Sciences, China  
Dr. Nouredine FENINECHE, Professor, ICB-PMDM-LERMPS, University of Technology of Belfort-Montbéliard, France  
Dr. Hanlin LIAO, Professor, ICB-PMDM-LERMPS, University of Technology of Belfort-Montbéliard, France



## Acknowledgments

Works performed in the frame of this thesis were mainly done in the Laboratoire Interdisciplinaire Carnot de Bourgogne (ICB), and more particularly within the Procédés métallurgiques, Durabilité, Matériaux-Laboratoire d'Etudes et de Recherches sur les Matériaux, les Procédés et les Surfaces (PMDM-LERMPS) team from University of Technology of Belfort-Montbéliard (UTBM), and supported by China Scholarship Council (CSC) in the framework of UT-INSA (2018). My first thanks go to all collaborating parties, which made this work possible at all. I would like to thank the CSC for giving me the chance to study abroad and broaden my vision, and the ICB-PMDM-LERMPS laboratory, to give me the opportunity to continue my study.

I avail this special opportunity to express my gratitude and indebtedness to my supervisors Prof. FENINECHE Nouredine and Prof. Hanlin LIAO (Materials Engineering, School of Materials, Université de Technologie de Belfort-Montbéliard, France), for their efficacious ideas and perpetual encouragement throughout my doctoral period, without which it would not have been possible to complete my PhD. Their patience and attitude as well as the relaxed way of handling problems also impress me a lot. It is not only the knowledge I could learn from them but also the confident and cheerful attitude toward obstacles that are of great inspiration to me on this road of science in the future.

My gratitude goes to the members of the defense jury for their efforts in examining this work. In particular, I am very thankful for Prof. Moataz ATTALLAH and Prof. Salim-Mourad CHERIF to take the time to be the reviewers and help me improve this thesis. Besides, I feel very honored to have Dr. Riad BADJI, be present among the jury members of the thesis defense session.

I would also like to express all my thanks to my co-supervisors Prof. Min LIU (Vice-president of Guangdong Academy of Sciences, China) and Associate Prof. Xingchen YAN, (Institute of New Materials, Guangdong Academy of Sciences, Chian), for providing all kinds of assistance and technical guidance throughout all this work.

Thanks to my colleagues at LERMPS, Dr. Christophe Verdy, Mr. Christian Adam, Charles, Joel, Ms. Emmanuelle, for their very kind help with my experiments. Especially, Mr. Charles helped me a lot in further understanding of SLM machine and doing the corresponding experiments.

I would like to thank a few other specific researchers and collaborators who helped me throughout the period of this work, and in particular Prof. Zhongwu Liu (Head of Department, Department of Metallic Materials Science and Engineering, South China University of Technology, China ), Mr. Eric AUBRY (Plateforme SURFACE, FEMTO-ST, UTBM, France), Mr. Jian WANG (Institute of New Materials, Guangdong Academy of Sciences, Chian), Mr. Jinwen Hu (Phd student in South China University of Technology, China ). Dr. Cheng CHANG, Zhaoyang DENG (Institute of New Materials, Guangdong Academy of Sciences, China), Mr. Qingkun CHU (Phd student in GuangDong University of Technology, China), Dr Xinliang XIE (Postdoc in Université Catholique de Louvain, Belgium), for their assistance and cooperation concerning of the corresponding experiments and characterization.

Acknowledgment is also expressed to all lab personnel in the LERMPS, for their kind cooperation. Thanks are due to associate professor Sihao DENG, Dr. Xiujuan FAN, Dr. Zexin YU, Dr. Tao JIANG, Dr. Meimei LIU, Dr. Hoangjian WU, Dr. Shimin XIE, Mr. Shaowu LIU, Yingjie Li, Wenbo Li, Yijun YAO, and other members of LERMPS group for their accompany and continuous support.

I also acknowledge the constant support and blessings from my family, especially my parents and younger sister. I also thank all my good friends for their continuous encouragement and spiritual support during these years.



## General introduction

Soft magnetic alloys are materials that are amenable to easy magnetization and demagnetization. In addition to high reliability, low cost, and suitability for mass production just like other commercial products. So far, soft magnetic alloys have been employed in a large variety of devices, such as transformers, generators, and motors, also have been used in the generation and distribution of electrical energy, household appliances, and scientific equipment. With the increasingly essential demand for soft magnetic materials in the industry, automotive, and household appliances, it is important and urgent to develop new soft magnetic materials and improve the performance of traditional soft magnetic materials. Soft magnetic alloy is an important soft magnetic material, especially the iron silicon (Fe-Si) soft magnetic alloy, also named silicon steel, which is the most important soft magnetic material occupying the large majority of the soft magnetic market. It is urgent to develop more efficient, more design freedom manufacturing methods and improve the properties of the products.

In recent years, metal additive manufacturing (AM) technology has attracted more attention since it can bring digital flexibility and efficiency to manufacturing operations. This technique allows the manufacturing of lighter, more complex designs that are more difficult or more expensive to fabricate by traditional dies, molds, milling, and machining. Selective laser melting (SLM), commonly known as laser-based powder bed fusion, a representative of sustainable metal fabrication, is one of the most attractive AM technologies. In the process of SLM, the powder is spread in thin layers and rapidly fused layer-by-layer via a high-density laser source to achieve products. Owing to the CAD-based design and fabrication process, the SLM process delivers a perfect challenge of improved performance, complex geometries, and simplified production for a variety of applications. It can be considered as an emerging technology to prepare metal components directly from raw materials.

The available range of magnetic properties of soft magnetic materials was expanding, iron and iron silicon alloys are the most widely used. To look for better-performing manufacturing technologies for soft magnetic materials, the AM technique has been attracted wide attention. The freeform capabilities of the SLM process and the magnetic efficiency of silicon steel have the potential for the development of electromechanical component designs that could be particularly attractive for certain electromechanical applications. However, the research about AM Fe-Si-based soft magnetic alloy is still insufficient, especially a systematic study on the microstructure and materials properties of Fe-Si soft magnetic alloy via SLM technology is still lacking. So far, the research on SLMed soft magnetic alloys is still insufficient, and the investigation on SLMed Fe-Si-based soft magnetic alloys is only in the preliminary stage, lacking systematic research. Hence, systematic and detailed studies on SLMed Fe-Si-based soft magnetic alloys should be conducted. To explore and develop this research field, a thorough investigation of SLMed Fe-Si soft magnetic alloy was studied in this thesis. This thesis is organized into six chapters, as follows:

Chapter 1 provided a brief introduction to magnetism, and the soft magnetic materials, especially, Fe-Si alloys and their general fabrication processes and applications. Then, a review of the state of the art of AM and a description of the SLM technique, a bibliographic study of the SLMed soft magnetic alloys from mixed powder and pre-alloyed powder are also summarized. Especially, the bibliography of SLMed Fe-Si alloys was discussed and described in detail. More attention has been paid to the developments of SLMed Fe-Si alloys, including the investigation on SLM fabrication parameters, scanning strategy, post heat treatments. and magnetic performances. Moreover, a review of the effects of geometric and structural design on the microstructure and magnetic properties of SLMed Fe-Si soft magnetic alloys is also presented. Finally, the objectives of this thesis are clearly declared.

Chapter 2 characterized the particle size distribution, morphologies, and microstructures of the raw powders. The SLM systems and their operation parameters, as well as the material and experimental procedures and test instruments used in this research work, are introduced.



To optimize the SLM parameters for producing Fe-Si alloy with good quality and understand the microstructure characteristics and material properties, chapter 3 discussed the effects of processing parameters on surface morphology, microstructure, and the magnetic properties of SLMed Fe-3wt.%Si alloy.

Chapter 4 investigated the microstructures, DC and AC magnetic properties, and mechanical properties of SLMed Fe-3wt.%Si soft magnet. Especially, it investigated the crystalline texture and oriented magnetic properties of the SLMed Fe-3wt.%Si alloy firstly, and summarized the relationship between the texture and magnetic characteristics, carried on the theoretical elaboration. Then, the mechanical performances including microhardness, tensile properties were evaluated. Besides, this chapter also evaluated the effects of heat treatments on the microstructures and magnetic properties of SLM-processed Fe-3wt.%Si parts.

In Chapter 5, the effects of silicon content on the microstructures and properties of selective laser melted silicon steels with the selected silicon contents of 3.5wt.%, 4.5wt.%, and 5.5wt.% were studied. The effects of annealed treatment on the microstructures, DC and AC magnetic properties of these SLMed silicon steels were also investigated and described.

Finally, the conclusions and perspectives for future work are presented

# Content

<b>Acknowledgments.....</b>	<b>I</b>
<b>General introduction.....</b>	<b>III</b>
<b>Content .....</b>	<b>V</b>
<b>List of figures .....</b>	<b>IX</b>
<b>List of tables .....</b>	<b>XV</b>
<b>Symbols .....</b>	<b>XVII</b>
<b>Chapter 1 Bibliography.....</b>	<b>1</b>
1.1 Introduction to magnetism .....	1
1.1.1 Magnetic fields.....	1
1.1.2 Magnetic induction.....	1
1.1.3 Magnetic materials and their important magnetic properties .....	3
1.2 Soft magnetic materials.....	5
1.2.1 The characteristics of soft magnetic materials .....	5
1.2.2 Classification and development.....	5
1.3 Iron silicon (Fe-Si) alloys .....	8
1.3.1 Crystallographic basis .....	8
1.3.2 Applications and traditional manufactured techniques .....	10
1.3.3 Potential applications and manufacturing techniques in electrical drive .....	13
1.4 Introduce to additive manufacturing .....	15
1.5 Introduce status and progress of additive manufactured soft magnetic materials...	16
1.6 The advanced technologies of metal additive manufacturing.....	17
1.6.1 Laser Engineered Net Shaping (LENS) .....	17
1.6.2 Electron beam melting (EBM) .....	18
1.6.3 Selective laser sintering/melting (SLS/M) .....	19
1.7 Fabrication of soft magnetic alloys via SLM technique from mixed powders .....	23
1.8 Selective laser melted soft magnetic alloys using pre-alloyed powders .....	25
1.8.1 Soft magnetic alloys based on Fe-Si .....	25
1.8.2 Other soft magnetic alloys and components.....	39
1.9 Conclusions.....	40
1.10 Objectives and motivation of this study.....	40
References of Chapter 1 .....	41
<b>Chapter 2 Materials characterization and experimental techniques .....</b>	<b>53</b>
2.1 Characterization of the raw materials .....	53
2.2 The SLM system.....	55
2.2.1 Introduce to the utilized machine .....	55
2.2.2 Working principle and main processing parameters.....	56
2.3 Materials characterization.....	57
2.3.1 Top surface morphology and porosity analysis .....	57
2.3.2 Microstructural characterization.....	57
2.3.3 Phase analysis.....	58
2.4 Post heat treatment.....	58
2.5 Measurement and study of magnetic properties .....	59
2.5.1 Test of magnetic properties using VSM method .....	59
2.5.2 Test of magnetic properties by AC method .....	59
2.5.3 Test of DC magnetic properties.....	61
2.6 Measurement and study of mechanical properties.....	61

---

2.6.1	Microhardness .....	61
2.6.2	Tensile test.....	61
	References of Chapter 2 .....	62
<b>Chapter 3 Effect of processing parameters on surface morphology, microstructure, and the magnetic properties of Fe-3wt.%Si alloys manufactured by selective laser melting .....</b>		<b>65</b>
3.1	Introduction.....	65
3.2	Preliminary experiment and selection of processing parameters .....	66
3.3	The influence of laser energy density on the surface morphology, microstructure and microhardness.....	68
3.3.1	Macroscopic morphology and surface roughness .....	69
3.3.2	Analysis of manufacturing defects .....	71
3.3.3	Evolution of the microstructures .....	73
3.3.4	Evolution of microhardness.....	77
3.4	Study of magnetic properties .....	78
3.4.1	Coercivity .....	78
3.4.2	Saturation magnetization.....	79
3.5	Summary .....	80
	References of Chapter 3 .....	81
<b>Chapter 4 Investigation on microstructures, properties, and heat treatment of SLMed Fe-3wt.%Si soft magnet.....</b>		<b>85</b>
4.1	Introduction.....	85
4.2	Experimental details.....	86
4.3	Microstructure and oriented magnetic properties analysis.....	87
4.3.1	Porosity and microstructure analysis.....	87
4.3.2	Study of magnetic anisotropy and crystallographic texture .....	88
4.4	Mechanical properties.....	92
4.4.1	Microhardness and tensile properties .....	92
4.5	Effect of heat treatment on the microstructures and magnetic properties.....	94
4.5.1	Microstructural evolution after heat treatment .....	94
4.5.2	Magnetic properties after heat treatment.....	101
4.6	Summary .....	105
	References of Chapter 4 .....	105
<b>Chapter 5 Effects of silicon content on the microstructures and properties of selective laser melted silicon steels .....</b>		<b>109</b>
5.1	Introduction.....	109
5.2	Materials and methods .....	109
5.3	Evolution of microstructures.....	109
5.4	Evolution of magnetic properties.....	111
5.5	Mechanical properties.....	113
5.5.1	Microhardness .....	113
5.5.2	Tensile properties .....	113
5.6	Effect of post-treatment on microstructure and magnetic properties.....	115
5.6.1	Microstructural evolution after heat treatment .....	115
5.6.2	Magnetic properties after heat treatment.....	117
5.7	Summary .....	120
	References of Chapter 5 .....	120
<b>Conclusions and perspectives .....</b>		<b>123</b>

Conclusions .....	123
Effect of processing parameters on surface morphology, microstructure, and the magnetic properties of Fe-3wt.%Si alloys manufactured by selective laser melting .....	123
Microstructures, magnetic properties, and mechanical properties of selective laser melted Fe-3wt.%Si soft magnet .....	124
Effects of silicon content on the microstructures and properties of selective laser melted silicon steels .....	124
Prospects and perspectives .....	125
<b>List of publications .....</b>	<b>127</b>
<b>Abstract .....</b>	<b>129</b>
<b>Résumé .....</b>	<b>131</b>



## List of figures

### Chapter1 Bibliography

Figure 1.1 Magnetic field lines: (a) around a single loop of current carrying a conductor, (b) around a solenoid, and (c) convention for finding which end of a solenoid acts as the north pole and the south pole [3].	1
Figure 1.2 An electric current $I$ in a wire generates a magnetic field measurable as magnetic field strength $H$ : (a) general view, (b) cross-sectional view [4].	2
Figure 1.3 (a) Magnetic field around a loop of current, (b) a computer simulation of the cross-section showing the magnetic field lines [4].	2
Figure 1.4 An example of a coil: (a) solenoid, (b) a computer simulation of the cross-section showing the magnetic field lines inside the solenoid [4].	3
Figure 1.5 A typical hysteresis loop [13].	4
Figure 1.6 A brief history of soft magnetic materials (not exhaustive, adapted from [9]).	6
Figure 1.7 Saturation magnetic induction in iron-nickel alloys [39].	6
Figure 1.8 Some commercial toroidal ferrite magnetic cores (adapted from [9]).	7
Figure 1.9 Two views of soft magnetic materials: (a) A row of three wound toroidal inductors mounted on a printed circuit board, (b) Magneto-optical Kerr effect image of the magnetization pattern on the surface of an amorphous alloy soft magnet, credits: (left to right) Billonll/Istock [9].	8
Figure 1.10 Variation in electrical resistivity of iron with the addition of selected impurities [58, 60].	8
Figure 1.11 Kubaschewski phase diagram for the Fe-Si system [72].	9
Figure 1.12 Superlattice crystal lattice of high silicon steel. For the disordered $A_2$ phase, Fe and Si can sit in any of the plotted sites. For $B_2$ , Fe prefers the sites denoted by solid black dots and gray dots, while Si prefers the sites denoted by gradient dots and open dots. For $DO_3$ , Si prefers the sites denoted by open dots, while Fe prefers all the other sites [68].	9
Figure 1.13 Soft magnetic materials applications market, by end-user industry, global, 2019 (%) [23].	11
Figure 1.14 Global soft magnetic materials market share, by product, 2019 (%) [75].	11
Figure 1.15 Two main applications for silicon steel: (a) transformers/inductors, (b) motors/generators.	12
Figure 1.16 (a) Steps in the traditional manufacturing process, (b) its demonstration for a motor core [25].	13
Figure 1.17 Twin motor of Audi e-tron S sportback series [93].	14
Figure 1.18 Volkswagen's innovative electric motor based on modular electric drive matrix [94].	14
Figure 1.19 Technological roadmap of AM [101].	15
Figure 1.20 Examples of AM parts for electrical machine (a) mechanical and thermal management assemblies [112, 113]; (b) coils/windings: [117, 118]; (c) permanent magnets (PM) [119, 120], (d) stator/rotor packs: [122, 124].	16
Figure 1.21 Diagram of LENS [159].	18
Figure 1.22 Schematic EBM system [168].	19
Figure 1.23 Diagram of schematic SLS/M system [161].	20
Figure 1.24 Example parts for biomedical applications: (a) MUTARS revision hip cup (courtesy of Implantcast GmbH) [187], (b) Individual hip implant in titanium (courtesy of SLM Solutions Group AG) [188].	21

Figure 1.25 Example parts for aerospace applications: (a) Combustion chamber in SuperDraco thruster engine, (b) Leap fuel nozzle in GE90 jet engine, (c) Monolithic Thrust Chamber - Cell Core GmbH, (d) Gooseneck Kueger Flap Actuation Bracket - Asco Industries [191-194] ..	21
Figure 1.26 (a) E-Drive Housing from Porsche, (b) a brake panel for a train From the company Wabtec [195] .....	22
Figure 1.27 Commercial laminated 8-pole SRM rotor and identical 3D printed rotor .....	22
Figure 1.28 SEM micrographs showing the microstructure of laser melting samples of FeNi alloy with scanning velocity: (a) 0.1 m/s, (b) 0.4 m/s, (c) 1.6 m/s and laser melting power 110 W [203] .....	23
Figure 1.29 (a) Crystallite size of Fe-80wt.%Ni versus laser scanning velocity, (b) Saturation magnetization and coercivity curves for Fe-80wt.%Ni alloy with laser scanning velocity [203] .....	24
Figure 1.30 SEM micrographs of metallic powders: (a) pre-alloyed Fe-6.9wt.%Si, (b) pure iron Fe (99.9%), (c) Fe-wt.% Si powder blend [204] and (d) Main components for the assembly of the SLMed soft magnetic rotor core, (e) Fully assembled 3D printed SRM rotor (Fe-5.0wt.%Si) [197] .....	24
Figure 1.31 Evolution of porosity: the optical micrographs of different SLMed Fe-6.9wt.Si samples (left) and alongside the values of percent porosity and cumulative crack length c.c.l. (right) [209] .....	25
Figure 1.32 Pole figures (PF) showing the preferred orientation of the <001> crystallographic direction of SLMed Fe-6.9wt.Si sample[209].....	26
Figure 1.33 (a), (b) EBSD maps; (c), (d) IPFs for the front and top views of SLMed Fe-6.9wt.Si sample S280 (Left: BD, Right: SDx and SDy) [209] .....	27
Figure 1.34 (a) SEM image of the investigated region, (b) EDX spectrum corresponding to region 1, (c) and chemical composition in the three regions under exam, of SLMed Fe-6.9wt.Si [209] .....	27
Figure 1.35 (a)-(c) Schematics of the scan patterns, (d) microstructures from the thin wall SLMed Fe-3Si samples [129].....	28
Figure 1.36 EBSD of the bulk cross-sections showing inverse pole figures of SLMed Fe-3Si specimens (top) and pole figures (bottom) for both scan patterns both normal (XY-plane) and parallel to the BD (XZ-plane) [129].....	29
Figure 1.37 Results of magnetic characterization of the two bulk (Fe-3Si) cross-sections with different scan patterns: (a) the hysteresis loss coefficients as a function of peak polarization, (b) the eddy current loss coefficient as a function of peak polarization, (c) the fraction of total losses accounted for by the eddy current development as a function of peak polarization for an operating frequency of 60 Hz [129].....	29
Figure 1.38 SEM micrographs representing microstructural evolution of the SLMed Fe-6.9wt.%Si samples after annealing for 1 h at: (a) 620 °C, (b) 700 °C, (c) 900 °C, (d) 900 °C with subsequent quenching [214].....	30
Figure 1.39 EBSD maps and PFs for SLMed Fe-6.9wt.%Si samples annealed 1h at 700 °C (a) front view, (b) top view and 1150 °C (c) front view, (d) top view; and Evolution of the magnetic properties with annealing temperature: (e) $\mu_{\max}$ , (f) $B_{10}$ and $B_{50}$ , (g) $H_c$ and $B_r$ , (h) power losses at $B_{\max}=1T$ and $f=50Hz$ (adapted from [211, 212]) .....	31
Figure 1.40 Influence of BPH temperature on the microstructure (average grain size $D_{50}$ ) and magnetic properties of $H_c$ and $\mu_{\max}$ for Fe-6.7wt.%Si parts (a) as-built state, (b) after annealing at 1150 °C for 1 h [108].....	32
Figure 1.41 Inverse pole figure maps for the Hilbert curve thin wall design: (a) Fe-3Si as-fabricated grain structure, (b) Fe-3Si annealed structure, and (c) Fe-6Si annealed structure [216].....	32

Figure 1.42 Inverse pole figure maps for the Hilbert transformer cores after annealing (a) Fe-3Si, (b) Fe-6Si [216] and Magnetic test results (c) maximum effective permeability for the HIP heat-treated samples, (d) total loss density at an applied field of 3000 A/m (adapted from [129]) .....	33
Figure 1.43 Variations of printed ring samples for magnetic characterization [217] .....	34
Figure 1.44 (a) Schematics of the complex thin wall Fe-3Si samples and (b) SLM-build thin wall cross-sections for magnetic characterization, Comparison of the loss behavior for bulk, thin wall, and mesh cross-sections (c) the hysteresis loss coefficient, (c) the eddy current loss coefficient as a function of peak polarization, and (e) a magnified view of the eddy current loss coefficients (adapted from [129]).....	35
Figure 1.45 (a) SLM-build Fe-6wt.%Si thin wall cross-sections for magnetic characterization, (b) transformer core dimensions in mm (c) schematic of the Hilbert cross-section for thin and thick legs, (d) a finished SLM build (d) a partially assembled core after machining (adapted from [216]) .....	35
Figure 1.46 (a) the measured hysteresis loss coefficients and (b) eddy current loss coefficients, as well as (c) the power losses per unit mass for 60 Hz operation, (d) Power losses per unit mass of the transformer cores compared to the simple Hilbert cross-sections (Fe-6Si, adapted from [216]).....	36
Figure 1.47 (a-b) Schematic illustration of surface insulation formed through sol-gel process (c) uniaxial compression, (d) magnified cross-sectional optical (d) SEM image, (e) corresponding EDS element mapping, (f) $M_s$ of structurally-layered SMCs depending on several stacked shells [152] .....	37
Figure 1.48 The photograph, EBSD map and SEM images of permalloy-80 built at different geometries: (a) (d) and (g) $\langle 100 \rangle$ geometry (b), (e) and (h) are $\langle 110 \rangle$ geometry, (c), (f) and (I) are designed according to $\langle 111 \rangle$ geometry. All the scalebars represent 200 $\mu\text{m}$ [218] ...	39
Figure 1.49 SLM rotor active part and shaft of a PM motor (Fe-Co alloy) [25].....	40
Figure 1.50 Example of an SMCs multilayered structures: (a) Schematic illustration, (b) AM Prototype of alternating layers of FeSi6.7, and FeAl16 (OM image shows part of the cross-section) [108].....	40
Figure 2.1 Laser diffraction powder sizer .....	53
Figure 2.2 Characterization of Fe-3wt.%Si: (a) morphology and cross-section of the particles, (b) particle size distribution, (c) the results of EDS.....	54
Figure 2.3 Characterization of Fe-3.5wt.%Si: (a) morphology and EDS mapping (b) cross-section of the particles, (c) the results of EDS, (d) particle size distribution .....	54
Figure 2.4 Characterization of Fe-4.5wt.%Si: (a-d) and Fe-5.5wt.%Si (e-h): (a) (e) morphology and EDS mapping (b) (f) cross-section of the particles, (c) (g) the results of EDS, (d) (h) particle size distributions.....	55
Figure 2.5 XRD spectra of the raw powders .....	55
Figure 2.6 (a) The utilized SLM system, (b) working chamber .....	56
Figure 2.7 (a) SLM manufacturing process, (b) Schematic diagram of scanning strategy and parameters .....	56
Figure 2.8 The profilometer system .....	57
Figure 2.9 (a) The optical microscope and (b) scanning electron microscopy.....	57
Figure 2.10 The X-Ray diffractometer .....	58
Figure 2.11 Home-made furnace (PMDM-LERMPS) .....	58
Figure 2.12 A schematic diagram and equipment of the VSM.....	59
Figure 2.13 (a) A schematic of the AC magnetic measurements setup, (b) a measured sample ...	60
Figure 2.14 AC magnetic property measurements system .....	61



Figure 2.15 The microhardness tester.....	61
Figure 2.16 (a) The tensile samples ; (b) static tensile test machine (c) polished SLMed samples for tensile test.....	62
Figure 3.1 (a) Scanning strategy, (b) SLMed specimens.....	66
Figure 3.2 Effect of processing LED on sample porosity: the OM images of different SLMed Fe-3wt.%Si samples fabricated under the parameters of group 1 .....	67
Figure 3.3 Effect of processing LED on sample porosity: the OM images of different SLMed Fe-3wt.%Si samples fabricated under the parameters of group 2 .....	67
Figure 3.4 Effect of processing LED on sample porosity: the OM images of different SLMed Fe-3wt.%Si samples fabricated under the parameters of group 3 .....	67
Figure 3.5 Effect of processing LED on sample porosity: the OM images of different SLMed Fe-3wt.%Si samples fabricated under the parameters of group 4 .....	68
Figure 3.6 The evolution of porosity of different SLMed Fe-3wt.%Si samples (a) group1, (b) group2, (c) group3, (d) group4.....	68
Figure 3.7 (a) 3D model of ring sample, (b) scanning strategy, (c) some samples .....	69
Figure 3.8 Macroscopic morphology and SEM images of surface morphology of SLMed samples at different LED: (a) Macroscopic morphology of the SLMed samples, (b) 150 J/m, (c) 210 J/m, (d) 300 J/m, (e) 420 J/m, (f) 540 J/m.....	70
Figure 3.9 Three-dimensional surface topographies and the values of roughness of the SLMed parts at different LED: (a) 150 J/m, (b) 210 J/m, (c) 300 J/m, (d) 420 J/m, (e) 540 J/m, (f) the values of roughness .....	71
Figure 3.10 OM images of cross-sectional (XZ plane) at different LED and porosity rate of SLMed specimens at different LED: (a) 150 J/m, (b) 210 J/m, (c) 300 J/m, (d) 420 J/m, (e) 540 J/m, (f) porosity rate changes as a function of laser energy density.....	72
Figure 3.11 Magnification OM images of XZ plane for SLMed specimens at different LED: (a) 210 J/m, (b) 540 J/m.....	72
Figure 3.12 OM images (XY plane) of the SLMed parts at different LED and 3D physical model of the samples: (a) 150 J/m, (b) 210 J/m, (c) 300 J/m, (d) 420 J/m, (e) 540 J/m, (f) 3D physical model of the samples .....	74
Figure 3.13 OM images of the microstructures (XZ plane) the SLMed specimens and 3D physical model of the samples: (a) 150 J/m, (b) 210 J/m, (c) 300 J/m, (d) 420 J/m, (e) 540 J/m, (f) 3D physical model of the samples.....	75
Figure 3.14 SEM images of the microstructures (XZ plane) of the SLMed specimens and 3D physical model of the samples (a-e): (a) E150, (b) E210, (c) E300, (d) E420, (e) E540; (f) The 3D physical model of the samples.....	76
Figure 3.15 SEM images of the high magnification for representative microstructures (XZ plane) at different LEDs: (a) 300 J/m, (b) 540 J/m .....	76
Figure 3.16 The results of EDS for the SLMed samples.....	77
Figure 3.17 Microhardness of the SLM parts prepared at the different LED.....	78
Figure 3.18 The value of coercivity changes as a function of laser energy density for SLMed Fe-3wt.% Si samples .....	79
Figure 3.19 Hysteresis loops of the initial powder and SLMed samples, the right set shows the enlargement part in the low magnetic field region .....	80
Figure 3.20 The value of saturation magnetization changes as a function of laser energy density for SLMed Fe-3wt.% Si samples .....	80
Figure 4.1 (a) 3D model, (b) an SLM fabricated sample for tensile test.....	87
Figure 4.2 OM images of the SLMed samples (a-c) XY plane, (d-f) XZ plane.....	87

Figure 4.3 The EBSD maps of grain structure and average grain size of SLMed Fe-3wt.%Si specimen in different planes (a-c) XY plane, (d-f) XZ plane.....	88
Figure 4.4 (a) XRD pattern, (b) phase composition from EBSD .....	88
Figure 4.5 The hysteresis loops of SLM produced sample along with three directions of measurements .....	89
Figure 4.6 The magnetization curves in different measured directions and their enlarged-view graphs of low magnetic field .....	89
Figure 4.7 The pole figures (PF) of two different planes (a) XY plane, (b) XZ plane .....	90
Figure 4.8 EBSD maps and IPFs (a) XY plane, (b) XZ plane.....	91
Figure 4.9 The magnetization curves of the single Bcc-iron crystal [28].....	92
Figure 4.10 (a) A simple cubic crystal structure, (b) A simple schematic diagram of SLMed part with cubic texture .....	92
Figure 4.11 Vickers microhardness of SLMed sample.....	93
Figure 4.12 Tensile stress-strain curves for SLMed Fe-3wt.%Si part.....	93
Figure 4.13 Fracture morphologies of the SLMed Fe-3wt.%Si part observed by SEM .....	94
Figure 4.14 Microstructure of the SLMed Fe-3wt.%Si samples observed via SEM after etching: (a-b) SLMed as-built sample, (c-d) SLMed AT750/3h sample, (e-f) SLMed AT850/3h sample .....	95
Figure 4.15 Microstructure of the SLMed Fe-3wt.%Si samples observed via SEM after etching: (a-b) SLMed as-built sample, (c-d) SLMed AT1000/1h sample, (e-f) SLMed AT1000/3h sample, (g-h) SLMed AT1000/5h sample.....	96
Figure 4.16 Microstructure of XY plane for SLMed Fe-3wt.%Si sample (a) as-built, (b) AT1000/3h .....	96
Figure 4.17 (a) SEM image of microstructure after etching, (b) EDS analysis of the SLMed Fe-3wt.%Si as-built sample .....	97
Figure 4.18 Microstructure under the high magnification of the SLMed Fe-3wt.%Si specimens observed via SEM after etching: (a-b) SLMed as-built specimen, (c-d) SLMed AT750/3hspecimen, (e-f) SLMed AT850/3h specimen .....	98
Figure 4.19 Microstructure under the magnification of the SLMed Fe-3wt.%Si specimens observed via SEM after etching: (a-b) SLMed as-built specimen, (c-d) SLMed AT1000/1h specimen, (e-f) SLMed AT1000/3h specimen, (g-h) SLMed AT1000/5h specimen .....	99
Figure 4.20 The pole figures (PF) after heat treatment of two different planes (a) XY plane, (b) XZ plane .....	100
Figure 4.21 EBSD maps and IPFs after heat treatment (a) XY plane, (b) XZ plane.....	100
Figure 4.22 XRD analysis of SLMed Fe-3wt.%Si magnets.....	101
Figure 4.23 The evolution of measured DC hysteresis loops of the SLMed Fe-3wt.%Si ring specimens .....	102
Figure 4.24 (a) The evolution of maximum relative permeability, and (b) the evolution of coercivity for SLMed Fe-3wt.%Si specimens before and after different annealed treatments .....	102
Figure 4.25 The evolution of saturation magnetic induction and remanence for SLMed Fe-3wt.%Si magnets before and after different annealed treatments .....	103
Figure 4.26 The evolution of the power losses in dynamic conditions of SLMed Fe-3wt.%Si magnets before and after different annealed treatments.....	104
Figure 5.1 The representative OM images of the microstructures of XZ planes without etching for the SLMed silicon steels (a) Fe-3.5wt.%Si, (b) Fe-4.5wt.%Si, (c) Fe-5.5wt.%Si, and after etching (d) Fe-3.5wt.%Si, (e) Fe-4.5wt.%Si, (f) Fe-5.5wt.%Si .....	110
Figure 5.2 The representative SEM images of the microstructures of XZ planes after etching for the SLMed silicon steels (a) Fe-3.5wt.%Si, (b) Fe-4.5wt.%Si, (c) Fe-5.5wt.%Si .....	110

---

Figure 5.3 The DC hysteresis loops of three SLMed silicon steels under different Si content ....	111
Figure 5.4 The evolution of DC magnetic properties for three SLMed silicon steels under different Si content .....	112
Figure 5.5 The evolution of AC power losses for three SLMed silicon steels under different Si content .....	112
Figure 5.6 The average values of microhardness including XY planes and XZ planes of the SLMed silicon steel parts with different Si content .....	113
Figure 5.7 The stress strain curves of the different SLMed silicon steels .....	114
Figure 5.8 Fracture morphology of the SLMed silicon steel samples under different Si content observed using SEM: (a-c) SLMed Fe-3.5wt.%Si silicon steel, (d-f) SLMed Fe-4.5wt.%Si silicon steel, (g-i) SLMed Fe-5.5wt.%Si silicon steel .....	115
Figure 5.9 Microstructure of the SLMed Fe-3.5wt.%Si samples observed via SEM after etching: (a-d) as-built sample, (e-h) AT1000/3h sample .....	116
Figure 5.10 Microstructure of the SLMed Fe-4.5wt.%Si samples observed via SEM after etching: (a-d) as-built samples, (e-h) AT1000/3h samples .....	116
Figure 5.11 Microstructure of the SLMed Fe-5.5wt.%Si samples observed via SEM after etching: (a-d) as-built samples, (e-h) AT1000/3h samples .....	116
Figure 5.12 XRD spectra of the SLMed as-built samples and AT1000/3h samples.....	117
Figure 5.13 The measured DC hysteresis loops of three types of SLMed silicon steels (a) Fe-3.5wt.%Si, (b) Fe-4.5wt.%Si, (c) Fe-5.5wt.%Si .....	118
Figure 5.14 The evolution of the (a) $\mu_{max}$ , (b) $H_c$ of the different SLMed silicon steel samples before and after annealing .....	118
Figure 5.15 The evolution of the (a) $B_s$ , (b) $B_r$ of the different SLMed silicon steel samples before and after annealing .....	119
Figure 5.16 The evolution of the power losses $P_{50-1}$ in dynamic conditions .....	119

---

## List of tables

### Chapter1 Bibliography

Table 1.1 Partial list of commercial soft magnetic materials with specific properties, and AMed manufacturing methods in the recent reports .....	17
Table 1.2 The properties of SLMed Fe-Si alloys reported in recent years .....	37
Table 2.1 The nominal composition of the powders.....	55
Table 3.1 The preliminary SLM parameters.....	66
Table 3.2 The detailed parameters.....	68
Table 4.1 The optimized linear energy density and SLM parameters .....	86
Table 4.2 Overview of the SLMed Fe-3wt.%Si samples and treated condition.....	86
Table 4.3 The average values of magnetic properties of SLM produced Fe-3wt.%Si alloy at different measured directions .....	89
Table 4.4 The statistical mechanical properties of SLMed Fe-3wt.%Si alloy.....	93
Table 4.5 Chemical composition in the five points under exam.....	97
Table 4.6 The detailed values of magnetic properties for SLMed Fe-3wt.%Si magnets before and after different annealed treatments .....	104
Table 5.1 The detailed average values of all measured DC magnetic properties and AC magnetic properties of the SLMed silicon steels .....	113
Table 5.2 The statistical values regarding the mechanical properties of the SLMed silicon steels .....	114
Table 5.3 The detailed average values of these magnetic properties for the SLMed samples after annealing at 1000 for 3 h.....	119



## Symbols

AM	Additive manufacturing
SLM	Selective laser melting
LED	Linear energy density
SLMed	Selective laser melted
H	Magnetic field
B	Magnetic induction
I	Electric current
l	Length
N	The number of wires
$\mu_0$	The magnetic permeability of the vacuum
M	Magnetization
M <sub>s</sub>	Saturation magnetization
M <sub>r</sub>	Remanent magnetization
B <sub>r</sub>	Remanent induction
B <sub>s</sub>	Saturation magnetic induction
H <sub>c</sub>	Coercivity
P <sub>50-1</sub>	Total power losses at excitation frequency f=50 Hz and maximum flux density B=1 T
$\mu_{\max}$	Maximum permeability
AC	Alternating current
DC	Direct current
SMCs	Soft magnetic composites
K	Magnetic anisotropy constant
$\lambda$	Magnetostriction constants
BD	Build direction
OM	Optical microscope
SEM	Scanning electron microscopy
EDS	Energy-dispersive X-ray spectroscopy
XRD	X-Ray diffraction
EBSD	Electron back-scattering diffraction
VSM	Vibrating sample magnetometer
UTS	Ultimate tensile strength
YS	Yield strength
EL	Elongation at break



## Chapter 1 Bibliography

Chapter I will introduce the current research progress of selective laser melting (SLM) technology to produce iron-based soft magnetic alloys. First, an introduction of magnetism and magnetic properties, especially, soft magnetic materials were provided. Then an introduction and review on additive manufacturing (AM) technology, especially the working principle, advantages, and applications of the SLM technique were presented. Finally, a state-of-the-art review on the production of SLM-produced soft magnetic alloys and composites was introduced. The objectives and researched contents were also described.

### 1.1 Introduction to magnetism

#### 1.1.1 Magnetic fields

The concept of the magnetic field is one of the most fundamental basics of magnetism. A magnetic field is produced whenever there is an electrical charge in motion. This can be due to an electrical current flowing in a conductor for example, as was first discovered by Oersted in 1819 [1]. A magnetic field is also produced by a permanent magnet. In this case, there is no conventional electric current, but there are the orbital motions and spins of electrons (the so-called 'Amperian currents') [2]. More specifically, when a field is generated in a volume of space it means that the energy of the volume has changed, and there is an energy gradient so that a force is produced which can be detected by the acceleration of an electric charge moving in the field, by the force on a current-carrying conductor, by the torque on a magnetic dipole such as a bar magnet or even by a reorientation of spins on electrons within certain types of atoms [3].

Magnetic fields are usually produced by solenoids or electromagnets, as shown in Figure 1.1, for a visual representation, the magnetic field is often depicted by magnetic field lines [3]. A solenoid is made by winding a large number of turns of insulated copper wire, or a similar electrical conductor, in a helical fashion on an insulated tube known as a 'former'. Solenoids are often cylindrical. An electromagnet is made in a similar way except that the windings are made on a soft ferromagnetic material, such as soft iron. The ferromagnetic core of an electromagnet generates a higher magnetic [3, 4].

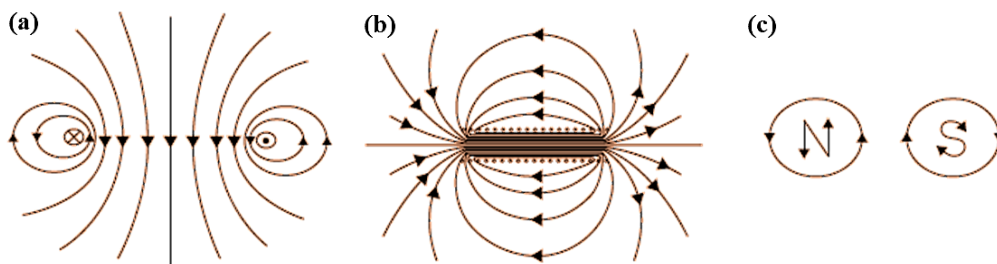


Figure 1.1 Magnetic field lines: (a) around a single loop of current carrying a conductor, (b) around a solenoid, and (c) convention for finding which end of a solenoid acts as the north pole and the south pole [3].

#### 1.1.2 Magnetic induction

When a magnetic field  $H$  has been generated in a medium by a current, following Ampere's law, the response of the medium is its magnetic induction  $B$ , also sometimes called the flux density. All media will respond with some induction and, the relation between magnetic induction and the magnetic field is a property called the permeability of the medium. Free space shall also be considered to be a medium since a magnetic induction is produced by the presence of a magnetic field in free space. The lines encircle the conductor with current, and the magnetic field strength,  $H$ , is always generated in a direction (and plane) perpendicular to the current causing it [3].



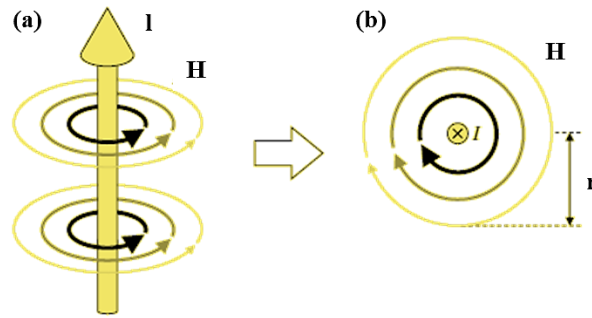


Figure 1.2 An electric current  $I$  in a wire generates a magnetic field measurable as magnetic field strength  $H$ : (a) general view, (b) cross-sectional view [4]

The strength of the magnetic field at a given point in space depends on the magnetic path length  $l$ , measured in meters (m), through which the field travels. From the example shown in Figure 1.2, path  $l$  increases proportionally with the distance  $l$ . At any point in space, a magnetic field can be described quantitatively by a value of magnetic field strength,  $H$ . From the Maxwell equations (describing the laws of electromagnetism), the magnetic field strength can be derived for the configuration shown in Figure 1.2, and for an infinitely long conductor, the magnetic field strength at a given point is [5, 6]:

$$H = \frac{I}{l} = \frac{I}{2\pi r} \quad \text{Equation 1.1}$$

If instead of a single wire, there are  $N$  closely positioned parallel wires carrying the same current  $I$  (e.g., as in a multi-stranded wire), therefore,

$$H = N \frac{I}{l} \quad \text{Equation 1.2}$$

When the current is 'wrapped' in a coil, the field inside such a loop is intensified due to the contributions from all the sides (Figure 1.3).

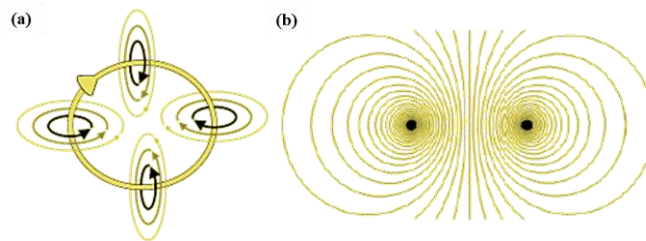


Figure 1.3 (a) Magnetic field around a loop of current, (b) a computer simulation of the cross-section showing the magnetic field lines [4]

It can be calculated that, at the center of such a single-turn flat loop with radius  $r$ , the magnetic field strength is equal to

$$H = N \frac{I}{l} \quad \text{Equation 1.3}$$

Besides, the current loops can be placed one after another in a series, creating a long coil or a solenoid (Figure 1.4). The magnetic field lines are concentrated inside the solenoid where the resulting magnetic field is the most uniform.

It can be derived mathematically that, for an infinitely long solenoid wound with a negligibly thin wire, the magnetic field strength at the geometrical center (inside the solenoid) is equal to [7]

$$H = \frac{NI}{l} \quad \text{Equation 1.4}$$

where  $N$  is the number of turns,  $I$  is the current (A) and  $l$  is the length of the solenoid.

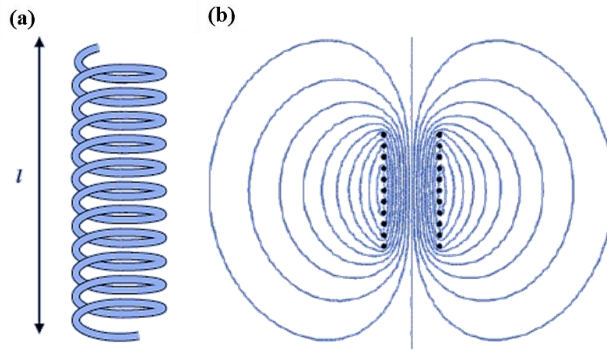


Figure 1.4 An example of a coil: (a) solenoid, (b) a computer simulation of the cross-section showing the magnetic field lines inside the solenoid [4]

Whenever a magnetic field is present in free space there will be a magnetic flux. This magnetic flux is measured in units of Webers and its rate of change can be measured since it generates an electromagnetic field in a closed circuit of a conductor through which the flux passes. It can be considered that the magnetic flux is caused by the presence of a magnetic field in a medium. Any medium exposed to a magnetic field is magnetized – that is, it responds with flux density,  $B$ . Substances consist of atoms, and these are spaced out by some distances so that a certain amount of ‘free space’ is present in any matter [3, 4, 8]. Hence, for a medium other than free space, the correlation between  $B$  and  $H$  should be written as a combination of the contributions from the free space (the  $\mu_0 \cdot H$  component) and the response of the material or substance (the  $\mu_0 \cdot M$  component) [7]. The defining relationship between the three magnetic field vectors is:

$$B = \mu_0(H + M) = \mu_0 H + J \quad \text{Equation 1.5}$$

where  $\mu_0$  is the magnetic permeability of the vacuum,  $B$  is the magnetic flux density or induction,  $H$  is the magnetic field,  $M$  is the magnetization or volume density of the magnetic moment, and  $J$  ( $\mu_0 M$ ) is the magnetic polarization. In materials science, it is more common to represent magnetic response in terms of  $M$ , whereas device technology most often uses  $J$ , which is analogous to the polarization ( $P$ ) in dielectric materials. The response of magnetic materials can be represented in terms of  $M(H)$ ,  $B(H)$ , or  $J(H)$ . Within this magnetic response is embedded a complex mix of processes that includes domain wall motion, rotation of magnetic moments, and eddy current losses [8, 9].

### 1.1.3 Magnetic materials and their important magnetic properties

Traditionally, only those materials that exhibit ferromagnetic or ferrimagnetic properties are called “magnetic.” Magnetic materials are broadly separated into two categories: soft and hard. When the magnetization processes (domain wall motion and domain magnetization rotation) occur in weak fields, the material is called a soft magnetic material or soft magnet. In some magnetic materials, the coercivity can be as high as  $2 \times 10^6$  A/m. Such materials resist demagnetization (once magnetized) and therefore are called hard magnetic materials or permanent magnets. Materials having the highest possible saturation magnetization, remanence, and coercive force are used as permanent magnets. The usefulness of a permanent magnet is determined by the magnetic energy it can deliver at various flux densities. These high-energy hard magnetic materials are employed in a host of different devices in a variety of technological fields, such as motors. Other common devices that employ these magnetic materials are speakers in audio systems, lightweight earphones, hearing aids, and computer peripherals. The permanent magnets are also used in instruments like galvanometers, ammeters, voltmeters, wattmeters, compasses, electron beam focusing and positioning, telephones, loudspeakers, eddy current brakes, etc. Soft magnetic materials are used for the construction of cores for electric machines, transformers, electromagnets, reactors, relays, etc. The economic construction of such equipment demands that the

magnetic flux should be produced in the minimum space and with minimum loss. This study is mainly focused on soft magnetic materials.

The most common way to represent the bulk magnetic properties of a magnetic material is by a plot of magnetic induction  $B$  for various field strengths  $H$ . Alternatively plots of magnetization  $M$  against  $H$  are used, but these contain the same information since  $B = \mu_0(H + M)$  [3, 10]. Hysteresis in iron was first observed by Warburg [11]. The term hysteresis, meaning to lag, was introduced by Ewing [12] who was the first to systematically investigate it. A typical hysteresis loop is shown in Figure 1.5.

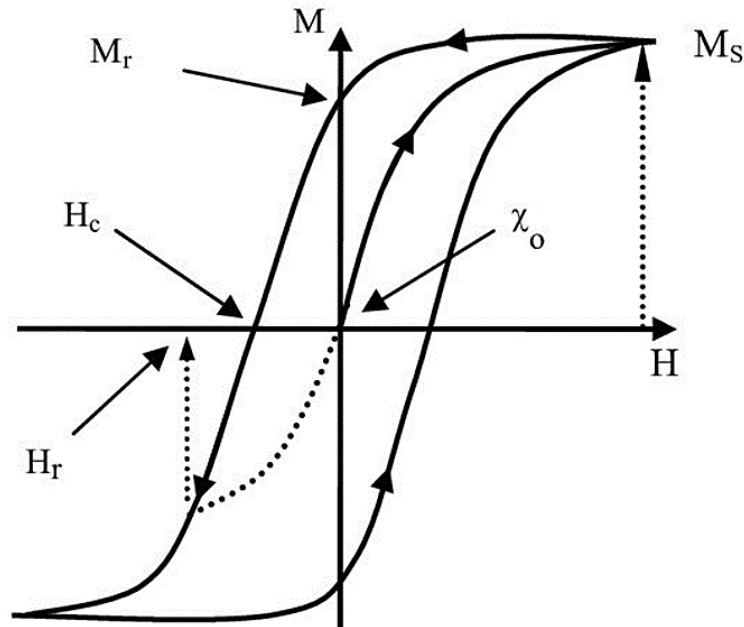


Figure 1.5 A typical hysteresis loop [13]

To characterize the properties of a given magnetic material it is necessary to measure the magnetic induction  $B$  as a function of  $H$  over a continuous range of  $H$  to obtain a hysteresis curve [14]. As displayed in Figure 1.5, it can be seen that the magnetic material in its initial state is not magnetized. The application of magnetic field  $H$  increases the magnetic induction in the direction of a magnetic field. If  $H$  is increased indefinitely the magnetization eventually reaches saturation. In this condition, all the magnetic dipoles within the material are aligned in the direction of the magnetic field  $H$ . The saturation magnetization ( $M_s$ ) is dependent only on the magnitude of the atomic magnetic moments and the number of atoms per unit volume [3, 15]. In another word, the  $M_s$  is the maximum magnetic moment per unit volume for a magnetic material. This intrinsic property is an important factor for soft magnetic applications since large values allow miniaturization [16].

The remanent induction (remanence,  $B_r$ ) or magnetization ( $M_r$ ) is used to describe the remaining induction or magnetization when the field has been removed after magnetization. The remanence becomes the upper limit for all remanent inductions or magnetizations [3, 6].

$$B_r = \mu_0 M_r \quad \text{Equation 1.6}$$

The coercivity ( $H_c$ ) is strongly dependent on the condition of the sample, being affected by such factors as heat treatment or deformation [17]. As with the remanence a distinction is drawn by some authors between the coercive field (or coercive force), which is the magnetic field needed to reduce the magnetization to zero from an arbitrary level, and the coercivity which is the magnetic field needed to reduce the magnetization to zero from saturation [3, 18]. Historically, the total magnetic loss was conceptually separated into three components: hysteresis, eddy currents, and excess [4, 19]. The hysteresis loss is related to domain walls. During magnetization, they are created and annihilated as well

as their movements are impeded by pinning sites such as impurities and crystal dislocations. Clearly for alternating current (AC) applications in which energy dissipation should be minimized the hysteresis loss should be as low as possible. This loss is closely related to coercivity so the processing of materials to reduce coercivity also reduces the hysteresis loss [20]. The eddy currents are always generated inside conducting material exposed to a varying magnetic field. For an idealized simplified case, such loss can be calculated from the first principles; hence this is often referred to as the classical eddy current loss [3, 21]. Indeed, Eddy current effects are dominant in metallic soft magnetic, where the principal magnetization process is just the eddy-current-damped motion of magnetic domain walls [22].

## 1.2 Soft magnetic materials

### 1.2.1 The characteristics of soft magnetic materials

Soft magnetic alloys are materials that are easy to magnetize and demagnetize. Coercivity is the parameter that is used to distinguish hard and soft magnetic materials. According to the international standard IEC 60404-1 (IEC, 2000) [23], soft magnetic materials are those materials with coercivity less than 1 kA/m. They are 'soft' because they can be magnetized to high values of B with low excitation. Broadly 'hard' magnetic materials were those with coercivities above 10 kA/m [4]. In an electrical machine, the magnetic losses or core losses are due to the soft magnetic material operating in a time-varying magnetic field. Core losses are made up of eddy current losses that arise from circulating electrical currents induced in conducting materials (the electrical steel used in the stator and copper used in the motor windings) and magnetic hysteresis losses which are proportional to the enclosed area of the B-H loop of the particular material [24].

The most important properties of soft magnetic materials, in addition to high reliability, low cost, and suitability for mass production just like other commercial products, the details are as follows:

- (1) high saturation magnetization;
- (2) low coercivity;
- (3) high initial/maximum permeability ( $\mu_{\max}$ );
- (4) low power losses;
- (5) high Curie temperature.

To realize or improve these properties, soft magnetic materials are alloyed with other materials and heat-treated to optimize microstructures. This process introduces defects, grain boundaries, and impurities that hinder magnetic domain wall movement and significantly impair magnetic properties [25-27].

### 1.2.2 Classification and development

The brief history of soft magnetic materials is summarized graphically in Figure 1.6, but it is by no means exhaustive. Magnetic iron and Fe-C alloys are also called low-carbon steel with carbon content are below 0.10wt.%, sometimes are also simply as soft iron [28]. They are the earliest soft magnetic materials, which have been used since the 1800s [29]. The common impurity elements in soft iron are O, N, Si, P, S, Mn, and Al [30]. They are still used nowadays due to their high saturation induction and lowest costs, although their original usage as the core material of transformers, generators, and motors is mostly substituted by Si-steels. The iron-silicon magnetic alloys were first investigated by Barrett, Brown, and Hadfield in 1900, they invented nonoriented silicon steel by adding up to 3% silicon to the iron and increasing its electrical resistivity while also increasing  $M_r$  [31, 32]. Since then, the soft magnetic alloy has entered the market. Often, aluminum is used as an additional intermediate grade because it promotes grain growth, which can lead to lower losses and higher electrical resistivity [30, 33]. The properties of aluminum-iron are very similar to those of silicon-iron, but since the economic cost of using aluminum is higher than silicon at that time, these alloys are unlikely to replace silicon iron in applications where they both compete. Furthermore, the presence of  $Al_2O_3$  particles in iron-

aluminum alloys causes rapid wear of punching dies, which is disadvantageous in the production process. They are used in electrical steel for special applications [3, 34].

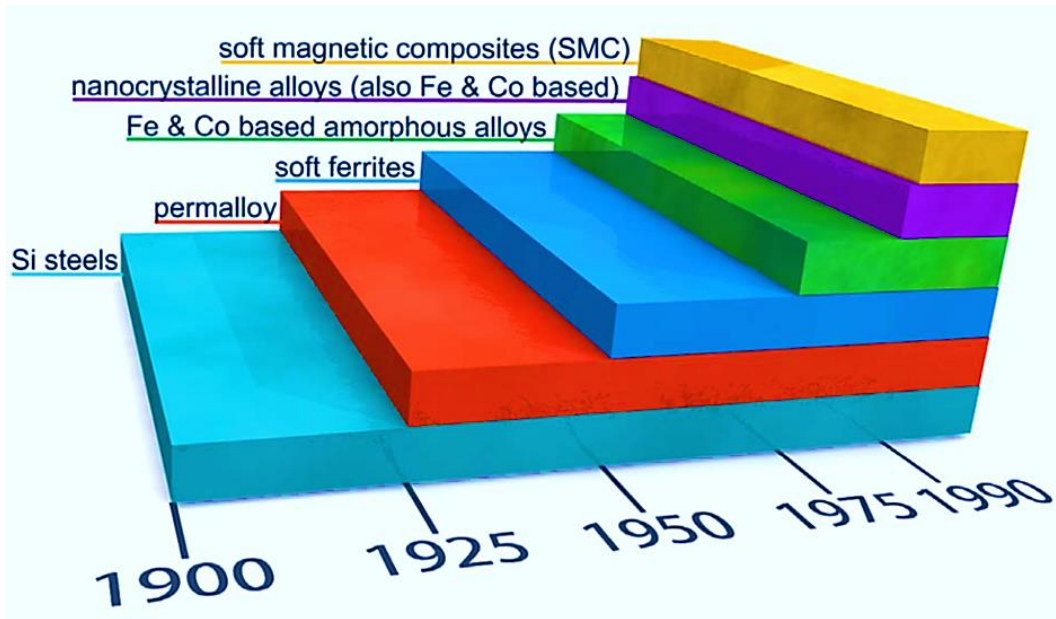


Figure 1.6 A brief history of soft magnetic materials (not exhaustive, adapted from [9])

In the 1910s, Gustav Elmen et al. studied nickel-iron alloys (permalloys) and discovered the nickel-rich (78%) permalloy composition [35]. Permalloys are well known to have superior soft magnetic properties in terms of losses, magnetic permeability, magnetic field annealing response [36], and lower saturation magnetization but are more expensive than Si steels [37]. The saturation magnetic induction in iron-nickel alloys is represented in Figure 1.7. At present, the definition of permalloys has been extended to the alloys with Ni proportions ranging from 35% to 90% which contain small amounts of other elements [25, 38]. Most commercial permalloys within these Nickel-iron alloys are still used in some specialty inductive applications today but are not common in power electronics and electrical machines [8, 9].

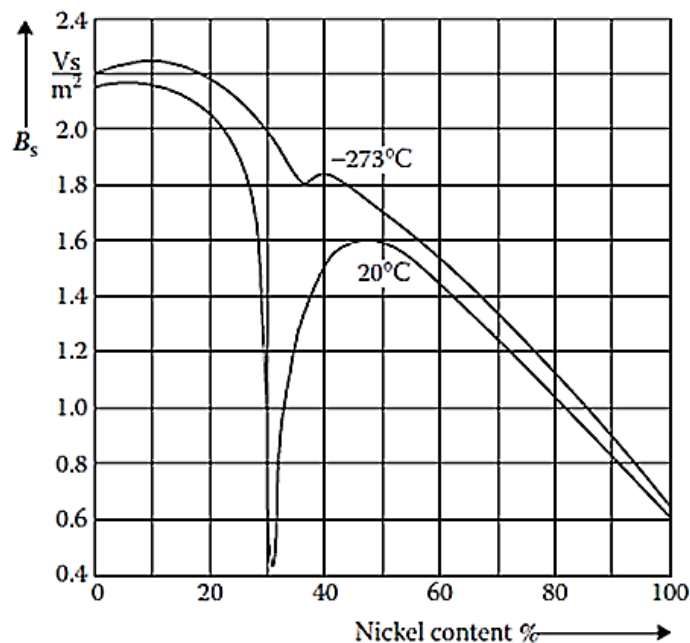


Figure 1.7 Saturation magnetic induction in iron-nickel alloys [39]

In the late 1940s, J. L. Snoek [40] invented magnetically soft ferrites. Soft magnetic ferrites are cubic spinel structures with low coercivity ceramics formed by alloying Ni-Zn, Mn-Zn, or Co-Zn with magnetite ( $\text{Fe}_3\text{O}_4$ ) [41, 42]. Since their higher electrical resistivity, ferrites are very popular in high-frequency electrical components such as transformer cores and inductive toroidal cores in antenna [9, 25, 43]. Some commercial toroidal ferrite magnetic cores are illustrated in Figure 1.8.



Figure 1.8 Some commercial toroidal ferrite magnetic cores (adapted from [9])

The first magnetic amorphous Fe–C–P alloy was fabricated by rapid quenching in 1967 [44]. By the mid-1970s, interest in the iron-based and cobalt-based amorphous alloy was surging, and these materials began to be applied [8]. The coercivity of these alloys is substantially reduced due to long-range disorders. They are unsurpassed in terms of high magnetic moments and high Curie temperature applications but are significantly more costly [45, 46]. Hence, they are mostly used for special applications and volume-constrained applications such as aerospace [47, 48]. In 1988, the nanocrystalline soft magnetic alloys were developed by Hitachi (Finemet alloys). It included Nb and Cu additives and added an annealing step to produce small and closely spaced crystallites of iron or cobalt within a matrix of amorphous material [49]. Figure 1.9 are three general commercial wound toroidal inductors and Magneto-optical Kerr effect image of the magnetization pattern on the surface of an amorphous alloy soft magnet. Compared with amorphous alloys, the formation of isolated transition metal grains reduces the eddy current loss of these materials. The market share of amorphous and nanocrystalline alloys in high-frequency power electronics and motors is increasing due to their low loss and competitiveness  $M_s$  [50, 51]. Although the initial cost is higher than that of silicon steel, these advanced alloys can reduce the total lifetime of power electronics and motors due to the reduction of losses [8, 9].

Soft magnetic composites (SMCs) gained acceptance in some soft magnetic applications in the early 1990s [52, 53]. These materials coat or mix magnetic particles including Fe powders and alloys such as Fe-P, Fe-Si, or Fe-Co between  $\sim 1$  and  $500 \mu\text{m}$  in diameter with insulating materials, and then combine them with high voltage. Of course, it can also be heated during or after this process to improve the magnetism [9, 52]. Although these materials have a distributed air gap that limits their relative permeability to a range of 100 to 500, they also have lower eddy current losses. The SMCs can also be pressed into more complex final geometry without any machining, which can greatly reduce

manufacturing costs. They have gained successful applications in rotating electrical machines since their isotropic nature, low cost, and ability to net-shape complex parts [54-57].

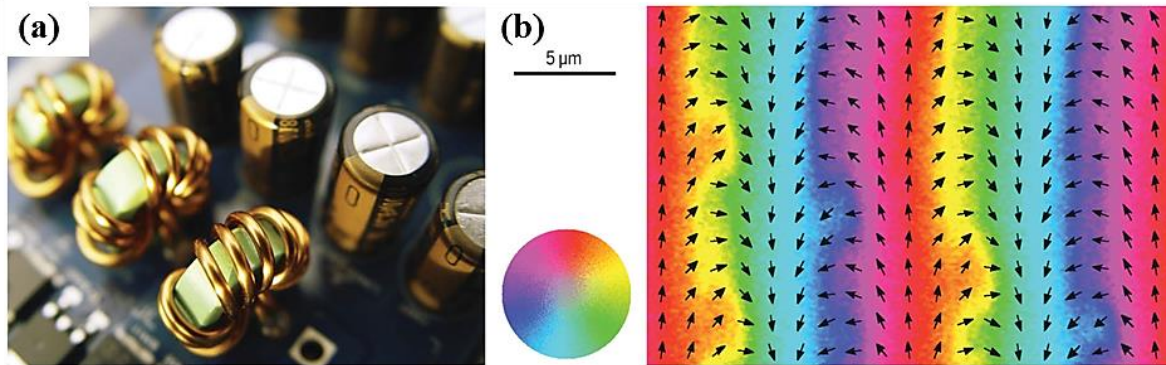


Figure 1.9 Two views of soft magnetic materials: (a) A row of three wound toroidal inductors mounted on a printed circuit board, (b) Magneto-optical Kerr effect image of the magnetization pattern on the surface of an amorphous alloy soft magnet, credits: (left to right) Billion1/Istock [9]

### 1.3 Iron silicon (Fe-Si) alloys

#### 1.3.1 Crystallographic basis

The magnetic Fe–Si alloy is usually called silicon steel or electrical steel. It is useful to modify iron with a small number of selected elements to increase electrical resistivity or change other favorable properties [39]. Figure 1.10 shows that iron, silicon, or aluminum additives produce the most dramatic increase in electrical resistivity [58]. The addition of a small amount of silicon improves the soft magnetic properties of materials, more than 3wt.% Silicon certainly increases the electrical resistivity and further degrades the magnetic anisotropy constant ( $K$ ) and magnetostriction constants ( $\lambda$ ) [39, 59].

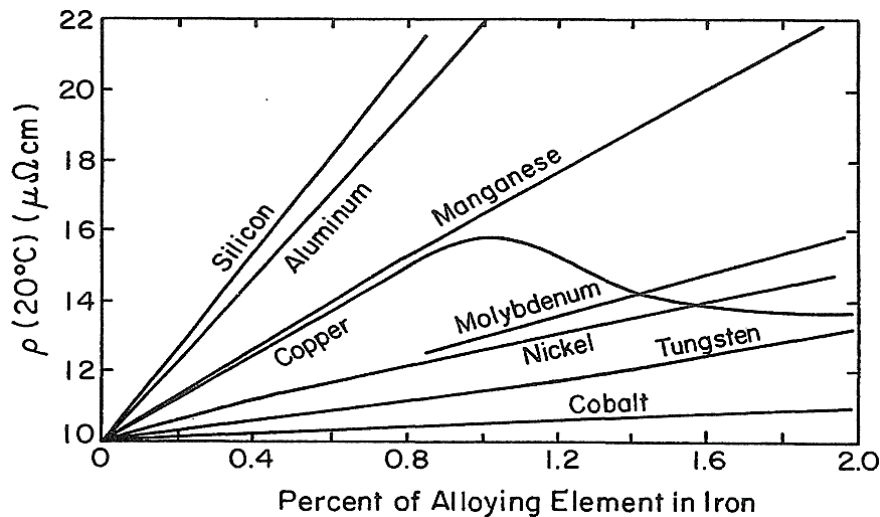


Figure 1.10 Variation in electrical resistivity of iron with the addition of selected impurities [58, 60]

The detailed information of the Fe-Si phase diagram shown in Figure 1.11 indicates that silicon is dissolved in  $\alpha$ -Fe, up about 4wt.% [39, 61, 62]. Behind this limit, the brittle intermetallic  $\text{Fe}_3\text{Si}$  ( $B_2$  or  $\text{DO}_3$ ) phase may also be present. Ductility decreases due to the appearance of the intermetallic  $\text{DO}_3$  [63, 64]. The ordering of Fe-Si can be best described using the superlattice structure consisting of four interpenetrating face-centered cubes (fcc) cells having a lattice parameter twice that of a single bcc cell [65, 66], as depicted in Figure 1.12. The terms  $A_2$ ,  $B_2$ , and  $\text{DO}_3$  are Strukturbericht symbols that specify the structure of a crystal, and represent monatomic bcc  $\alpha$ -Fe, CsCl-type AB compounds, and  $\text{AlFe}_3$ -type  $A_mB_n$  compounds, respectively. The magnetic properties of silicon iron are dependent on the

microstructure and texture [67-69]. These are altered by rolling mechanical treatment and by heat treatment. Depending on the type of rolling and heat treatment silicon iron can be produced in a nonoriented form or a grain-oriented form [3, 70, 71].

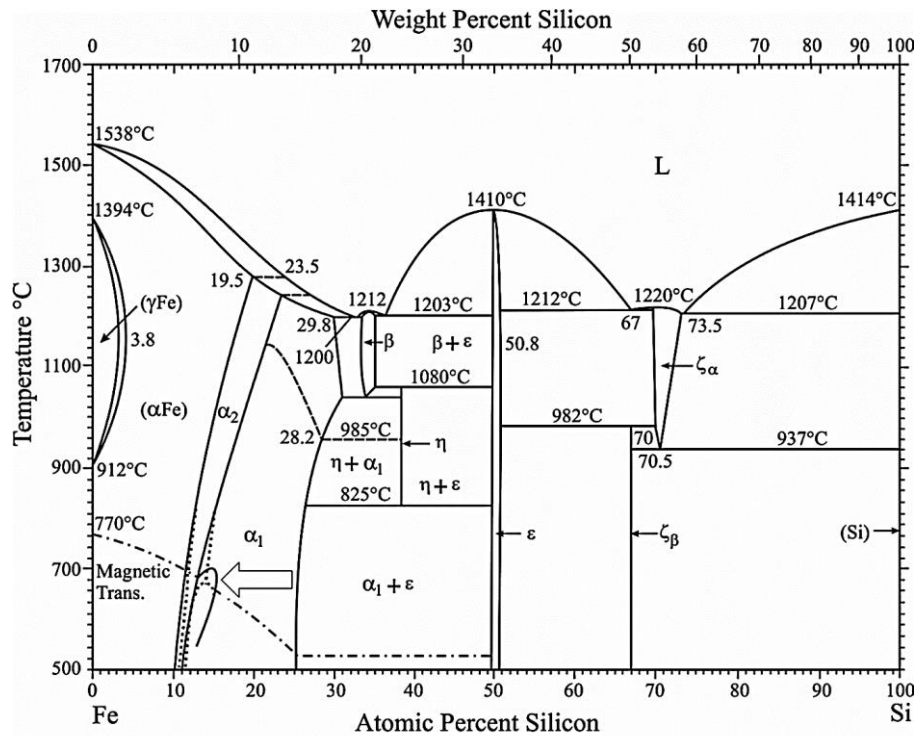


Figure 1.11 Kubaschewski phase diagram for the Fe-Si system [72]

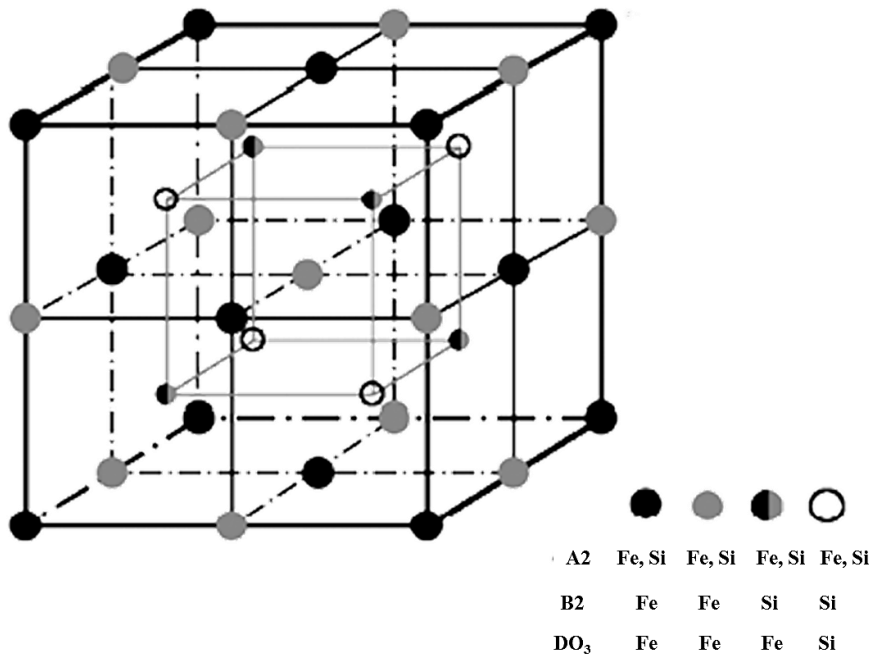


Figure 1.12 Superlattice crystal lattice of high silicon steel. For the disordered A<sub>2</sub> phase, Fe and Si can sit in any of the plotted sites. For B<sub>2</sub>, Fe prefers the sites denoted by solid black dots and gray dots, while Si prefers the sites denoted by gradient dots and open dots. For DO<sub>3</sub>, Si prefers the sites denoted by open dots, while Fe prefers all the other sites [68]



### 1.3.2 Applications and traditional manufactured techniques

Soft ferromagnetic materials are widely used because they can enhance the magnetic flux density generated by an electric current. Therefore, the uses of soft materials are closely related to the generation, transmission, distribution of electrical power, reception of radio signals, microwaves, inductors, relay and electromagnet, and other electrical applications [73, 74]. The basic requirement of achieving good soft magnetic properties with high permeability and low coercivity is the low anisotropy of magnetic materials, which determines the difficulty of changing the direction of the magnetic moment when a magnetic field is applied [68]. From the global soft magnetic material market, it can be known that soft magnetic materials occupy about one-third of the total magnetic materials market [75]. The available range of magnetic properties of soft magnetic materials was expanding, iron and iron silicon alloy are the most widely used, accounting for about 80% of the soft magnetic materials market [50, 76]. More specifically, silicon steel accounts for the majority of the rotating electric machine market (as isotropic non-oriented steel), and its perfect combination of price and performance is suitable for large-scale industrial applications [77, 78]. Fe-Si Alloys with Si content  $< 9.5\text{wt.}\%$  are the main soft magnets employed in various types of electric motor cores due to their relatively high electrical resistivity, near-zero magnetostriction, and low magneto crystalline anisotropy [100] (characterized by high initial permeability). More importantly, reasonable commercial prices and necessary specific power for electrical machines made they are the most suitable materials [79, 80]. At present, the Fe-Si alloy can be processed by the conventional cold rolling process, accounting for about 90% of the low-frequency motor. To be used in high-frequency electric machines, Fe-Si alloy with high silicon content needs high permeability and electrical resistivity [25].

The increasing number of industries and the growing demand for electricity and electronic devices are driving the requirement growth of soft magnetic materials. According to the report [23] of Motor Intelligence, as given by Figure 1.13, in 2019, in the distribution proportion of soft magnetic materials global market in end-use industrial applications, electronic and automotive applications occupied the first and second positions respectively. Furthermore, the market trend of soft magnetic materials can be summarized as follows:

- (1) The usage of soft magnetic material has been increasing in the electronics and energy generation industries. Soft magnetic materials find their application in AC and direct current (DC) converter devices, electric motors, transformers, alternators, power inductors, and computers, amongst others;
- (2) Transformers made of soft magnetic materials transfer electric energy from one circuit to another through electromagnetic induction;
- (3) Soft magnetic materials are also used in various electronic devices such as wireless charging, data storage devices, sensors, high-frequency products amongst others;
- (4) With the rising number of power generation plants in Asia-Pacific, the demand for transformers, actuators, electric motors have increased significantly in recent years;
- (5) Technological advancements in AC and DC electric motors and telecommunications in developed regions promote the demand for advanced materials, which in turn is expected to promote the development of the soft magnetic materials market in the next few years.

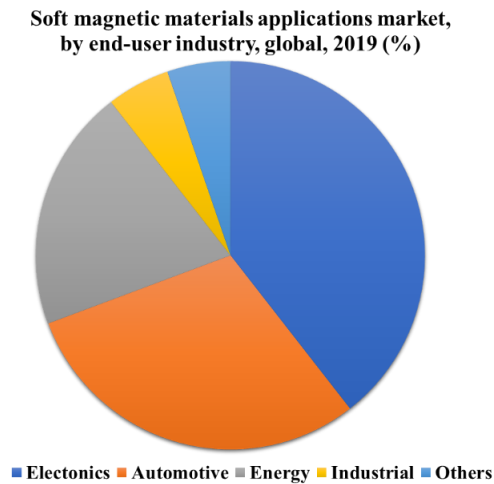


Figure 1.13 Soft magnetic materials applications market, by end-user industry, global, 2019 (%) [23]

Based on the product, the market has been segmented into Fe-Si alloy, ferrites, permalloy alloys, and others. Electrical steel accounted for the highest revenue share of over 60.0% in 2019. Fe-Si alloys find application in transformer cores, since, silicon helps in increasing electrical resistivity and reducing the length of magnetization.

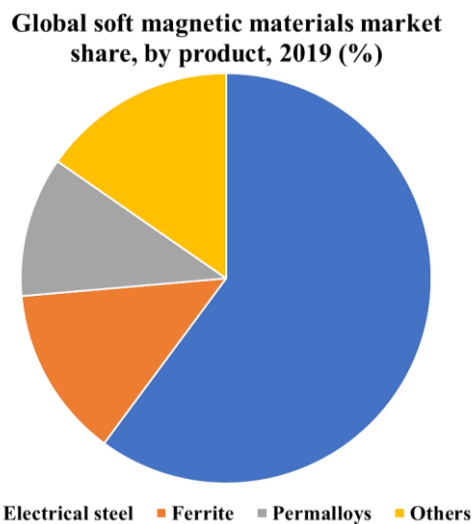


Figure 1.14 Global soft magnetic materials market share, by product, 2019 (%) [75]

The two major uses for Fe-Si alloys are transformers/inductors and motors/generators respectively [81] (see Figure 1.15). More detailly:

- (1) Transformers are used not only for Electrical Power Distribution but in virtually every power supply in every electrically powered electronic device in offices and homes;
- (2) Motors have moved from industrial uses in the 1800s and early 1900s to home and automotive uses. In homes, for example, the motors can be used in garage door openers, washing machines and dryers, furnaces for home heating, refrigerator compressor pumps, bathroom exhaust fans, garbage disposals, and electric-powered shop tools;
- (3) Motor usage in automobiles has expanded to include windshield wiper motors, seat adjusting motors, starters, cooling fans, passenger compartment fans, alternators, etc.

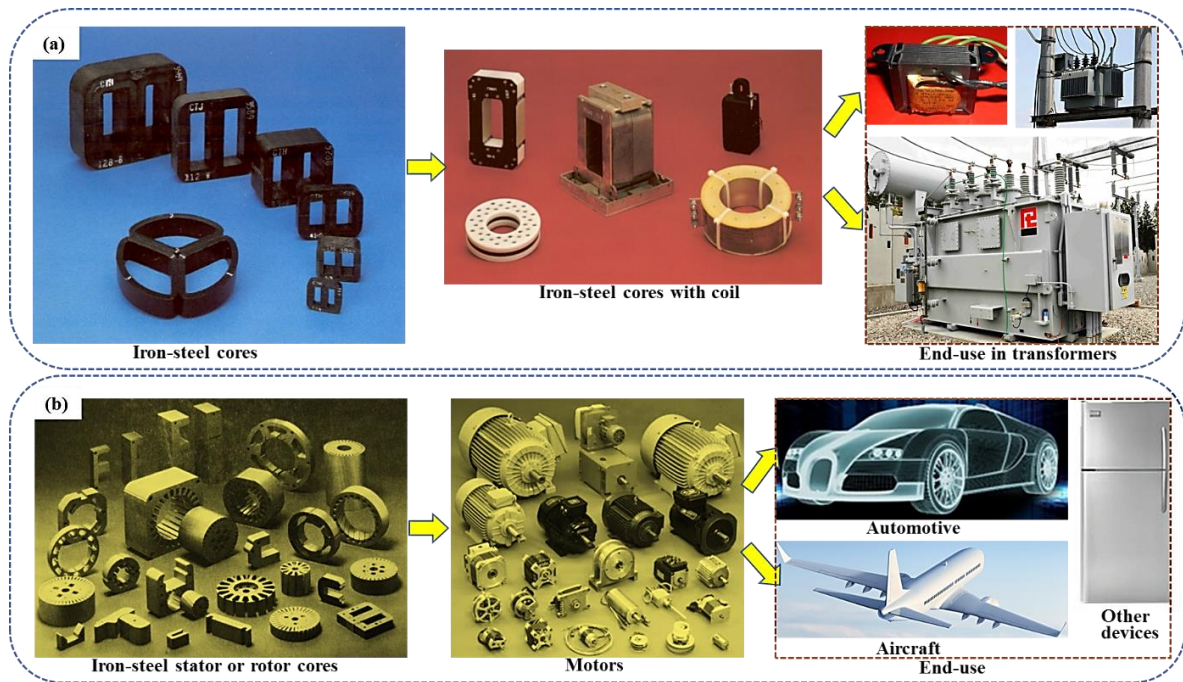


Figure 1.15 Two main applications for silicon steel: (a) transformers/inductors, (b) motors/generators

Nowadays, the traditional production method of these products is rolling silicon steel sheets firstly and then stamping. Figure 1.16 (a) and (b) show the traditional production flow chart of the motors core and transformer [82, 83]. The first step in this process is to produce the Fe-Si sheet with the required thickness for lamination by cold-rolled technique. And then to make a detailed computer-aided design (CAD) drawing of the movement and evaluate it carefully, to determine and develop special precision tools for cutting and punching dies for mold forming and stamping. These sheets are coated with insulating material to prevent the flow of eddy currents. Cutting, stamping, and punching form the sheet into the required size and geometry. The plates are then stacked on the alignment fixture by fixing or welding [84]. As part of quality assurance, stacking usually requires post-machining and heat treatment to prevent deterioration due to stresses caused by stamping, welding, and interlocking, as described in Figure 1.16 (b). In the traditional process, several laminations are individually punched, stacked, measured, die-cast, and finished in a separate process [85]. So labor and production time can be very important. Considering the multiple steps and touch-times, some manufacturers have introduced some automatic stamping, stacking, and laminating, which can reduce the labor counts by 35% and 40% [83].

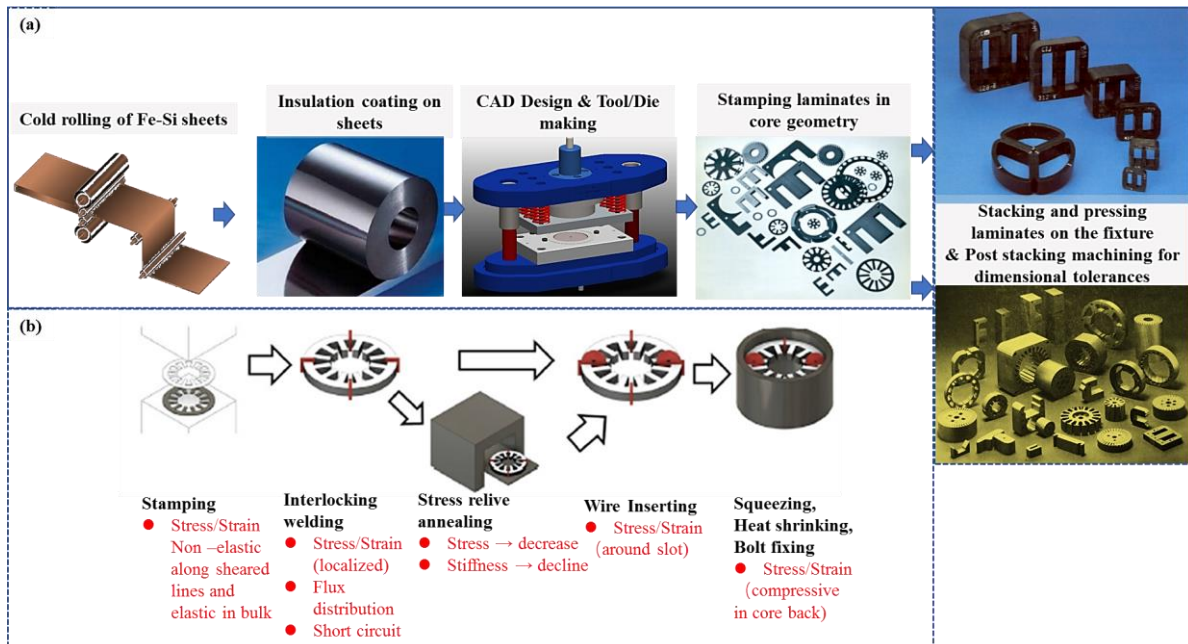


Figure 1.16 (a) Steps in the traditional manufacturing process, (b) its demonstration for a motor core [25]

The lamination of high efficiency and high dynamic electric motors produced by traditional technology exhibit appreciable losses. The core loss can be minimized by using thinner laminations, however, thinner materials require more rolling steps, further stress relief annealing, and more lamination for a given stack height, resulting in higher manufacturing costs [86]. In addition, excessive rolling increases the brittleness of the steel and imposes a practical lower limit on the usable thickness of the lamination (about 0.1-0.5 mm thick). The second key limitation is the loss of dimensional accuracy due to burrs and warps caused by stamping and stacking operations. The alternative method of stamping is wire electrical discharge machining (EDM), but this increases the cost of the mold, so mass production is required to justify this cost. In addition, when the laminations are shaped into a complex design, it results in significant waste [87, 88].

### 1.3.3 Potential applications and manufacturing techniques in electrical drive

With the growing interest in the electrification of clean energy technologies (such as wind power generation) and the use of pure electric power systems in various applications, the demand for the next-generation, high-performance soft magnetic materials has risen significantly [25]. The electric vehicle is a safe, economic and green transportation tool based on electric drive. It has unique advantages and competitiveness in energy and environment, and can easily use modern control technology to realize its mechatronics, which has broad development prospects. The motor drive system is the power source of the electric vehicle, which is the main body and internal basis to determine the performance index of the vehicle. At present, electric vehicle motor mainly includes DC motor, induction motor, permanent magnet brushless motor, and switched reluctance motor (SRM). The newest example of lamination steel used in cars is the electric drive motor of hybrids or fully electric vehicles [89, 90]. The core material non-oriented silicon steel sheet is the key material of the drive motor, and its performance affects the drive characteristics and service performance of the drive motor. The core material non-oriented silicon steel sheet is the key material of the drive motor, and its performance affects the drive characteristics and service performance of the drive motor. It requires not only excellent magnetic properties but also high strength. In addition, the brush motor is also required to have a certain friction performance [91, 92].

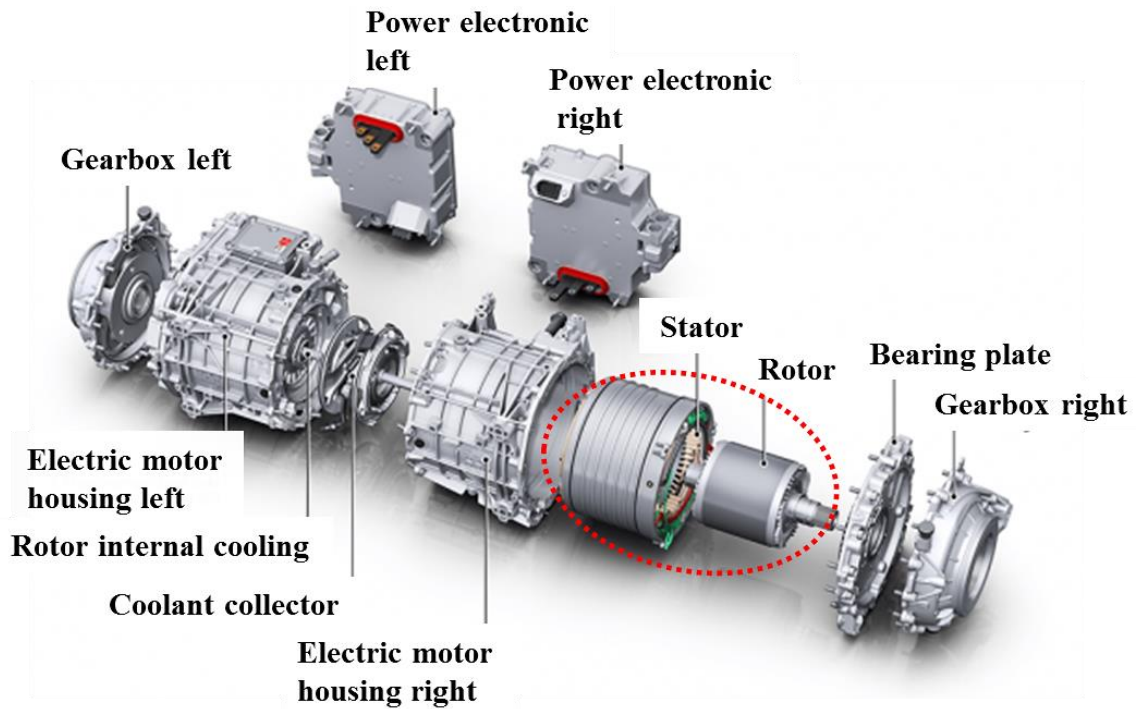


Figure 1.17 Twin motor of Audi e-tron S sportback series [93]

With the continuous development of electric vehicles, more and more kinds of motors need to be designed and used. As shown in Figure 1.17 and Figure 1.18, they are two kinds of decomposition diagrams for the twin motor of Audi e-trons Sportback series [93] and Volkswagen's innovative electric motor based on modular electric drive matrix (MEB), respectively [94]. It can be seen that the rotor and stator (as indicated by red circles) are the core components of the motor.

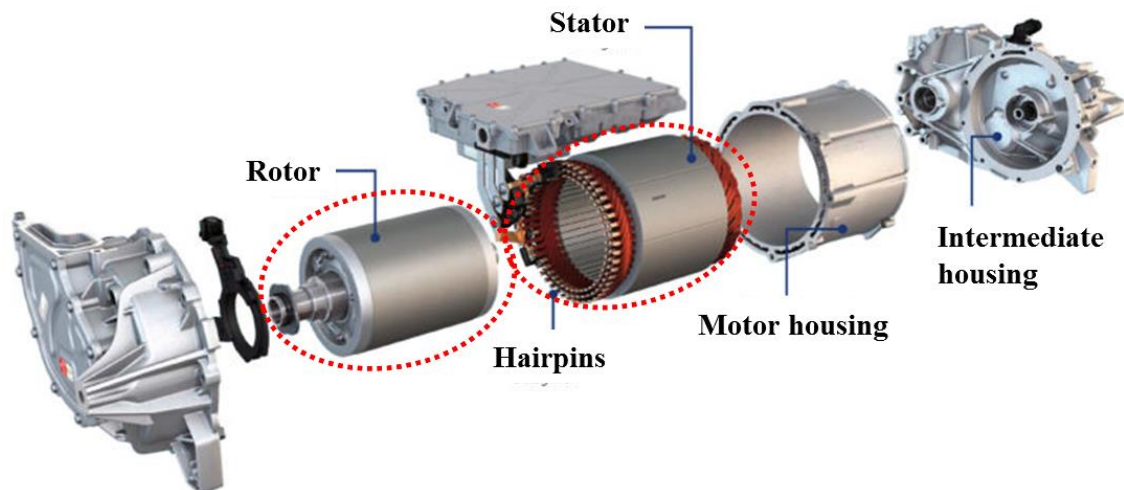


Figure 1.18 Volkswagen's innovative electric motor based on modular electric drive matrix [94]

Of course, in addition to silicon steel, people are constantly seeking and developing more soft magnetic materials to meet these application requirements [95]. Moreover, for high specific power and torque applications, the lamination must provide the same flux, but the material in the yoke and teeth is lower. With the continuous emergence of new material processing methods, motor designers are constantly looking for better-performing manufacturing technologies to provide greater design freedom [96, 97]. Additive manufacturing (AM) technology can certainly solve some of these requirements, and it provides a new opportunity for motor design [25].

## 1.4 Introduce to additive manufacturing

In ISO/ASTM 52900:2017, additive manufacturing also known as 3D printing is defined as a general technology that fabricates substances by continuous addition of raw materials based on 3D model data designed by CAD [98, 99]. Generally, AM includes the manufacturing methods that process materials layer by layer, which is opposed to subtractive manufacturing processing routes [100]. Various types of AM methods have emerged, such as stereolithography (SLA), selective laser sintering (SLS), fused deposition modeling (FDM), laminated object manufacturing (LOM), binder jetting (BJ), and selective laser melting (SLM), etc. The AM materials include promising materials, polymers, metals, ceramics, glasses, biomaterials, and composite materials [101-104]. Figure 1.19 illustrated the technological roadmap of AM.

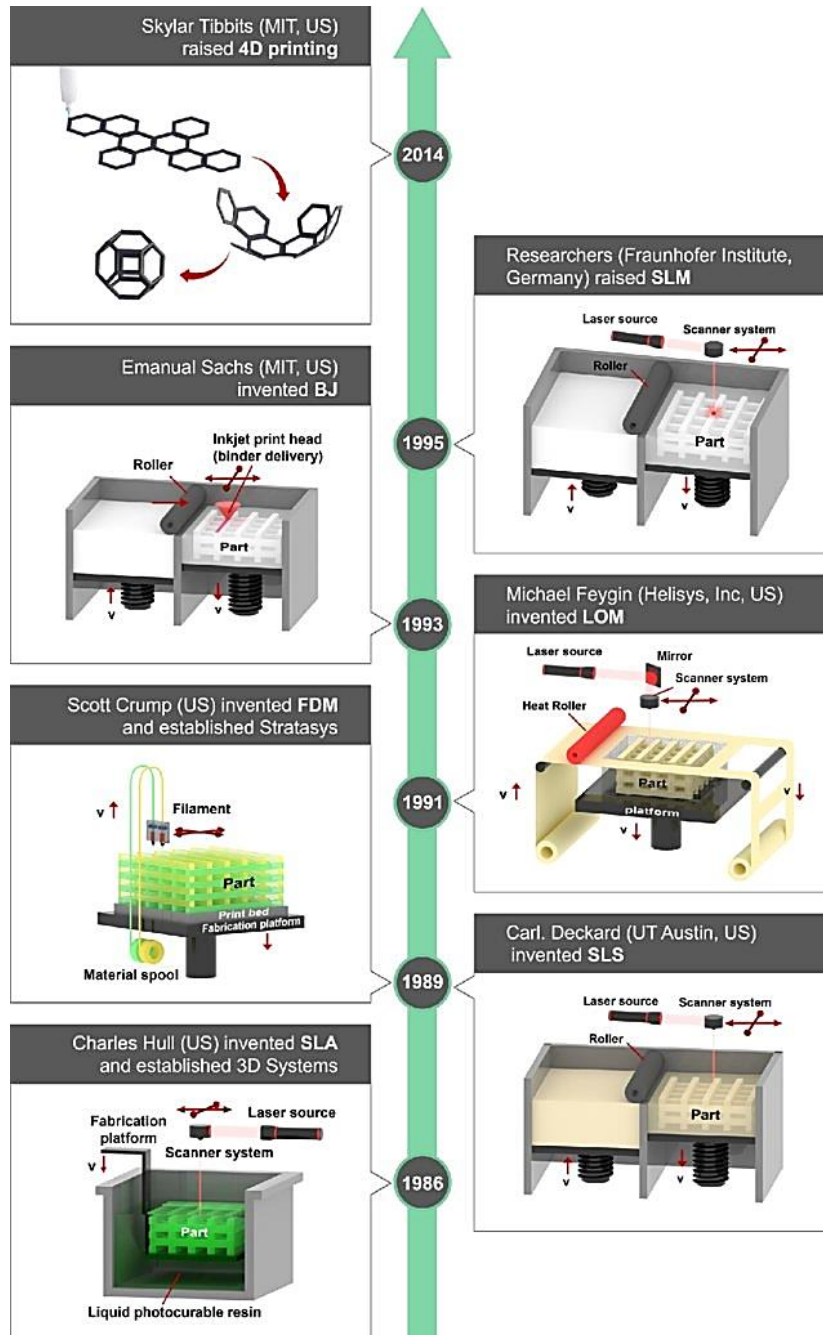


Figure 1.19 Technological roadmap of AM [101]

Compared to traditional industrial processing, like casting and forging, AM has the great ability to produce machinery parts of complex geometries or unify parts to reduce the complex parts count and it can greatly reduce the production cost of developing molds and meet the needs of an industry with individualized demand [105, 106]. It can facilitate the manufacturing of gigantic machines at the installation site and avoid shipping and installation complications. AM can also significantly decrease the materials requirements to produce the parts. Besides, another factor that is important to manufacturing is cost control, especially when processing high-priced materials such as Ti-, Ni- and Cr-based alloys. AM can allow material recycling, which also greatly reduces production costs and improves the market competitiveness of AM products [103, 107]. Similarly, in soft magnetic materials manufacturing, AM can not only provide the net-shaping of complex machine parts but also can facilitate the processing of higher quality alloys [108, 109]. AM has shown a greater potential than conventional manufacturing to improve the functionalities of manufactured parts and components in various applications such as medical, aerospace, and electrical industries [110]. At present, research work has been done on the AM of materials and individual working parts for various electrical machines, like mechanical and thermal management assemblies, coils/windings, permanent magnets (PM), and stator/rotor packs, etc. [111-124], some examples of AM parts for the electrical machine were given by Figure 1.20. But a complete AM-built and user-ready electrical machine, for large scale production and industrial applications, is a feat that is yet to be accomplished owing to a few challenges regarding slow manufacturing speed, internal constructional defects, limited multi-material printing capability and the need for post-processing of printed parts [125, 126].

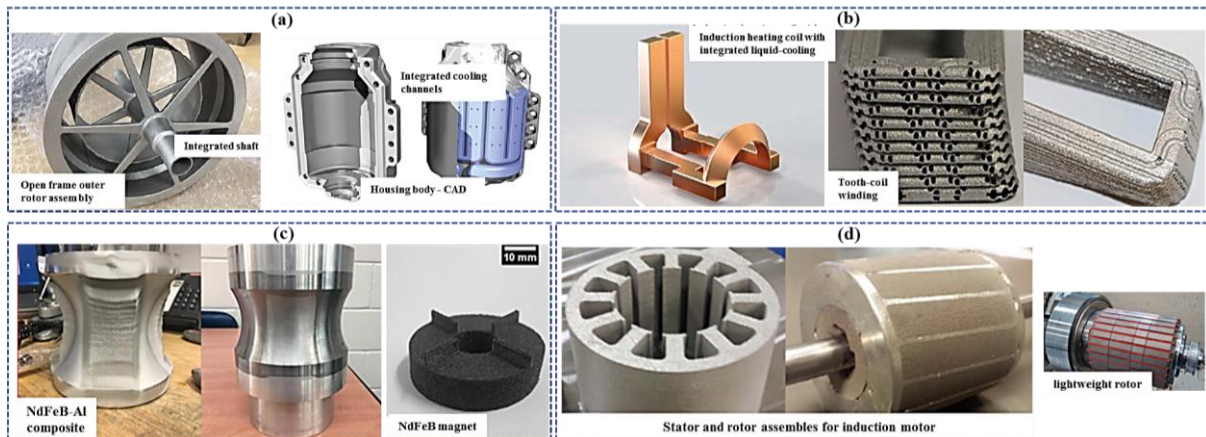


Figure 1.20 Examples of AM parts for electrical machine (a) mechanical and thermal management assemblies [112, 113]; (b) coils/windings: [117, 118]; (c) permanent magnets (PM) [119, 120], (d) stator/rotor packs: [122, 124]

### 1.5 Introduce status and progress of additive manufactured soft magnetic materials

Compared with traditional manufacturing methods, an obvious advantage offered by AM is the elimination of multiple processes resulting in substantially faster production times for machine cores. The absence of traditional tooling and processing is expected to reduce fabrication costs significantly [127]. Many efforts have been focused on developing materials with suitable electromagnetic properties using a variety of methods, including SLM, FDM, and BJT. Other reported processes include cold spray, SLA, and LOM. In these methods, the printing quality was found to be extremely sensitive to process parameters [128-134]. Apart from conventional iron alloys, there have been ongoing efforts to explore printing techniques for SMCs [108, 135]. Several other research efforts [135-137] focused their attention on additive designs and printed soft magnet materials for motors. Soft ferrites could replace insulating materials in electrical laminates as a small 3D-printed boundary layer between the electrical steel layers. Among several available reports on AM for soft magnets and electric machines [38, 113, 136, 138-140],

it is observed that SLM and its variants, including laser powder bed fusion (LPBF) and laser engineered net shaping (LENS), are the most extensively practiced methods [25, 133, 141-143]. The following Table 1.1 lists partial subcategories of commercial grade materials with specific properties and their AMed methods in the recent reports [25].

Table 1.1 Partial list of commercial soft magnetic materials with specific properties, and AMed manufacturing methods in the recent reports

Materials families & Ref.		Density (g/cc)	Magnetic properties			
			$\mu_r$	$M_s$ (T)	$\rho$ ( $\mu\Omega\text{cm}$ )	AM types & Ref.
Ferrites	NiZnFe <sub>2</sub> O <sub>4</sub>	-	15-2000	0.22-0.44	(1.26-6.84) $\times 10^{11}$ [144]	FDM [145] FDM+UV cure [146]
Fe-Ni based alloys	Permalloy	-	8000-120000 [35]	1.08	-	SLM [38, 147]
	Supermalloy [148]	-	40,000 - 100,000	0.66-0.82	-	SLM [149, 150]
Fe-Si based alloy	Fe-3%Si	7.34	25	2.15	20-60 [151]	SLM [25, 129]
	Fe-6.5Si	7.3-7.7	10,700	1.8	82 [151]	SLM [152] BJT [153]
Fe-Co based alloy	Permendur (Supermendur) [154]/Hyperco [155] 49% Fe-49% Co-2% V	8.12	20000-66000	2.4	40	SLM [109, 156]
SMC and other soft magnets	SMC, <1% lubrication, Fe balanced [151]	7.57	-	0.71-1.22	20000	SLM [156]

$\mu_r$ : Relative permeability;  $M_s$ : Saturation magnetization;  $\rho$ : Core resistivity; SMC: soft magnetic composite; FDM: fused deposition modeling; SLM: selective laser melting; BJT: binder jetting technology; AM: additive manufacturing.

## 1.6 The advanced technologies of metal additive manufacturing

AM can expand the applications of metals by forming complex structures, reducing the number of required structural components and production costs, and shortening the processing timescale. It is necessary to get a better scientific understanding of AM-produced components and broaden its industrial application.

### 1.6.1 Laser Engineered Net Shaping (LENS)

LENS is also named directed energy deposition (DED) or laser consolidation (LC). It was initially created at the Sandia National Laboratories in 1998 [157]. LENS is used to build elements into a laser, primarily laser cladding using a metal powder feed either by gravity or by using a pressurized carrier gas. Through a highly intense laser beam into a molten metal pool, the manufacturing method takes place for oxygen-free operation in a low-pressure argon chamber [158]. As a schematic diagram of the LENS illustrates in Figure 1.21, a movement scheme drives a platform through x and y planes (two-dimensional) as the laser beam traces the cross-section of the fabricated portion [159, 160]. LENS has many industrial applications like rapid prototyping, rapid tooling, and dissimilar metal joining [161]. Series of materials like nickel-based alloys [162], ferrous alloys [163], titanium alloy [164], and



intermetallic compounds [165] have been investigated and developed by the LENS technique. Compared to other AM technologies like SLS, LENS can break through the limitation of size and produce super-large parts. However, the drawback is the high cost of this technique and lower resolution.

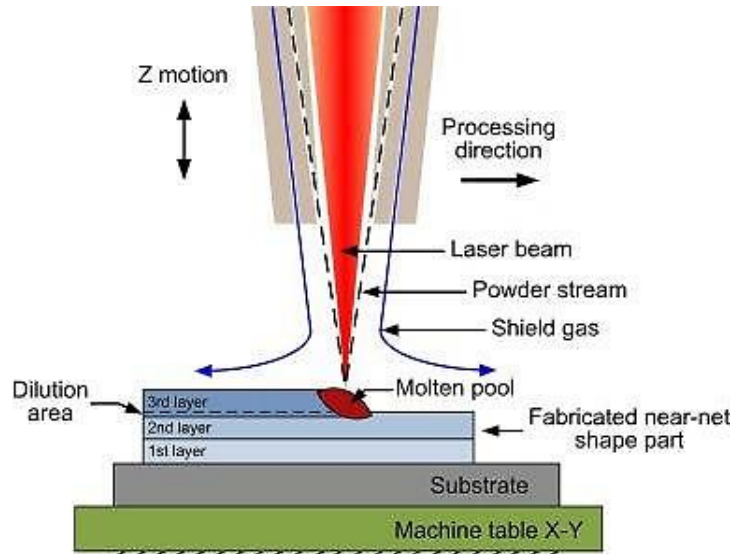


Figure 1.21 Diagram of LENS [159]

### 1.6.2 Electron beam melting (EBM)

The electron beam melting (EBM) technique is a type of AM created by Lars-Erik Andersson and Morgan Larsson (Arcam AB, Sweden) in 2000 [166]. As a presented EBM working principle in Figure 1.22, electrons are generated in a gun by heating a tungsten filament and accelerated by applying a high potential, melting the powder layer by layer with selected control of computer and 3D CAD model data [167]. This technology requires low energy for the production process and is capable of building implants with good mechanical characteristics and porosities. Meanwhile, the EBM process can provide porosity integrated to bulk substrates and fabricate objects having low internal residual stresses [168]. Recently, a variety of suitable materials for EBM such as nickel-based alloys [169], titanium alloy [170] and CoCrMo alloys [171], copper alloys [172], and iron-based alloys [173] have been developed. After more than ten years of development, EBM has been successfully applied in aerospace and biomedical applications [174].

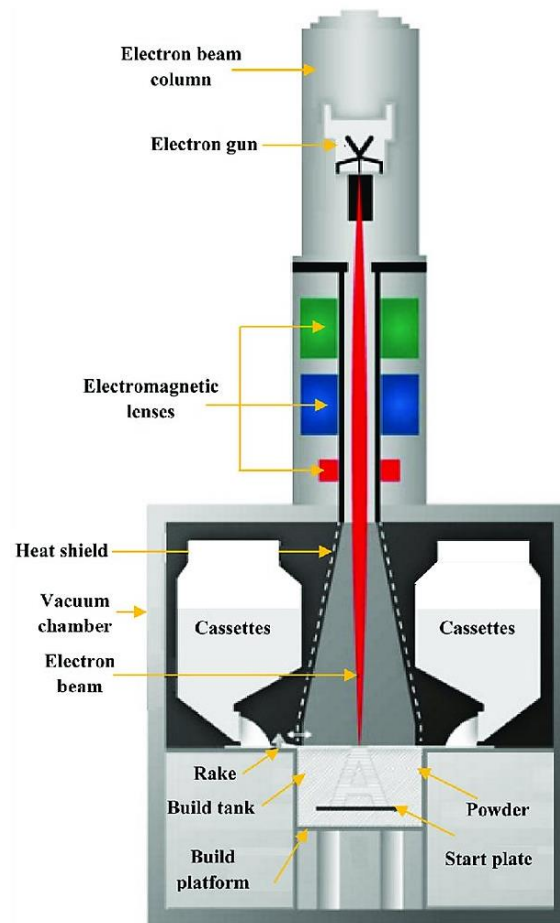


Figure 1.22 Schematic EBM system [168]

### 1.6.3 Selective laser sintering/melting (SLS/M)

SLS is also a kind of AM technology, it was created in 1986 by Carl Deckard and Joe Beaman at the University of Texas at Austin [175]. This technique produces metal parts using a high-energy laser source to sinter powder layer-by-layer and finally form the 3D parts based on the initial CAD description. In each layer, the raw powder is sintered and bonded by the laser spot over the required cross-sectional area [176]. A diagram of the SLS is described in Figure 1.23, it is referred to as a process applied to a variety of materials like plastics, ceramics, and especially metal alloys. The sintering processes do not mean to fully melt the powder but heat it to the point that the powder can fuse on a molecular level; and with sintering, the porosity of the material can be controlled. Nowadays, SLS has been mainly applied to rapid tooling [177] in the aeronautics and astronautics [178] industries. Generally, the SLS-produced highly dense components need the support of post-processing.

SLM is a kind of AM technology using a laser beam as the energy input, it is also named direct metal laser sintering (DMLS) or laser powder bed fusion (LPBF) technology, which was invented at the Fraunhofer Institute ILT in Aachen, Germany, in 1995 [179, 180]. The schematic diagram of the SLM system is similar to that of SLS in Figure 1.23. During the SLM process, a metallic powder bed is selectively melted layer-by-layer by a high-energy laser beam and builds the parts with a designed strategy, rapid solidification ( $10^3$ - $10^6$  K/s) can result in an ultra-fine microstructure [181]. Owing to the CAD-based design and fabrication process, SLM technology plays a vital role in the extended potential applications for manufacturing net-shape production of complex-shaped, high-performance components. In some cases, SLM is considered to be as a subcategory of SLS. However, unlike SLS, the metal powder can be fully melted by the SLM process to build solid 3D parts. Considering the fully melted rather than the sintered condition, SLM can produce fully dense parts [182].

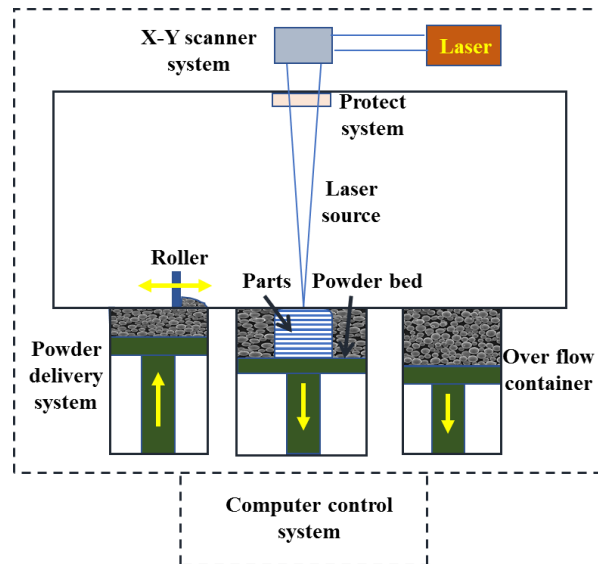


Figure 1.23 Diagram of schematic SLS/M system [161]

### 1.6.3.1 Advantages of SLM technology

Due to the superior features, primary advantages of the SLM technology unlike other AM technologies can be summarized as follows [183, 184]:

- (1) High melting point refractory materials and metal matrix composite materials can be used as raw materials.
- (2) The surface quality of the finished parts is quite high.
- (3) The mechanical properties of the formed parts are superb.
- (4) Suitable for manufacturing structural parts with extremely sophisticated geometry.
- (5) Since the powders can be recycled, the wastage of raw materials can be negligible.

### 1.6.3.2 The applied or potential applications of SLM technology

In industries like biomedical, aerospace, automotive, molds, etc., SLM technology has been popularly applied in the fabrication of high-quality metallic parts with brilliant properties [185]. Apart from the structural applications, the SLM also has great potential in the production of functional parts such as soft magnetic alloys [186].

In biomedical applications, SLM technology has been applied to manufacture a variety of biomedical products, especially implant prostheses. In Figure 1.24 (a), a Ti6Al4V revision acetabular cup was developed and manufactured by the SLM technique [187]. As given by Figure 1.24, for the patient with severe bone defects, the X-ray computer tomography (XCT) method can support the customized design of an SLM-produced specific implant [188]. Aiming at the problem of excessive surface roughness of SLM-produced parts, Yan et al [181] customized a process plan to reduce surface roughness and improve fatigue strength. And they also fabricated successfully tailored medical implants such as acetabular cups and crowns [181, 189]. Based on patient imagery, customized upper extremity replacements of the clavicle and scapula are also benefited by the SLM process. A report about scaphoid scapula and strip-like scapula reconstruction surgery using Ti6Al4V alloy has been developed in Xi'an, China (Figure 1.24 c-d) [190].

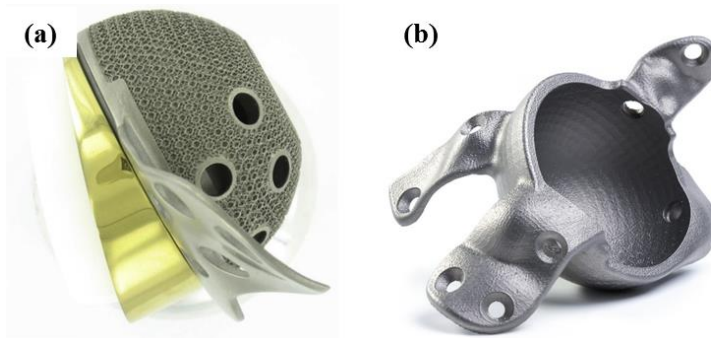


Figure 1.24 Example parts for biomedical applications: (a) MUTARS revision hip cup (courtesy of Implantcast GmbH) [187], (b) Individual hip implant in titanium (courtesy of SLM Solutions Group AG) [188]

Additionally, in industrial aerospace applications, SpaceX company fabricated a SuperDraco engine chamber using Inconel via SLM, which is revealed in Figure 1.25 (a). Using the SLM technique reduced lead-time by an order of magnitude compared to traditional machining: from the first concept to the first hot-fire test took slightly more than three months [191]. GE Additive company used the SLM process to manufacture the near-net-shape forming of the Leap fuel nozzle (Figure 1.25 b), integrating over 20 parts into a single part for manufacturing and hence reducing weight by 25 %, and they have also successfully produced 30000 pieces of these products commercial for commercial application [192, 193]. Besides, as can be seen in Figure 1.25 (c) SLM Solutions collaborated with CellCore in the preparation of the highly complex Monolithic Thrust Chamber by SLM process. Monolithic Thrust Chamber has an improved functional cooling due to an innovative lattice structure, which also increases stability. It is highly efficient and minimizes individual process steps while combining multiple parts into a single component; production time is reduced from months to days [194]. The company SLM Solution has chosen a collaborative approach to achieve the best design of the new Gooseneck Bracket and then built by SLM technology, see it in Figure 1.25 (d). There was 31% weight savings and a shortened total assembly time. It integrates three parts into one to reduce assembly and has an improved buy-to-fly ratio from 17 minimized to 1.5 [194].

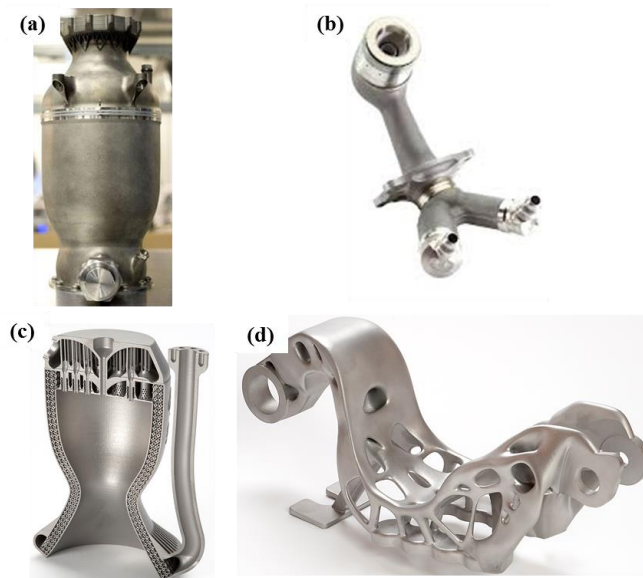


Figure 1.25 Example parts for aerospace applications: (a) Combustion chamber in SuperDraco thruster engine, (b) Leap fuel nozzle in GE90 jet engine, (c) Monolithic Thrust Chamber - Cell Core GmbH, (d) Gooseneck Kueger Flap Actuation Bracket - Asco Industries [191-194]

Moreover, in automotive applications, the company Wabtec has significantly improved a brake panel for a train using SLM technology. The conventional part consisted of several individual components and was unnecessarily heavy, which impacted the train's performance. With the help of the SLM<sup>®</sup> 800 system, not only the weight was reduced and the lead time shortened, but the safety-critical component also passed all the tests for qualification and certification [195]. SLM Solutions and Porsche successfully printed a complete E-drive housing with an innovative AM Design. All the advantages of additive manufacturing have been implemented in this housing such as topology optimization with lattice structures to reduce the weight, functional integration of cooling channels, higher stiffness, and reduced assembly time by the integration of parts as well as improvements in part quality [195].

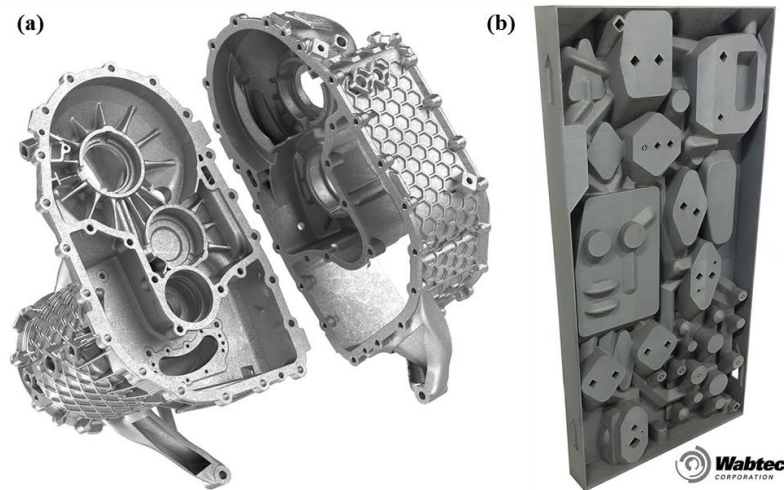


Figure 1.26 (a) E-Drive Housing from Porsche, (b) a brake panel for a train From the company Wabtec [195]

In addition to the above applications, SLM is also expected to deliver considerable assistance in the mold industries, due to its ability to produce sophisticated molds with internal conformal cooling channels at high efficiency [196]. Furthermore, it has great potential in the production of electronic machines such as the core of transformers, rotors, and stators of the motors. Gargalis et al. adopted a blend in which pure Fe powder is mixed with pre-alloyed silicon steel, and then manufactured a rotor via SLM process. The rotor was assembled into a conventionally laminated stator (Figure 1.27) and the performance of the whole machine was evaluated. The collected results confirmed the viability of additive manufacturing technology in the electrical machine field [197].

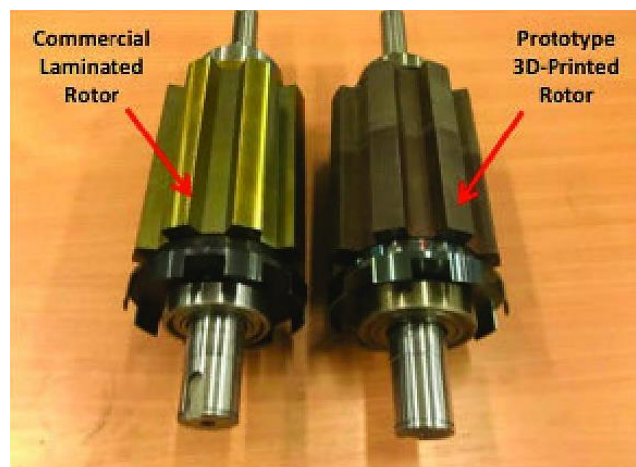


Figure 1.27 Commercial laminated 8-pole SRM rotor and identical 3D printed rotor

### 1.6.3.3 Challenges of SLM technology

Although SLM technology has aroused the attention of the engineering community in various application fields, SLM technology still undergoes the following severe challenges [184, 198, 199].

- (1) For SLM equipment: For large parts, the processing efficiency is still poor, and the price of equipment suitable for large parts is high. How to develop more efficient and economical large-scale systems is still a challenge to be solved urgently;
- (2) For original materials: Yet, there are currently no metallic powder materials produced specifically for the SLM process. How to develop the produced methods of SLM special materials, and obtain high-quality special powders is still another challenge;
- (3) For processing parameters: SLM technology has poor process stability and strong dependence upon the manufactured equipment. It is also necessary to improve the process stability of SLM and establish more parameter guidance.

### 1.7 Fabrication of soft magnetic alloys via SLM technique from mixed powders

In the early years, the research of SLM soft magnetic alloy was based on mixed powder. Zhang et al. [200, 201] investigated the SLM processed Fe-Ni alloys using the Iron and Nickel mixed powders of Fe-30wt.%Ni, Fe-80wt.%Ni as raw materials. Figure 1.28 shows the microstructural characteristics of the Fe-30wt.%Ni samples produced by different parameters on the etched section. The samples exhibited fine grains with homogenous distribution when a low laser scanning velocity of 0.1 m/s was used. EDS results reveal that the Fe and Ni elements in the sample are nearly equal to the atomic proportion of 7:3 within these grains, however, the disorder and gross grain within the matrix with scanning velocities of 0.4 m/s and 1.6 m/s is composed of the Fe and Ni elements with atomic ratio of about 3:2. The magnetic properties of SLM Fe-30wt.%Ni alloy showed a strong parameters dependence due to the influence of microstructure. The sample with 0.4 m/s exhibited favorable values of magnetic properties, which are better than the Fe-30wt.%Ni alloy fabricated by LENS according to the study of Mikler et al. [202].

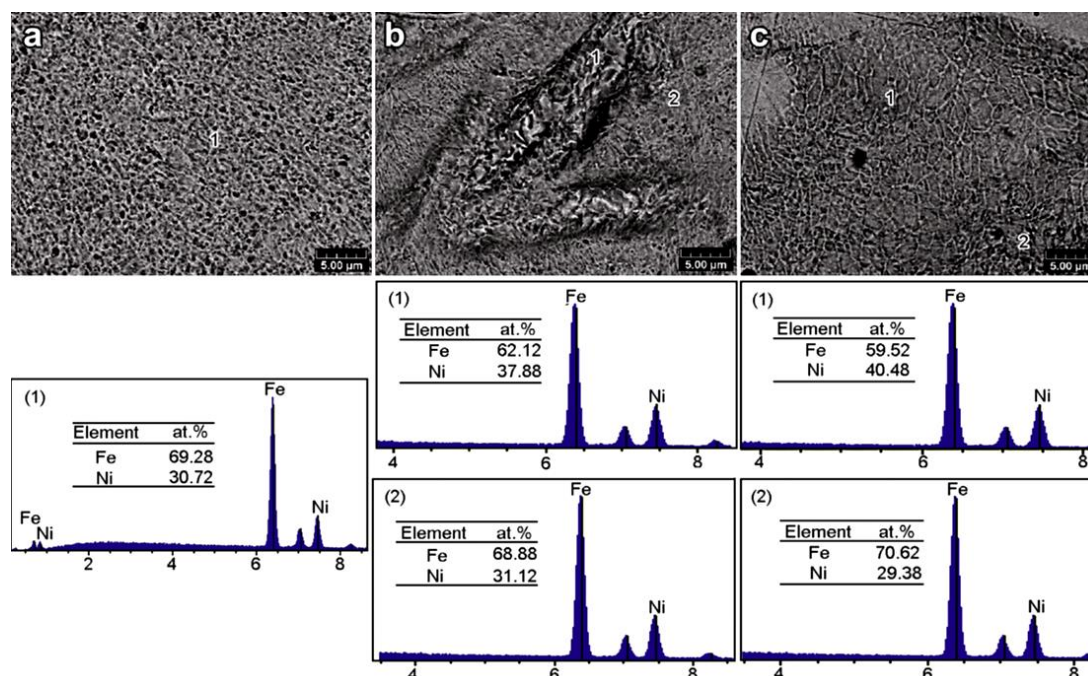


Figure 1.28 SEM micrographs showing the microstructure of laser melting samples of FeNi alloy with scanning velocity: (a) 0.1 m/s, (b) 0.4 m/s, (c) 1.6 m/s and laser melting power 110 W [203]

For the Fe-80wt.%Ni samples, the results presented the evolution of crystallite size as a function of the laser scanning parameter. It was observed that the grain sizes increased under the conditions of

the increase of laser scanning velocity. According to the velocity increase to 0.4 m/s, the grain size of Fe–Ni alloy is similar to the grain size of Fe–Ni mixed powder. The magnetic properties of laser melted Fe-80wt.%Ni alloys are also influenced by laser parameters. SLM seems to be suitable for the fabrication of these alloys.

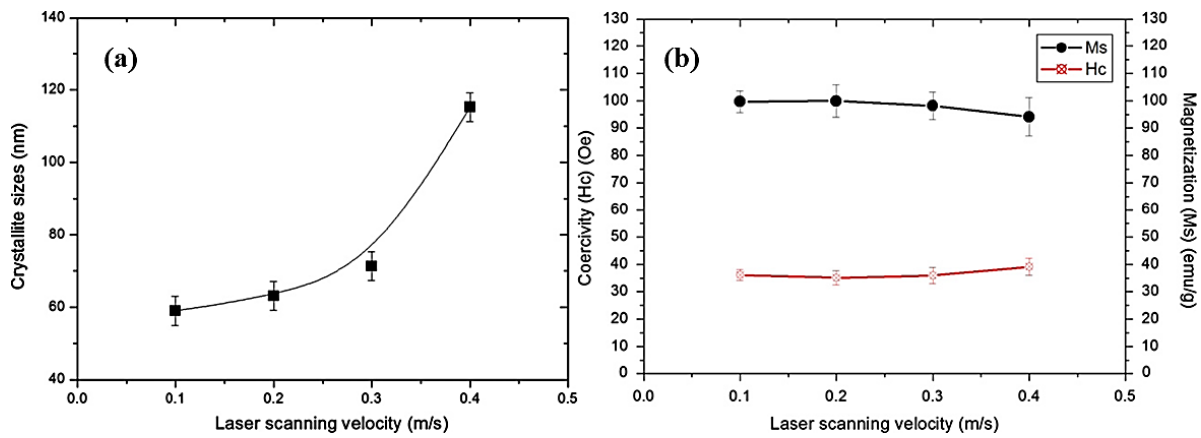


Figure 1.29 (a) Crystallite size of Fe-80wt.%Ni versus laser scanning velocity, (b) Saturation magnetization and coercivity curves for Fe-80wt.%Ni alloy with laser scanning velocity [203]

As can be seen in Figure 1.30 (a-c), Gargalis et al. [197, 204] developed a soft magnetic material featuring high silicon content (Fe-5.0wt.%Si) by mixing a high silicon steel pre-alloyed (Fe-6.9wt.%Si) with high purity Fe powder (99.9wt.% Fe). The samples for mechanism tests and a salient 8 pole rotors for a switched reluctance machine (SRM) were fabricated via the SLM technique from the obtained material. The yield strength of the as-built parts is well above the required/minimum 400MPa of conventional lamination steels with 3.5% wt. Si. As displayed in Figure 1.30 (d-e), the selective laser melted (SLMed) rotor was assembled into a conventionally laminated stator and the performance of the whole machine was evaluated. The collected results of this report confirmed the viability of SLM technology in the electrical machine field. However, until now, the detailed microstructure of the as-built parts did not present in their report.

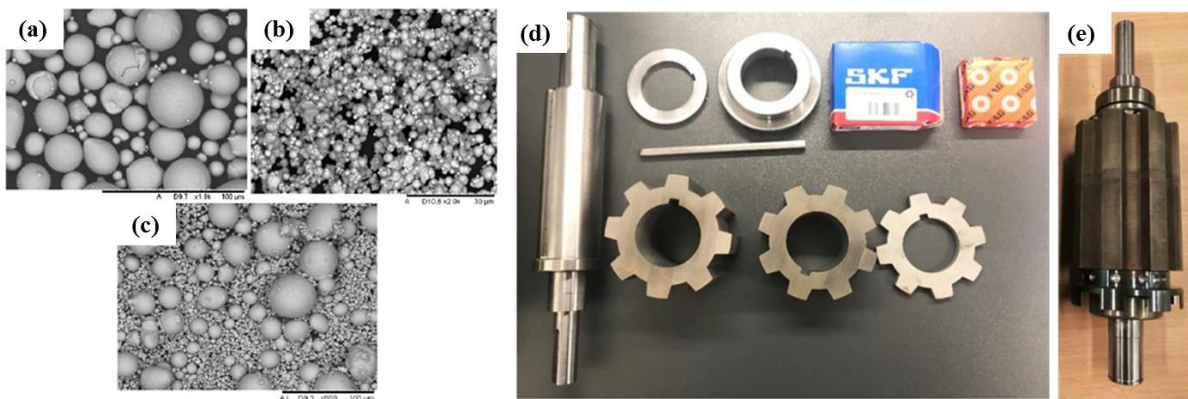


Figure 1.30 SEM micrographs of metallic powders: (a) pre-alloyed Fe-6.9wt.%Si, (b) pure iron Fe (99.9%), (c) Fe-wt.% Si powder blend [204] and (d) Main components for the assembly of the SLMed soft magnetic rotor core, (e) Fully assembled 3D printed SRM rotor (Fe-5.0wt.%Si) [197]

In summary, the SLMed alloy parts with target composition can be obtained by mixing powder. However, powder mixing might make the stability of the SLM process worse. At the same time, it offers a large possibility of uneven composition.

## 1.8 Selective laser melted soft magnetic alloys using pre-alloyed powders

As so far, the investigations into the fabrication of Fe-based soft magnetic alloys by SLM have been focused on Fe-Si and Fe-Ni alloys. In the next sections, the research status and progress will be introduced in detail, and representative studies involving other alloys.

### 1.8.1 Soft magnetic alloys based on Fe-Si

#### 1.8.1.1 SLM fabrication parameters

The most relevant SLM fabrication parameters are the laser power ( $P$ ), the laser spot diameter, the scanning velocity ( $v$ ), and the scanning strategy [205, 206]. Laser power and scanning velocity certainly have the greatest effect on the molten pool, which can therefore influence the microstructure and porosity of the SLM material [205-207].

Garibaldi et al. [208, 209] studied the effect of the laser energy input ( $E$ ) which was calculated by  $E=P/v$  on the microstructures and magnetic properties of SLMed Fe-6.9wt.%Si soft magnets using a Realizer SLM-50 (Realizer GmbH, Borchten, Germany), the values of the fixed SLM process parameters were as follow:  $P$ : 70 (W), laser beam focus position: 13.1 (mm), hatch spacing 60 ( $\mu\text{m}$ ), layer thickness 25 ( $\mu\text{m}$ ), scan strategy: bidirectional X-Y,  $V$ : 0.125, 0.250, 0.5 (m/s), laser linear energy inputs ( $E$ ) were 140, 280, 420, 560 (J/m). In Figure 1.31, the results show that the porosities of the samples decreased as laser energy inputs increased. But increasing the  $E$  at 280 J/m induced crack formation. With  $E \geq 420$  J/m, small bubble-like voids (i.e., circular pores) appeared, while crack formation was promoted. They explained that the formation of cracks could be attributed to the thermal stresses induced during the SLM process. They found that the lattice parameter of the SLM samples linearly decreased with increasing  $E$  [209]. The microstructure of the samples is characterized by columnar grains oriented towards the build direction (BD). The coarse areas of ordered phases  $B_2$  and  $DO_3$  were not presented in the microstructure. As displayed in Figure 1.32 and Figure 1.33, the maximum texture intensity of S280 was found to be almost twice the maximum intensity of S140, which suggested that a larger  $E$  produced a more textured, and crystallographic  $\langle 001 \rangle$  fibre texture could be altered into a cube texture. They also found that microhardness did not seem to be affected by the processing parameters.

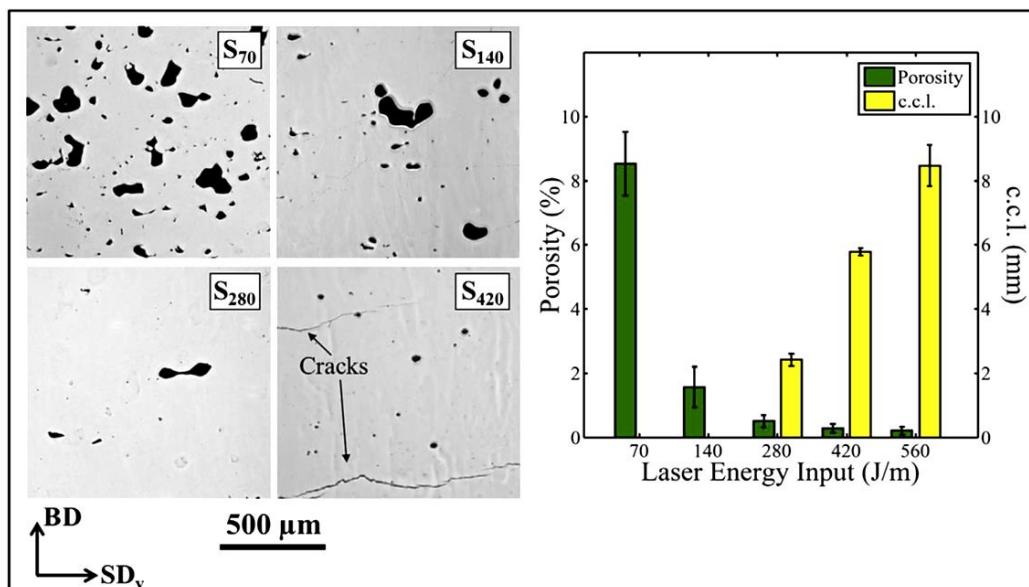


Figure 1.31 Evolution of porosity: the optical micrographs of different SLMed Fe-6.9wt.%Si samples (left) and alongside the values of percent porosity and cumulative crack length c.c.l. (right) [209]



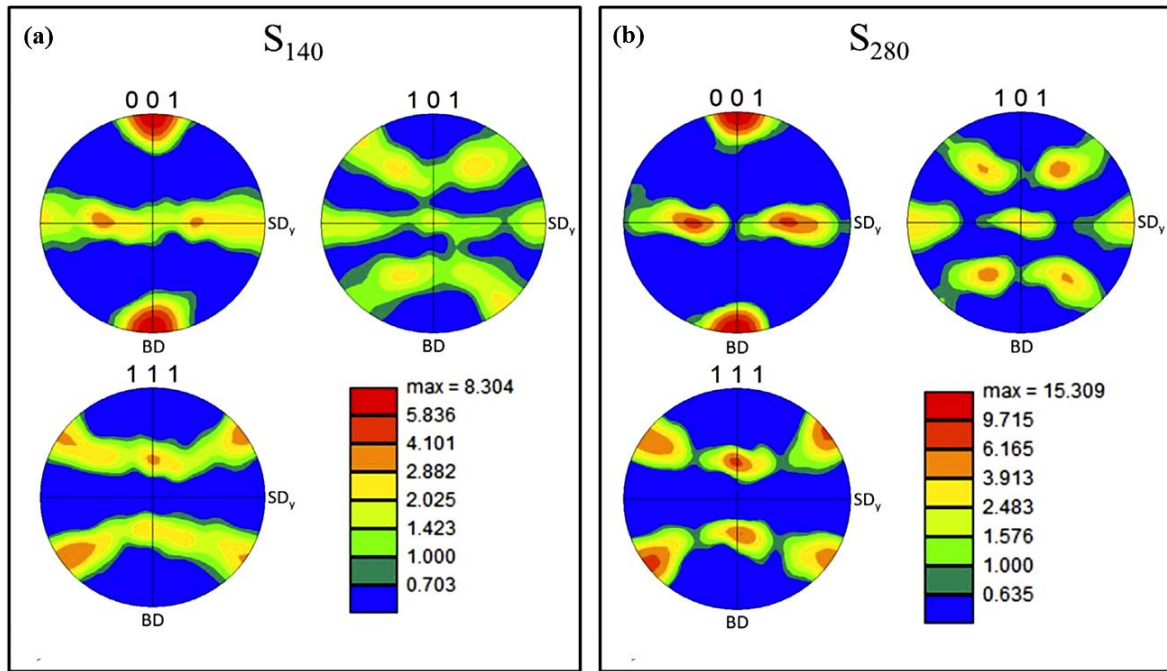


Figure 1.32 Pole figures (PF) showing the preferred orientation of the  $\langle 001 \rangle$  crystallographic direction of SLMed Fe-6.9%wt.Si sample [209]

According to the results of magnetic measurements of the SLMed ring samples, they found that the  $\mu_{\max}$  did not seem to change significantly for the two samples at lower  $E$ , but seem to decrease slightly at  $E=420$  J/m. While different behavior was found for  $\mu_{40}$ , which increased significantly from  $E=140$  J/m to  $E=280$  J/m. The value of property  $B_{50}$  was significantly different, and at  $E=280$  J/m was the best. A decrease in  $H_c$  from 140 J/m to 280 J/m was found while a further increase in  $E$  did not seem to affect it. The  $B_r$  showed a slowly decreasing behavior throughout the  $E$  range considered.  $P_{50-1}$  showed a strong non-monotonous trend, with a clear minimum value observed at  $E=280$  J/m [208]. Although the magnetic properties can be improved under better parameters, segregation of silicon was still found in these high silicon steels (see in Figure 1.34) [208]. This may lead to the inhomogeneity of microstructure composition, which may lead to the local instability of the magnetic properties of these samples in the working magnetic field.

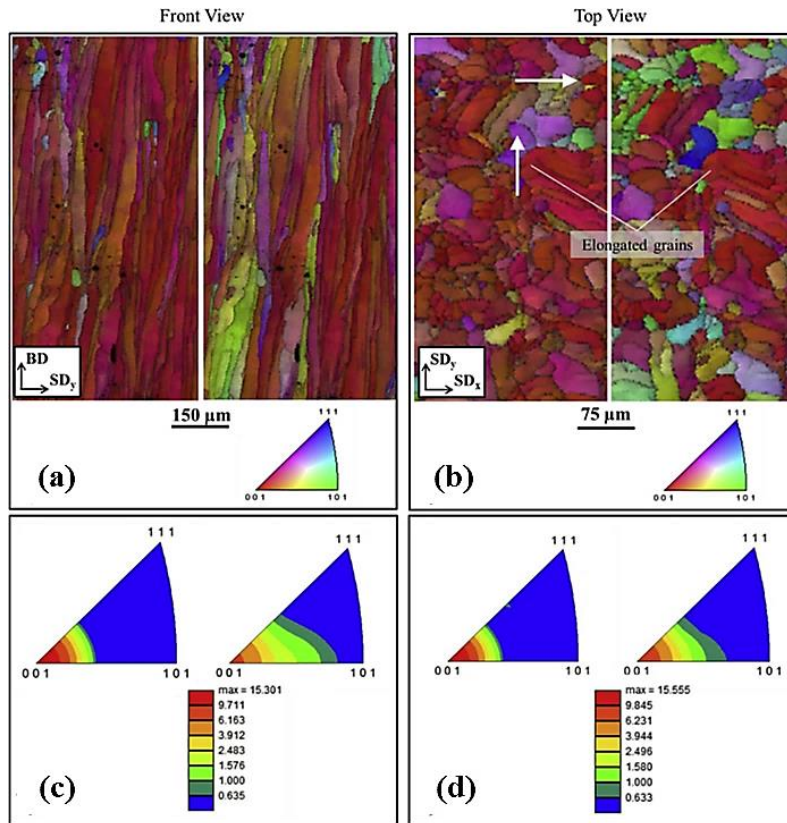
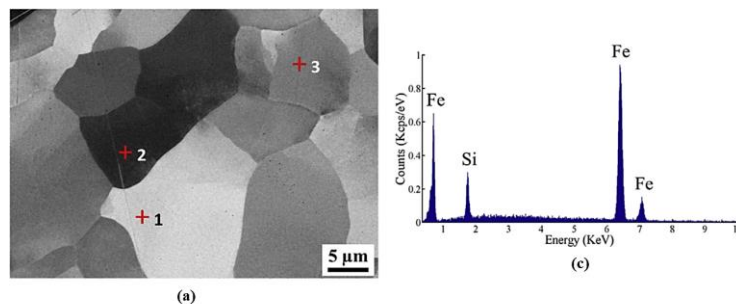


Figure 1.33 (a), (b) EBSD maps; (c), (d) IPFs for the front and top views of SLMed Fe-6.9%wt.Si sample S280 (Left: BD, Right: SDx and SDy) [209]



Region	1	2	3
Fe (wt%)	93.15	91.75	93.32
Si (wt%)	6.85	8.25	6.68

(c)

Figure 1.34 (a) SEM image of the investigated region, (b) EDX spectrum corresponding to region 1, (c) and chemical composition in the three regions under exam, of SLMed Fe-6.9%wt.Si [209]

Goll et al. [108] reported that the SLMed (SLM 280 H L, SLM Solutions) Fe-6.7wt.%Si components with higher laser power, the cooling rate is decreased, resulting in larger average grain size and lower losses. However, for higher laser powers also the tendency for residual stresses and therefore towards crack formation is enhanced. They also evaluated the effects of building platform heating (BPH) temperature on the microstructures and magnetic properties when laser power  $P=300$  W, laser scan velocity  $v=500$  mm/s. They found that the coercivity continuously decreases with increasing BPH temperature (varied between 200 °C and 600 °C), and the  $\mu_{\max}$  and grain size increase steadily (see in Figure 1.40).

Besides, Alleg et al. [210] prepared the SLM Fe-Si-B soft magnetic parts using Fe92.4Si3.1B4.5 pre-alloyed powder. They indicated that the increase of the laser scanning rate led to deep cracks on the

surface of laser-melted tracks, and the variation of the microstructures and magnetic properties of the SLMed parts were closely related to the laser scanning velocity. The produced samples show soft magnetic properties with  $M_s = 188.6\text{--}199$  emu/g and  $H_c = 43.8\text{--}73$  Oe.

### 1.8.1.2 Influence of scanning strategy

Plotkowski et al. [129] investigated the influence of geometry and scan patterns on the microstructure evolution and eddy current loss of SLMed (Renishaw AM250 system) Fe-3wt.%Si components. They studied the effects of remelted (double scan) on the microstructures and power losses of the bulk samples, the scan pattern was rotated by  $67^\circ$  between layers, which is illustrated in Figure 1.35 (c). Besides, they designed the thin wall samples with a series thickness of 400, 600, 800, 1000  $\mu\text{m}$  respectively, which were produced with each of the three scan patterns with transverse, longitudinal, rotated by  $67^\circ$  (shown in Figure 1.35 (a-c)). Two types of bulk samples have different microstructures as shown in EBSD figures (Figure 1.36). The single scan pattern bulk sample exhibits a chaotic structure with many small grains while the double scan pattern sample shows a significant orientation of the  $\langle 100 \rangle$  type crystallographic direction along the BD with larger grains. Both samples exhibit the expected fiber texture, but the strength of this texture in the former is weaker than that in the former. As the magnetic test results are replayed in Figure 1.37, they indicated that the double scan pattern shows lower hysteresis loss coefficients, however, changing magnetic properties through the manipulation of the crystallographic texture makes for only a small improvement in the overall efficiency on a device level.

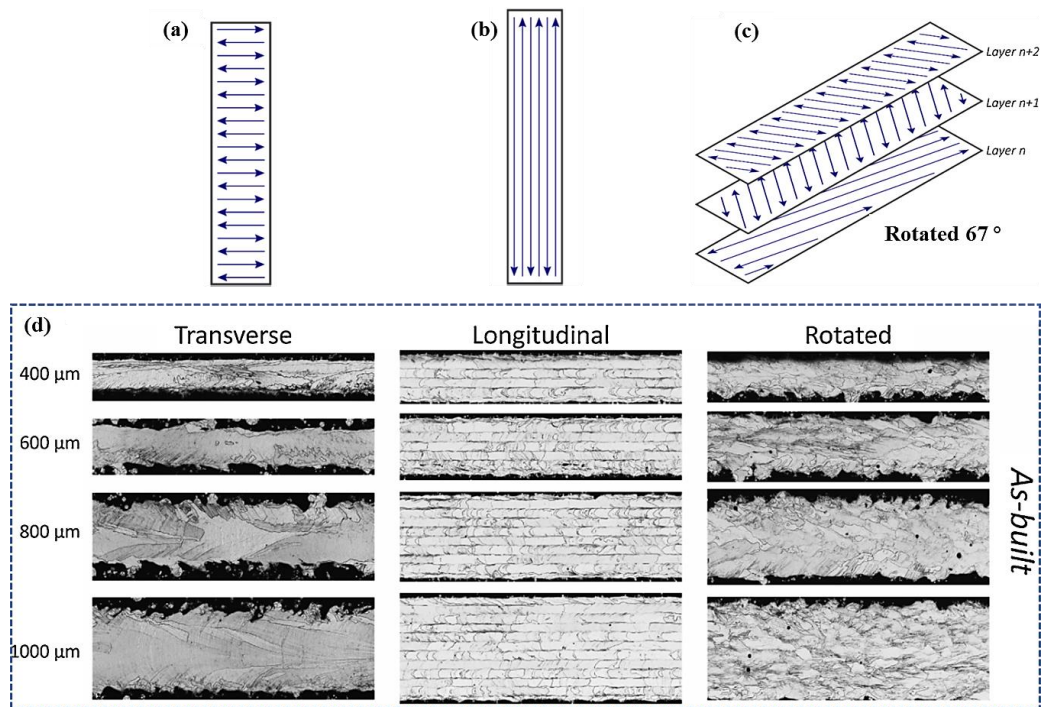


Figure 1.35 (a)-(c) Schematics of the scan patterns, (d) microstructures from the thin wall SLMed Fe-3Si samples [129]

The optical microscopy (OM) images of the microstructures of thin walls presented in Figure 1.37 (d) showed that the transverse scan strategy resulted in large grains compared to the longitudinal scan pattern. They suggested that the grain structure in the longitudinal sample is clearly defined by the hatch pattern while the transverse scan pattern is not clear. The rotated scan pattern seems to show a mixed structure somewhat between the transverse and longitude extremes in both the size and morphology of the grains. The difference in grain structure as a function of scan pattern is more significant than changes in structure with wall thickness [129].

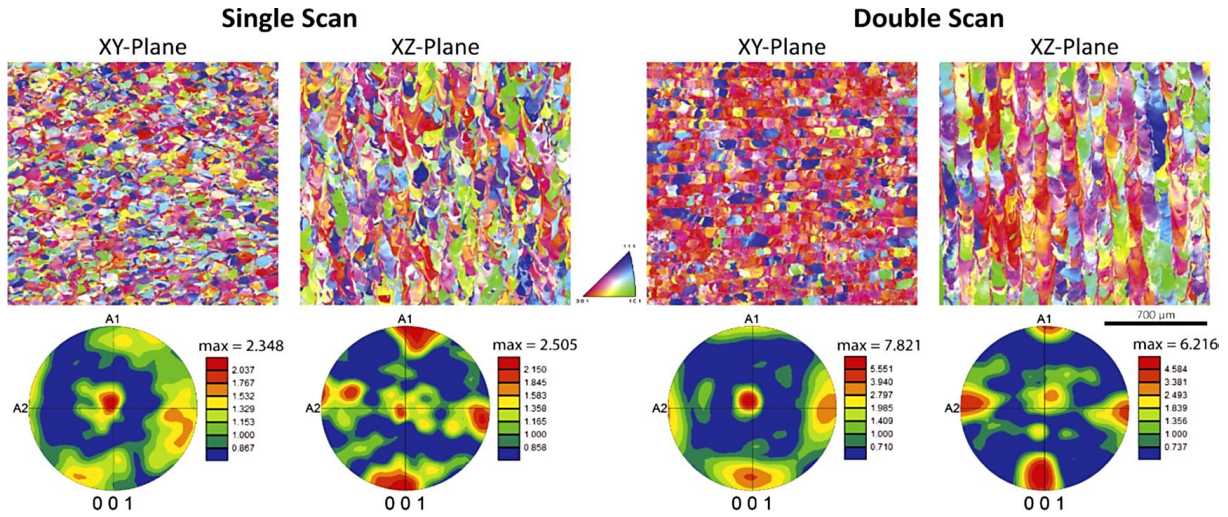


Figure 1.36 EBSD of the bulk cross-sections showing inverse pole figures of SLMed Fe-3Si specimens (top) and pole figures (bottom) for both scan patterns both normal (XY-plane) and parallel to the BD (XZ-plane) [129]

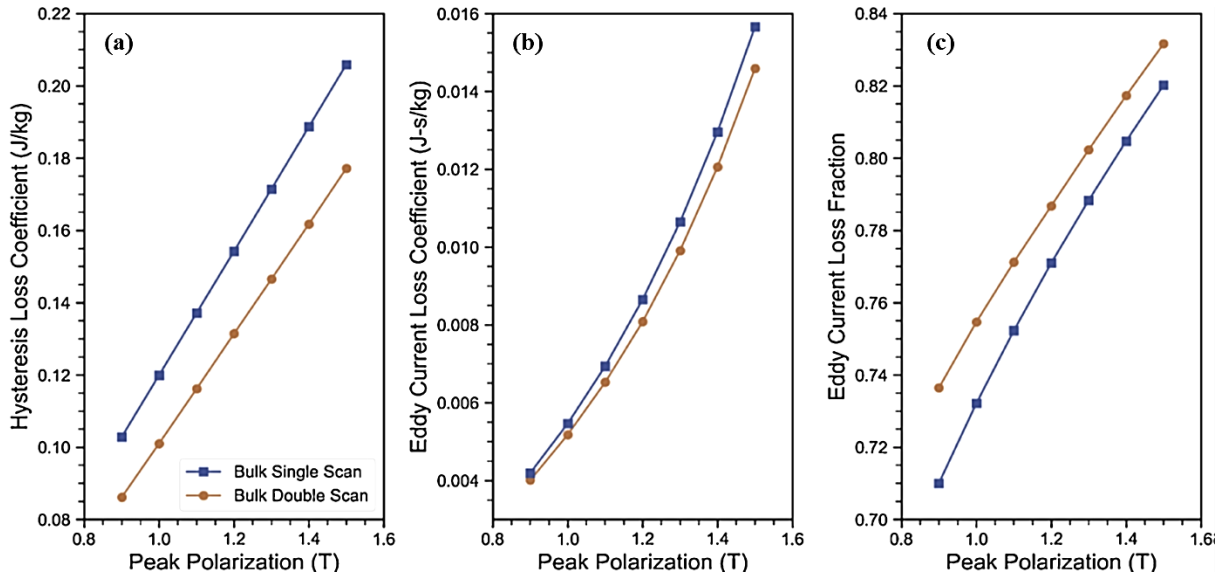


Figure 1.37 Results of magnetic characterization of the two bulk (Fe-3Si) cross-sections with different scan patterns: (a) the hysteresis loss coefficients as a function of peak polarization, (b) the eddy current loss coefficient as a function of peak polarization, (c) the fraction of total losses accounted for by the eddy current development as a function of peak polarization for an operating frequency of 60 Hz [129]

### 1.8.1.3 Impact of post heat treatments

Lemke and Garibaldi et al. [211, 212] conducted a series of heat treatments (annealed and quenched at different temperatures and time) to the SLMed high silicon steel Fe-6.9wt.%Si. They found that when cooling is sufficiently slow, the ordered phases of type  $B_2$  and  $DO_3$  form inside the grains in proportions. As described in Figure 1.38, the believed that the onset temperature for micro-segregation dissolution was found to be around 700 °C, and the onset temperature for grain growth was around 900 °C. On the other hand, they found that the stress relief heat-treatment (annealed at 700 °C, 5 h) could significantly increase the microhardness of the samples, they believed that is attributed to the redistribution of the Si-rich micro-segregates and the relief of the internal stress and phase-ordering [208, 211, 213].

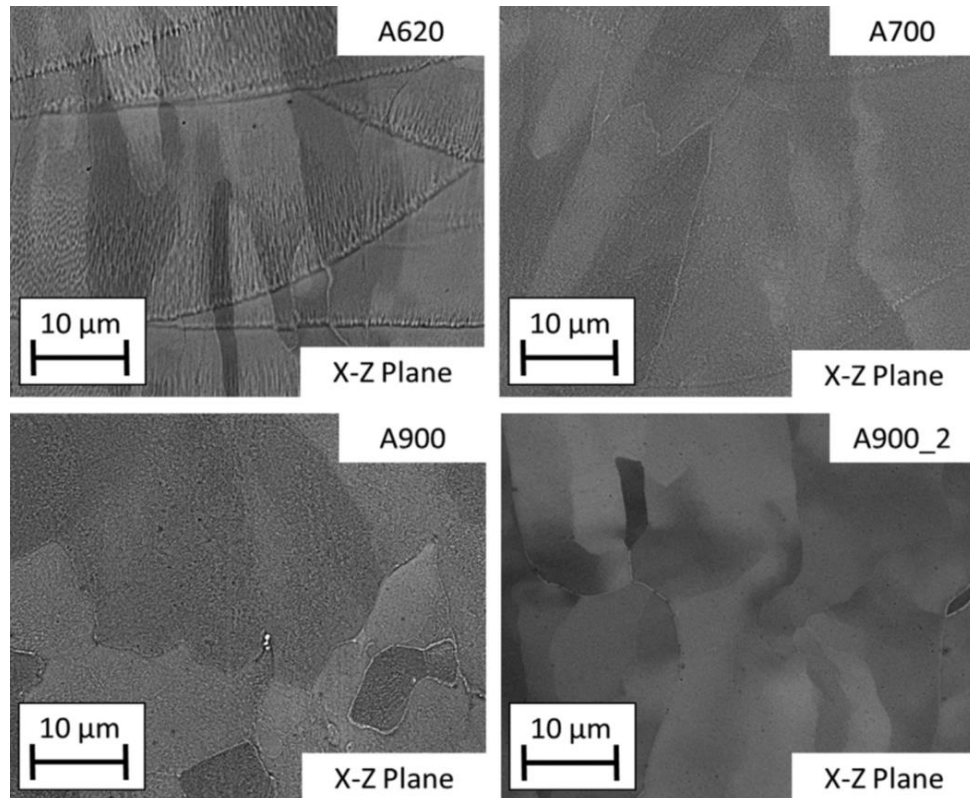


Figure 1.38 SEM micrographs representing microstructural evolution of the SLMed Fe-6.9wt.%Si samples after annealing for 1 h at: (a) 620 °C, (b) 700 °C, (c) 900 °C, (d) 900 °C with subsequent quenching [214]

They described that annealing in the high portion of the  $A_2$  leads to marked grain growth, but it should be noted that obvious phase disorder-order transformation of type  $DO_3$  appeared when the annealing temperature was higher than 900 °C. According to the previous introduction of silicon steel, this ordering phase is harmful to the mechanical properties due to material embrittlement. Also, when the annealing temperature was 1150 °C, the  $Fe_2O_3$  phase would be formed due to the leak of oxygen into the furnace from the surrounding environment during heat-treatment [211]. They believed that to avoid extensive ordering, rapid cooling can be performed from temperatures in the  $A_2$  phase region. As indicated in Figure 1.39, annealing does not alter significantly the  $\langle 001 \rangle$  texture induced by SLM along the BD through EBSD analysis. They thought that is an important finding since high-temperature annealing can be performed on the as-built samples to induce stress relief and produce grain growth without weakening the beneficial crystallographic texture induced by SLM [212].

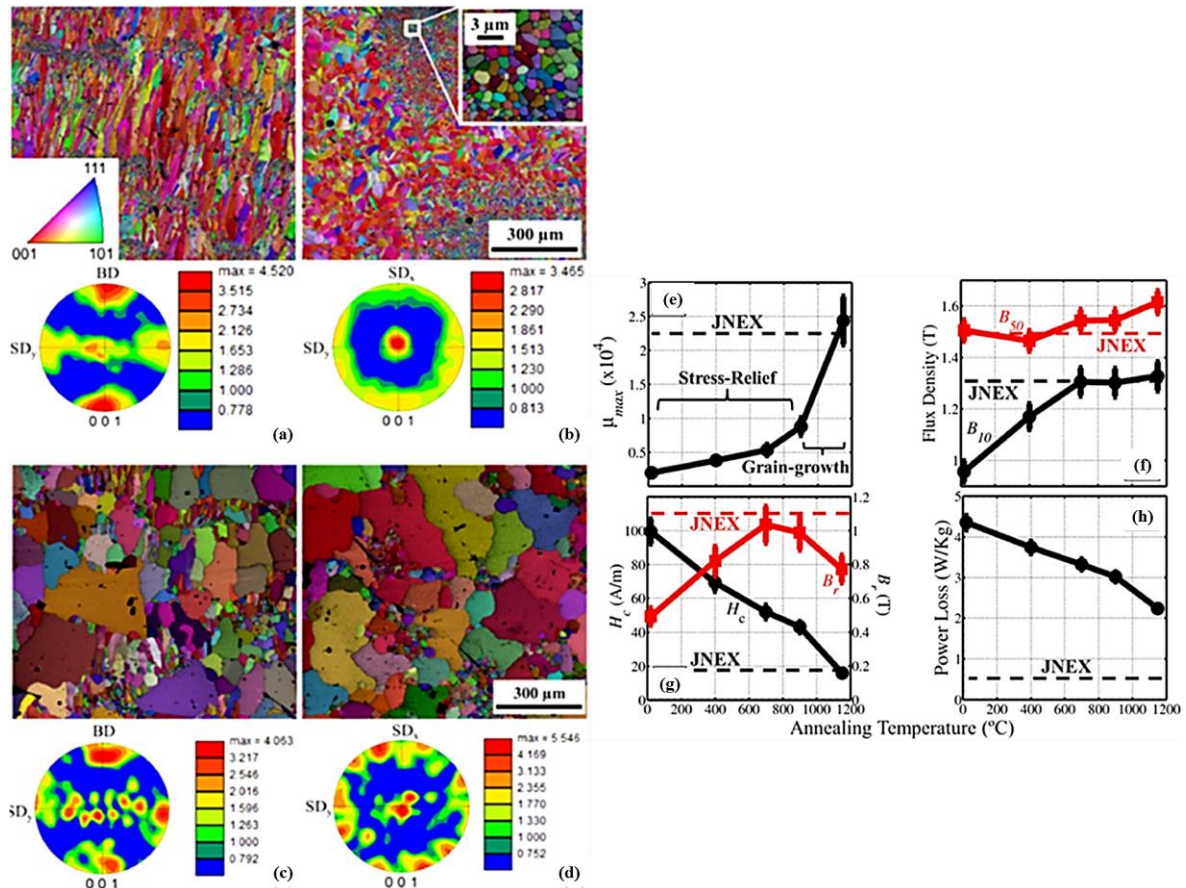


Figure 1.39 EBSD maps and PFs for SLMed Fe-6.9wt.%Si samples annealed 1h at 700 °C (a) front view, (b) top view and 1150 °C (c) front view, (d) top view; and Evolution of the magnetic properties with annealing temperature: (e)  $\mu_{max}$ , (f)  $B_{10}$  and  $B_{50}$ , (g)  $H_c$  and  $B_r$ , (h) power losses at  $B_{max}=1$  T and  $f=50$  Hz (adapted from [211, 212])

As given in Figure 1.39 (e-h), with comparative analysis, they concluded that the  $\mu_{max}$  of the SLMed samples increased with increasing annealing temperature. Until 900 °C the curve increased with a constant slope under the effect of stress relief, which can be reasonably expected to be completed after annealing at 900 °C [215].  $B_{10}$  increased with annealing temperature while increasing the annealing temperature beyond 700 °C did not improve further.  $B_{50}$  was only moderately affected by annealing. This indicated that the considered applied field of 5000 A/m is strong enough to overcome most of the manufacturing-induced obstacles to magnetization.  $H_c$  decreased with the increase of annealing temperature and obtained a minimum value of 16 A/m at 1150 °C. The remanence  $B_r$  presented a non-monotonic dependence with annealing temperature. Specifically,  $B_r$  increased up to 700 °C but, as the annealing temperature increases further it decreased. The total power losses decreased with increasing annealing temperature. The trend of the total power losses is qualitatively similar to that of  $H_c$ , so they suggested that the eddy current loss component does not increase significantly with grain growth. In summary, they concluded that the annealing of parts built by SLM with subsequent quenching could be a promising strategy for the production of parts with a more homogeneous microstructure, more suitable for magnetic applications [211].

Similarly, see in Figure 1.40, Goll et al. [108] reported that the hysteresis losses and coercivities, of SLMed Fe-6.7wt.%Si parts, were decreased, and  $\mu_{max}$  were increased due to the grain growth through annealing at 1150 °C for 1 h, except for  $\mu_{max}$  decreased when the utilized BPH was 600 °C, which was explained that related to the gas porosity was formed at higher BPH temperatures.

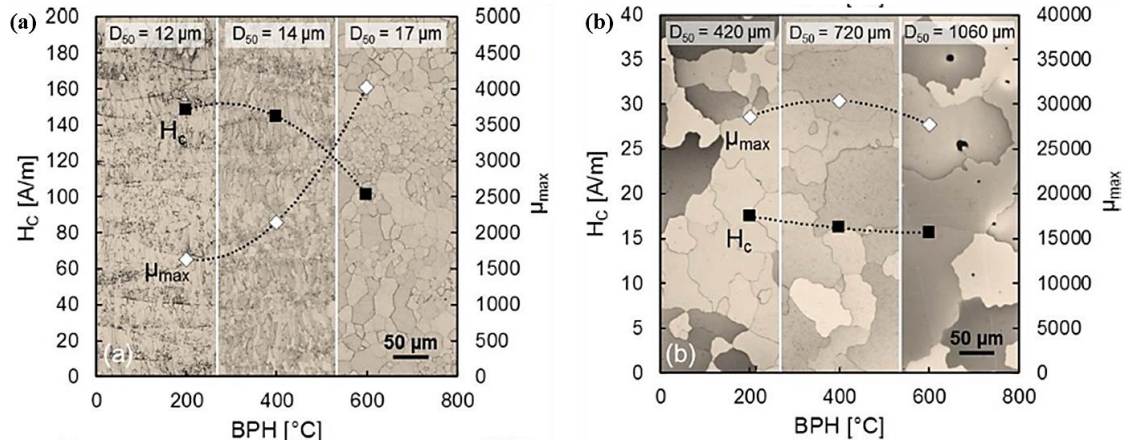


Figure 1.40 Influence of BPH temperature on the microstructure (average grain size  $D_{50}$ ) and magnetic properties of  $H_c$  and  $\mu_{max}$  for Fe-6.7wt.%Si parts (a) as-built state, (b) after annealing at 1150 °C for 1 h [108]

As mentioned earlier, Plotkowski et al. [129, 216] produced the thin wall Fe-3wt.%Si, Fe-6wt.%Si samples with series thickness and Hilbert transformer cores (see in Figure 1.44) by SLM technique respectively, the thin wall samples were subjected to hot isostatic pressing (HIP) at a temperature of 1150 °C for 2 h and pressure of 200 MPa. The Hilbert transformer cores were also annealed in an argon atmosphere for 4 h at 1200 °C. They observed that bimodal grain size comprised primarily of very large grains was obtained following annealing heat treatment, but retained some smaller grains as well (see in Figure 1.41). The grain size of the samples annealed at 1200 °C for 4h is much smaller than the samples annealed by HIP, lying between the as-fabricated and annealed conditions (see in Figure 1.42 (a)-(b)). They deduced that it can be attributed to the carbides and the oxide particles at nano-scale produced in the SLM process or precipitated during the annealing process, which was insoluble during annealing and could be present during the grain growth process to act as pinning sites. The Fe-3Si annealed transformer sample also showed a preference for 001 crystallographic direction parallel to the build direction like before heat treatment. While the Fe-6Si sample did not show any strong textural preference. Due to the grain growth and some level of grain boundary pinning like carbides and oxides particles from nano-scale constituents. The HIP heat treatment resulted in a net decrease in power losses and improved both the  $\mu_{max}$  and decreased hysteresis losses (see in Figure 1.42 (c-d)) [216].

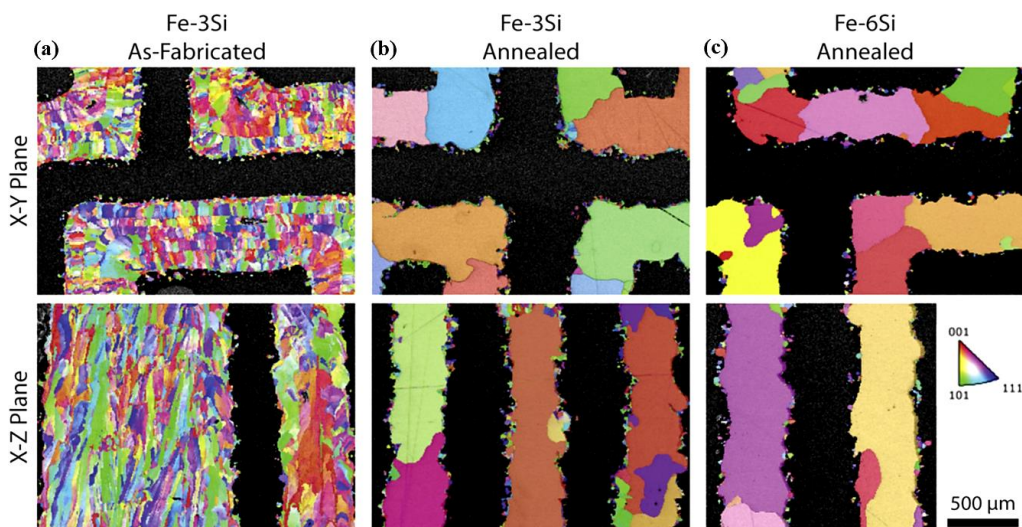


Figure 1.41 Inverse pole figure maps for the Hilbert curve thin wall design: (a) Fe-3wt.%Si as-fabricated grain structure, (b) Fe-3wt.%Si annealed structure, and (c) Fe-6wt.%Si annealed structure [216]

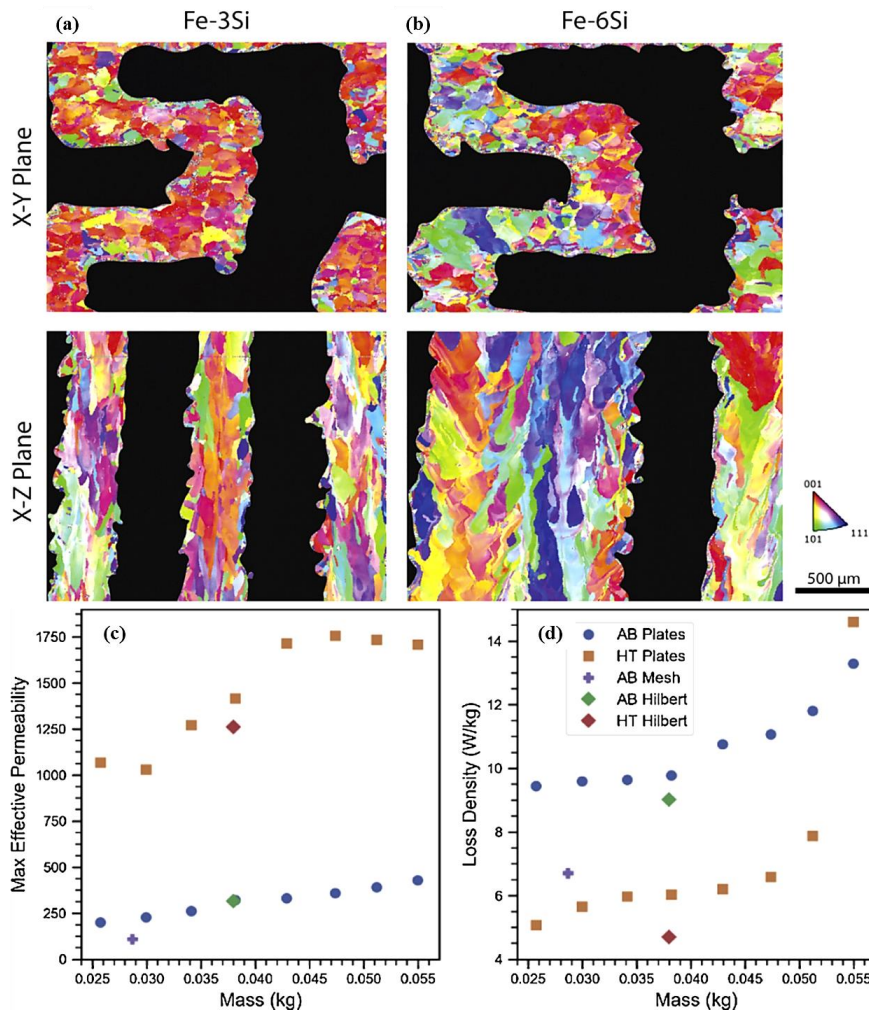


Figure 1.42 Inverse pole figure maps for the Hilbert transformer cores after annealing (a) Fe-3wt.%Si, (b) Fe-6wt.%Si [216] and Magnetic test results (c) maximum effective permeability for the HIP heat-treated samples, (d) total loss density at an applied field of 3000 A/m (adapted from [129])

Koo et al. [152] indicated that heat treatment at 1000-1200 °C in the Ar atmosphere has a positive effect on the magnetic properties of the SLMed Fe-6.5wt%Si sheet-type specimens. They pointed out that the  $M_s$  values were almost identical before and after heat treatment.  $M_s$  depends on magnetic moment per volume, which depends on the crystal structure of the alloy, not on the grain size. However, the coercivity significantly decreased, and maximum relative permeability ( $\mu_{rmax}$ ) greatly increased which can be attributable to grain growth. In the investigation of Tiismus et al. [217], it has been indicated that the total core losses of the SLMed Fe-3.7wt%Si toroidal samples were reduced via annealed at 800 °C and 1200 °C respectively while the electrical resistivity was also reduced.

#### 1.8.1.4 Geometric, structural design, and magnetic performances

In the report of Tiismus et al. [217], as shown in the fig1.30, they focused on the effect of air gaps on AC core losses at the 50 Hz frequency. A clear trend of core loss reduction due to the increased segregation of the specimen cross-sectional topology was observed for all samples.



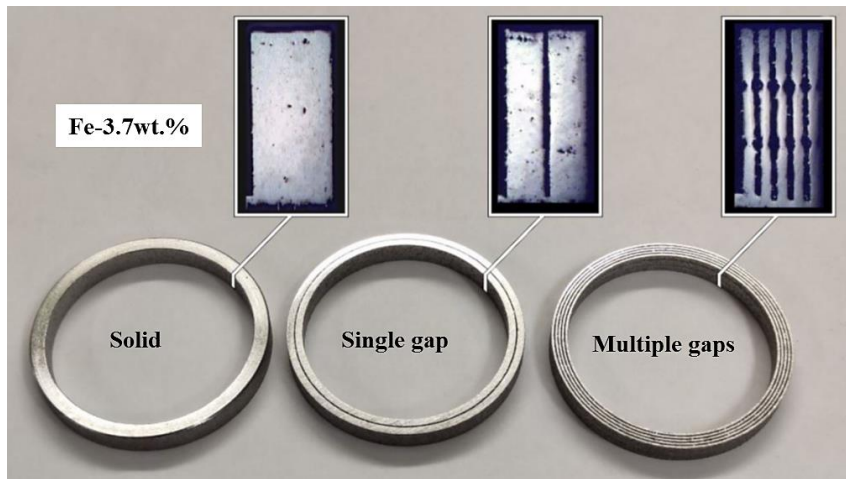


Figure 1.43 Variations of printed ring samples for magnetic characterization [217]

As represented in Figure 1.44 (a-b), Plotkowski et al. [216] designed and manufactured the Fe-3wt.%Si samples consisting of parallel plates at various spacings, a mesh structure, and a Hilbert curve via SLM technology, the wall thickness for all sets was nominally 400  $\mu\text{m}$ . For the parallel plates, integer numbers of plates were included and the wall thickness and outer dimensions were kept constant, they were built with between 6 and 13 walls, inclusive. In Figure 1.44 (c-e), they presented that the thin wall cross-sections had a lower hysteresis loss coefficient and eddy current loss coefficients than the bulk cross-sections while the mesh structure shows very similar behavior to the bulk components, but with a lower saturation inductance. The power losses increased with the increasing number of thin walls in the parallel plate samples. They conclude that the Hilbert curve exhibited the best performance of the samples tested. However, the excess surface roughness of closely spaced thin walls caused unwanted contact between neighboring walls.

They designed a variety of thin wall (also nominally 400  $\mu\text{m}$ ) geometries and three cross-sectional geometries (clock spring, Hilbert, and radial, see in Figure 1.45 (a)) were fabricated by SLM technology. These samples were characterized for AC magnetic performance after HIP annealed treatment for 2 h at 1150  $^{\circ}\text{C}$ . As seen in Figure 1.46 (a-c), compared to the annealed Fe-3wt.%Si sample, the results indicated that for low polarization, the Fe-3wt.%Si sample showed lower hysteresis losses than the Fe-6Si designs. However, for polarization above approximately 1.3 T, the Fe-6wt.%Si materials showed lower hysteresis losses. On the other hand, the eddy current losses for the Hilbert and clock-spring designs of the Fe-6wt.%Si alloy were lower than the Fe-3wt.%Si Hilbert design across all polarization levels. The radial design had a lower eddy current loss at low polarization but higher above about 1.5 T. The result of these trends was that the Fe-6wt.%Si samples generally show lower overall power losses at 60 Hz across a wide range of polarization. They concluded that the Hilbert design is especially effective at reducing eddy current losses and results in the lowest overall power losses for 60 Hz operation. Relative to the M15 non-oriented laminated sheet reference, the Fe-3wt.%Si steel only shows better performance for low polarization, but the Fe-6wt.%Si Hilbert design shows improved performance across all polarizations [216].

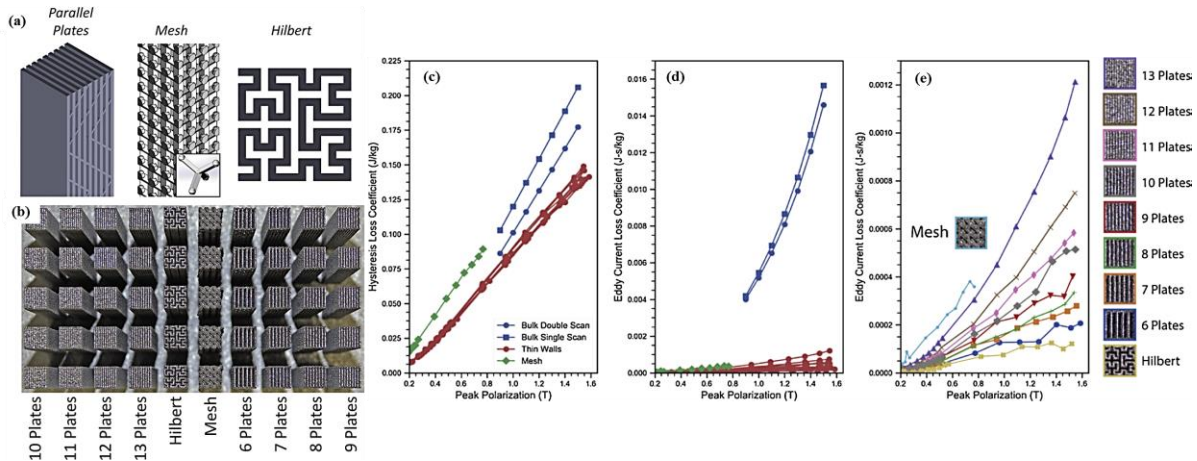


Figure 1.44 (a) Schematics of the complex thin wall Fe-3Si samples and (b) SLM-build thin wall cross-sections for magnetic characterization, Comparison of the loss behavior for bulk, thin wall, and mesh cross-sections (c) the hysteresis loss coefficient, (c) the eddy current loss coefficient as a function of peak polarization, and (e) a magnified view of the eddy current loss coefficients (adapted from [129])

Based on the results mentioned above, they have developed a novel transformer core design to incorporate a cross-sectional geometry inspired by a Hilbert curve. The cores were additively manufactured, annealed, machined, pickled, and assembled for magnetic testing. The nominal dimensions for the benchtop scale core and the cross-section design for the thin and thick legs of the transformer core are shown in Figure 1.45 (b). The mathematical definition of a Hilbert curve only fills squares, so this design was adapted for the specific transformer core leg cross-sections by assembling 4th order Hilbert curves as exhibited in Figure 1.45 (c). Similar to the simple 6.35 mm square cross-section, the wall thickness was nominally 400  $\mu\text{m}$ . Each leg of the core (7 in total) was additively manufactured separately with the magnetic flux direction built parallel to the build direction (see in Figure 1.45 (d)), using the same process conditions as the simple square geometries. Once removed from the build chamber, the build plate and transformer components were annealed in an argon atmosphere for 4 h at a temperature of 1200  $^{\circ}\text{C}$ . Figure 1.45 (e) shows an example of a partially assembled core following machining.

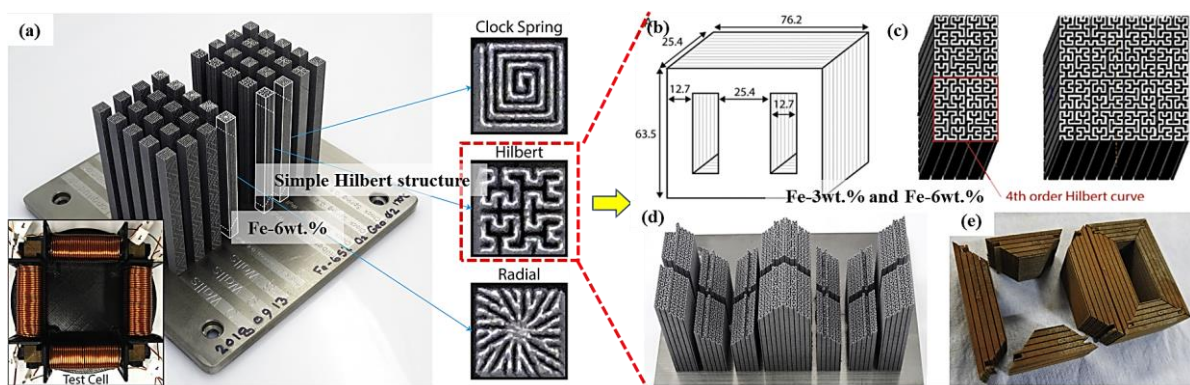


Figure 1.45 (a) SLM-build Fe-6wt.%Si thin wall cross-sections for magnetic characterization, (b) transformer core dimensions in mm (c) schematic of the Hilbert cross-section for thin and thick legs, (d) a finished SLM build (d) a partially assembled core after machining (adapted from [216])

According to the results of the magnetic tests shown in Figure 1.46 (d), they found that the Fe-6wt.%Si cores exhibited lower power losses across all measured polarization. Overall, the transformer cores showed somewhat higher power losses than the 6.35 mm sq. Hilbert cross-sections. The Fe-3wt.%Si transformer cores showed a greater increase in power losses relative to the square cross-

sections than did the Fe-6wt.%Si transformer cores. They conclude that the transformer cores were found to produce slightly higher power losses under 60 Hz operation than comparable additively manufactured 6.35 mm square cross-sections, which was attributed to variations in grain structure and defects incurred during machining and assembly, particularly for the Fe-6wt.%Si alloy where embrittlement due to the high silicon content led to the fracture of fine features during machining. The additively manufactured cores showed performance roughly comparable or better than the conventional non-oriented sheet, but higher power losses than Goss oriented steel [216].

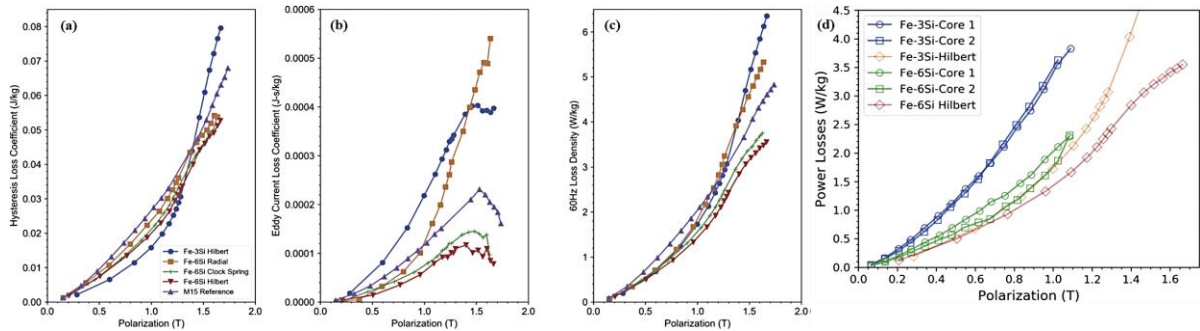


Figure 1.46 (a) the measured hysteresis loss coefficients and (b) eddy current loss coefficients, as well as (c) the power losses per unit mass for 60 Hz operation, (d) Power losses per unit mass of the transformer cores compared to the simple Hilbert cross-sections (Fe-6wt.%Si, adapted from [216])

Koo et al. [152] prepared structurally-layered (see in Figure 1.47 (a)) with shell's thicknesses in a range of 0.2–1 mm Fe-6.5wt.%Si alloy by SLM technology firstly, magnetic measurement results show that the lowest possible core loss was obtained with sheet thickness of 0.2 mm. Then the surface was insulated by the sol-gel method to form a  $\text{SiO}_2$  layer on each shell (with a shell thickness of 0.5 mm). Finally, specimens were uniaxially compressed (Figure 1.47 (c)) to obtain densely packed structurally-layered SMCs, which compacted to yield dense SMCs while preserving  $M_s$  above 1.65 T up to 11 layers.

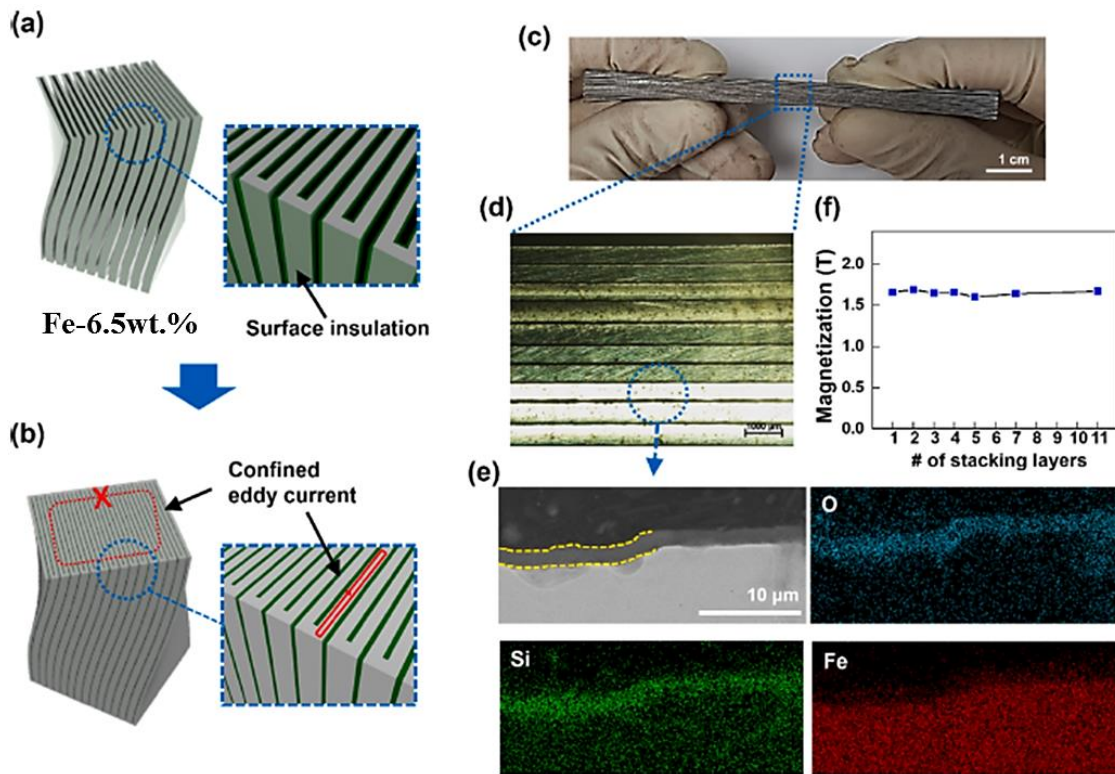



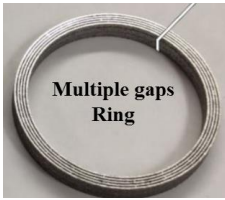


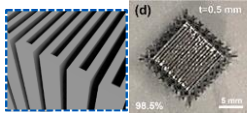


Figure 1.47 (a-b) Schematic illustration of surface insulation formed through a sol-gel process (c) uniaxial compression, (d) magnified cross-sectional optical (d) SEM image, (e) corresponding EDS element mapping, (f)  $M_s$  of structurally-layered SMCs depending on several stacked shells [152]

Based on the previous review, SLMed Fe-Si alloys has been attracting more and more attention and research. The properties of SLMed Fe-Si alloys reported in recent years are summarized in Table 1.2. It is suggested that different post-treatments have different effects on the magnetic properties of the SLMed parts, which exhibited non-monotonicity influence. Most of the studies focused on the effect of annealing treatment on magnetic properties. Similarly, the cores with different shapes and structures also show different magnetic properties, among which the influence on the power losses is the most significant.

Table 1.2 The properties of SLMed Fe-Si alloys reported in recent years

Materials & Ref.	Post-treatments	Samples structures	Magnetic properties			
			$H_c$ (A/m)	$\mu_{max}$	$M_s/B_s$	$P_L$ (W/kg)
Fe-3wt.%Si [129, 216]	As-built		-	290	-	~9 (60 Hz, 1 T)
	HIP/200 Mpa/1150 °C/2 h		-	1250	-	~1.8 (60 Hz, 1 T)
	Annealed/1200 °C/4 h		-	-	-	~3.6 (60 Hz, 1 T)

Fe-3.7wt.%Si [217]	As-built		205 (1.5 T)	3220	1.5 T at 1800 A/m	-
	Annealed/800 °C/1 h		132 (1.5 T)	7460	1.5 T at 2500 A/m	~15.3 (50 Hz, 1 T)
	Annealed/1200 °C/1 h		41 (1.5 T)	28900	-	~10.4 (50 Hz, 1 T)
	Annealed/800 °C/1 h		-	-	-	~3.3 (50 Hz, 1 T)
	Annealed/1200 °C/1 h		-	-	-	~1.2 (50 Hz, 1 T)
Fe-6.0wt.%Si [129, 216]	HIP/200 MPa/1150 °C/2 h		-	-	-	~1.4 (60 Hz, 1 T)
	Annealed/1200 °C/4 h		-	-	-	~2.0 (60 Hz, 1 T)
Fe-6.5Si [152]	As-built		165	797	-	~2.81 (50 Hz, 1 T)
	HT1200 °C		34.6	7393	-	~1.35 (50 Hz, 1 T)
Fe-6.7wt.%Si [108]	HT1050 °C/1 h/vacuum	Ring-H5 mm-D1/D2 40/30 mm	16	31000	-	~0.7 (50 Hz, 1 T)
Fe-6.9wt.%Si [212]	Annealed/1150 °C/1 h/Ar	Ring-H5 mm-D1/D2 40/30 mm	16	24000	1.6T at 50 A/m	~2.2 (50 Hz, 1 T)

$H_c$ : Coercivity;  $M_{max}$ : Maximum permeability;  $M_s/B_s$ : Saturation magnetization;  $P_L$ : Power losses; HIP: hot isostatic pressing; HT: Heat treatment.

### 1.8.1.5 Soft magnetic alloys based on Fe-Ni

Mazeeva et al. [38] presented a study on the relations of microstructure, heat treatment parameters, and magnetic properties of Fe-50wt.%Ni permalloy bulk samples prepared by the SLM technique from gas atomized powder with the same chemical composition. They found that a stable polycrystalline structure was obtained, which could provide stable values of permeability and coercivity. Appropriate heat treatment led to a partial decrease in  $H_c$  and an increase in  $\mu_{max}$  due to partial stress relaxation. The

effects of the SLM parameters on the structure and magnetic properties were not discussed, and the power losses of the samples were not evaluated in this investigation. Zou et al. [218] optimized the build condition of SLMed permalloy-80 from gas atomized powder using an island scanning strategy with an island. After that, see in Figure 1.48, they controlled the grain orientations of the alloys via titled one or two rotational angles to the substrate to achieve improved magnetic properties in the build directions during laser powder bed processing. Similarly, magnetic shielding promotion via the control of magnetic anisotropy and thermal post-processing (HT and HIP) in LPBF-processed NiFeMo-based soft magnet (pre-alloyed powder 82.77Ni, 12.8Fe, 4.37Mo, wt.%) has been reported by Mohamed [219]. The microstructures and magnetic properties could be promoted while the strength of the material could be reduced by the thermal treatments.

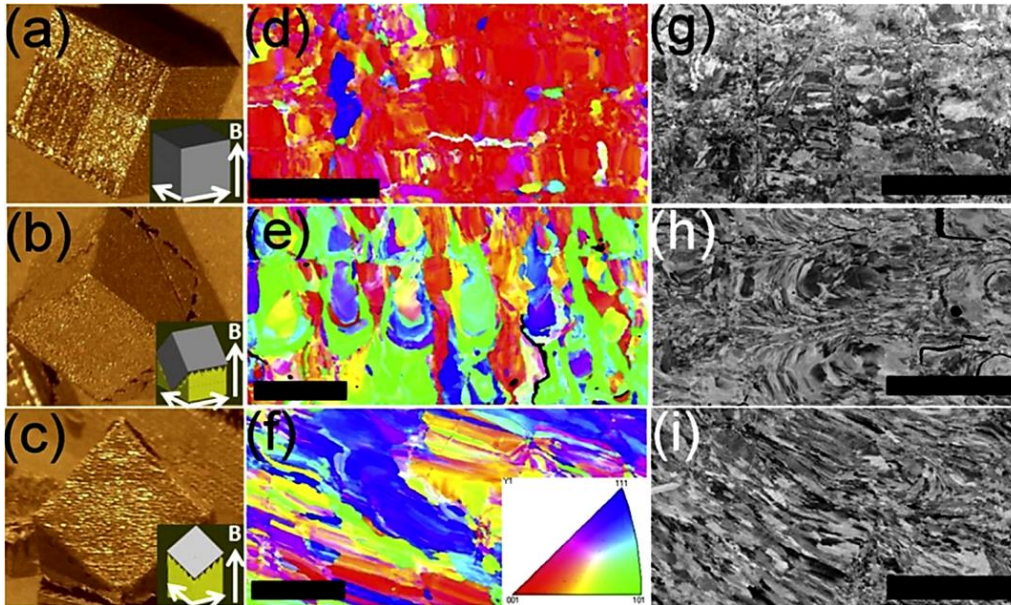


Figure 1.48 The photograph, EBSD map and SEM images of permalloy-80 built at different geometries: (a) (d) and (g)  $\langle 100 \rangle$  geometry (b), (e) and (h) are  $\langle 110 \rangle$  geometry, (c), (f) and (I) are designed according to  $\langle 111 \rangle$  geometry. All the scalebars represent  $200 \mu\text{m}$  [218]

## 1.8.2 Other soft magnetic alloys and components

Several other types of research have been concentrated on soft magnetic materials such as Fe-Co [220, 221] based alloys, SMCs [108, 137, 222], amorphous alloys [156, 223] processing using the SLM technique. Riipinen fabricated the Fe-49Co-2V soft magnetic alloys by the LPBF process [220], and the samples were exposed to different heat treatment cycles to improve the magnetic properties. Researchers from VTT Research Center Finland [224] printed and designed a 6/4 pole switch reluctance motor with complex cavities (see in Figure 1.49) using a Fe-Co alloy processed from SLM. The results demonstrated comparable magnetic saturation and mechanical properties with the standard Fe-Co alloy, although the specific power loss from eddy currents was high. Goll et al. [108] suggested multilayered structures of alternating layers of electrically insulating material and soft magnetic material to further reduce eddy current losses, as shown in Figure 1.50, they manufactured an SMCs combined complex topological structure and alternating layers of FeSi<sub>6.7</sub> (thickness:  $600 \mu\text{m}$ ), and FeAl<sub>16</sub> ( $140 \mu\text{m}$ ) by the industrial scale equipment (SLM 280 H L, SLM Solutions) and two process chambers developed for lab scale experimentation (homemade). They indicated that could reduce the eddy current losses.

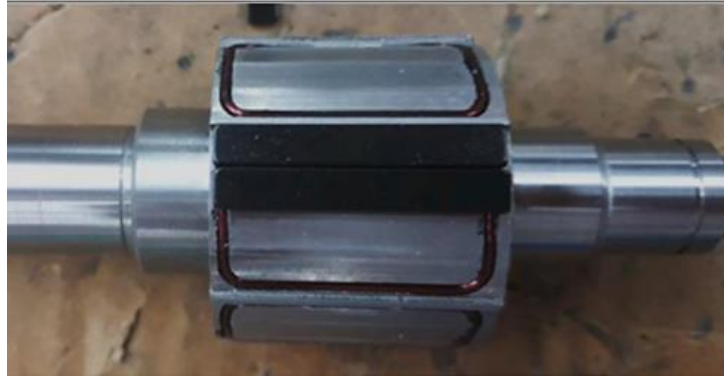


Figure 1.49 SLM rotor active part and shaft of a PM motor (Fe-Co alloy) [25]

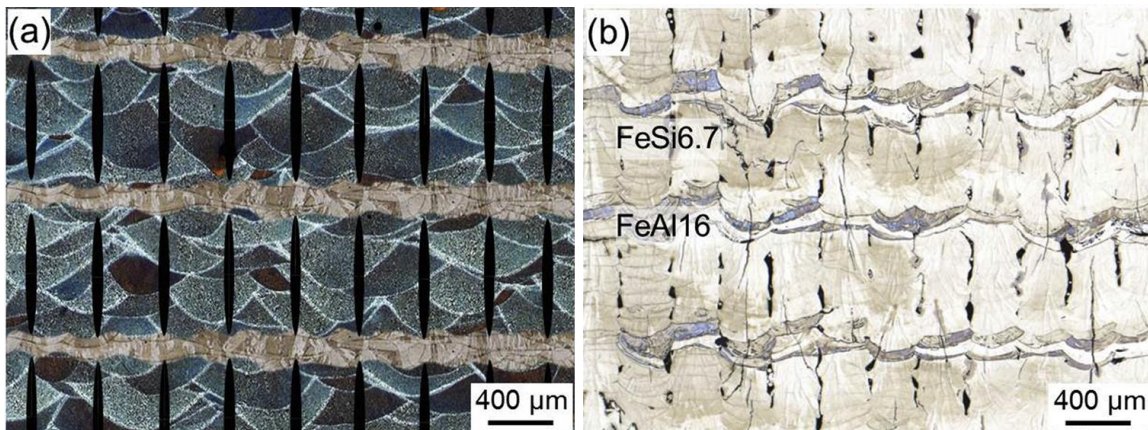


Figure 1.50 Example of an SMCs multilayered structures: (a) Schematic illustration, (b) AM Prototype of alternating layers of FeSi<sub>6.7</sub>, and FeAl<sub>16</sub> (OM image shows part of the cross-section) [108]

At present, in the available databases, there are dozens of public literatures about AM soft magnetic materials and their use in electrical machines manufacturing, SLM soft magnetic materials account for the highest proportion (~50%) [25]. However, there is still a lack of literature about SLM magnetic alloys.

## 1.9 Conclusions

With the increasingly essential demand for soft magnetic materials in the industry, automotive, and household appliances, it is important and urgent to develop new soft magnetic materials and improve the performance of traditional soft magnetic materials. Soft magnetic alloy is an important soft magnetic material, especially the Fe-Si-based soft magnetic alloy, which is the most important soft magnetic material occupying the vast majority of the soft magnetic market. It is urgent to develop more efficient, more design freedom manufacturing methods and improve the properties of the products. The freeform capabilities of the additive process and the magnetic efficiency of silicon steel have the potential for the development of electromechanical component designs that could be particularly attractive for certain electromechanical applications. In particular, the high efficiency and design freedom of the SLM technology in the manufacturing of complex shape products had made it show great potential.

So far, the research on SLMed soft magnetic alloys is still insufficient, and the investigation on SLMed Fe-Si-based soft magnetic alloy is only in the preliminary stage, lacking systematic research. Hence, systematic and detailed studies on SLMed Fe-Si-based soft magnetic alloys should be conducted.

## 1.10 Objectives and motivation of this study

A detailed literature review of the SLMed Fe-Si-based soft magnetic alloys has been performed as mentioned above. The AM technique has been attracted wide attention for manufacturing soft magnetic

alloys. The freeform capabilities of the SLM process and the magnetic efficiency of silicon steel have the potential for the development of electromechanical component designs that could be particularly attractive for certain electromechanical applications. However, the research about AM Fe-Si-based soft magnetic alloy is still insufficient, especially a systematic study on the microstructure and materials properties of Fe-Si soft magnetic alloy via SLM technology is still lacking. Given the increasing demand for Fe-Si soft magnetic alloys, especially their great application potential in the new electric machines such as motors and devices. The objective of the work presented in this thesis is to systematically study the microstructure evolution and the magnetic properties of the Fe-Si-based soft magnetic alloys produced by the SLM technique, to seek better-performing manufacturing technologies for soft magnetic materials. This work is mainly presented in several parts:

(1) Fe-3wt.%Si pre-alloy powder was adopted for the raw material in this study. Optimization parameters have been established for manufacturing SLMed dense parts. The effects of the parameters on finished surface quality, relative density, microstructure, magnetic properties, etc. have been characterized and described in detail.

(2) The oriented magnetic properties and mechanical properties of the SLMed samples fabricated via optimized processing parameters have been discussed. The influence of different heat treatments on the microstructure and magnetic properties of the SLMed Fe-3wt.%Si alloys manufactured by optimized processing parameters have been investigated.

(3) Fe-3.5wt.%Si, Fe-4.5wt.%Si, Fe-5.5wt.%Si pre-alloy powders were used to study the effects of silicon content on microstructures, magnetic properties, and mechanical properties of these SLMed silicon steels. Detailed investigation of the effect of the heat treatment on their microstructures and magnetic properties has been also presented.

## References of Chapter 1

- [1] H.C. Oersted, Experiments on the Effect of a Current of Electricity on the Magnetic Needle, 1820, in.
- [2] J.M. Coey, Magnetism and magnetic materials, Cambridge university press, 2010.
- [3] D. Jiles, Introduction to magnetism and magnetic materials, CRC press, 2015.
- [4] S. Zurek, Characterisation of soft magnetic materials under rotational magnetisation, CRC Press, 2017.
- [5] H.P. Baltés, R.S. Popovic, Integrated semiconductor magnetic field sensors, Proc. IEEE, 74 (1986) 1107-1132.
- [6] B.D. Cullity, C.D. Graham, Introduction to magnetic materials, John Wiley & Sons, 2011.
- [7] S. Chikazumi, C.D. Graham, Physics of Ferromagnetism 2e, Oxford University Press on Demand, 2009.
- [8] T. Monson, J. Silveyra, E. Ferrara, M. Taheri, T. Thiringer, Soft Magnetic Materials: Synthesis, Characterization, and Applications Introduction, (2018).
- [9] J.M. Silveyra, E. Ferrara, D.L. Huber, T.C. Monson, Soft magnetic materials for a sustainable and electrified world, Science, 362 (2018).
- [10] C. Heck, Magnetic materials and their applications, Elsevier, 2013.
- [11] E. Warburg, Magnetische untersuchungen, Ann. Phys., 249 (1881) 141-164.
- [12] J.A. Ewing, VII. On the production of transient electric currents in iron and steel conductors by twisting them when magnetised or by magnetising them when twisted, Proceedings of the Royal Society of London, 33 (1882) 21-23.
- [13] S. Ghosh, The preparation of magnetic nanoparticle assemblies for biomedical applications, in, Dublin City University, 2006.
- [14] G. Filipcsei, I. Csetneki, A. Szilágyi, M. Zrínyi, Magnetic field-responsive smart polymer composites, Oligomers-Polymer Composites-Molecular Imprinting, (2007) 137-189.



- [15] G. Bertotti, *Hysteresis in magnetism: for physicists, materials scientists, and engineers*, Gulf Professional Publishing, 1998.
- [16] M.A. Willard, M. Daniil, Nanocrystalline soft magnetic alloys two decades of progress, in: *Handbook of Magnetic Materials*, Elsevier, 2013, pp. 173-342.
- [17] P. Müllner, V. Chernenko, M. Wollgarten, G. Kostorz, Large cyclic deformation of a Ni-Mn-Ga shape memory alloy induced by magnetic fields, *J. Appl. Phys.*, 92 (2002) 6708-6713.
- [18] C.-W. Chen, *Magnetism and metallurgy of soft magnetic materials*, Courier Corporation, 2013.
- [19] P. Mohn, E. Wohlfarth, The Curie temperature of the ferromagnetic transition metals and their compounds, *J. Phys. F: Met. Phys.*, 17 (1987) 2421.
- [20] A.J. Moses, Energy efficient electrical steels: Magnetic performance prediction and optimization, *Scr. Mater.*, 67 (2012) 560-565.
- [21] C.-G. Stefanita, *Micromagnetism and the Magnetization Process*, in: *Magnetism*, Springer, 2012, pp. 39-67.
- [22] G. Bertotti, F. Fiorillo, *Magnetic Losses*, in: *Reference Module in Materials Science and Materials Engineering*, Elsevier, 2016.
- [23] <https://webstore.iec.ch/publication/2051#additionalinfo>.
- [24] S.J. Collocott, *Magnetic Materials: Domestic Applications*, in: *Reference Module in Materials Science and Materials Engineering*, Elsevier, 2016.
- [25] T.N. Lamichhane, L. Sethuraman, A. Dalagan, H. Wang, J. Keller, M.P. Paranthaman, Additive manufacturing of soft magnets for electrical machines—A review, *Mater. Today Phys.*, (2020) 100255.
- [26] A. Krings, A. Boglietti, A. Cavagnino, S. Sprague, Soft magnetic material status and trends in electric machines, *IEEE Trans. Ind. Electron.*, 64 (2016) 2405-2414.
- [27] A. Zhukov, *High performance soft magnetic materials*, Springer, 2017.
- [28] G. Chin, J. Wernick, *Soft magnetic metallic materials*, *Handbook of Ferromagnetic Materials*, 2 (1980) 55-188.
- [29] X. Xing, *Soft magnetic materials and devices on energy applications*, (2011).
- [30] M. Littmann, Iron and silicon-iron alloys, *IEEE Trans. Magn.*, 7 (1971) 48-60.
- [31] W.F. Barrett, On the electrical conductivity and magnetic permeability of various alloys of iron, *Sci. Trans. Royal. Dublin Society*, 67 (1900).
- [32] H. Helms Jr, *Review of Aluminum-Iron Magnetic Alloys and Associated Systems (0 to 10% Aluminum)*, in: *NAVAL ORDNANCE LAB WHITE OAK MD*, 1962.
- [33] R. Rana, R. Purohit, S. Das, Reviews on the influences of alloying elements on the microstructure and mechanical properties of aluminum alloys and aluminum alloy composites, *International Journal of Scientific and research publications*, 2 (2012) 1-7.
- [34] E.C. Buc, *Metallurgy and magnetism of soft magnetic iron-aluminum alloys*, in: *Wayne State University*, 2004.
- [35] H. Arnold, G. Elmen, Permalloy, a new magnetic material of very high permeability, *Bell system technical journal*, 2 (1923) 101-111.
- [36] M. Ghassemi, High power density technologies for large generators and motors for marine applications with focus on electrical insulation challenges, *High Voltage*, 5 (2019) 7-14.
- [37] S. Simizu, P.R. Ohodnicki, M.E. McHenry, Metal amorphous nanocomposite soft magnetic material-enabled high power density, rare earth free rotational machines, *IEEE Trans. Magn.*, 54 (2018) 1-5.
- [38] A. Mazeeva, M. Staritsyn, V. Bobyr, S. Manninen, P. Kuznetsov, V. Klimov, Magnetic properties of Fe–Ni permalloy produced by selective laser melting, *J. Alloys Compd.*, 814 (2020) 152315.
- [39] R.C. O'handley, *Modern magnetic materials: principles and applications*, Wiley, 2000.
- [40] J. Snoek, On the effective length of a small barkhausen discontinuity, *Physica*, 7 (1940) 609-624.

- [41] K. Praveena, K. Sadhana, H.S. Virk, Structural and magnetic properties of Mn-Zn ferrites synthesized by microwave-hydrothermal process, in: *Solid State Phenomena*, Trans Tech Publ, 2015, pp. 45-64.
- [42] E. Peng, X. Wei, T.S. Heng, U. Garbe, D. Yu, J. Ding, Ferrite-based soft and hard magnetic structures by extrusion free-forming, *RSC Adv.*, 7 (2017) 27128-27138.
- [43] C. Zachariades, R. Shuttleworth, R. Giussani, R. MacKinlay, Optimization of a high-frequency current transformer sensor for partial discharge detection using finite-element analysis, *IEEE Sens. J.*, 16 (2016) 7526-7533.
- [44] P. Duwez, S. Lin, Amorphous ferromagnetic phase in iron - carbon - phosphorus alloys, *J. Appl. Phys.*, 38 (1967) 4096-4097.
- [45] R. Hasegawa, Advances in amorphous and nanocrystalline magnetic materials, *J. Magn. Magn. Mater.*, 304 (2006) 187-191.
- [46] T. Egami, Magnetic amorphous alloys: physics and technological applications, *Rep. Prog. Phys.*, 47 (1984) 1601.
- [47] R. Hasegawa, Present status of amorphous soft magnetic alloys, *J. Magn. Magn. Mater.*, 215 (2000) 240-245.
- [48] M. Nabiałek, Soft magnetic and microstructural investigation in Fe-based amorphous alloy, *J. Alloys Compd.*, 642 (2015) 98-103.
- [49] Y.a. Yoshizawa, S. Oguma, K. Yamauchi, New Fe - based soft magnetic alloys composed of ultrafine grain structure, *J. Appl. Phys.*, 64 (1988) 6044-6046.
- [50] G. Herzer, Modern soft magnets: Amorphous and nanocrystalline materials, *Acta Mater.*, 61 (2013) 718-734.
- [51] H. Gavrilă, V. Ionita, Crystalline and amorphous soft magnetic materials and their applications - status of art and challenges, *Journal of Optoelectronics and Advanced Materials(Romania)*, 4 (2002) 173-192.
- [52] H. Shokrollahi, K. Janghorban, Soft magnetic composite materials (SMCs), *J. Mater. Process. Technol.*, 189 (2007) 1-12.
- [53] B.A. Briones, *Wiley Encyclopedia of Electrical and Electronics Engineering*, The Charleston Advisor, 21 (2019) 51-54.
- [54] E.A. Perigo, B. Weidenfeller, P. Kollár, J. Füzér, Past, present, and future of soft magnetic composites, *Appl. Phys. Rev.*, 5 (2018) 031301.
- [55] K.J. Sunday, M.L. Taheri, Soft magnetic composites: recent advancements in the technology, *Met. Powder Rep.*, 72 (2017) 425-429.
- [56] L. Hultman, A. Jack, Soft magnetic composites-materials and applications, in: *IEEE International Electric Machines and Drives Conference, 2003. IEMDC'03.*, IEEE, 2003, pp. 516-522.
- [57] M. Dias, H. Mozetic, J. Barboza, R. Martins, L. Pelegri, L. Schaeffer, Influence of resin type and content on electrical and magnetic properties of soft magnetic composites (SMCs), *Powder Technol.*, 237 (2013) 213-220.
- [58] R.M. Bozorth, *Ferromagnetism*, 1993.
- [59] Y. Wang, Y. Huang, Y. Song, X. Zhang, Y. Ma, J. Liang, Y. Chen, Room-temperature ferromagnetism of graphene, *Nano Lett.*, 9 (2009) 220-224.
- [60] R. Bozorth, *Ferromagnetism*, An IEEE Classic Reissue, New York; IEEE Press, 1994: 849-852, (1994).
- [61] R. Hilzinger, W. Rodewald, *Magnetic materials: fundamentals, products, properties, applications*, Vacuumschmelze, 2013.
- [62] T. Muto, Y. Takagi, The theory of order-disorder transitions in alloys, in: *Solid State Physics*, Elsevier, 1955, pp. 193-282.

- [63] J. Yu, J. Shin, J. Bae, Z.-H. Lee, T.D. Lee, H. Lee, E. Lavernia, The effect of heat treatments and Si contents on B2 ordering reaction in high-silicon steels, *Mater. Sci. Eng., A*, 307 (2001) 29-34.
- [64] D. Bonnenberg, K. Hempel, H. Wijn, Magnetic properties of Metals, Landolt-Bornstein New Series Group III, 19 (1986) 178.
- [65] M. Marcinkowski, N. Brown, Theory and direct observation of dislocations in the Fe<sub>3</sub>Al superlattices, *Acta Metall.*, 9 (1961) 764-786.
- [66] H. Shimanaka, Y. Ito, K. Matsumara, B. Fukuda, Recent development of non-oriented electrical steel sheets, *J. Magn. Magn. Mater.*, 26 (1982) 57-64.
- [67] U. Starke, J. Schardt, W. Weiss, W. Meier, C. Polop, P. De Andres, K. Heinz, Structural and compositional reversible phase transitions on low-index Fe<sub>3</sub>Si surfaces, *EPL (Europhysics Letters)*, 56 (2001) 822.
- [68] G. Ouyang, X. Chen, Y. Liang, C. Macziewski, J. Cui, Review of Fe-6.5 wt% Si high silicon steel—A promising soft magnetic material for sub-kHz application, *J. Magn. Magn. Mater.*, 481 (2019) 234-250.
- [69] E. Gomes, J. Schneider, K. Verbeken, J. Barros, Y. Houbaert, Correlation between microstructure, texture, and magnetic induction in nonoriented electrical steels, *IEEE Trans. Magn.*, 46 (2010) 310-313.
- [70] T. Kubota, M. Fujikura, Y. Ushigami, Recent progress and future trend on grain-oriented silicon steel, *J. Magn. Magn. Mater.*, 215 (2000) 69-73.
- [71] O. Fischer, J. Schneider, Influence of deformation process on the improvement of non-oriented electrical steel, *J. Magn. Magn. Mater.*, 254 (2003) 302-306.
- [72] O. Kubaschewski, *Iron—Binary phase diagrams*, Springer Science & Business Media, 2013.
- [73] O. Gutfleisch, M.A. Willard, E. Brück, C.H. Chen, S. Sankar, J.P. Liu, Magnetic materials and devices for the 21st century: stronger, lighter, and more energy efficient, *Adv. Mater.*, 23 (2011) 821-842.
- [74] A.M. Leary, P.R. Ohodnicki, M.E. McHenry, Soft magnetic materials in high-frequency, high-power conversion applications, *JOM*, 64 (2012) 772-781.
- [75] G.M. Size, Share & Trends Analysis Report By Application (Electronics, Composites, Energy), By Product (Graphene Nanoplatelets, Graphene Oxide), By Region, And Segment Forecasts, 2020–2027, Accessed from [https://www.grandviewresearch.com/industry-analysis/graphene-industry#:~: text= The% 20global% 20graphene% 20market% 20s ize, to% 20drive% 20the% 20product% 20demand. On, 28](https://www.grandviewresearch.com/industry-analysis/graphene-industry#:~:text=The%20global%20graphene%20market%20size,to%20drive%20the%20product%20demand.On,28) (2020).
- [76] A. Kitanovski, Energy applications of magnetocaloric materials, *Adv. Energy Mater.*, 10 (2020) 1903741.
- [77] A. Moses, Electrical steels: past, present and future developments, *IEE Proceedings A (Physical Science, Measurement and Instrumentation, Management and Education)*, 137 (1990) 233-245.
- [78] A. Saleem, Effect of manufacturing on microstructure and magnetic properties of non-oriented electrical steel, McGill University (Canada), 2018.
- [79] I.-V. Nemoianu, V.M. Paltanea, G. Paltanea, M.-I. Dascalu, R.M. Ciuceanu, Electric motors of large consumer products, challenges and trends from the perspective of power efficiency improvement through modern cutting technologies, in: 2019 Zooming Innovation in Consumer Technologies Conference (ZINC), IEEE, 2019, pp. 76-81.
- [80] H.B. Ertan, M.Y. Üçtug, R. Colyer, A. Consoli, *Modern electrical drives*, Springer Science & Business Media, 2013.
- [81] E. Bruck, *Handbook of Magnetic Materials*, Elsevier, 2017.
- [82] J.-Y. Lai, A study of the fabrication of thin lamination stator cores by the uniform droplet spray process, in, Massachusetts Institute of Technology, 1997.
- [83] T. Wakisaka, S. Arai, Y. Kurosaki, Electrical Steel Sheet for Traction Motor of Hybrid/Electrical Vehicles, Nippon Steel Technical Report, (2013).

- [84] A.B. Kustas, D.R. Johnson, K.P. Trumble, S. Chandrasekar, Enhancing workability in sheet production of high silicon content electrical steel through large shear deformation, *J. Mater. Process. Technol.*, 257 (2018) 155-162.
- [85] P. Beckley, *Electrical steels for rotating machines*, IET, 2002.
- [86] G.E. Fish, *Soft magnetic materials*, *Proc. IEEE*, 78 (1990) 947-972.
- [87] T. Tanaka, *Controlled rolling of steel plate and strip*, *International metals reviews*, 26 (1981) 185-212.
- [88] V. Panin, L. Derevyagina, M. Lebedev, A. Syromyatnikova, N. Surikova, Y.I. Pochivalov, B. Ovechkin, *Scientific basis for cold brittleness of structural BCC steels and their structural degradation at below zero temperatures*, *Phys. Mesomech.*, 20 (2017) 125-133.
- [89] P. Ramesh, N. Lenin, *High power density electrical machines for electric vehicles—Comprehensive review based on material technology*, *IEEE Trans. Magn.*, 55 (2019) 1-21.
- [90] R. Pei, J. Xu, L. Gao, H. Zheng, X. Zhou, Y. Yuan, L. Zeng, *Studies of magnetic and thermodynamic characteristics iron core under high frequencies for traction motors*, *AIP Adv.*, 10 (2020) 035107.
- [91] D.S. Petrovic, *Non-oriented electrical steel sheets*, *Mater. Tehnol.*, 44 (2010) 317-325.
- [92] A. Krings, *Iron losses in electrical machines-Influence of material properties, manufacturing processes, and inverter operation*, in, *KTH Royal Institute of Technology*, 2014.
- [93] <https://www.electrive.com/>.
- [94] <https://www.electrichybridvehicletechnology.com/>.
- [95] Y. Wang, Y. Ma, W. Hu, J. Hong, *Research on the variable mechanical properties and application in vibration control of soft magnetic entangled metallic wire material*, *Smart Mater. Struct.*, 30 (2021) 045026.
- [96] J. Pyrhonen, V. Hrabovcova, R.S. Semken, *Electrical machine drives control: An introduction*, John Wiley & Sons, 2016.
- [97] P. Tavner, L. Ran, J. Penman, H. Sedding, *Condition monitoring of rotating electrical machines*, IET, 2008.
- [98] J.H.K. Tan, S.L. Sing, W.Y. Yeong, *Microstructure modelling for metallic additive manufacturing: a review*, *Virtual Phys. Prototyping*, 15 (2020) 87-105.
- [99] E. DIN, *ISO/ASTM 52900: 2017-06: Additive Fertigung-Grundlagen-Terminologie (ISO/ASTM 52900: 2015); Deutsche Fassung EN\_ISO/ASTM 52900: 2017*, Beuth, Berlin.
- [100] I. Gibson, D.W. Rosen, B. Stucker, *Additive manufacturing technologies*, Springer, 2014.
- [101] G. Liu, X. Zhang, X. Chen, Y. He, L. Cheng, M. Huo, J. Yin, F. Hao, S. Chen, P. Wang, *Additive manufacturing of structural materials*, *Materials Science and Engineering: R: Reports*, (2021) 100596.
- [102] I. Gibson, D. Rosen, B. Stucker, M. Khorasani, *Additive manufacturing technologies*, Springer, 2014.
- [103] I. Gibson, D. Rosen, B. Stucker, M. Khorasani, *Development of additive manufacturing technology*, in: *Additive manufacturing technologies*, Springer, 2021, pp. 23-51.
- [104] A. Bandyopadhyay, S. Bose, *Additive manufacturing*, CRC press, 2019.
- [105] I. Gibson, D. Rosen, B. Stucker, M. Khorasani, *Design for additive manufacturing*, in: *Additive manufacturing technologies*, Springer, 2021, pp. 555-607.
- [106] T. Pham, P. Kwon, S. Foster, *Additive Manufacturing and Topology Optimization of Magnetic Materials for Electrical Machines—A Review*, *Energies*, 14 (2021) 283.
- [107] J.-Y. Lee, A.P. Nagalingam, S. Yeo, *A review on the state-of-the-art of surface finishing processes and related ISO/ASTM standards for metal additive manufactured components*, *Virtual Phys. Prototyping*, 16 (2021) 68-96.
- [108] D. Goll, D. Schuller, G. Martinek, T. Kunert, J. Schurr, C. Sinz, T. Schubert, T. Bernthaler, H. Riegel, G. Schneider, *Additive manufacturing of soft magnetic materials and components*, *Addit. Manuf.*, 27 (2019) 428-439.

- [109] T.F. Babuska, M.A. Wilson, K.L. Johnson, S.R. Whetten, J.F. Curry, J.M. Rodelas, C. Atkinson, P. Lu, M. Chandross, B.A. Krick, Achieving high strength and ductility in traditionally brittle soft magnetic intermetallics via additive manufacturing, *Acta Mater.*, 180 (2019) 149-157.
- [110] S. Afkhami, M. Amraei, A. Unt, H. Piili, T. Björk, Metal additive manufacturing for industrial applications, (2021).
- [111] European Powder Metallurgy Association (EPMA)—Cooling Jacket with Internal Helix Structure. Available online: <https://www.epma.com/spotlight-on-pm/cooling-jacket-with-internal-helix-structure>.
- [112] Nottingham PhD Student Wins Additive World Design Challenge Award. Available online: <https://exchange.nottingham.ac.uk/blog/phd-student-wins-additive-world-design-challenge-award/>.
- [113] R. Wrobel, B. Mecrow, Additive manufacturing in construction of electrical machines—a review, in: 2019 IEEE Workshop on Electrical Machines Design, Control and Diagnosis (WEMDCD), IEEE, 2019, pp. 15-22.
- [114] W. Sixel, M. Liu, G. Nellis, B. Sarlioglu, Cooling of Windings in Electric Machines via 3-D Printed Heat Exchanger, *IEEE Trans. Ind. Appl.*, 56 (2020) 4718-4726.
- [115] N. Simpson, D.J. North, S.M. Collins, P.H. Mellor, Additive manufacturing of shaped profile windings for minimal AC loss in electrical machines, *IEEE Trans. Ind. Appl.*, 56 (2020) 2510-2519.
- [116] N. Simpson, P.H. Mellor, Additive manufacturing of shaped profile windings for minimal AC loss in gapped inductors, in: 2017 IEEE International Electric Machines and Drives Conference (IEMDC), IEEE, 2017, pp. 1-7.
- [117] C. Wohlers, P. Juris, S. Kabelac, B. Ponick, Design and direct liquid cooling of tooth-coil windings, *Electrical Engineering*, 100 (2018) 2299-2308.
- [118] (2018, July). “GKN Powder Metallurgy identifies potential of metal AM for production of copper induction coils,” *Metal Additive Manufacturing*, vol. 4, no. 3, pp. 32.
- [119] M. Mapley, J.P. Pauls, G. Tansley, A. Busch, S.D. Gregory, Selective laser sintering of bonded magnets from flake and spherical powders, *Scr. Mater.*, 172 (2019) 154-158.
- [120] J.-M. Lamarre, F. Bernier, Permanent magnets produced by cold spray additive manufacturing for electric engines, *J. Therm. Spray Technol.*, 28 (2019) 1709-1717.
- [121] M. Ibrahim, F. Bernier, J.-M. Lamarre, Novel Multi-layer Design and Additive Manufacturing Fabrication of a High Power Density and Efficiency Interior PM Motor, in: 2020 IEEE Energy Conversion Congress and Exposition (ECCE), IEEE, 2020, pp. 3601-3606.
- [122] H.-S. Hong, H.-C. Liu, S.-Y. Cho, J. Lee, C.-S. Jin, Design of high-end synchronous reluctance motor using 3-D printing technology, *IEEE Trans. Magn.*, 53 (2017) 1-5.
- [123] Z.-Y. Zhang, M.-C. Tsai, P.-W. Huang, C.-W. Cheng, J.-M. Huang, Characteristic comparison of transversally laminated anisotropic synchronous reluctance motor fabrication based on 2D lamination and 3D printing, in: 2015 18th International Conference on Electrical Machines and Systems (ICEMS), IEEE, 2015, pp. 894-897.
- [124] M. Chinthavali, 3D printing technology for automotive applications, in: 2016 International Symposium on 3D Power Electronics Integration and Manufacturing (3D-PEIM), IEEE, 2016, pp. 1-13.
- [125] H. Tiismus, A. Kallaste, A. Belahcen, A. Rassõlkin, T. Vaimann, Challenges of additive manufacturing of electrical machines, in: 2019 IEEE 12th International Symposium on Diagnostics for Electrical Machines, Power Electronics and Drives (SDEMPED), IEEE, 2019, pp. 44-48.
- [126] M.U. Naseer, A. Kallaste, B. Asad, T. Vaimann, A. Rassõlkin, A Review on Additive Manufacturing Possibilities for Electrical Machines, *Energies*, 14 (2021) 1940.
- [127] A. Krings, A. Boglietti, A. Cavagnino, S. Sprague, Soft Magnetic Material Status and Trends in Electric Machines, *IEEE Trans. Ind. Electron.*, PP (2016) 1-1.
- [128] F. Wu, A.M. El-Refaie, Towards fully additively-manufactured permanent magnet synchronous machines: Opportunities and challenges, in: 2019 IEEE International Electric Machines & Drives Conference (IEMDC), IEEE, 2019, pp. 2225-2232.

- [129] A. Plotkowski, J. Pries, F. List, P. Nandwana, B. Stump, K. Carver, R. Dehoff, Influence of scan pattern and geometry on the microstructure and soft-magnetic performance of additively manufactured Fe-Si, *Addit. Manuf.*, 29 (2019) 100781.
- [130] M. Garibaldi, C. Gerada, R. Hague, Laser additive manufacturing of soft magnetic cores for rotating electrical machinery: Materials development and part design, in, University of Nottingham, 2018.
- [131] V. Chaudhary, N.M.S.K.K. Yadav, S.A. Mantri, S. Dasari, A. Jagetia, R. Ramanujan, R. Banerjee, Additive manufacturing of functionally graded Co-Fe and Ni-Fe magnetic materials, *J. Alloys Compd.*, 823 (2020) 153817.
- [132] B. Khatri, K. Lappe, D. Noetzel, K. Pursche, T. Hanemann, A 3D-printable polymer-metal soft-magnetic functional composite—Development and characterization, *Materials*, 11 (2018) 189.
- [133] N. Urban, A. Meyer, M. Leckel, M. Leder, J. Franke, Additive manufacturing of an electric drive a feasibility study, in: 2018 International Symposium on Power Electronics, Electrical Drives, Automation and Motion (SPEEDAM), IEEE, 2018, pp. 1327-1331.
- [134] X. Xie, C. Chen, Y. Xie, Z. Ren, E. Aubry, G. Ji, H. Liao, A novel approach for fabricating Ni-coated FeSiAl soft magnetic composite via cold spraying, *J. Alloys Compd.*, 749 (2018) 523-533.
- [135] H. Tiismus, A. Kallaste, A. Rassõlkin, T. Vaimann, Preliminary analysis of soft magnetic material properties for additive manufacturing of electrical machines, in: *Key Eng. Mater.*, Trans Tech Publ, 2019, pp. 270-275.
- [136] F. Bernier, M. Ibrahim, M. Mihai, Y. Thomas, J.-M. Lamarre, Additive manufacturing of soft and hard magnetic materials used in electrical machines, *Met. Powder Rep.*, 75 (2020) 334-343.
- [137] N.C. Benack, T. Wang, K. Matthews, M.L. Taheri, Additive manufacturing methods for soft magnetic composites (SMCs), *Microsc. Microanal.*, 24 (2018) 1066-1067.
- [138] I. Gul, A. Abbasi, F. Amin, M. Anis-ur-Rehman, A. Maqsood, Structural, magnetic and electrical properties of  $\text{Co}_{1-x}\text{Zn}_x\text{Fe}_2\text{O}_4$  synthesized by co-precipitation method, *J. Magn. Mater.*, 311 (2007) 494-499.
- [139] H. Fayazfar, M. Salarian, A. Rogalsky, D. Sarker, P. Russo, V. Paserin, E. Toyserkani, A critical review of powder-based additive manufacturing of ferrous alloys: Process parameters, microstructure and mechanical properties, *Mater. Des.*, 144 (2018) 98-128.
- [140] L.M. Bollig, P.J. Hilpisch, G.S. Mowry, B.B. Nelson-Cheeseman, 3D printed magnetic polymer composite transformers, *J. Magn. Mater.*, 442 (2017) 97-101.
- [141] E. Périgo, J. Jacimovic, F.G. Ferré, L. Scherf, Additive manufacturing of magnetic materials, *Addit. Manuf.*, 30 (2019) 100870.
- [142] L. Thijs, K. Kempen, J.-P. Kruth, J. Van Humbeeck, Fine-structured aluminium products with controllable texture by selective laser melting of pre-alloyed AlSi10Mg powder, *Acta Mater.*, 61 (2013) 1809-1819.
- [143] A. Páez-Pavón, A. Jiménez-Morales, M. Rodríguez-Arbaizar, E. Carreño-Morelli, J. Torralba, Sintering optimisation of Fe-Si soft magnetic materials processed by metal injection moulding, *Powder Metall.*, 60 (2017) 112-119.
- [144] K. Jalaiah, K.C. Mouli, R. Krishnaiah, K.V. Babu, P.S. Rao, The structural, DC resistivity and magnetic properties of Zr and Co co-substituted  $\text{Ni}_{0.5}\text{Zn}_{0.5}\text{Fe}_2\text{O}_4$ , *Heliyon*, 5 (2019) e01800.
- [145] C. Ding, L. Liu, Y. Mei, K.D. Ngo, G.-Q. Lu, Magnetic paste as feedstock for additive manufacturing of power magnetics, in: 2018 IEEE Applied Power Electronics Conference and Exposition (APEC), IEEE, 2018, pp. 615-618.
- [146] L. Liu, T. Ge, K.D. Ngo, Y. Mei, G.-Q. Lu, Ferrite paste cured with ultraviolet light for additive manufacturing of magnetic components for power electronics, *IEEE Magn. Lett.*, 9 (2018) 1-5.

- [147] H. Schönrrath, M. Spasova, S. Kilian, R. Meckenstock, G. Witt, J. Sehr, M. Farle, Additive manufacturing of soft magnetic permalloy from Fe and Ni powders: Control of magnetic anisotropy, *J. Magn. Mater.*, 478 (2019) 274-278.
- [148] I. Chicinas, V. Pop, O. Isnard, Synthesis of the supermalloy powders by mechanical alloying, *J. Mater. Sci.*, 39 (2004) 5305-5309.
- [149] C. Mikler, V. Chaudhary, T. Borkar, V. Soni, D. Choudhuri, R. Ramanujan, R. Banerjee, Laser additive processing of Ni-Fe-V and Ni-Fe-Mo permalloys: microstructure and magnetic properties, *Mater. Lett.*, 192 (2017) 9-11.
- [150] C. Mikler, V. Chaudhary, T. Borkar, V. Soni, D. Jaeger, X. Chen, R. Contieri, R. Ramanujan, R. Banerjee, Laser additive manufacturing of magnetic materials, *JOM*, 69 (2017) 532-543.
- [151] A. Krings, M. Cossale, A. Tenconi, J. Soulard, A. Cavagnino, A. Boglietti, Magnetic materials used in electrical machines: A comparison and selection guide for early machine design, *IEEE Ind. Appl. Mag.*, 23 (2017) 21-28.
- [152] B. Koo, M.-S. Jang, Y.G. Nam, S. Yang, J. Yu, Y.H. Park, J.W. Jeong, Structurally-layered soft magnetic Fe-Si components with surface insulation prepared by shell-shaping selective laser melting, *Appl. Surf. Sci.*, 553 (2021) 149510.
- [153] C.L. Cramer, P. Nandwana, J. Yan, S.F. Evans, A.M. Elliott, C. Chinnasamy, M.P. Paranthaman, Binder jet additive manufacturing method to fabricate near net shape crack-free highly dense Fe-6.5 wt.% Si soft magnets, *Heliyon*, 5 (2019) e02804.
- [154] K. Minet, A. Saharan, A. Loesser, N. Raitanen, Superalloys, powders, process monitoring in additive manufacturing, in: *Additive Manufacturing for the Aerospace Industry*, Elsevier, 2019, pp. 163-185.
- [155] A.B. Kustas, D.F. Susan, K.L. Johnson, S.R. Whetten, M.A. Rodriguez, D.J. Dagel, J.R. Michael, D.M. Keicher, N. Argibay, Characterization of the Fe-Co-1.5 V soft ferromagnetic alloy processed by Laser Engineered Net Shaping (LENS), *Addit. Manuf.*, 21 (2018) 41-52.
- [156] Y.G. Nam, B. Koo, M.S. Chang, S. Yang, J. Yu, Y.H. Park, J.W. Jeong, Selective laser melting vitrification of amorphous soft magnetic alloys with help of double-scanning-induced compositional homogeneity, *Mater. Lett.*, 261 (2020) 127068.
- [157] F. P. Jeantette, D. M. Keicher, J. A. Romero and L. P. Schanwald: 'Method and system for producing complex-shape objects', US Patent US 6046426 A, 1996., in.
- [158] I. Palčić, M. Balažic, M. Milfelner, B. Buchmeister, Potential of Laser Engineered Net Shaping (LENS) Technology, *Materials and Manufacturing Processes*, 24 (2009) 750-753.
- [159] W. Cong, F. Ning, A fundamental investigation on ultrasonic vibration-assisted laser engineered net shaping of stainless steel, *Int. J. Mach. Tools Manuf.*, 121 (2017) 61-69.
- [160] K. Ersoy, B. Çelik, Utilization of Additive Manufacturing to Produce Tools.”, in: *Design and Manufacturing*, IntechOpen, 2019.
- [161] S.M. Thompson, L. Bian, N. Shamsaei, A. Yadollahi, An overview of Direct Laser Deposition for additive manufacturing; Part I: Transport phenomena, modeling and diagnostics, *Additive Manufacturing*, 8 (2015) 36-62.
- [162] B. Onuik, B. Heer, A. Bandyopadhyay, Additive manufacturing of Inconel 718—Copper alloy bimetallic structure using laser engineered net shaping (LENS™), *Additive Manufacturing*, 21 (2018) 133-140.
- [163] K. Karczewski, M. Dąbrowska, M. Ziętała, M. Polański, Fe-Al thin walls manufactured by Laser Engineered Net Shaping, *Journal of Alloys and Compounds*, 696 (2017) 1105-1112.
- [164] H. Attar, S. Ehtemam-Haghighi, D. Kent, X. Wu, M.S. Dargusch, Comparative study of commercially pure titanium produced by laser engineered net shaping, selective laser melting and casting processes, *Materials Science and Engineering: A*, 705 (2017) 385-393.

- [165] F. Niu, D. Wu, G. Ma, J. Wang, J. Zhuang, Z. Jin, Rapid Fabrication of Eutectic Ceramic Structures by Laser Engineered Net Shaping, *Procedia CIRP*, 42 (2016) 91-95.
- [166] W.J. Sames, F. List, S. Pannala, R.R. Dehoff, S.S. Babu, The metallurgy and processing science of metal additive manufacturing, *Int. Mater. Rev.*, 61 (2016) 315-360.
- [167] J. Parthasarathy, B. Starly, S. Raman, A. Christensen, Mechanical evaluation of porous titanium (Ti6Al4V) structures with electron beam melting (EBM), *J. Mech. Behav. Biomed. Mater.*, 3 (2010) 249-259.
- [168] M. Bahraminasab, F. Farahmand, State of the art review on design and manufacture of hybrid biomedical materials: hip and knee prostheses, *Proceedings of the Institution of Mechanical Engineers, Part H: Journal of Engineering in Medicine*, 231 (2017) 785-813.
- [169] E. Chauvet, C. Tassin, J.-J. Blandin, R. Dendievel, G. Martin, Producing Ni-base superalloys single crystal by selective electron beam melting, *Scripta Materialia*, 152 (2018) 15-19.
- [170] H. Yue, Y. Chen, X. Wang, F. Kong, Effect of beam current on microstructure, phase, grain characteristic and mechanical properties of Ti-47Al-2Cr-2Nb alloy fabricated by selective electron beam melting, *Journal of Alloys and Compounds*, 750 (2018) 617-625.
- [171] X. Gong, Y. Li, Y. Nie, Z. Huang, F. Liu, L. Huang, L. Jiang, H. Mei, Corrosion behaviour of CoCrMo alloy fabricated by electron beam melting, *Corrosion Science*, (2018).
- [172] R. Guschlbauer, S. Momeni, F. Osmanlic, C. Körner, Process development of 99.95% pure copper processed via selective electron beam melting and its mechanical and physical properties, *Materials Characterization*, (2018).
- [173] J. Olsén, Z. Shen, L. Liu, A. Koptyug, L.-E. Rännar, Micro- and macro-structural heterogeneities in 316L stainless steel prepared by electron-beam melting, *Materials Characterization*, 141 (2018) 1-7.
- [174] L.E. Murr, S.M. Gaytan, D.A. Ramirez, E. Martinez, J. Hernandez, K.N. Amato, P.W. Shindo, F.R. Medina, R.B. Wicker, Metal Fabrication by Additive Manufacturing Using Laser and Electron Beam Melting Technologies, *Journal of Materials Science & Technology*, 28 (2012) 1-14.
- [175] J. Gardan, Additive manufacturing technologies: state of the art and trends, *Additive Manufacturing Handbook*, (2017) 149-168.
- [176] E.O. Olakanmi, R.F. Cochrane, K.W. Dalgarno, A review on selective laser sintering/melting (SLS/SLM) of aluminium alloy powders: Processing, microstructure, and properties, *Progress in Materials Science*, 74 (2015) 401-477.
- [177] H.J. Niu, I.T.H. Chang, Selective laser sintering of gas atomized M2 high speed steel powder, *Journal of Materials Science*, 35 (2000) 31-38.
- [178] W.W. Wits, S.J. Weitkamp, J. van Es, Metal Additive Manufacturing of a High-pressure Micro-pump, *Procedia CIRP*, 7 (2013) 252-257.
- [179] H. Lee, C.H.J. Lim, M.J. Low, N. Tham, V.M. Murukeshan, Y.-J. Kim, Lasers in additive manufacturing: A review, *International Journal of Precision Engineering and Manufacturing-Green Technology*, 4 (2017) 307-322.
- [180] M. Brandt, The role of lasers in additive manufacturing, in: *Laser Additive Manufacturing*, Woodhead Publishing, 2017, pp. 1-18.
- [181] X. Yan, S. Yin, C. Chen, C. Huang, R. Bolot, R. Lupoi, M. Kuang, W. Ma, C. Coddet, H. Liao, Effect of heat treatment on the phase transformation and mechanical properties of Ti6Al4V fabricated by selective laser melting, *J. Alloys Compd.*, 764 (2018) 1056-1071.
- [182] S. Das, M. Wohlert, J.J. Beaman, D.L. Bourell, Producing metal parts with selective laser sintering/hot isostatic pressing, *JOM*, 50 (1998) 17-20.
- [183] C.Y. Yap, C.K. Chua, Z.L. Dong, Z.H. Liu, D.Q. Zhang, L.E. Loh, S.L. Sing, Review of selective laser melting: Materials and applications, *Appl. Phys. Rev.*, 2 (2015) 041101.
- [184] J. Gunasekaran, P. Sevel, I.J. Solomon, Metallic materials fabrication by selective laser melting: a review, *Mater. Today: Proc.*, 37 (2021) 252-256.



- [185] A. Uriondo, M. Esperon-Miguez, S. Perinpanayagam, The present and future of additive manufacturing in the aerospace sector: A review of important aspects, *Proc. Inst. Mech Eng. G. J. Aerosp Eng.*, 229 (2015) 2132-2147.
- [186] M. Garibaldi, C. Gerada, I. Ashcroft, R. Hague, H. Morvan, The impact of additive manufacturing on the development of electrical machines for MEA Applications: A feasibility study, in, 2015.
- [187] C. Emmelmann, P. Scheinmann, M. Munsch, V. Seyda, Laser Additive Manufacturing of Modified Implant Surfaces with Osseointegrative Characteristics, *Physics Procedia*, 12 (2011) 375-384.
- [188] <https://www.slm-solutions.com/>.
- [189] X. Yan, Q. Li, S. Yin, Z. Chen, R. Jenkins, C. Chen, J. Wang, W. Ma, R. Bolot, R. Lupoi, Mechanical and in vitro study of an isotropic Ti6Al4V lattice structure fabricated using selective laser melting, *J. Alloys Compd.*, 782 (2019) 209-223.
- [190] H. Fan, J. Fu, X. Li, Y. Pei, X. Li, G. Pei, Z. Guo, Implantation of customized 3-D printed titanium prosthesis in limb salvage surgery: a case series and review of the literature, *World journal of surgical oncology*, 13 (2015) 308.
- [191] SpaceX Reveals 3D-Printed Rocket Engine Parts <https://www.designnews.com/design-hardware-software/spacex-reveals-3d-printed-rocket-engine-parts>.
- [192] T. Kellner, How 3D Printing Will Change Manufacturing, GE Reports. <https://www.ge.com/reports/epiphany-disruption-ge-additive-chief-explains-3d-printing-will-upend-manufacturing/>.
- [193] New manufacturing milestone: 30,000 additive fuel nozzles. <https://www.ge.com/additive/stories/new-manufacturing-milestone-30000-additive-fuel-nozzles>.
- [194] 3D Printing Solutions for Aerospace and Defense. <https://www.slm-solutions.com/industries/aerospace-and-defense/>.
- [195] 3D Printing Solutions for Automotive, <https://www.slm-solutions.com/industries/automotive/>.
- [196] B. Song, X. Zhao, S. Li, C. Han, Q. Wei, S. Wen, J. Liu, Y. Shi, Differences in microstructure and properties between selective laser melting and traditional manufacturing for fabrication of metal parts: A review, *Frontiers of Mechanical Engineering*, 10 (2015) 111-125.
- [197] L. Gargalis, V. Madonna, P. Giangrande, R. Rocca, I. Ashcroft, R. Hague, M. Galea, Development and Testing of Soft Magnetic Rotor for a Switched Reluctance Motor Built Through Additive Manufacturing Technology, in: 2020 23rd International Conference on Electrical Machines and Systems (ICEMS), IEEE, 2020, pp. 263-268.
- [198] X. Zhang, C.J. Yocom, B. Mao, Y. Liao, Microstructure evolution during selective laser melting of metallic materials: A review, *J. Laser Appl.*, 31 (2019) 031201.
- [199] J. Zhang, B. Song, Q. Wei, D. Bourell, Y. Shi, A review of selective laser melting of aluminum alloys: Processing, microstructure, property and developing trends, *Journal of Materials Science & Technology*, 35 (2019) 270-284.
- [200] B. Zhang, N.-E. Fenineche, H. Liao, C. Coddet, Magnetic properties of in-situ synthesized FeNi<sub>3</sub> by selective laser melting Fe-80% Ni powders, *Journal of Magnetism and Magnetic Materials*, 336 (2013) 49-54.
- [201] B. Zhang, N.-E. Fenineche, H. Liao, C. Coddet, Microstructure and magnetic properties of Fe–Ni alloy fabricated by selective laser melting Fe/Ni mixed powders, *Journal of Materials Science & Technology*, 29 (2013) 757-760.
- [202] C. Mikler, V. Chaudhary, V. Soni, B. Gwalani, R. Ramanujan, R. Banerjee, Tuning the phase stability and magnetic properties of laser additively processed Fe-30at% Ni soft magnetic alloys, *Materials Letters*, 199 (2017) 88-92.
- [203] B. Zhang, N.E. Fenineche, H. Liao, C. Coddet, Microstructure and Magnetic Properties of Fe–Ni Alloy Fabricated by Selective Laser Melting Fe/Ni Mixed Powders, *Journal of Materials Science & Technology*, 29 (2013) 757-760.

- [204] L. Gargalis, V. Madonna, P. Giangrande, R. Rocca, M. Hardy, I. Ashcroft, M. Galea, R. Hague, Additive manufacturing and testing of a soft magnetic rotor for a switched reluctance motor, *IEEE Access*, 8 (2020) 206982-206991.
- [205] H. Shipley, D. McDonnell, M. Culleton, R. Coull, R. Lupoi, G. O'Donnell, D. Trimble, Optimisation of process parameters to address fundamental challenges during selective laser melting of Ti-6Al-4V: A review, *International Journal of Machine Tools and Manufacture*, 128 (2018) 1-20.
- [206] L. Thijs, F. Verhaeghe, T. Craeghs, J.V. Humbeeck, J.-P. Kruth, A study of the microstructural evolution during selective laser melting of Ti-6Al-4V, *Acta Materialia*, 58 (2010) 3303-3312.
- [207] G. Kasperovich, J. Haubrich, J. Gussone, G. Requena, Correlation between porosity and processing parameters in TiAl6V4 produced by selective laser melting, *Materials & Design*, 105 (2016) 160-170.
- [208] M. Garibaldi, I. Ashcroft, N. Hillier, S. Harmon, R. Hague, Relationship between laser energy input, microstructures and magnetic properties of selective laser melted Fe-6.9% wt Si soft magnets, *Materials Characterization*, 143 (2018) 144-151.
- [209] M. Garibaldi, I. Ashcroft, M. Simonelli, R. Hague, Metallurgy of high-silicon steel parts produced using Selective Laser Melting, *Acta Mater.*, 110 (2016) 207-216.
- [210] S. Alleg, R. Drablia, N. Fenineche, Effect of the Laser Scan Rate on the Microstructure, Magnetic Properties, and Microhardness of Selective Laser-Melted FeSiB, *J. Supercond. Novel Magn.*, 31 (2018) 3565-3577.
- [211] J. Lemke, M. Simonelli, M. Garibaldi, I. Ashcroft, R. Hague, M. Vedani, R. Wildman, C. Tuck, Calorimetric study and microstructure analysis of the order-disorder phase transformation in silicon steel built by SLM, *J. Alloys Compd.*, 722 (2017) 293-301.
- [212] M. Garibaldi, I. Ashcroft, J. Lemke, M. Simonelli, R. Hague, Effect of annealing on the microstructure and magnetic properties of soft magnetic Fe-Si produced via laser additive manufacturing, *Scr. Mater.*, 142 (2018) 121-125.
- [213] P. Mercelis, J.P. Kruth, Residual stresses in selective laser sintering and selective laser melting, *Rapid Prototyping J.*, (2006).
- [214] P. Jang, B. Lee, G. Choi, Effects of annealing on the magnetic properties of Fe-6.5% Si alloy powder cores, *J. Appl. Phys.*, 103 (2008) 07E743.
- [215] C. Weisman, W. Kearns, *Welding Handbook: Metals and their weldability*, American Welding Society, 1976.
- [216] A. Plotkowski, K. Carver, F. List, J. Pries, Z. Li, A.M. Rossy, D. Leonard, Design and performance of an additively manufactured high-Si transformer core, *Mater. Des.*, 194 (2020) 108894.
- [217] H. Tiismus, A. Kallaste, A. Belahcen, M. Tarraste, T. Vaimann, A. Rassõlkin, B. Asad, P. Shams Ghahfarokhi, AC Magnetic Loss Reduction of SLM Processed Fe-Si for Additive Manufacturing of Electrical Machines, *Energies*, 14 (2021) 1241.
- [218] J. Zou, Y. Gaber, G. Voulazeris, S. Li, L. Vazquez, L.-F. Liu, M.-Y. Yao, Y.-J. Wang, M. Holynski, K. Bongs, Controlling the grain orientation during laser powder bed fusion to tailor the magnetic characteristics in a Ni-Fe based soft magnet, *Acta Mater.*, 158 (2018) 230-238.
- [219] A.E.-M.A. Mohamed, J. Zou, R.S. Sheridan, K. Bongs, M.M. Attallah, Magnetic shielding promotion via the control of magnetic anisotropy and thermal Post processing in laser powder bed fusion processed NiFeMo-based soft magnet, *Addit. Manuf.*, 32 (2020) 101079.
- [220] T. Riipinen, S. Metsä-Kortelainen, T. Lindroos, J.S. Keränen, A. Manninen, J. Pippuri-Mäkeläinen, Properties of soft magnetic Fe-Co-V alloy produced by laser powder bed fusion, *Rapid Prototyping J.*, (2019).
- [221] I. GAVRIKOV, D. ANISIMOV, D. SOZINOV, M. FEDOSEEV, STRUCTURE AND MAGNETIC PROPERTIES OF THE MATERIAL OF THE Fe-Cr-Co SYSTEM PRODUCED BY THE SELECTIVE LASER MELTING, *SCIENTIFIC AND TECHNICAL JOURNAL*, (2020) 12.

- [222] S. Gao, X. Yan, C. Chang, E. Aubry, P. He, M. Liu, H. Liao, N. Fenineche, Microstructure and magnetic properties of FeSiBCrC soft magnetic alloy manufactured by selective laser melting, *Mater. Lett.*, 290 (2021) 129469.
- [223] M.G. Ozden, N.A. Morley, Laser Additive Manufacturing of Fe-Based Magnetic Amorphous Alloys, *Magnetochemistry*, 7 (2021) 20.
- [224] S. Metsä-Kortelainen, T. Lindroos, M. Savolainen, A. Jokinen, A. Revuelta, A. Pasanen, K. Ruusuvoori, J. Pippuri, Manufacturing of topology optimized soft magnetic core through 3D printing, in: *NAFEMS Exploring the Design Freedom of Additive Manufacturing through Simulation*, 2016.

## Chapter 2 Materials characterization and experimental techniques

### 2.1 Characterization of the raw materials

In this work, Fe-3wt.%Si, Fe-3.5wt.%Si, Fe-4.5wt.%Si, Fe-5.5wt.%Si, pre-alloy powders were used as the raw materials respectively. The Fe-3wt.%Si powder was purchased from POCO Holding CO., LTD (Shenzhen, China), the others were purchased from HUNAN HUALIU NEW MATERIALS CO., LTD. The shape, morphology, and chemical composition of the powder were characterized by scanning electron microscopy (SEM JEOL-5900 LV, Japan), equipped with energy-dispersive X-ray spectroscopy (EDS) unit. The particle size distributions of the powders were measured by a laser diffraction powder sizer (Mastersizer 2000, Malvern Instruments Ltd., UK) which is displayed in Figure 2.1. The cross-sections of the particles were observed by an optical microscope (OM, Nikon, Japan). Besides, the overview and representative magnified morphology of the used metallurgical powder were presented. The phase composition was performed by XRD analyses on an X-Ray diffractometer (XRD-6100, Shimadzu Co. Ltd., Japan).



Figure 2.1 Laser diffraction powder sizer

As can be seen in Figure 2.2-Figure 2.4, the powder particles were mainly spherical and near-spherical in shape, without satellite particles on the surface. That is an important characteristic of excellent flowability which meets exactly the requirement during the SLM process. The particle size distributions are concentrated on 15  $\mu\text{m}$ -40  $\mu\text{m}$ . From the cross-sectional OM pictures of the particles, it can be observed that there are no obvious hollows and pores in the powders. The results of EDS characterization are agreed with the chemical composition that is listed in Table 2.1. The XRD spectra of the powders depicted in Figure 2.5 (a) show only the peaks of the bcc-Fe phase in Fe-3wt.%Si, Fe-3.5wt.%Si, Fe-4.5wt.%Si, Fe-5.5wt.%Si alloys.

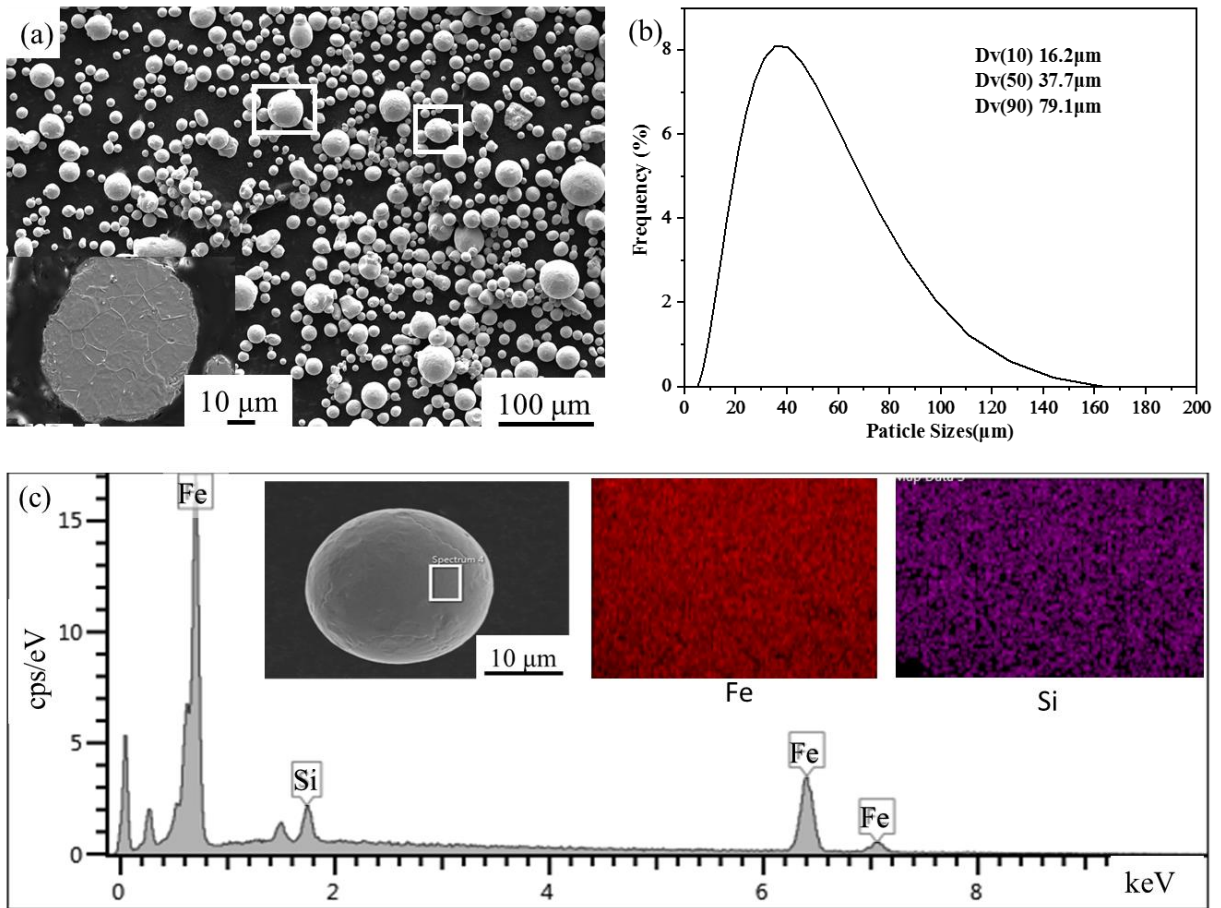


Figure 2.2 Characterization of Fe-3wt.%Si: (a) morphology and cross-section of the particles, (b) particle size distribution, (c) the results of EDS

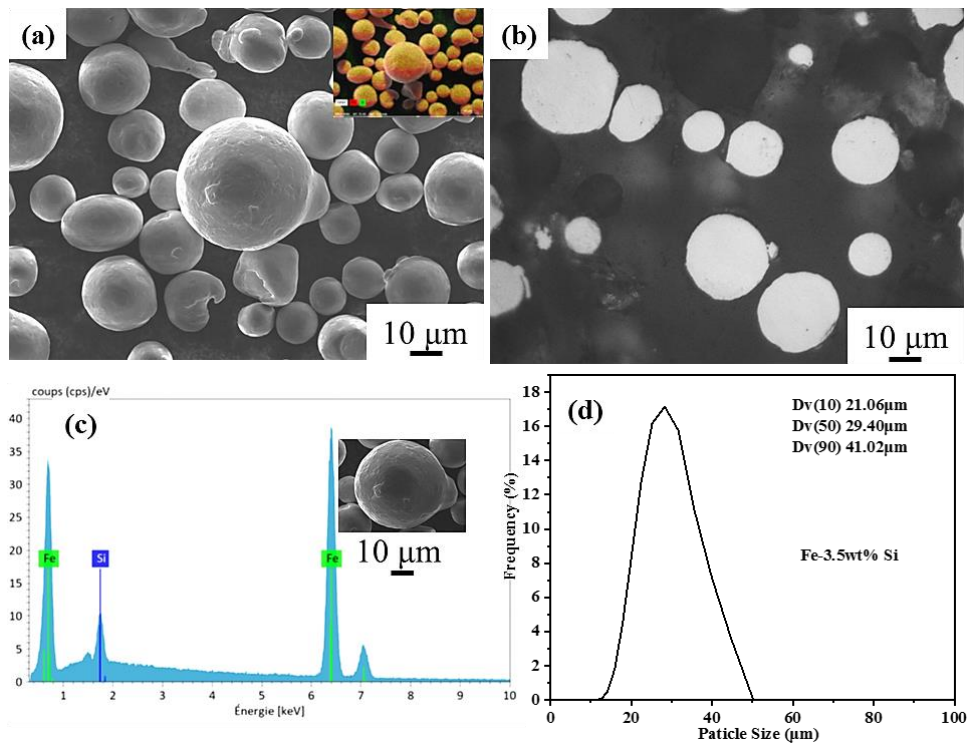


Figure 2.3 Characterization of Fe-3.5wt.%Si: (a) morphology and EDS mapping (b) cross-section of the particles, (c) the results of EDS, (d) particle size distribution

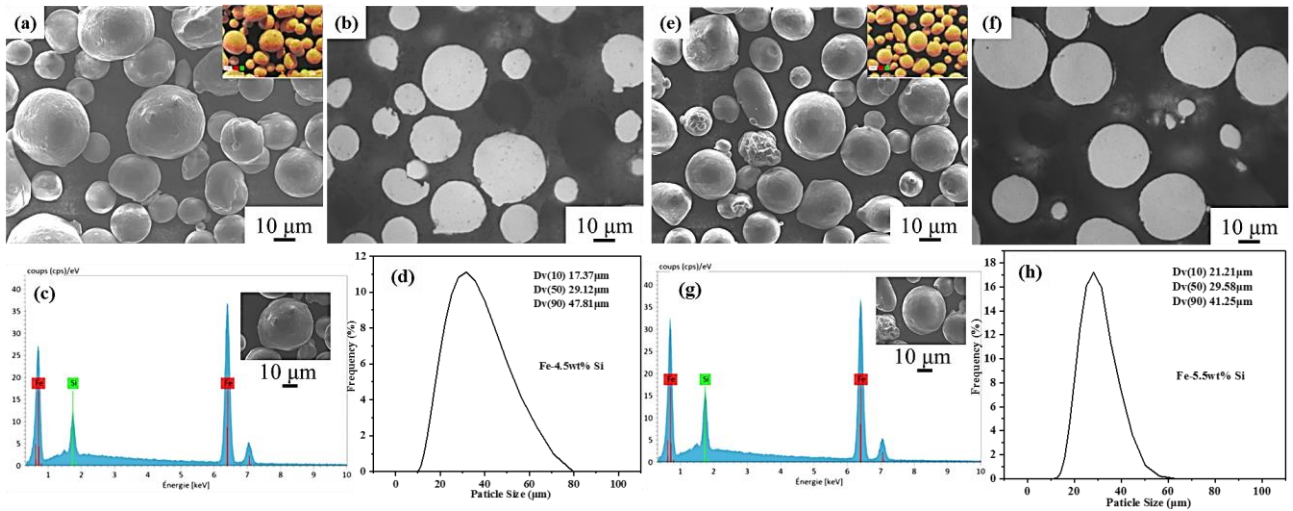


Figure 2.4 Characterization of Fe-4.5wt.%Si: (a-d) and Fe-5.5wt.%Si (e-h): (a) (e) morphology and EDS mapping (b) (f) cross-section of the particles, (c) (g) the results of EDS, (d) (h) particle size distributions

Table 2.1 The nominal composition of the powders

Alloy	Nominal composition (wt.%)							
	Fe	Si	C	O	S	P	Ni	Cr
Fe-3Si	Bal	3±0.1	≤0.03	≤0.04	≤0.01	≤0.02	-	-
Fe-3.5Si	Bal	3.5±0.15	≤0.03	≤0.04	≤0.01	≤0.02	-	-
Fe-4.5Si	Bal	4.5±0.15	≤0.03	≤0.04	≤0.01	≤0.02	-	-
Fe-5.5Si	Bal	5.5±0.15	≤0.03	≤0.04	≤0.01	≤0.02	-	-

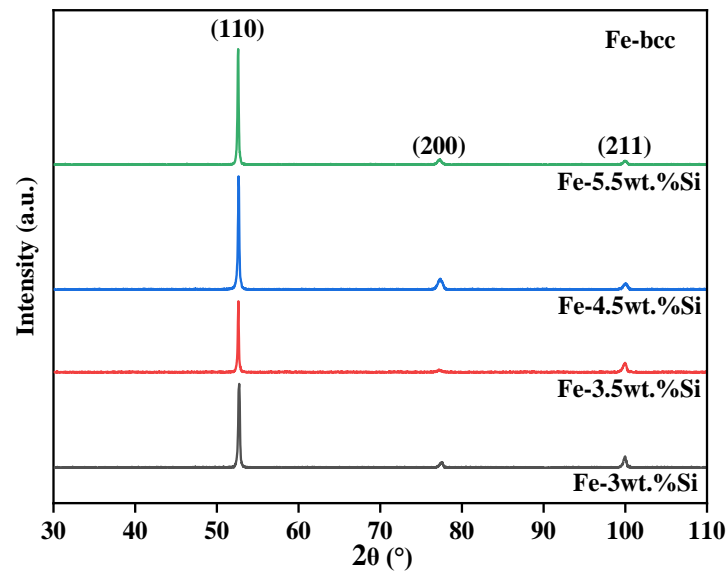


Figure 2.5 XRD spectra of the raw powders

## 2.2 The SLM system

### 2.2.1 Introduce to the utilized machine

A series of specimens were prepared using a selective laser melting machine MCP Realizer SLM 250 system (MCP-HEK Tooling GmbH, Germany). It is equipped with an Nd-YAG fiber laser. The maximum power is 400W. The photos of this machine and working chamber are exhibited in Figure 2.6. It employs a hopper of feedstock powder. The chamber can be filled with argon. The gas circulation

system can discharge the splashed powder or dregs to the side. The platform can be moved up and down by motor control. The oxygen content can be kept below 0.2 vol.% using neutral gas (such as argon) controlled by a sensor to avoid material oxidation during manufacturing. In this work, the 316L steel was used as a platform for manufacturing.

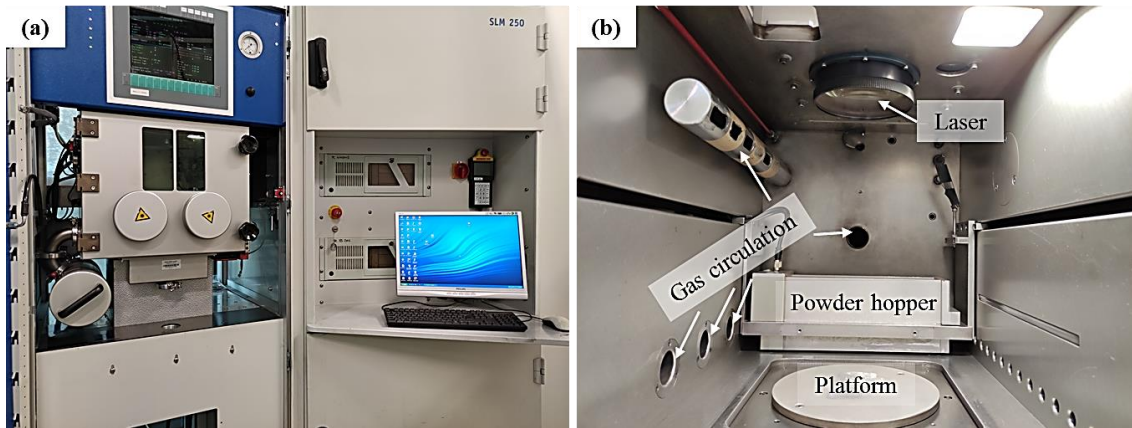


Figure 2.6 (a) The utilized SLM system, (b) working chamber

## 2.2.2 Working principle and main processing parameters

Before starting all the works, the 3D design software was used to design the building models, then, the models were imported into the SLM computer system for slicing and setting parameters. In the system of SLM 250, the laser beam (with a laser power) expose (exposure in a time at a level of  $\sim\mu\text{s}$ ) and scan rapidly (with a scanning speed) with the designed strategy, which was controlled by the computer, Figure 2.7 (a) is a picture of SLM manufacturing process. As shown in Figure 2.7 (b), the distance between the centers of each laser spot is defined to point distance, and the distance between each laser track is hatch distance. When the first layer powder was selectively melted fully, the platform could be dropped a height to spreading the second powder, the value of the height is layer thickness. The processing parameters can be set in the computer system. As depicted in Figure 2.7 (b), the planes of the SLMed samples are referred to the conventions in ISO ASTM 52 921: 2013[1], where XY plane is the transversal plane (scanning plane of the laser beam) and XZ/YZ planes are the lateral planes of the building direction.

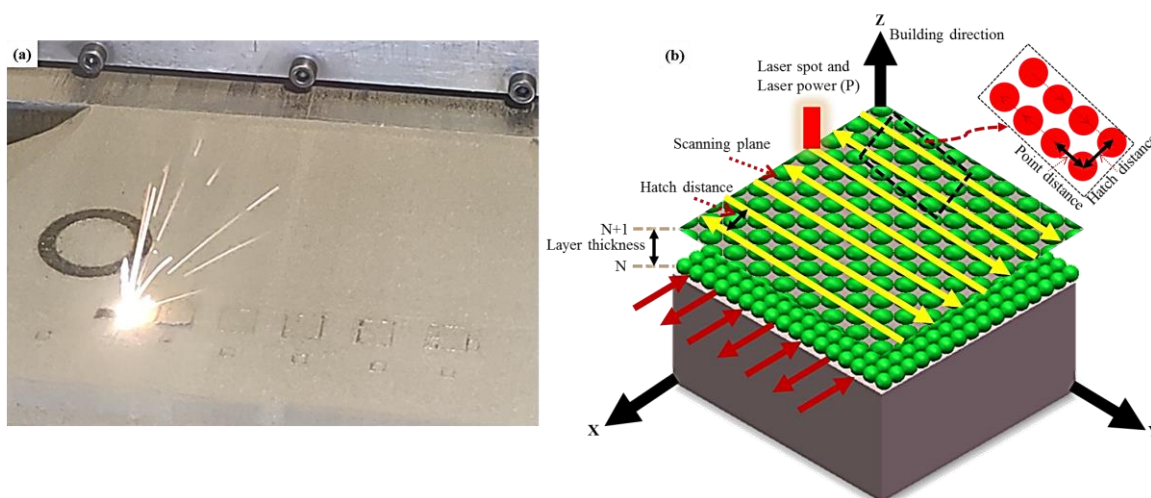


Figure 2.7 (a) SLM manufacturing process, (b) Schematic diagram of scanning strategy and parameters

## 2.3 Materials characterization

### 2.3.1 Top surface morphology and porosity analysis

The roughness and surface morphology of the top side (XY plane) of each SLM sample was investigated by a DektakXT profilometer (Bruker, American, see in Figure 2.8) and an SEM instrument (JSM5800LV, JEOL, Japan). These SLMed samples were embedded in resin, polished, and then etched. As shown in Figure 2.9 (a), an optical microscope was used to obtain optical micrographics and observe the defects distributions. The porosity was determined from the OM micrographs by an image analysis method. To achieve repeatability, the XZ plane of each sample was analyzed with a minimum of five optical micrographs at different areas alternatively via the image processing software ImageJ.



Figure 2.8 The profilometer system

### 2.3.2 Microstructural characterization

To clearly observe the microstructure, specimens were polished and etched at room temperature using a Nital solution (3% nitric + 97% ethanol) for 30-40 s, then, were observed by the OM (Figure 2.9 (a)). The etched samples were also observed by SEM system (Figure 2.9 (b)), equipped with an EDS unit.

Texture and crystallographic orientations of SLMed specimens were observed by electron back-scattering diffraction (EBSD) spectrometer (NordlysMax3, Oxford Instruments, UK) with a step size of 0.15  $\mu\text{m}$  and analyzed using Channel 5 software. Samples for EBSD characterization were prepared by mechanical polishing and final surface iron milling.

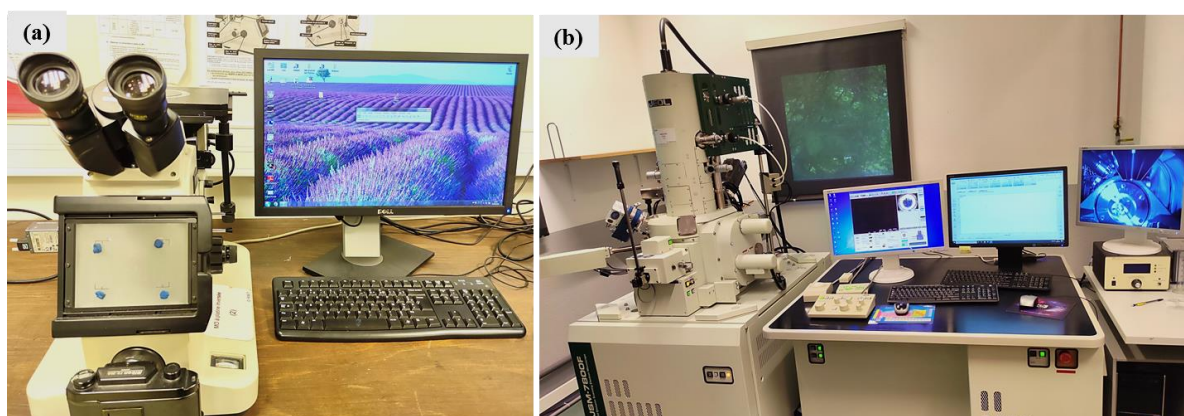


Figure 2.9 (a) The optical microscope and (b) scanning electron microscopy



### 2.3.3 Phase analysis



Figure 2.10 The X-Ray diffractometer

The XRD analyses were performed on an X-Ray diffractometer (XRD-6100, Shimadzu Co. Ltd., Japan), as presented in Figure 2.10, operating at 40 kV/40 mA and using Cu K $\alpha$  radiation ( $\lambda=0.15406$  nm). 2 $\theta$  scans were performed between 30 ° and 110 ° with a scan speed of 5 °·min<sup>-1</sup>.

### 2.4 Post heat treatment

As shown in Figure 2.11, post heat treatments were performed using a homemade furnace (PMDM-LERMPS) under Argon protective atmosphere to prevent the samples from oxidation. The furnace temperature can reach 1100 °C. The heating rate was about 5 °C min<sup>-1</sup> and the samples can be cooled in different ways, such as with furnace cooling, air cooling, or water quenching, depending on the requirements of the experiment.



Figure 2.11 Home-made furnace (PMDM-LERMPS)

## 2.5 Measurement and study of magnetic properties

### 2.5.1 Test of magnetic properties using VSM method

A vibrating sample magnetometer (VSM) operates on Faraday's Law of Induction, which tells us that a changing magnetic field will produce an electric field. This electric field can be measured and can tell us information about the changing magnetic field. A VSM is used to measure the magnetic behavior of magnetic materials. A VSM operates by first placing the sample to be studied in a constant magnetic field. If the sample is magnetic, this constant magnetic field will magnetize the sample by aligning the magnetic domains, or the individual magnetic spins, with the field. The stronger the constant field, the larger the magnetization will be. The magnetic dipole moment of the sample will create a magnetic field around the sample, sometimes called the magnetic stray field. As the sample is moved up and down, this magnetic stray field is changing as a function of time and can be sensed by a set of pick-up coils. The alternating magnetic field will cause an electric field in the pick-up coils according to Faraday's Law of Induction. This current will be proportional to the magnetization of the sample. The greater the magnetization, the greater the induced current. The induction current is amplified by a transimpedance amplifier and lock-in amplifier. The various components are hooked up to a computer interface. Using controlling and monitoring software, it can be known how much the sample is magnetized and how its magnetization depends on the strength of the constant magnetic field. Thus, through the measurement of the VSM method, the hysteresis loop of magnetic samples can be obtained. Based on the hysteresis loop, the magnetic characteristic such as magnetization-magnetic field ( $M-H$ ) curve, saturation magnetization ( $M_s$ ), remanent magnetization ( $M_r$ ), coercivity  $H_c$ , and the slope of  $H_c$ , etc. can be obtained. In this study, the static magnetic measurements were achieved employing a Lakeshore 7404 vibrating sample VSM at room temperature, under an applied magnetic field of 20 kOe. This VSM system can be used to characterize the static magnetic properties of materials as a function of the magnetic field, temperature, and time. Available in three different variable gap electromagnet configurations providing fields over 2 T. The specimens with dimensions of 3 mm  $\times$  3 mm  $\times$  3 mm were adopted to VSM measurements. Its schematic diagram and equipment are shown in Figure 2.12. In this VSM test, the Gauss system of units (CGS) was adopted.

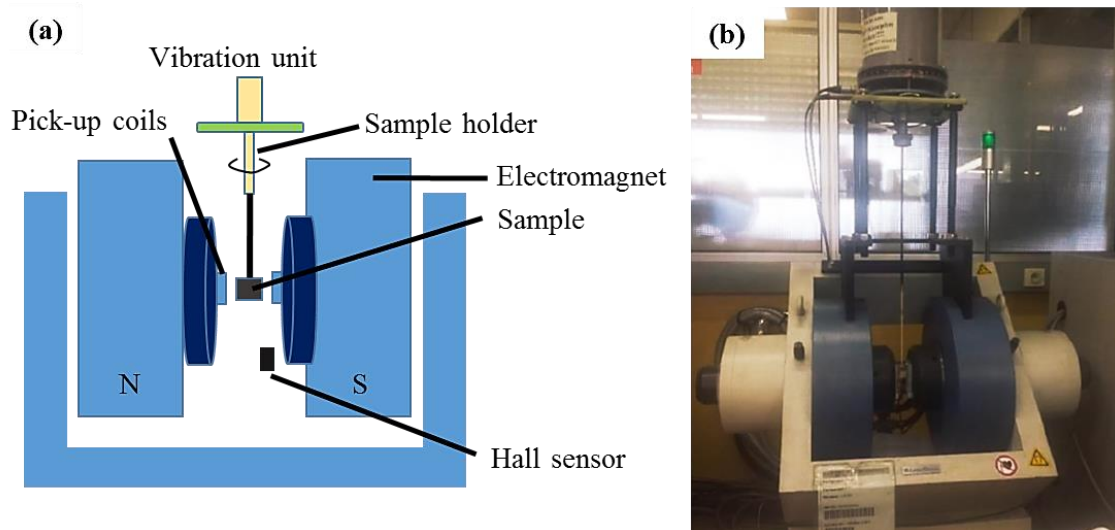


Figure 2.12 A schematic diagram and equipment of the VSM

### 2.5.2 Test of magnetic properties by AC method

The ring method was also employed for the measurement of material magnetic properties. The measurements were conducted at the frequencies of 50 Hz for the investigation of AC losses. A magnetic measure system (MATS-2010SA, see in Figure 2.14) was used to automate measurement and data post-

processing with good repeatability. Experiments were conducted at the ambient temperature of  $\sim 20^\circ\text{C}$ , without a significant increase in the sample temperature during the measurements. A schematic of the AC magnetic property measurements is shown in Figure 2.13 (a), as well as a measured sample in Figure 2.13. The bottom surfaces of the ring specimens were ground for surface finish. The final sample height was  $h=4 \pm 0.1$  mm. Total power losses ( $P_{50-1}$ ) at excitation frequency  $f=50$  Hz and maximum flux density  $B=1$  T were also determined, following the guidelines presented in [2] for the measurement of the AC magnetic properties of soft magnetic materials using ring samples. The magnetic measurements were repeated for each ring specimen until for each of the magnetic properties considered a level of uncertainty  $<3\%$  could be achieved. Uncertainty was calculated using the standard error. Furthermore, for each of the process parameters considered, several ring samples were manufactured to assess the repeatability of the manufacturing process. From the experimental data, the magnetic field strength  $H$  was calculated by the following equation respectively [3]:

$$H = \frac{N_1 I}{l_r} \quad \text{Equation 2.1}$$

$$B = \frac{1}{N_2} (\int V(t) dt) \quad \text{Equation 2.2}$$

where  $N_1$  is the number of turns of the primary coil,  $N_2$  is the number of turns of the secondary coil,  $I$  is the instantaneous current value,  $e$  is the instantaneous induced electromotive force,  $l_r$  is the ring average length.

In particular, the property in this study was the total specific power losses at fixed excitation frequency and output magnetic flux density. The total losses are the total loss per unit of sample mass and were calculated using the wattmeter method using the following equation [4, 5]:

$$P_{\text{cycle}} = C_{\text{hyst}} (B)f + C_{\text{eddy}} (B)f^2 \quad \text{Equation 2.3}$$

where  $P_{\text{cycle}}$  is the total power losses per cycle,  $f$  is frequency,  $C_{\text{hyst}}$  is a coefficient associated with hysteresis (materials) losses, and  $C_{\text{eddy}}$  is a coefficient associated with eddy current losses.

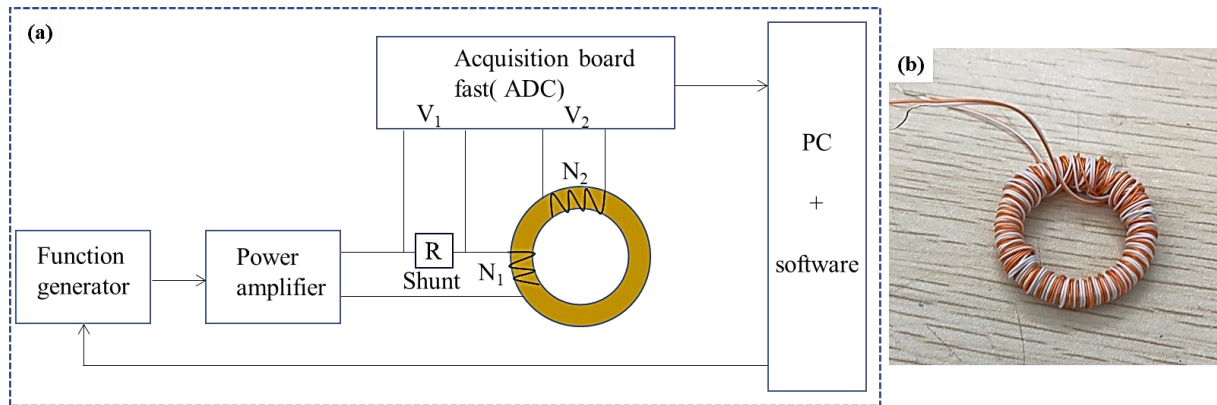


Figure 2.13 (a) A schematic of the AC magnetic measurements setup, (b) a measured sample



Figure 2.14 AC magnetic property measurements system

### 2.5.3 Test of DC magnetic properties

According to the guidelines presented in Ref.[6], the DC hysteresis loop (B-H curve) of the samples was measured by using a standard method based on a commutation curve registration which demands a ring-shaped sample to obtain a closed magnetic field in the measuring circuit to provide high accuracy of the measurements. Maximum relative permeability ( $\mu_{\max}$ ) of the samples was determined at an applied flux density  $H=5000$  A/m were employed to assess their magnetic properties, while saturation magnetic induction ( $B_s$ ) remanence ( $B_r$ ) and coercivity ( $H_c$ ) were determined from the B-H loop to assess loop, respectively. In the AC and DC magnetic properties measurements, the International System of Units (SI) was adopted.

## 2.6 Measurement and study of mechanical properties

### 2.6.1 Microhardness

The Vickers hardness measurements were carried out at different locations on the XY and XZ planes, respectively. The Vickers hardness was measured using a microhardness tester (Leiz-Wetzlar, Germany) at a condition with a load of 100 g and an indentation time of 25 s. To ensure accuracy, the average value of the hardness was recorded by 10 measurements.



Figure 2.15 The microhardness tester

### 2.6.2 Tensile test

The tensile samples were fabricated parallel to the platform and removed from the platform along the XY plane, as depicted in Figure 2.16 (a). Macro morphology of the polished tensile samples with a gauge length of 25 mm, a width of 3 mm, and a thickness of 3.5 mm for mechanical properties test were

shown in Figure 2.16 (c). Tensile tests were carried out at room temperature according to the ASTM E 8M standard at a displacement rate of 1 mm/min [7]. The morphology of tensile testing equipment was displayed in Figure 2.16 (b). Mechanical properties including ultimate tensile strength (UTS), yield strength (YS), and fracture strain were read directly from the INSTRON tensile tester. The elongation at break (EL) was measured based on the guidance of the ASTM E 111 standard. The strain-to-failure was evaluated through strain gauges and electronic extensometers with a range of 10 mm that were mounted on the gauge section of the test samples. For each experimental group, three samples were tested, and the averaged values were calculated. The fracture morphologies of the tensile samples were then observed and investigated using SEM.

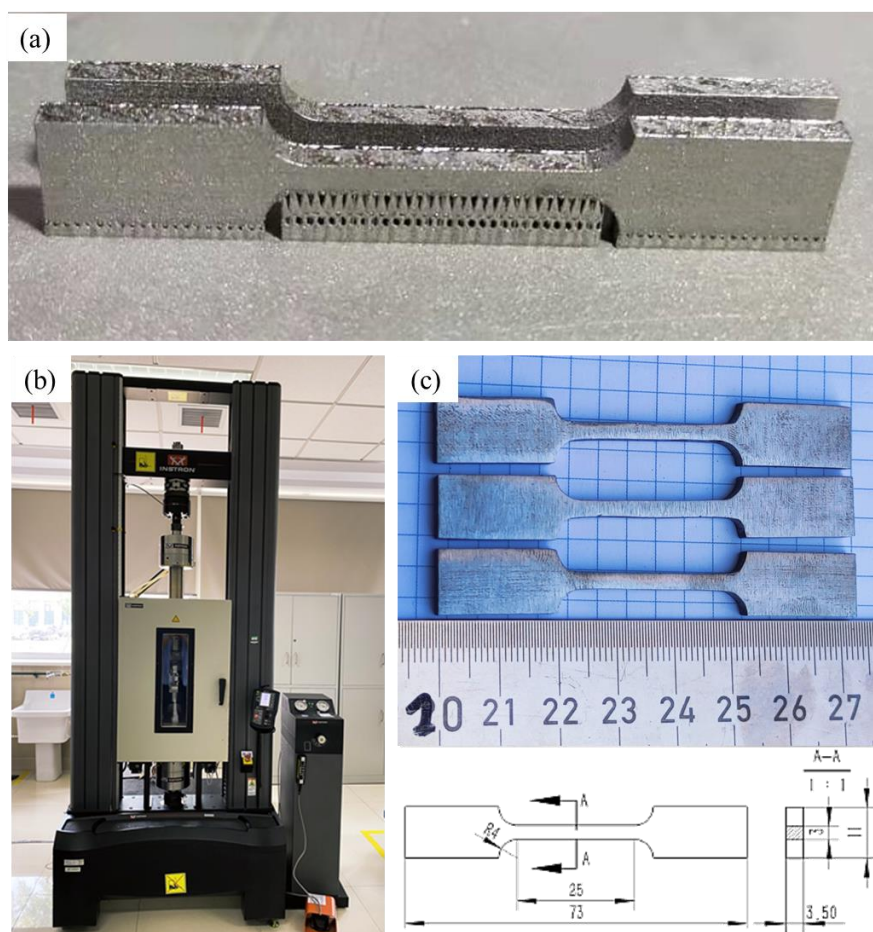


Figure 2.16 (a) The tensile samples ; (b) static tensile test machine (c) polished SLMed samples for tensile test

## References of Chapter 2

- [1] I. ISO, ASTM 52921: 2013. Standard Terminology for Additive Manufacturing—Coordinate Systems and Test Methodologies, International Organization for Standardization: Geneva, Switzerland, (2013).
- [2] G. Hilton, IEC Magnetic Materials 60404-Part 6: Methods of measurement of the magnetic properties of magnetically soft metallic and powder materials at frequencies in the range 20 Hz to kHz by the use of ring specimens, (2003).
- [3] H. Tiismus, A. Kallaste, A. Belahcen, M. Tarraste, T. Vaimann, A. Rassõlkin, B. Asad, P. Shams Ghahfarokhi, AC Magnetic Loss Reduction of SLM Processed Fe-Si for Additive Manufacturing of Electrical Machines, *Energies*, 14 (2021) 1241.
- [4] S. Tumanski, Handbook of magnetic measurements, CRC press, 2016.

- [5] A. Plotkowski, K. Carver, F. List, J. Pries, Z. Li, A.M. Rossy, D. Leonard, Design and performance of an additively manufactured high-Si transformer core, *Mater. Des.*, 194 (2020) 108894.
- [6] I.I.E. Commission, Magnetic materials-Part 4: Methods of measurement of dc magnetic properties of magnetically soft materials, in, IEC, 2000.
- [7] A. E8, ASTM E8/E8M standard test methods for tension testing of metallic materials 1, *Annu. B. ASTM Stand.*, 4 (2010) 1-27.



## **Chapter 3 Effect of processing parameters on surface morphology, microstructure, and the magnetic properties of Fe-3wt.%Si alloys manufactured by selective laser melting**

### **3.1 Introduction**

Soft magnetic materials are regarded as a type of materials that are easy to be magnetized and demagnetized [1], such as Fe-Ni, Fe-Co, Fe-Si alloys, etc. Owing to the high permeability, low coercivity, and low hysteresis loss, soft magnetic materials are widely used in the magnetic field [2]. Silicon steel, an iron-based alloy with Si element in concentrations between 2-7wt.%, is a quite significant class of soft magnetic materials [3]. Within the family of silicon steel, due to high magnetic transition temperature and low economic cost, Fe-3wt.%Si soft magnetic alloy obtained extensive attraction in many industrial applications including sensors, transformers, inductive devices, electric motors, etc. [4]. Traditionally, silicon steel is fabricated via an extrusion process or multiple rolling processes followed by an annealing heat treatment [5]. Unique forming processes of silicon steel have been reported in many studies including powder metallurgy [6], cast strips [7], and electron-beam physical vapor deposited [8]. Even if these methods have been investigated in the past decades, they are rarely used in commercial applications.

The SLM technology plays a vital role in the extended potential applications for manufacturing high-performance alloys. In the automotive, medical, and aerospace industries, SLM technology has been applied in the fabrication of high-quality metallic structural parts with brilliant properties [9]. Apart from the structural applications, the SLM also has great potential in the production of functional parts such as soft magnetic alloys [10]. As mentioned above, Fe-based soft magnetic alloy produced through SLM has attracted much attention. However, the research about the SLMed Fe-3wt.%Si alloy is relatively scarce.

Additionally, the investigations about Fe-Si soft magnetic alloys processed via SLM technology are also insufficient, especially the study on SLMed Fe-Si alloy using the pre-alloy powder as raw materials. Therefore, this work focused on the systematical investigation for optimizing the processing of SLMed Fe-3wt.%Si alloy, preliminary experiment and selection of processing parameters were investigated firstly, to improve the microstructures and the properties of SLMed Fe-Si soft magnetic alloys. The effects of the laser energy density (LED) on surface morphology, the microstructures, and the magnetic properties of SLMed Fe-3wt.%Si alloys were explained in detail. The roughness and surface morphology of the top side (XY plane) of the SLMed samples were investigated by a DektakXT profilometer (Bruker, American) and scanning electron microscopy (SEM). An optical microscope (OM) was used to obtain optical micrographics and observe the microstructure characteristics. The porosity was determined from the OM micrographs by an image analysis method. To achieve repeatability, each sample was analyzed with a minimum of five optical micrographs at different areas alternatively via the image processing software ImageJ. The SEM system was also employed to evaluate the feature of the microstructures. The phase composition was performed by an X-Ray diffractometer. The Vickers hardness measurements were carried out at different locations on the XY and XZ planes, respectively. To ensure accuracy, the average value of the hardness was recorded by 10 measurements. The magnetic properties of SLMed specimens were evaluated by a vibrating sample magnetometer (VSM) at room temperature.



### 3.2 Preliminary experiment and selection of processing parameters

The detailed preliminary process parameters used for SLM process optimization are listed in Table 3.1. A series of cubic specimens with dimensions of 8 mm × 8 mm × 8 mm were prepared by these 4 groups of parameters. The laser power (P, W), exposure time (t, μs), and point distance (d, μm) of these four groups of parameters were adjusted to study their comprehensive influence on porosity. As described in Figure 3.1 (a), a zigzag scanning pattern with the neighboring laser track rotation of 90 ° was utilized during the SLM process. To avoid oxidation, the chamber was adopted under an argon atmosphere to maintain the content of residual oxygen content below 1.0%. And the platform was preheated at 200 °C during the process.

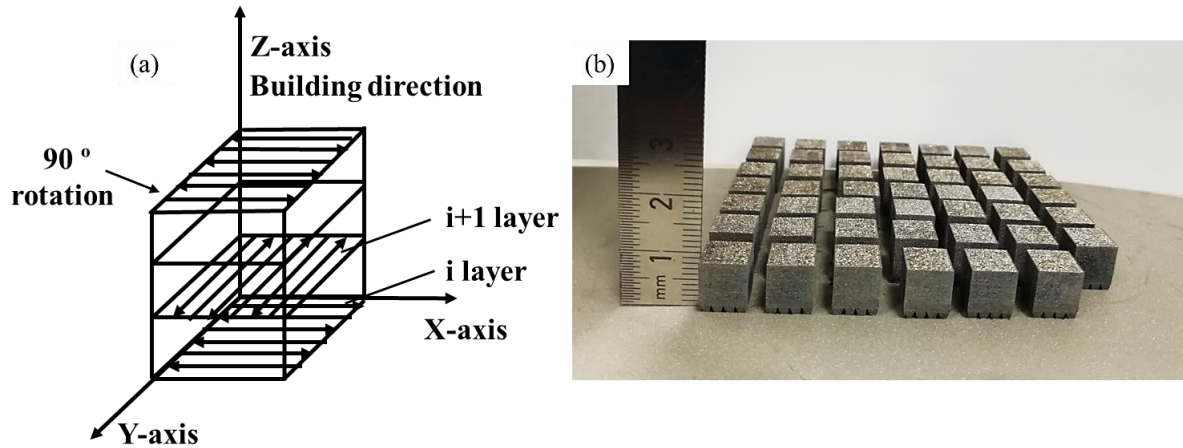


Figure 3.1 (a) Scanning strategy, (b) SLMed specimens

Moreover, the linear energy density LED (E, J/m) was calculated via the equation as a linear function of the scanning speed (v, m/s) and laser power:

$$LED = \frac{P}{v} = \frac{Pt}{d} \quad \text{Equation 3.1}$$

The obtained specimens are shown in Figure 3.1 (b). After static analysis, the OM images and porosities of the samples are presented in Figure 3.2-Figure 3.6, it can be observed that the porosities of each group of samples decrease with the increase of LED.

Table 3.1 The preliminary SLM parameters

Group	Group 1-3	Group 4
Laser spot diameter (μm)	35	35
Layer thickness (μm)	30	30
Hatch distance (μm)	60	60
Laser Power (P/W)	70,80,90	80
Exposure time (t/μs)	144	33.3,50,100,150,250,300
Point distance (d/μm)	80,70,60,50,40,30	40

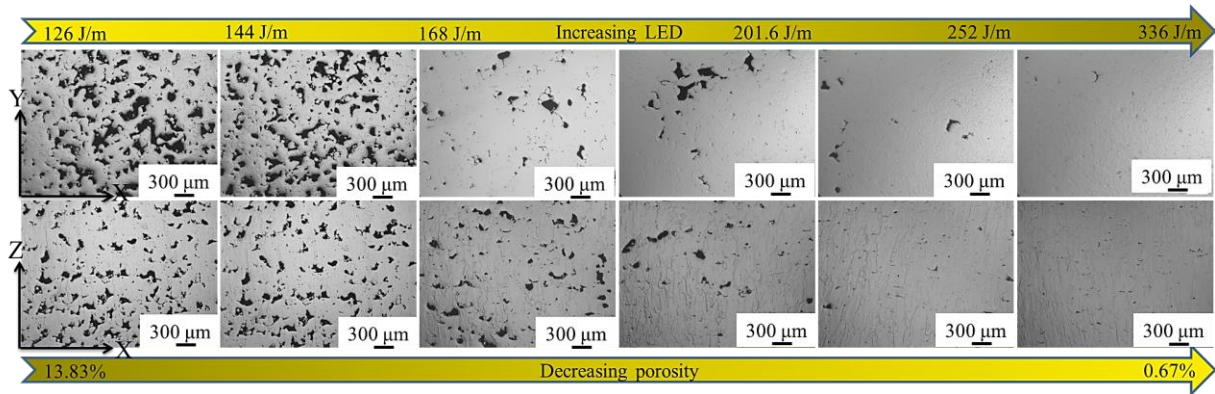


Figure 3.2 Effect of processing LED on sample porosity: the OM images of different SLMed Fe-3wt.%Si samples fabricated under the parameters of group 1

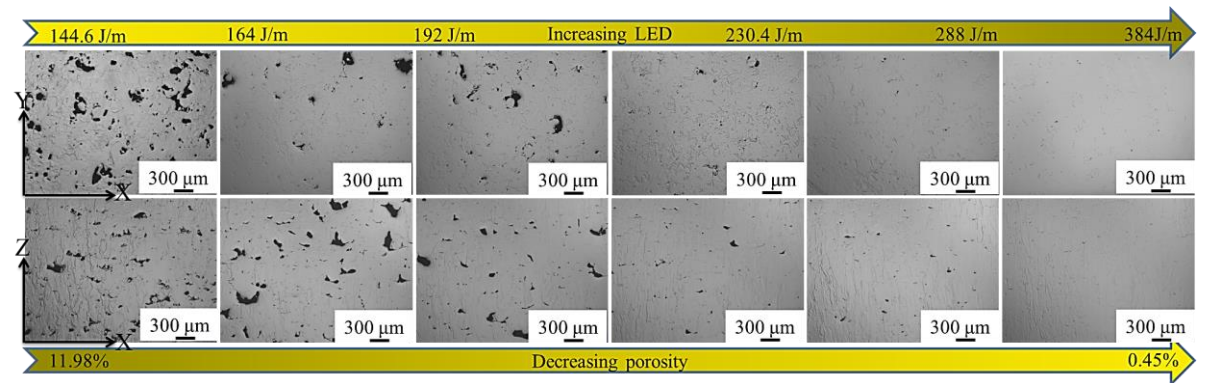


Figure 3.3 Effect of processing LED on sample porosity: the OM images of different SLMed Fe-3wt.%Si samples fabricated under the parameters of group 2

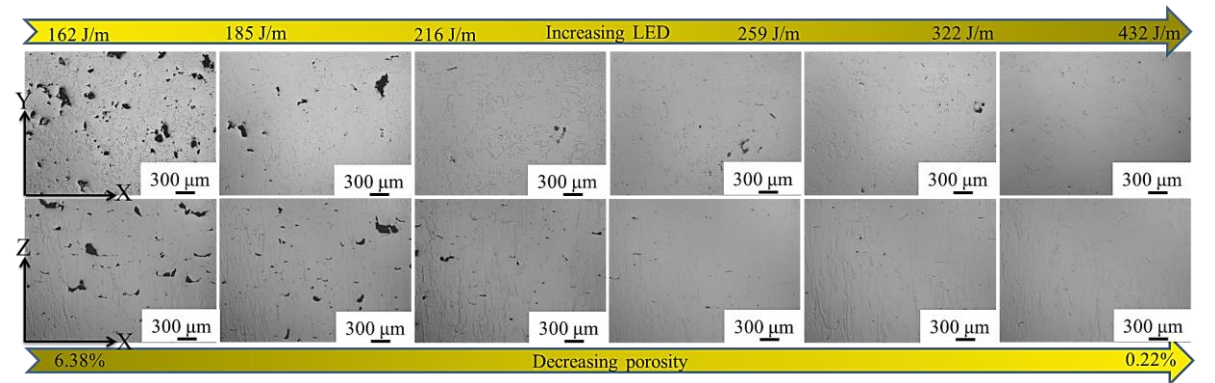


Figure 3.4 Effect of processing LED on sample porosity: the OM images of different SLMed Fe-3wt.%Si samples fabricated under the parameters of group 3

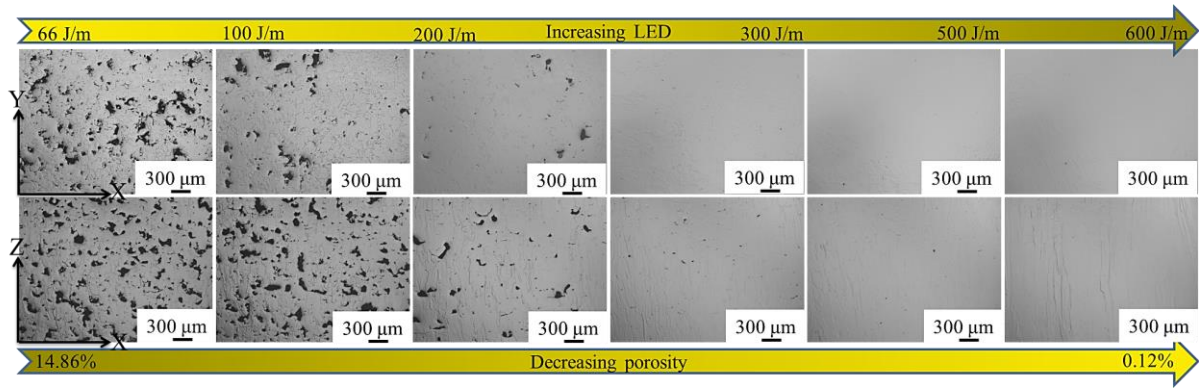


Figure 3.5 Effect of processing LED on sample porosity: the OM images of different SLMed Fe-3wt.%Si samples fabricated under the parameters of group 4

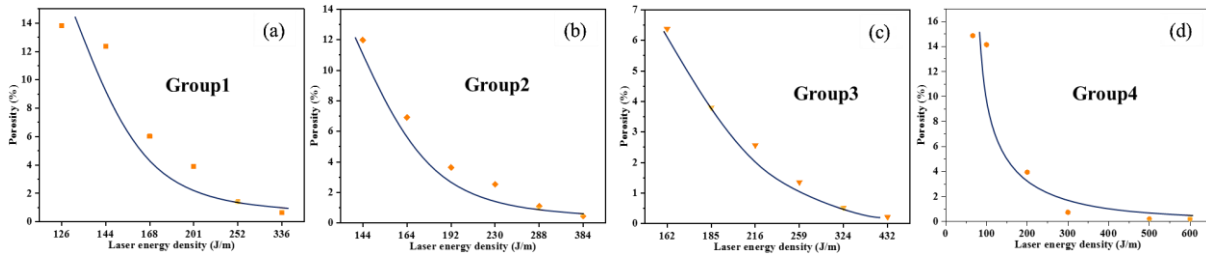


Figure 3.6 The evolution of porosity of different SLMed Fe-3wt.%Si samples (a) group1, (b) group2, (c) group3, (d) group4

### 3.3 The influence of laser energy density on the surface morphology, microstructure and microhardness

From the above results of the preliminary selection of the SLM process, LED is a comprehensive factor affecting the porosity. Therefore, this part mainly studies and analyzes the influence of LED on surface morphology, microstructure, and microhardness of SLMed Fe-3wt.%Si. Different laser power with 50 W, 70 W, 100 W, 140 W, 180 W were used to prepare a series of SLM cubic samples. The laser spot, laser scanning speed, hatch distance, and layer thickness were kept in a constant value with 35  $\mu\text{m}$ , 0.33 m/s, 60  $\mu\text{m}$ , and 30  $\mu\text{m}$  respectively. To avoid oxidation, the chamber was adopted under an argon atmosphere to maintain the content of residual oxygen content below 1.0%. The platform was also preheated at 200  $^{\circ}\text{C}$  during the process. Apart from specimens with dimensions of 8 mm  $\times$  8 mm  $\times$  8 mm, the specimens with dimensions of 3 mm  $\times$  3 mm  $\times$  3 mm and the ring samples of height  $h=4$  mm, external diameter  $d_1=26$  mm, internal diameter  $d_2=18$  mm, were manufactured for the measurement of magnetic properties, the scanning strategy and some of the samples are replayed in Figure 3.7. The specimens named hereafter E150, E210, E300, E420 and E540 according to LED = 150 J/m, 210 J/m, 300 J/m, 420 J/m and 540 J/m, respectively. The detailed parameters are listed in Table 3.2.

Table 3.2 The detailed parameters

Specimen	Laser Power (W)	Laser spot ( $\mu\text{m}$ )	Laser Scanning Speed (m/s)	Hatch Distance ( $\mu\text{m}$ )	Layer Thickness ( $\mu\text{m}$ )
E150	50				
E210	70				
E300	100	35	0.33	60	30
E420	140				
E540	180				

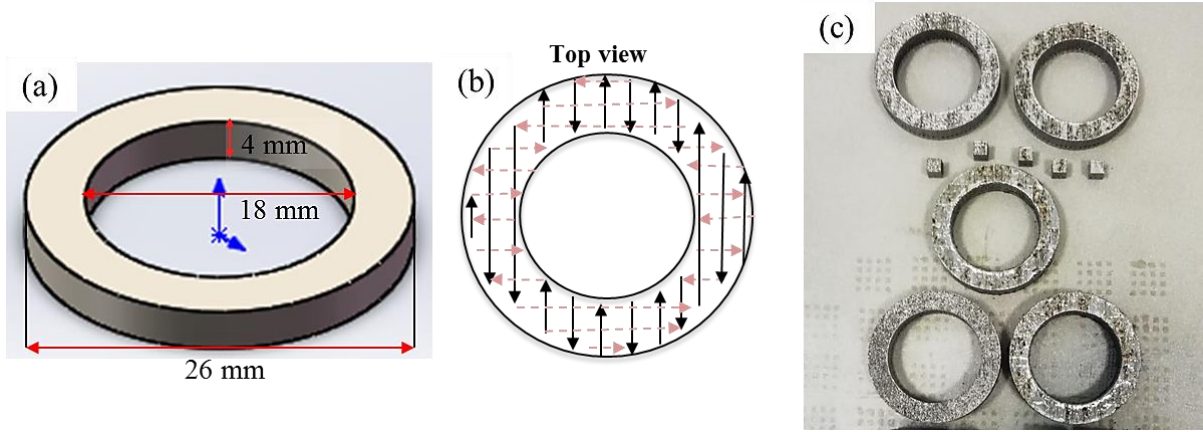


Figure 3.7 (a) 3D model of ring sample, (b) scanning strategy, (c) some samples

### 3.3.1 Macroscopic morphology and surface roughness

Surface morphology is an important feature of SLMed products, which can reflect manufacturing quality. To investigate the influence of LED on surface morphology, the top surface (XY plane) of SLM Fe-3wt.%Si alloy was characterized. The macroscopic surfaces of the corresponding samples are shown in Figure 3.8 (a). As displayed in Figure 3.8 (b-f), with various LEDs, the SEM surface macroscopic morphology images of different specimens were obtained. Although the spattering particles are almost found on the surface of all specimens, significant distinctions with different molten pools and laser track patterns (marked by orange lines in Figure 3.8 (d) and Figure 3.8 (e)) are still observed. Under low LED, not only some spherical shape particles but also irregular protuberances (marked by white arrows in Figure 3.8 (b) and Figure 3.8 (c)) can be observed on the surface of samples E150 and E210. The laser tracks on the surface of these samples are incomplete and discontinuous with a curved geometry, which is the result of a segmentation effect on the elongated molten pool. The reasons for these phenomena would be summarized by the following aspects. On one side, during the SLM process, some powder particles could not be fully melted due to the low temperature in the molten pool with a low LED. In this situation, those un-melted particles were left on the surfaces. On the other hand, according to the reports [11, 12], the physical model for the surface tension of liquid metal mainly contains a normal component and tangential component of the surface. They can be calculated via the two following equations [11, 12]:

$$f_s^{(nd)} = -\hat{\alpha}\sigma(T)(\nabla \cdot \hat{\alpha}) \quad \text{Equation 3.2}$$

$$f_s^{(td)} = \nabla\sigma(T) - \hat{\alpha}(\hat{\alpha} \cdot \nabla)\sigma(T) \quad \text{Equation 3.3}$$

where  $f_s^{(nd)}$ ,  $f_s^{(td)}$ , represent the normal component and the tangential component of surface tension respectively,  $\hat{\alpha}$  represents the unit normal of the interface, and where  $\sigma(T)$  is the surface tension coefficient that can be given by a function of the temperature i.e.,  $\sigma(T) = \sigma_0 + \gamma(T - T_m)$ , here  $\sigma_0$  is the surface tension at the melting point,  $T$  is the temperature of liquid metal,  $T_m$  represents the melting temperature of the metal powder.  $\gamma$  is the surface tension gradient coefficient, which in general has a negative value for most of the liquid metals. In other words,  $\sigma(T)$  will reduce with the increase in temperature.  $\nabla$  represents the surface gradient in the tangent plane, low LED that had a low temperature in the molten pool which would lead to the high tension of both normal and tangential components [11-13]. The melting powder would shrink into spherical particles due to the high surface tension, which leads to the formation of a series of discrete molten pools and several irregular protuberances. It is defined as a balling effect [14]. Additionally, the balling effect occurred when the melted powder did not wet the underlying layer due to oxide contamination of the layer on the substrate and the surface of the melt. Besides, an insufficient heat transmission will also lead to a failure spreading

of the laser tracks, which results in the clearance leakage between the adjacent laser tracks. It would cause the formation of the void. With the increase of LED, the laser tracks are gradually clear, completing a regular pattern. The adjacent laser tracks are also closely connected. Meanwhile, there are a few fine particles marked by white arrows in Figure 3.8 (f) on the surface of sample E540 at the highest LED with 540 J/m. Some of them are the general spattering particles, and others are special spattering particles i.e. over-burning debris caused by excessive LED [15].

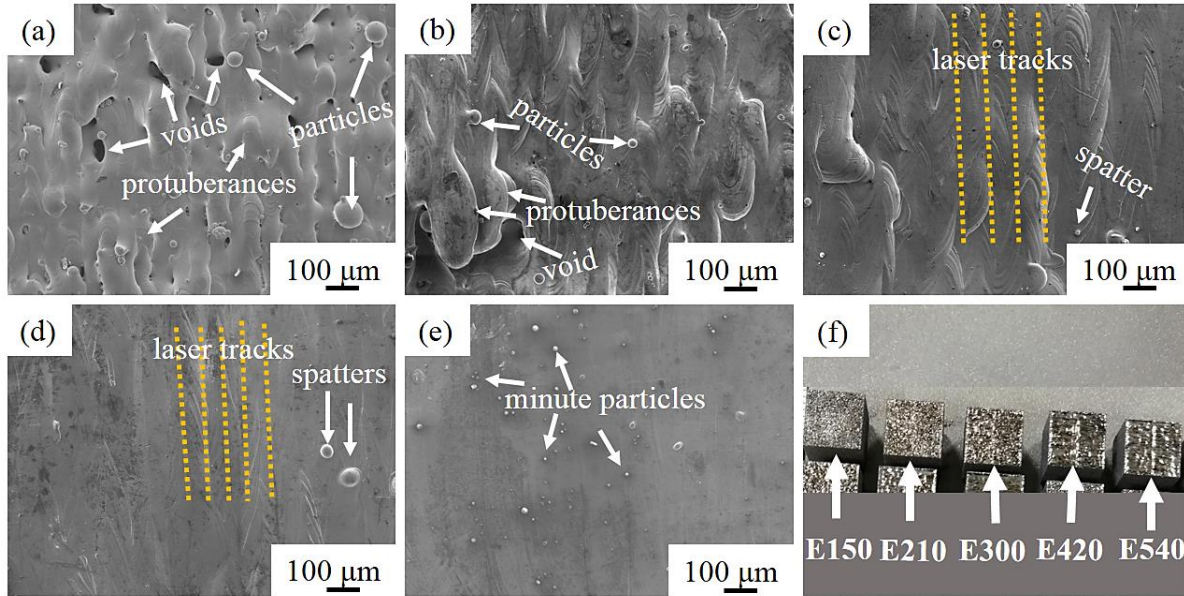


Figure 3.8 Macroscopic morphology and SEM images of surface morphology of SLMed samples at different LED: (a) Macroscopic morphology of the SLMed samples, (b) 150 J/m, (c) 210 J/m, (d) 300 J/m, (e) 420 J/m, (f) 540 J/m

It is well known that roughness is an important index to evaluate the surface quality of SLMed products. It has a direct relationship between roughness and surface morphology. To understand the impact of the LED on the surface roughness of the SLMed Fe-3wt.%Si alloy, the three-dimensional surface topographies, and surface roughness (Ra) were further analyzed by a profilometer. As represented in Figure 3.9 (a-e), the three-dimensional surface topographies of the SLMed parts are consistent with the morphology under SEM (Figure 3.8 a-e). The surface macroscopic morphologies present a phenomenon of gradual smoothing with the increase of LED. In Figure 3.9 (f), it can also be reflected that the variation in surface roughness decreases as the increase of LED. In fact, the balling effect [16] and the spattering phenomenon [17] are the primary factors affecting the surface roughness of the SLMed parts. At low LED, the liquid phase is insufficient which leads to poor fluidity of the powder and short lifetime of the molten pool, contributing to the formation of the balling effect [16]. As it can be seen in both Figure 3.8 and Figure 3.9, with the increase of LED, the effect of the balling becomes gradually less prominent. Meanwhile, a high LED ( $\geq 300$  J/m) per unit area that leads to parts of spattering particles are melted through intensive heat transfer [17]. In high LED, the number of spattering particles is less and their size is smaller. All these contribute to the decrease of surface roughness ( $24.36 \mu\text{m}$ - $11.30 \mu\text{m}$ ) of the samples with the increase of LED. The roughness of the top surface is strongly dependent on LED, which can be proved by the mentions above. It can be concluded that the surface roughness of the SLMed parts decreases with the increase of LED. Insufficient energy density causes a rough surface and obvious voids, but excessive energy density leads to overburning.

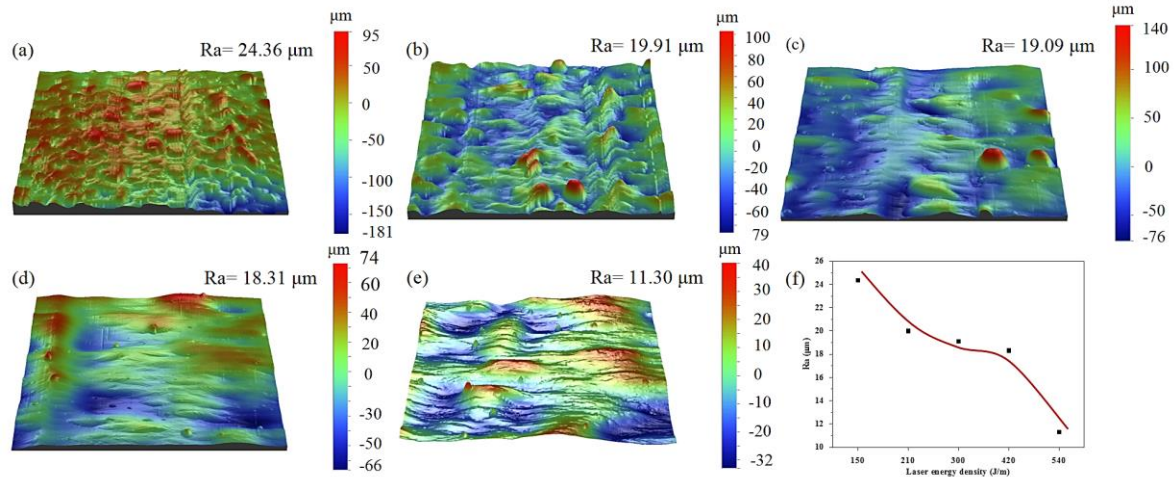


Figure 3.9 Three-dimensional surface topographies and the values of roughness of the SLMed parts at different LED: (a) 150 J/m, (b) 210 J/m, (c) 300 J/m, (d) 420 J/m, (e) 540 J/m, (f) the values of roughness

### 3.3.2 Analysis of manufacturing defects

It is well known that the SLMed parts have two main internal defects: cracks and pores. They can be observed by an optical microscope [18]. This part aims to describe the impact of LED on the internal defects of Fe-3wt.%Si alloys produced by SLM. The internal quality could mostly be reflected in the cross-section plane (parallel to building direction) of SLM products. And the cross-sectional (XZ plane) OM images of SLMed Fe-3wt.%Si parts are demonstrated in Figure 3.10 (a–e). It is noted that macrocracks are not obvious in all samples, only some pore defects were observed. The absence of microcracks benefits the performance of SLMed products. Moreover, it could be seen that the number of pores in the sample decreases with the increase of LED. In the meantime, it is found that only some small pores with regular shapes are observed in the sample E540, but both large pores with irregular shapes and small pores with regular shapes are observed in the other samples (as shown in Figure 3.10, which are highlighted by different symbols). Both the size and the number of large pores decrease with the increase of LED.

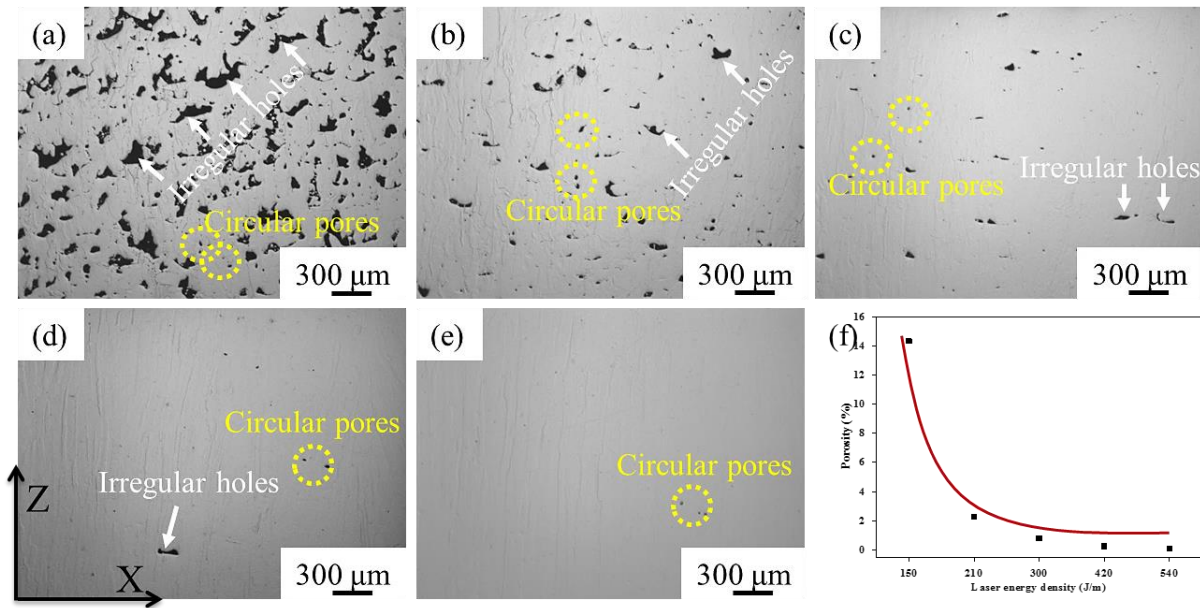


Figure 3.10 OM images of cross-sectional (XZ plane) at different LED and porosity rate of SLMed specimens at different LED: (a) 150 J/m, (b) 210 J/m, (c) 300 J/m, (d) 420 J/m, (e) 540 J/m, (f) porosity rate changes as a function of laser energy density

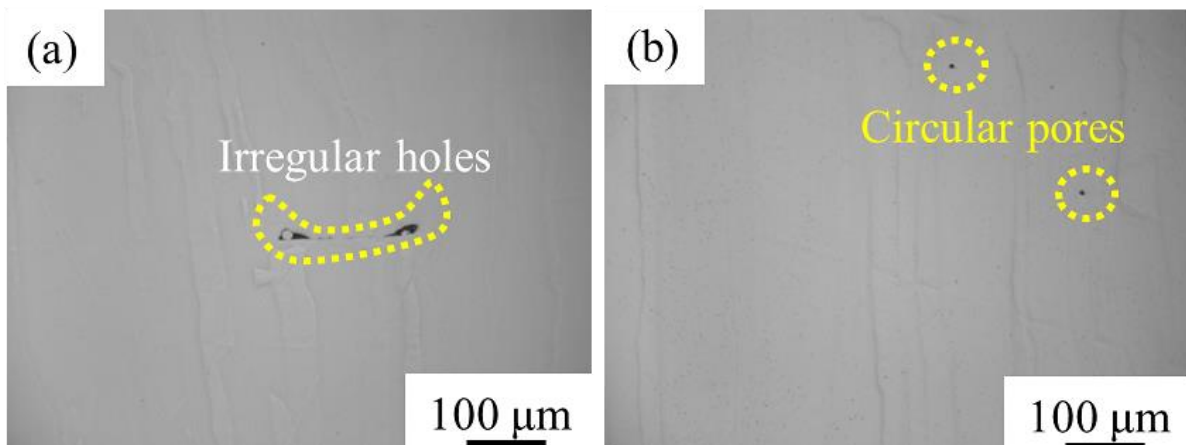


Figure 3.11 Magnification OM images of XZ plane for SLMed specimens at different LED: (a) 210 J/m, (b) 540 J/m

The large pores mentioned above are identified as irregular holes (marked by white arrows) due to their irregular shape and their larger size above 100 μm while the small pores are identified as gas pores (marked by orange circles) according to their size smaller than 100 μm with circular shapes [19, 20]. In Figure 3.11, magnification OM images of the XZ plane for SLMed specimens fabricated with a LED of 210 J/m and 540 J/m show the irregular holes and circular, it can be seen the shape clearly. The formation of irregular holes is attributed to rapid solidification of the metal powder without complete filling, leading to gaps and balling effects on the surface of the layer in the SLM process. Especially, as a low LED reduces the operative temperature within a molten pool, resulting in a limited amount of liquid within the molten pool and a restriction of the complete spreading of the liquid powder. And the previous layers couldn't be re-melted totally in this case [21]. The balling effects on the surface of each layer were also serious at low laser energy laser input. Accordingly, irregular holes with large sizes could be obtained in adjacent layers due to the above comprehensive reasons. It was explained in the previous section: with the increase of LED, the solidification time can be extended. In the process of SLM, not only the spreading of the liquid metal was improved, but also the balling phenomenon became weak.

For these reasons, both the size and the number of large pores decrease with the increase of LED. Gas pores can be created by two types of gases that existed during the SLM process. One is trapped within the molten pool, the other is from the powder during consolidation [20]. During the SLM process, turbulent flow is formed in molten pools with strong gas rolling due to a high energy density [18]. To a certain extent, the increase of the LED might lead the dynamics of Marangoni which affects the increase of the possibility of pores formed in the solidified molten pools [22]. However, it can also promote the ability of gas to roll and escape from the molten pools, which can reduce the pores and increase the densification at a high level [13]. As displayed in Figure 3.10 (f), it can be also proved that the internal porosity of the samples would decrease with the increase of LED. Additionally, the reduction of the porosity rate is the largest when the LED increases from 150 J/m to 240 J/m. With increasing the LED from 240 J/m to 300 J/m, the porosity decreases significantly until lower than 1%. A further increase in LED can result in the evaporation and burning of elements, which causes the formation of a few pores [23]. Thence, the internal porosity rate of E420 and E540 samples is approximative, while it's still lower than 1%. The internal manufacturing defects at low LED are irregular pores but near-circular pores at high LED. Under the suitable LED, no cracks can be observed and the porosity is lower than 1%, which improve significantly the properties of the SLMed parts.

### 3.3.3 Evolution of the microstructures

The internal microstructure of the soft magnetic alloy is quite significant for its properties, especially its magnetic properties. The microstructure of the alloy produced by SLM is not only affected by its material composition but also strongly related to the parameters during the SLM fabrication process. The defects of the SLMed products can be generally divided into porosity and cracks, which have been described in the previous analysis of porosity. However, in a further OM observation of etching samples, it can be found clearly that un-melted particles (as indicated by yellow arrows) were also one of the defects in the SLMed samples [24] because unmelted powders are usually spherical shapes and in dendritic phases. After etching, the corresponding microstructures of the XY plane of SLMed Fe-3wt.%Si alloys are presented in Figure 3.12. It is identified clearly that there are un-melted particles in E150 and E210 samples at low LED. Some obvious cavities (as indicated by white arrows) are found around these un-melted particles, resulting in a microstructural discontinuity. As discussed, the LED plays a significant role in determining the amount and magnitude of such un-melted particles [14, 25]. Unmelted particles come from a lack of fusion, that's to say the input energy was not enough to melt the whole powders, which led to an unstable molten pool. A lack of fusion presents large cavities around un-melted particles, which is due to the poor bonding between the molten pools or laser tracks [26, 27]. Although a few pores can be observed in the sample E300, neither un-melted particles can be found, nor in other samples (E420, E540). It can be indicated that all powder particles can be almost melted completely when the LED exceeds 300 J/m.



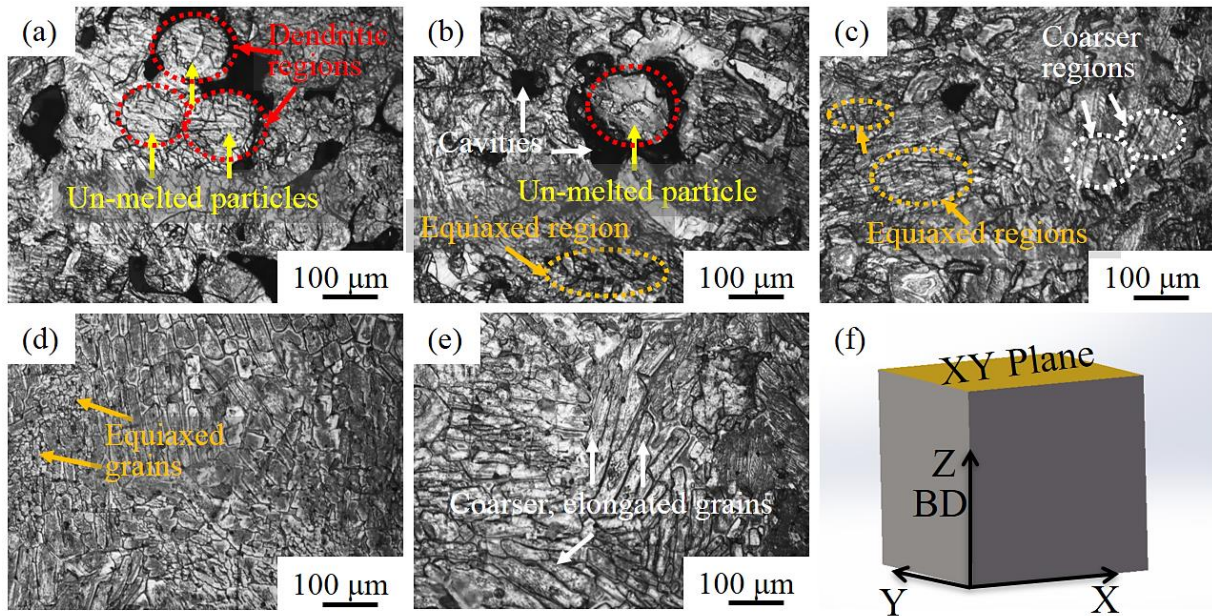


Figure 3.12 OM images (XY plane) of the SLMed parts at different LED and 3D physical model of the samples: (a) 150 J/m, (b) 210 J/m, (c) 300 J/m, (d) 420 J/m, (e) 540 J/m, (f) 3D physical model of the samples

Moreover, a few equiaxed regions (as indicated by orange circles and arrows) are found besides some regions of dendritic grains in the samples E150 and E210 at low LED, while no regions of coarser, elongated grains (as indicated by white circles and arrows) were identified clearly. However, when the LED was 300 J/m, in the sample E300, the microstructure consists of mainly equiaxed grains and coarser grains. With the increase of LED, the grain boundaries on the surface are visible and appear significantly. Furthermore, the microstructures are more homogeneous and regular. The regions of equiaxed grains and coarser elongated grains are observed clearly in the samples E420 and E540 with high LED. By comparing samples E150 and E300, it could be noticed that increasing the LED promotes columnar grain formation. These phenomena also occurred when the LED is increased from 400 W to 1000 W in the literature [28]. According to the report of Michele Garibaldi [29], when the LED was doubled, the increasing dependency of morphological and crystallographic texture on SLMed parts could be noted remarkably. Therefore, the correlation between LED and grain formation could be explained by the increasing amount of partial re-melting and the enhancing smoothness of the deposited layers. Unfortunately, due to the Marangoni effects and over burning, some black particles also appear in samples E420 and E540.

Similarly, the OM micrographs in Figure 3.13 provide insights into the microstructural features of corresponding samples at different LEDs for the XZ plane (the microstructures for the XZ plane of the samples were also found for the YZ plane, and are therefore not shown here). Their regular pattern of structural evolution was found equivalent to the XY plane of previously analyzed. With the increase of LED, the microstructures of specimens become denser, and the boundaries of grains clearer and easier to be recognized. When  $E \geq 300$  J/m, the obvious and overall columnar structures oriented along the building direction are identified clearly in the corresponding samples. According to the fundamentals of solidification, a grain selection process in which grains whose “easy growth” directions (the  $\langle 001 \rangle$  family for the bcc system) are oriented along the direction of solidification [29, 30]. For this reason, it is concluded that the epitaxial growth of the grains accrued at high LED.

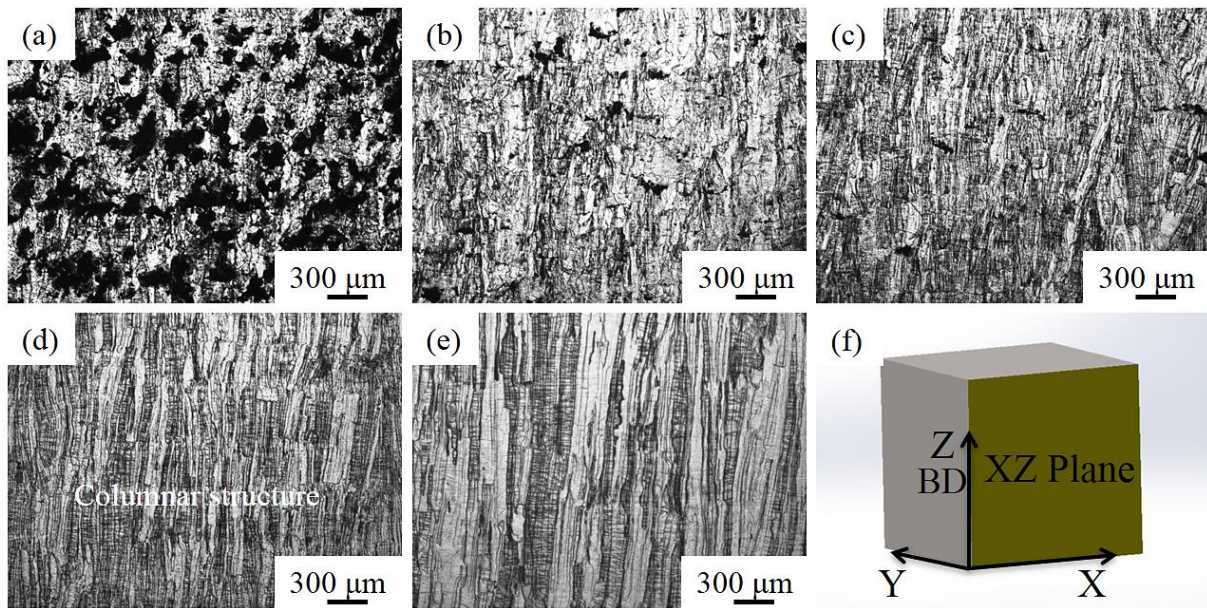


Figure 3.13 OM images of the microstructures (XZ plane) the SLMed specimens and 3D physical model of the samples: (a) 150 J/m, (b) 210 J/m, (c) 300 J/m, (d) 420 J/m, (e) 540 J/m, (f) 3D physical model of the samples

Furthermore, it is observed that fine structures usually appear in the areas between the coarse columnar structures. Moreover, the proportion of coarse columnar structures is the largest when  $E=500$  J/m. Those microstructures of the XZ plane could correspond to those of the XY plane, i.e. the regions of fine equiaxed structures corresponded to the equiaxed regions on the XY plane, while the coarse columnar structures corresponded to the coarse elongated grains. It is known that two main stages are divided into the metal solidification process, that is, crystal nucleation and growth. A certain degree of undercooling is required for nucleation. Increasing the undercooling has a great effect on the nucleation rate and growth rate [30]. Meanwhile, combining the theory of metal solidification under the laser energy source reported by Liu et al. [31], during the SLM process, the powders were fused into liquid after heating by laser, then the equiaxed solidification was accrued firstly at some degree of undercooling. Then, the number of grains remains constant. The solidification proceeded firstly via the lengthening of dendrites. Lower LED led to a lower temperature in the molten pool which resulted in unmelted particles and insufficient nucleation, thus the dendritic phase or equiaxed grains were obtained. The LED was increased, which induced a complete melt of the powder in the molten layer. The undercooling was also increased. Then, the new nucleation was almost formed, therefore the initially equiaxed grains could still grow further. Finally, dendritic crystals were filled with liquid metal. Therefore, coarse columnar structures could be observed obviously in the SLMed Fe-3wt.%Si alloys, instead of dendritic crystals. Besides, with a further increase in LED, a higher temperature in the molten pool was obtained. The movement of the atomic was also enhanced, which contributes to the further growth of the crystal. In the same situation, the formation of columnar structures was also further promoted. These result in columnar structures when the LED reached 300 J/m, and a gradual increase in size and number of columnar structures corresponding to the samples E420 and E540.

The representative SEM graphics of the side view XZ plane are presented in Figure 3.14. The unmelted particles with a dendritic phase and the columnar structures are observed clearly, which further proves that the LED was impacted significantly on the microstructures as mentioned previously. Unfortunately, the feature of the molten pools cannot be distinguished clearly in this situation. The XZ planes of samples E300 and E540 are further enlarged to observe the section features of molten pools and columnar structures, and the results are shown in Figure 3.15. It can be observed the boundaries of

some molten pools (as indicated by orange dotted lines) and the existing columnar grains grow across multiple molten pools. The molten pools are relatively wide and deep at high LED, which is one of the reasons for increasing the amount of coarse columnar structures.

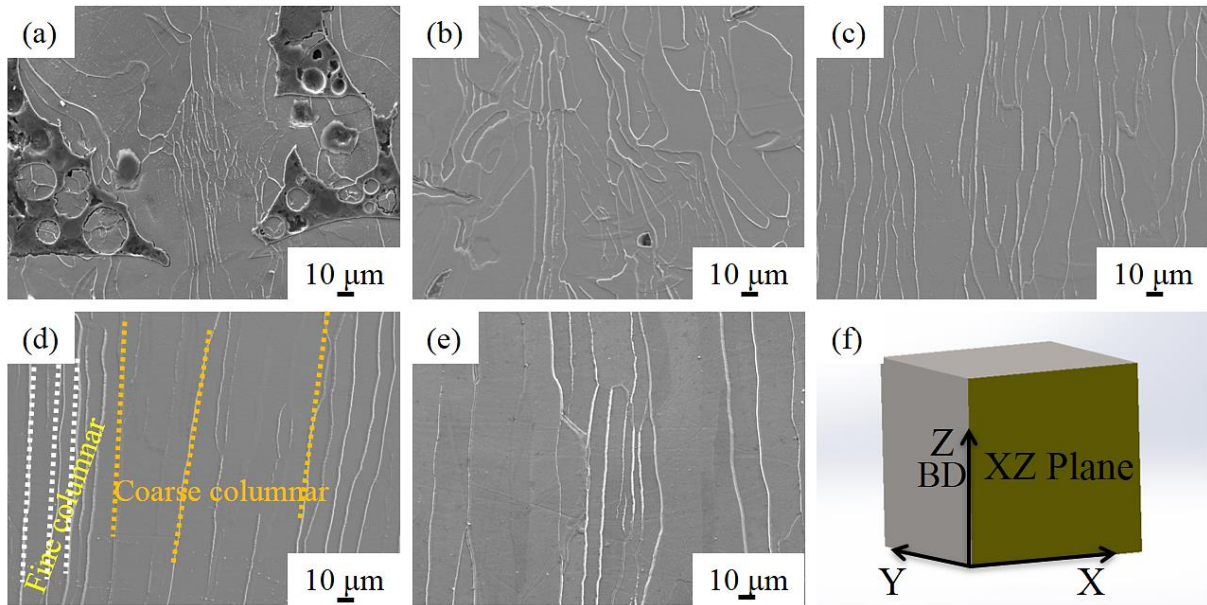


Figure 3.14 SEM images of the microstructures (XZ plane) of the SLMed specimens and 3D physical model of the samples (a-e): (a) E150, (b) E210, (c) E300, (d) E420, (e) E540; (f) The 3D physical model of the samples

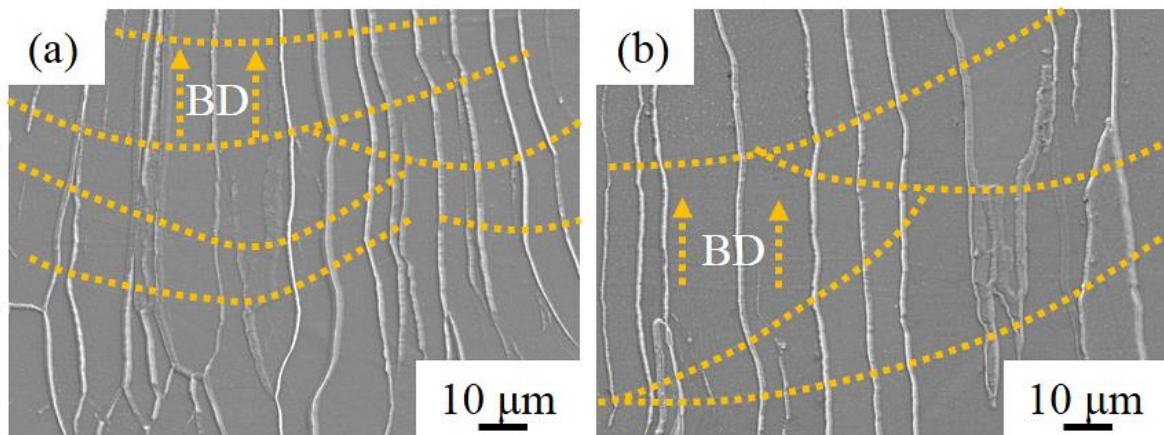


Figure 3.15 SEM images of the high magnification for representative microstructures (XZ plane) at different LEDs: (a) 300 J/m, (b) 540 J/m

To further specify the chemical composition of the SLMed parts, the results of EDS analysis are illustrated in Figure 3.16. It can be detected the content of Si was about 3wt% in the SLMed specimens. This is consistent with the EDS results of pre-alloyed powder before manufacturing. It indicates that no obvious elements were burned loss during the SLM process. Furthermore, the EDS line scan was carried out and the results are also shown in Figure 3.16. No obvious evidence for the occurrence of rich in Fe or poor in Si is detected by the element distribution line at grain boundaries.

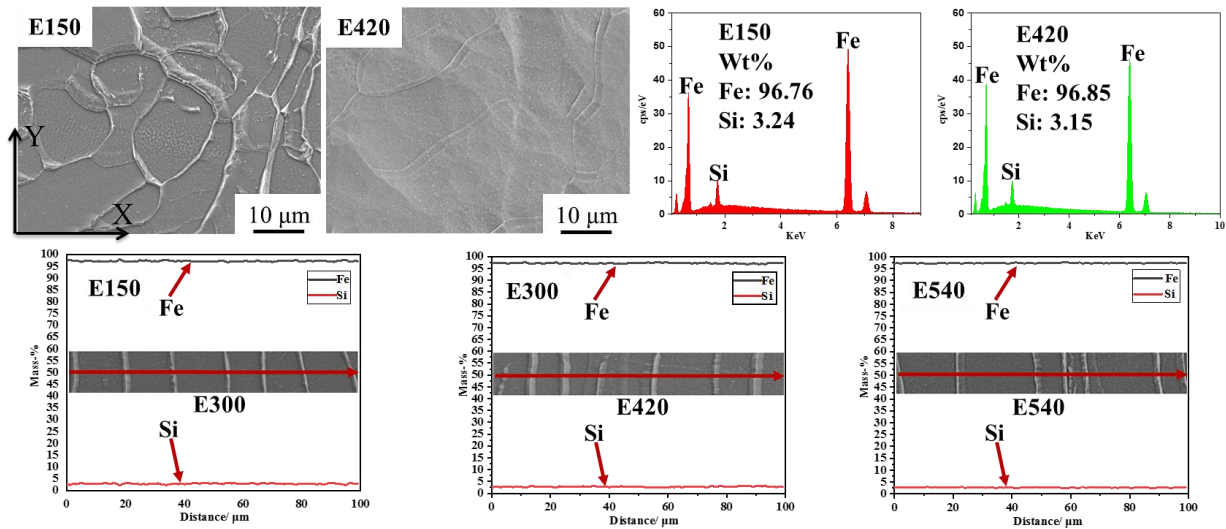


Figure 3.16 The results of EDS for the SLMed samples

### 3.3.4 Evolution of microhardness

The microhardness of SLMed samples is significantly related to their internal microstructure. The results of the microhardness measurement (XY and XZ planes) for SLMed Fe-3wt.%Si alloys under different laser energy densities are shown in the histogram in Figure 3.17. In both XY and XZ planes, the microhardness value of each sample is higher than 200 HV<sub>0.1</sub>. As a result of the inhomogeneous distribution of defects, the hardness of XY and XZ planes is slightly different. The microhardness value of the sample E150 is the lowest. It is associated with the maximum number of un-melted particles and the highest porosity rate. The augmentation of the microhardness value of the corresponding samples is also related to the reduction of the porosity rate. Due to the largest reduction of porosity rate between the sample E150 and E210, the increasing extent of microhardness is also the largest. Then, the increasing extent of microhardness between the sample E150 and E210 is significant, although the microhardness changes slightly when the LED increases from 300 J/m to 420 J/m. It should be noted the decrease of microhardness value when E=420 J/m up to E=540 J/m. According to the previous analysis, the porosity rate of samples E420 and E540 was almost similar. Besides, the over burning phenomenon and Marangoni effects appeared in sample E540, which leads to a decrease in microhardness value [27, 32].

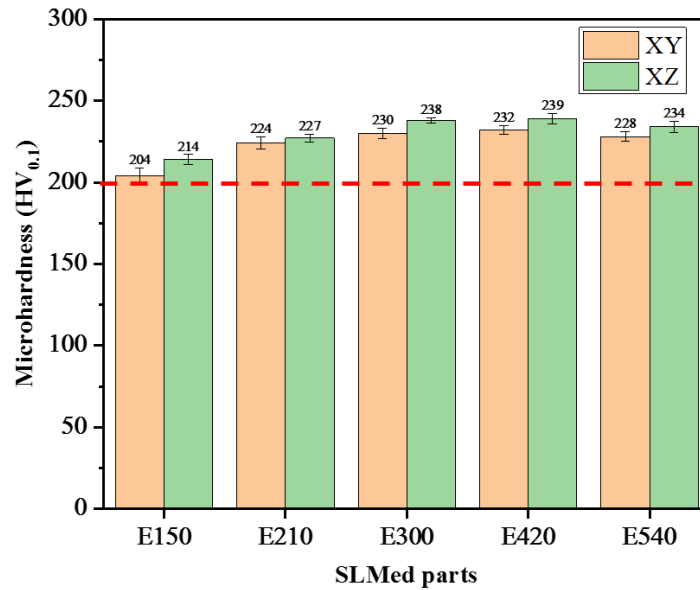


Figure 3.17 Microhardness of the SLM parts prepared at the different LED

### 3.4 Study of magnetic properties

#### 3.4.1 Coercivity

Coercivity ( $H_c$ ) is an important criterion for determining whether a ferromagnetic material is soft or hard. One of the goals in the preparation of soft magnetic material is keeping coercivity at a minimum level. The variation of coercivity of the SLMed Fe-3wt.%Si samples is displayed in Figure 3.18 as a function of LED. Although the fluctuation of coercivity between different samples is not very strong. It could still be found that  $H_c$  decreases with increasing the LED when the LED is lower than 300 J/m. On the contrary, both  $H_c$  show an increase when the LED increases from 300 J/m to 420 J/m and 500 J/m. Theoretically, the coercivity of material is usually related to the microstructural characteristics, including the defects; the shape, size, and dispersion degree of the grains, and lattice distortion. Internal stress also strongly impacts coercivity with a negative relationship. In fact, due to the irreversible movement of domain walls is responsible for the coercive force, manufacturing defects, such as porosity, cracks, and impurities, represent pinning sites obstructing the movement of the magnetic domain walls under the external magnetic field effect, increasing coercivity [33, 34]. Additionally, the coercivity is inversely proportional to grain size for polycrystalline magnetic materials with grain sizes above 150 nm following the  $1/D$  law [35, 36]. Hence, a relatively higher value of  $H_c$  for the samples E150 could be attributed to the structural defects, including a relatively higher porosity rate and more un-melted particles. The reduction of  $H_c$  for SLMed Fe-3wt.%Si samples when  $E=150$  J/m up to  $E=300$  J/m could be related to the reduction of porosity rate and the homogenous evolution of microstructure. Nevertheless, the increase of  $H_c$  when  $E=300$  J/m up to  $E=540$  J/m could be associated with higher internal stress. According to the report of Garibaldi et al., for high-silicon steel (Fe-6.9%wt.Si) parts processed using the SLM technique, the results show that the crack formation is promoted in the samples obtained with laser energy inputs  $\geq 420$  J/m. They indicated that the formation of cracks can be attributed to the thermal stresses induced during the SLM process. Besides, it is known that the internal stress of the SLM samples using high LED is higher than that of using low LED from the literature [37]. Thus, it could be indicated that while both grains coarsen and internal stress increase could contribute to the magnetic behavior of the samples, the internal stress became the principal obstruction in a magnetic field when the LED is higher than 300 J/m.

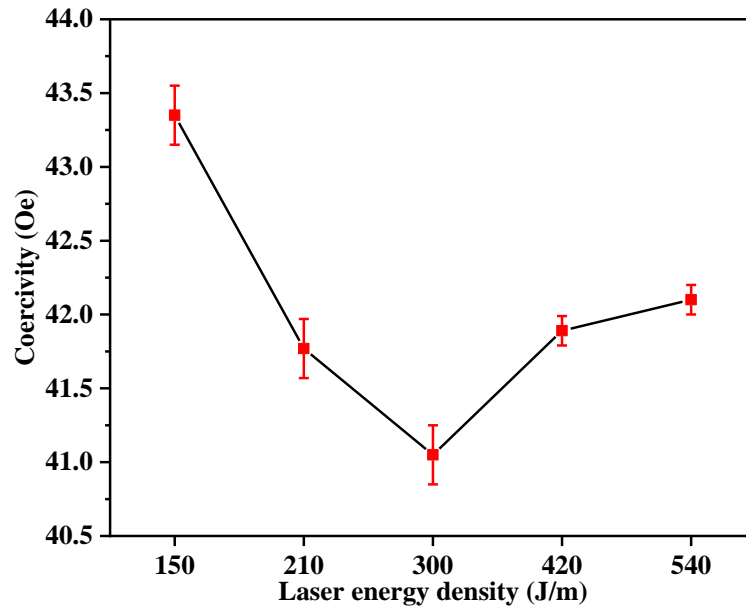


Figure 3.18 The value of coercivity changes as a function of laser energy density for SLMed Fe-3wt.% Si samples

### 3.4.2 Saturation magnetization

The saturation magnetization of the material corresponds to the limiting case that all atomic moments take the allowed angular position nearest to the field. The saturation magnetization is also a prominent structure-insensitive property [1, 34]. The hysteresis curves of the SLMed samples are depicted in Figure 3.19, the right set shows the enlargement part in the low magnetic field region. It can be found that the differences of the saturation magnetization ( $M_s$ ), the small differences of the hysteresis might be related to the composition fluctuations since the  $M_s$  is determined by the composition, atomic-level structures, and the amount of each phase. The evolution of  $M_s$  of the SLMed samples is given in Figure 3.20. With the increase of LED,  $M_s$  increases at first, reaching a maximum value of about 220 emu/g when the LED is 300 J/m, and then decreases gradually. It is well known that the crystal eventually reaches saturation magnetization when all spins have rotated into the field direction [1]. A relatively high porosity rate can lead to a relatively low saturation magnetization. So, the increase of  $M_s$  when  $E=150$  J/m up to  $E=300$  J/m owing to the reduction of porosity. With the increase of temperature in the molten pool at  $E>300$  J/m, the ability of atom activity was promoted. The reduction of  $M_s$  is also related to the nearest-neighbor configuration of Fe atoms through their substitution by non-magnetic Si atoms, leading to the reduction of the magnetic moment per atom [38]. It can be reasonably indicated that the magnetic properties of coercivity and saturation magnetization of SLMed Fe-3wt.%Si alloy strongly depend on the parameters such as the number of defects, grain size and internal stress, etc.

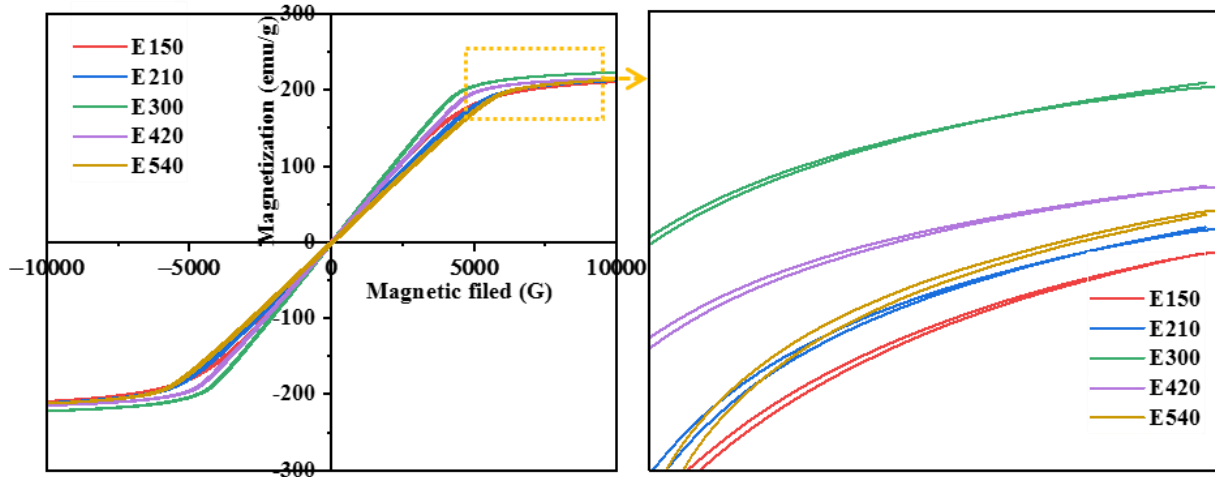


Figure 3.19 Hysteresis loops of the initial powder and SLMed samples, the right set shows the enlargement part in the low magnetic field region

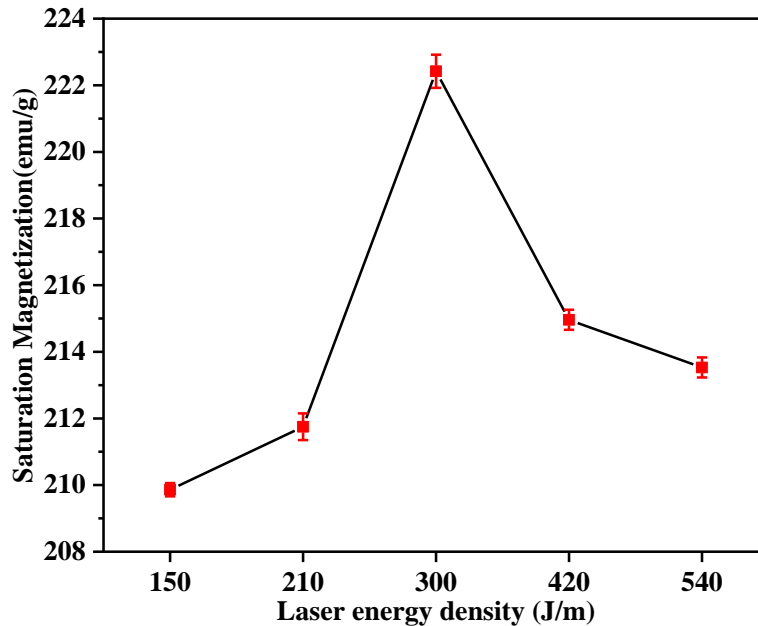


Figure 3.20 The value of saturation magnetization changes as a function of laser energy density for SLMed Fe-3wt.% Si samples

In this section, the investigation of the magnetic properties was mainly focused on coercivity and saturation magnetization. The saturation magnetization value (222.4 emu/g) of the prepared samples is higher than that of SLMed FeSiB parts (199 emu/g) reported by Alleg et al.[38], and the lowest coercivity of the samples is 41.05 Oe which is slightly lower than the value (43.8 Oe) in the same report [38]. It indicates that the SLMed parts in this work exhibit better soft magnetic properties. The coercivity of the samples in this work is higher than the result (27 Oe) of the report [39], but the saturation magnetization is better than their result (91.8 emu/g). Although the comprehensive magnetic properties are still not excellent to commercial requirements, the cracks do not exist on SLMed parts of this work, and certain results are better than those reported in some related studies.

### 3.5 Summary

In this chapter, a series of Fe-3wt.%Si alloys were successfully prepared by SLM technology using pre-alloyed powder from different SLM parameters. According to the results of the preliminary selection of the SLM process, it can be known that LED is a comprehensive factor affecting the porosity. Then,

the impact of LED on the surface morphology, surface roughness, microstructure of the selective laser melted Fe-3wt.%Si alloy was analyzed and described in detail. Summary conclusions are obtained from this chapter as follows:

- (1) The surface morphology of the corresponding SLM Fe-3wt.%Si alloy is improved by higher LED, which results in a low value of surface roughness. The decrease of the porosity rate of corresponding specimens is related to the increase of LED.
- (2) The cross-sectional microstructure of SLM Fe-3wt.%Si parts is a typical columnar structure with an oriented growth of building direction. The columnar structure at high LED is coarser than that at low LED.
- (3) The microhardness value of each SLM part is higher than 200 HV<sub>0.1</sub>. The microhardness value of the corresponding samples when LED lower than 420 J/m increases accordingly. However, it is decreased when LED=420 J/m up to LED=540 J/m due to the almost similar porosity, the burning phenomenon, and Marangoni effects in sample E540.
- (4) The coercivity of SLM specimens decreases first and then increases with the increase of LED, while the evolution of saturation magnetization and LED is opposite. The specimen with a LED at 300 J/m exhibits better comprehensive magnetic properties than other specimens. It can be concluded that the magnetic properties of coercivity and saturation magnetization of Fe-3wt.%Si alloy produced by SLM are affected by the LED, which can be attributed to the parameters such as the number of defects, grain size, etc.

This chapter demonstrated that the LED has an obvious influence on the surface morphology and microstructure of the SLMed Fe-3wt.%Si alloy. It can be concluded that the surface morphology and the microstructure are improved by using higher energy input. It also exhibited the potential possibility of three-dimensional Fe-Si soft magnetic alloys manufactured by SLM technology.

### References of Chapter 3

- [1] G.E. Fish, Soft magnetic materials, Proc. IEEE, 78 (1990) 947-972.
- [2] C.-W. Chen, Magnetism and metallurgy of soft magnetic materials, Courier Corporation, 2013.
- [3] H. Shokrollahi, K. Janghorban, Soft magnetic composite materials (SMCs), Journal of Materials Processing Technology, 189 (2007) 1-12.
- [4] K.I. Arai, K. Ishiyama, Rolled texture and magnetic properties of 3% silicon steel, Journal of applied physics, 64 (1988) 5352-5354.
- [5] J.S. Robles, A.S. Zamarripa, M.G. Mata, J. Cabrera, Texture evolution of experimental silicon steel grades. Part I: Hot rolling, J. Magn. Mater., 429 (2017) 367-371.
- [6] P. Jang, B. Lee, G. Choi, Effects of annealing on the magnetic properties of Fe-6.5% Si alloy powder cores, Journal of Applied Physics, 103 (2008) 07E743.
- [7] A.S.M.P. Materials Science & Engineering, Microstructure and Processing Song, Hong-Yu, H.-T. Liu, H.-H. Lu, H.-Z. Li, W.-Q. Liu, X.-M. Zhang, G.-D. Wang, Effect of hot rolling reduction on microstructure, texture and ductility of strip-cast grain-oriented silicon steel with different solidification structures, Mater. Sci. Eng., A, 605 (2014) 260-269.
- [8] X. He, X. Li, Y. Sun, Microstructure and magnetic properties of high silicon electrical steel produced by electron beam physical vapor deposition, J. Magn. Mater., 320 (2008) 217-221.
- [9] A. Uriondo, M. Esperon-Miguez, S. Perinpanayagam, The present and future of additive manufacturing in the aerospace sector: A review of important aspects, Proc. Inst. Mech Eng. G. J. Aerosp Eng., 229 (2015) 2132-2147.
- [10] M. Garibaldi, C. Gerada, I. Ashcroft, R. Hague, H. Morvan, The impact of additive manufacturing on the development of electrical machines for MEA Applications: A feasibility study, in, 2015.
- [11] S. Liu, J. Liu, J. Chen, X. Liu, Influence of surface tension on the molten pool morphology in laser melting, Int. J. Therm. Sci., 146 (2019) 106075.



- [12] C. Ma, D. Bothe, Direct numerical simulation of thermocapillary flow based on the volume of fluid method, *Int. J. Multiphase Flow*, 37 (2011) 1045-1058.
- [13] M. Guo, D. Gu, L. Xi, H. Zhang, J. Zhang, J. Yang, R. Wang, Selective laser melting additive manufacturing of pure tungsten: role of volumetric energy density on densification, microstructure and mechanical properties, *Int. J. Refract. Met. Hard Mater*, 84 (2019) 105025.
- [14] J. Yi, J. Kang, T. Wang, X. Wang, Y. Hu, T. Feng, Y. Feng, P. Wu, Effect of laser energy density on the microstructure, mechanical properties, and deformation of Inconel 718 samples fabricated by selective laser melting, *Journal of Alloys and Compounds*, 786 (2019) 481-488.
- [15] M.H. Nasab, D. Gastaldi, N.F. Lecis, M. Vedani, On morphological surface features of the parts printed by selective laser melting (SLM), *Addit. Manuf.*, 24 (2018) 373-377.
- [16] D. Gu, Y. Shen, Balling phenomena in direct laser sintering of stainless steel powder: Metallurgical mechanisms and control methods, *Mater. Des.*, 30 (2009) 2903-2910.
- [17] G. Dursun, S. Ibekwe, G. Li, P. Mensah, G. Joshi, D. Jerro, Influence of laser processing parameters on the surface characteristics of 316L stainless steel manufactured by selective laser melting, *Materials Today: Proceedings*, (2020).
- [18] G. Ng, A. Jarfors, G. Bi, H. Zheng, Porosity formation and gas bubble retention in laser metal deposition, *Appl. Phys. A*, 97 (2009) 641-649.
- [19] R. Xiao, X. Zhang, Problems and issues in laser beam welding of aluminum–lithium alloys, *J. Manuf. Processes*, 16 (2014) 166-175.
- [20] N.T. Aboulkhair, N.M. Everitt, I. Ashcroft, C. Tuck, Reducing porosity in AlSi10Mg parts processed by selective laser melting, *Addit. Manuf.*, 1 (2014) 77-86.
- [21] M. Xia, D. Gu, G. Yu, D. Dai, H. Chen, Q. Shi, Porosity evolution and its thermodynamic mechanism of randomly packed powder-bed during selective laser melting of Inconel 718 alloy, *International Journal of Machine Tools and Manufacture*, 116 (2017) 96-106.
- [22] C. Qiu, C. Panwisawas, M. Ward, H.C. Basoalto, J.W. Brooks, M.M. Attallah, On the role of melt flow into the surface structure and porosity development during selective laser melting, *Acta Mater.*, 96 (2015) 72-79.
- [23] M. Boivineau, C. Cagran, D. Doytier, V. Eyraud, M.-H. Nadal, B. Wilthan, G. Pottlacher, Thermophysical properties of solid and liquid Ti-6Al-4V (TA6V) alloy, *Int. J. Thermophys.*, 27 (2006) 507-529.
- [24] B. Zhang, Y. Li, Q. Bai, Defect formation mechanisms in selective laser melting: a review, *Chinese Journal of Mechanical Engineering*, 30 (2017) 515-527.
- [25] W. Yuan, H. Chen, T. Cheng, Q. Wei, Effects of laser scanning speeds on different states of the molten pool during selective laser melting: Simulation and experiment, *Mater. Des.*, 189 (2020) 108542.
- [26] E.O. Olakanmi, R. Cochrane, K. Dalgarno, A review on selective laser sintering/melting (SLS/SLM) of aluminium alloy powders: Processing, microstructure, and properties, *Prog. Mater Sci.*, 74 (2015) 401-477.
- [27] L. Tonelli, A. Fortunato, L. Ceschini, CoCr alloy processed by selective laser melting (SLM): Effect of laser energy density on microstructure, surface morphology, and hardness, *Journal of Manufacturing Processes*, 52 (2020) 106-119.
- [28] T. Niendorf, S. Leuders, A. Riemer, H.A. Richard, T. Tröster, D. Schwarze, Highly anisotropic steel processed by selective laser melting, *Metall. Mater. Trans. B*, 44 (2013) 794-796.
- [29] M. Garibaldi, I. Ashcroft, M. Simonelli, R. Hague, Metallurgy of high-silicon steel parts produced using Selective Laser Melting, *Acta Materialia*, 110 (2016) 207-216.
- [30] W. Kurz, D.J. Fisher, *Fundamentals of solidification*, (1989).
- [31] S. Liu, Y. Li, F. Liu, H. Zhang, H. Ding, Effects of relative positioning of energy sources on weld integrity for hybrid laser arc welding, *Opt. Lasers Eng.*, 81 (2016) 87-96.

- [32] S.L. Sing, F.E. Wiria, W.Y. Yeong, Selective laser melting of titanium alloy with 50 wt% tantalum: effect of laser process parameters on part quality, *International Journal of Refractory Metals and Hard Materials*, 77 (2018) 120-127.
- [33] M. Garibaldi, I. Ashcroft, N. Hillier, S. Harmon, R. Hague, Relationship between laser energy input, microstructures and magnetic properties of selective laser melted Fe-6.9% wt Si soft magnets, *Materials Characterization*, 143 (2018) 144-151.
- [34] R. Hilzinger, W. Rodewald, *Magnetic materials: fundamentals, products, properties, applications*, Vacuumschmelze, 2013.
- [35] F. Pfeifer, C. Radloff, Soft magnetic Ni-Fe and Co-Fe alloys-some physical and metallurgical aspects, *J. Magn. Magn. Mater.*, 19 (1980) 190-207.
- [36] G. Ouyang, X. Chen, Y. Liang, C. Macziewski, J. Cui, Review of Fe-6.5 wt% Si high silicon steel—A promising soft magnetic material for sub-kHz application, *Journal of Magnetism and Magnetic Materials*, (2019).
- [37] B. Zhang, N.-E. Fenineche, H. Liao, C. Coddet, Microstructure and magnetic properties of Fe–Ni alloy fabricated by selective laser melting Fe/Ni mixed powders, *Journal of Materials Science & Technology*, 29 (2013) 757-760.
- [38] S. Alleg, R. Drablia, N. Fenineche, Effect of the Laser Scan Rate on the Microstructure, Magnetic Properties, and Microhardness of Selective Laser-Melted FeSiB, *J. Supercond. Novel Magn.*, 31 (2018) 3565-3577.
- [39] N. Kang, M. El Mansori, F. Guittonneau, H. Liao, Y. Fu, E. Aubry, Controllable mesostructure, magnetic properties of soft magnetic Fe-Ni-Si by using selective laser melting from nickel coated high silicon steel powder, *Appl. Surf. Sci.*, 455 (2018) 736-741.



## Chapter 4 Investigation on microstructures, properties, and heat treatment of SLMed Fe-3wt.%Si soft magnet

### 4.1 Introduction

Originating from their intrinsic anisotropy, crystalline materials could exhibit directionally dependent physical and mechanical properties, if a preferred crystallographic orientation exists within the grain structure, forming a crystallographic texture [1, 2]. The properties such as the magnetic properties of the material are abnormal in the specific texture direction. The texture is one of the most important parameters determining the magnetic properties of silicon steels [3]. In ferromagnetic materials, the anisotropy in magnetic susceptibility can be controlled by aligning the grains under a moderate magnetic field during high-temperature annealing, sintering, or solidification [4, 5]. Due to the laser-induced directional cooling/solidification and the layer-by-layer nature in the SLM process, it is customary to create a strong texture on the SLMed parts [6]. For example, Zou et al. [4] controlled the grain orientations of the SLMed permalloy-80 alloys via tilted one or two rotational angles to the substrate to achieve improved magnetic properties in the build directions during laser powder bed processing. For different materials, different scanning strategies and construction directions, the produced textures in the SLM process are also diverse [7, 8]. It is necessary to study the crystallographic texture and oriented magnetic properties of SLM-produced alloys. Except for the magnetic properties, mechanical performance is a quite significant indicator of magnetic alloy applied in various industrial applications. Especially when silicon steels are used in high-speed motors, in addition to the requirements of magnetic properties, mechanical performance, such as high strength is also required [9-11]. The current researches have few detailed reports on the mechanical properties of SLMed Fe-Si alloys.

In general, cause of the complex thermal history of the SLM process, thermal stress is unavoidable in the samples [12]. Post-treatment is one of the crucial steps for improving microstructures and magnetic properties of the SLMed magnetic materials. The influence of post-treatment on microstructures and magnetic properties should be systematically and thoroughly studied [13]. There are also some reports on this field in the existing literature, most of which focus on the improvement of partial magnetic properties by heat treatment. There is still a lack of detailed descriptions of the evolution in the microstructure and the overall impact of magnetic properties [14-16]. Generally, any form of mechanical deformation will result in a deterioration of the magnetic properties of soft iron for electromagnet applications. The internal stresses produced by cold working can be removed by annealing at temperatures between 725 °C and 900 °C, provided the material does not suffer oxidation during annealing, which would also result in impaired magnetic properties [17].

This chapter focused on the crystalline texture and oriented magnetic properties of the SLMed Fe-3wt.%Si alloy firstly, summarized the relationship between the texture and magnetic characteristics, and carried on the theoretical elaboration. And then, the mechanical performances including microhardness, tensile properties were evaluated. Besides, considering the aforementioned situation, it appears that a systematic study simultaneously considering the effects of the manufacturing parameters and post-heat treatments on the overall microstructures and magnetic properties is lacking; therefore, this chapter also evaluated the effect of heat treatment on the microstructures and magnetic properties of SLM-processed Fe-3wt.%Si alloy samples. Combine with the annealing times and temperatures fall within the range of conventional processing and previous studies on Fe-Si alloys [14, 18-22], the SLMed Fe-3wt.%Si parts were annealed at 750 °C, 850 °C, 1000 °C for 3 h, and 1000 °C for 1 h, 3 h in argon protective atmosphere, respectively.

## 4.2 Experimental details

In this chapter, the Fe-3wt.%Si soft magnet samples were fabricated via SLM technology according to previously optimized parameters. According to the results in Chapter 3, among the Fe-3wt.%Si samples manufactured with different linear energy densities (LEDs), when the linear energy density was 300J/m, the specimen with a LED at 300 J/m exhibited better comprehensive magnetic properties than other specimens. The pores were still presented in the sample, to further reduce the porosity, the LED was increased to 320 J/m. The detailed parameters are given in Table 4.1. Apart from cubic specimens with dimensions of 8 mm × 8 mm × 8 mm, 3 mm × 3 mm × 3 mm and the ring samples of height h=4 mm, external diameter  $d_1=26$  mm, internal diameter  $d_2= 18$  mm were manufactured for microstructural observation and magnetic properties measurements respectively. As described in Figure 3.1 (a) and Figure 3.7 (b), the zigzag scanning pattern with a neighboring laser track rotation of 90 ° was utilized during the SLM process. To explore the effect of heat treatments on the microstructure and properties, the SLMed samples were annealed under different temperatures and different dwell times in the nitrogen atmosphere, the detailed conditions of the heat treatment are listed in Table 4.2. To simplify the discussion, the following nomenclature will be used. The parts printed by SLM before treatment in the as-built condition are referred to as ‘As-built’. The printed samples that were annealed at different temperatures (T) and which were kept constant at different times (t) are denoted by ‘AT T/t’ and a number representing the annealing temperature, which is listed in Table 4.2.

Moreover, standard samples which were mentioned previously for the tensile test were also fabricated, a 3D model and a fabricated sample are shown in Figure 4.1. Optical microscopy (OM) and scanning electron microscopy (SEM) were used to characterize the microstructures. The phase composition was also performed by an X-Ray diffractometer. Texture and crystallographic orientations of SLMed specimens were observed by electron back-scattering diffraction (EBSD). The oriented magnetic properties of the SLMed samples were characterized by a vibrating sample magnetometer (VSM) at different field directions. The schematic diagram of VSM was shown in Figure 2.12. To evaluate the magnetic properties of samples in different directions, un sample is placed in the magnetic field, and the X, Y, Z directions are parallel to the external magnetic field direction respectively based on the building coordinate system which is presented in Figure 3.1. The detailed mechanical tests were adopted as mentioned in chapter 2. The quasi-static magnetic properties for the as-built and annealed ring samples were measured by the method of DC magnetic property measurement, and the dynamic magnetic property of power losses was characterized in AC conditions, which were described in detail in Chapter 2.

Table 4.1 The optimized linear energy density and SLM parameters

P (W)	t ( $\mu$ s)	d (mm)	Laser spot ( $\mu$ m)	Layer thickness ( $\mu$ m)	Hatch distance ( $\mu$ m)	Linear energy density (J/m)
80	120	30	35	30	60	320

Table 4.2 Overview of the SLMed Fe-3wt.%Si samples and treated condition

Named	Annealed temperature (°C)	Dwell time (h)	Cooling	Atmosphere
AT750/3h	750	3	Furnaced	Ar
AT850/3h	850	3		
AT1000/1h	1000	1		
AT1000/3h	1000	3		
AT1000/5h	1000	3		

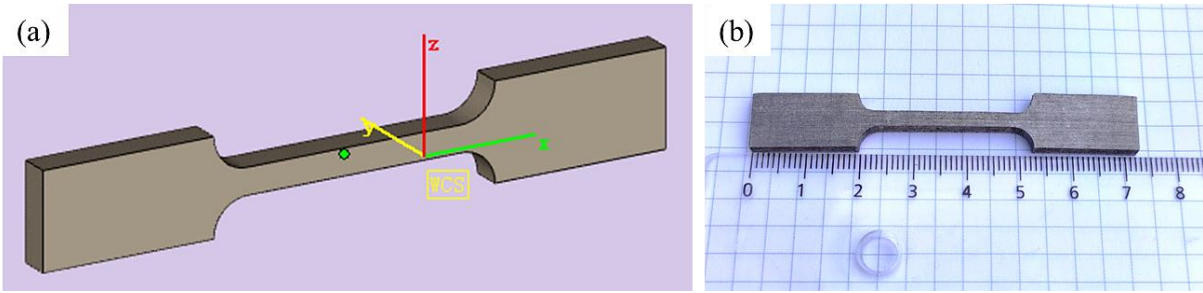


Figure 4.1 (a) 3D model, (b) an SLM fabricated sample for tensile test

### 4.3 Microstructure and oriented magnetic properties analysis

#### 4.3.1 Porosity and microstructure analysis

The OM images before etching of XY and XZ planes are shown in Figure 4.2 (a) and Figure 4.2 (d) respectively, and the porosity is given in these pictures, which is lower than 0.5%. No cracks appear in the sample. It should be noted that the samples were processed with a 200 °C preheat, which had an evident impact on the magnitude of thermal stresses, hence crack-free samples were successfully produced. A few small circular pores appear in the sample, which can be attributed to the gas being trapped into the molten pool during the solidification in the SLM process.

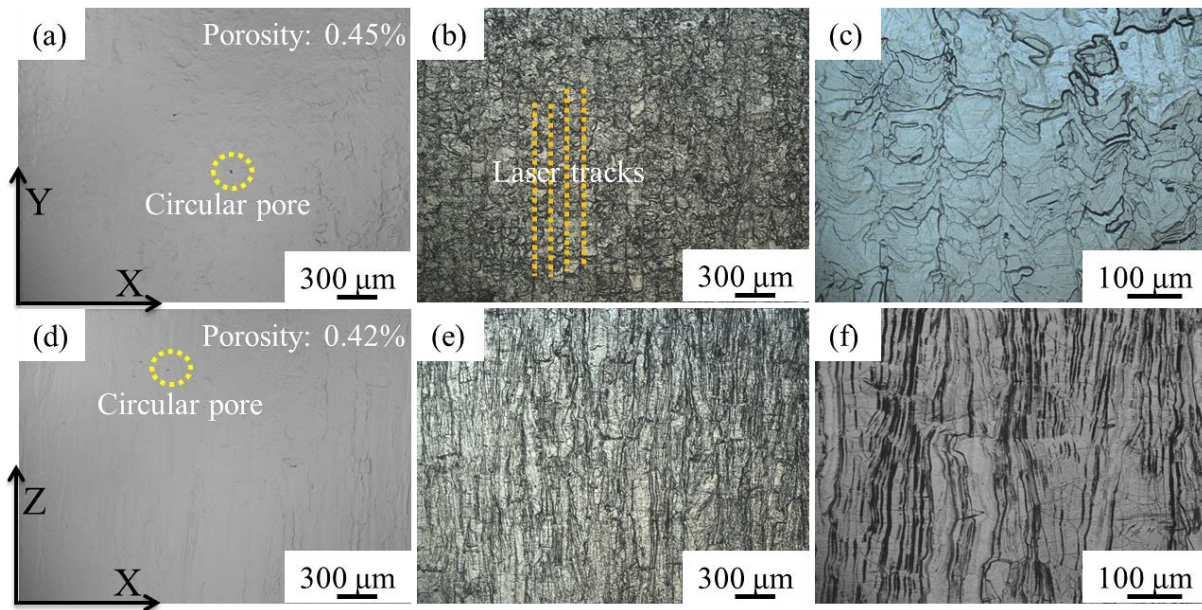


Figure 4.2 OM images of the SLMed samples (a-c) XY plane, (d-f) XZ plane

According to an estimate, the focused laser spot diameter in this study is 35  $\mu\text{m}$ . The formations in Figure 4.2 (b) that correspond to the structure in the scanning plane have a diameter of about 30-70  $\mu\text{m}$ . This size is in good agreement with the laser spot diameter though it is marginally larger due to the presence of the heat-affected zone around the laser passing track [15]. As represented in the magnified OM image, Figure 4.2 (c) shows an inhomogeneous structure in the XY plane. In the XZ plane, as displayed in Figure 4.2 (e) and Figure 4.2 (f), the microstructure of the SLMed parts is a typical columnar structure with an oriented growth of building direction.

The grain structure of the selected Fe-3wt.%Si specimen is shown in Figure 4.3 from electron backscatter diffraction (EBSD) data. Crystallographic structure analysis shows that the molten alloy crystallizes erratically with a few fine grains and coarser grains having different sizes in the surface (XY) plane. The size of finer grains is concentrated on several micrometers, and the size of coarser grains is about 20 to 30  $\mu\text{m}$ . As a result, it can be known that the average grain size is about 14.6  $\mu\text{m}$ . Moreover,

in the cross-section (XZ) plane, the alloy crystallizes erratically with the formation of elongated grains along the building direction and with the size from several micrometers up to twenties micrometers, the average grain size is about 12.77  $\mu\text{m}$ . The XRD pattern is given in Figure 4.4 (a), only peaks related to the Bcc-Fe phase were observed in the samples. The analysis of phase composition from EBSD in Figure 4.4 (b) also confirmed that the Fe-3wt.%Si alloy is a one-phase alloy.

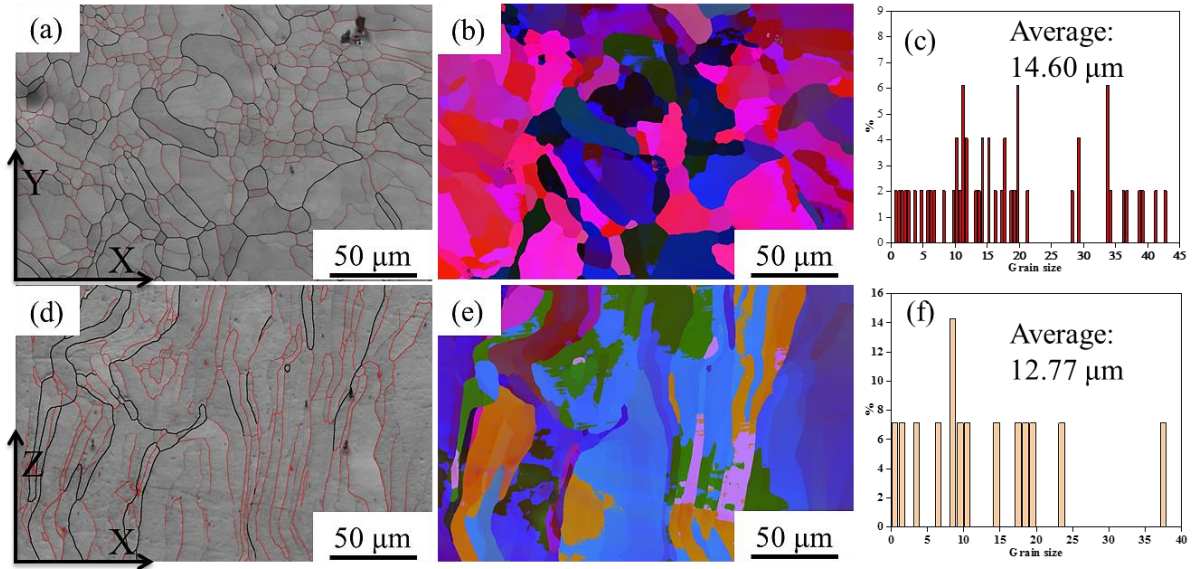


Figure 4.3 The EBSD maps of grain structure and average grain size of SLMed Fe-3wt.%Si specimen in different planes (a-c) XY plane, (d-f) XZ plane

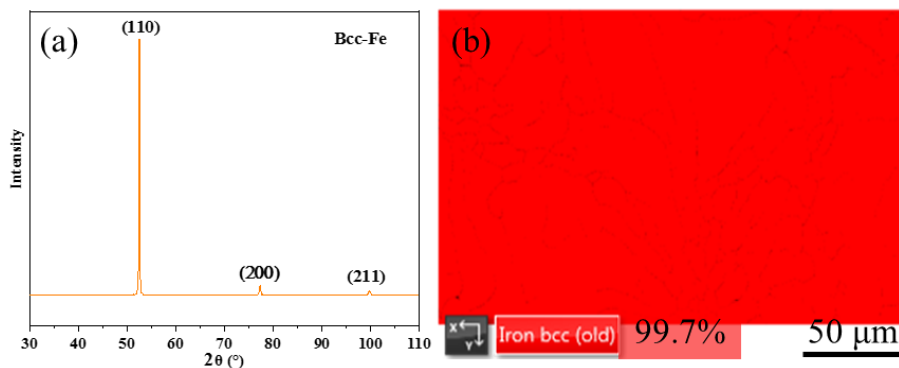


Figure 4.4 (a) XRD pattern, (b) phase composition from EBSD

### 4.3.2 Study of magnetic anisotropy and crystallographic texture

The hysteresis loops of SLM produced sample along three different directions X, Y and Z (build direction) are shown in Figure 4.5. The three curves are almost coincident, which illustrates no anisotropic magnetic properties in different measured directions. Figure 4.6 (a), (b), and (c) are the magnetization curves in different measured directions and their enlarged-view graphs of low magnetic field region, from which can get the values of corresponding magnetic properties. The average values of coercivity ( $H_c$ ), magnetization saturation ( $M_s$ ), and residual magnetization ( $M_r$ ) of SLM-produced Fe-3wt.%Si alloy at different measured directions are summarized in Table 4.3. Meanwhile, the ratios between  $M_s$  and  $M_r$ , which presents the soft magnetic properties, were also calculated and shown as S in Table 4.3. It can be observed that the average values of each magnetic property are almost similar, which further confirm that the sample has isotropy magnetic properties at different three measured directions. The value of S is only about 0.81, indicating the SLMed Fe-3wt.%Si alloy has good soft magnetic properties.

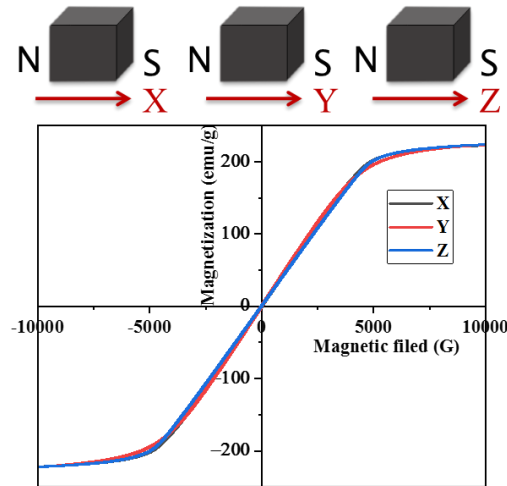


Figure 4.5 The hysteresis loops of SLM produced sample along with three directions of measurements

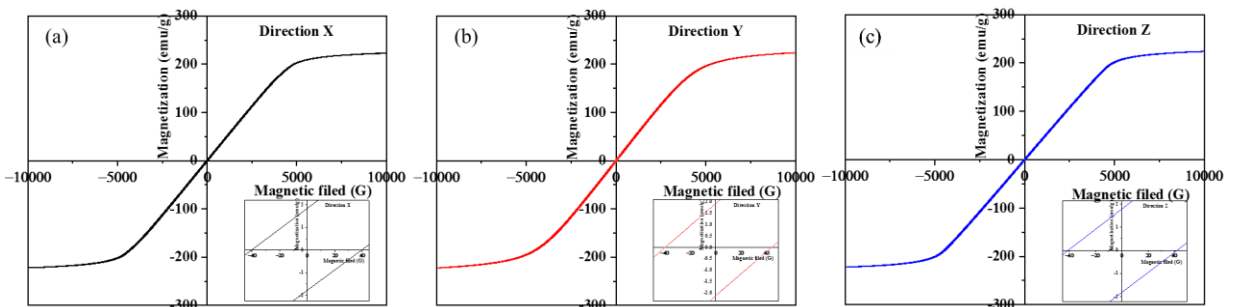


Figure 4.6 The magnetization curves in different measured directions and their enlarged-view graphs of low magnetic field

Table 4.3 The average values of magnetic properties of SLM produced Fe-3wt.%Si alloy at different measured directions

Directions	X	Y	Z
$H_c$ (Oe)	$40.7 \pm 0.3$	$40.6 \pm 0.2$	$40.6 \pm 0.2$
$M_s$ (emu/g)	$222.8 \pm 0.5$	$223.4 \pm 0.6$	$223.8 \pm 0.6$
$M_r$ (emu/g)	$1.87 \pm 0.04$	$1.86 \pm 0.03$	$1.81 \pm 0.04$
S (%)	$0.84 \pm 0.02$	$0.83 \pm 0.02$	$0.81 \pm 0.02$

In general, during the SLM process, the surroundings, for example, the thermal conductivity of powder and solidified material near the molten pool, affect the temperature gradient significantly. Therefore, the heat conduction in the building direction is higher than that of spatial directions. It causes anisotropy in both microstructure and mechanical/physical properties [23]. The magnetic properties of SLMed Fe-3wt.%Si show isotropy in three different measurement directions, which is related to its microstructure, especially its crystal structure and texture.

EBSD data analysis shows a crystallographic texture in the grains of SLMed Fe-3wt.%Si alloy. Figure 4.7 shows the pole figures (PF) of two different planes. The sample mainly presents a  $\{100\}\langle 001\rangle$  cubic texture, i.e. a  $\langle 001\rangle$  texture along the BD, which is consistent with the morphological orientation of the columnar grains. The EBSD maps and IPFs for two different planes in Figure 4.8 provide an overview of the correlation between grain morphology and their  $\langle 001\rangle$  texture, both along the BD. It is noteworthy that the nature of the specific alloy in this study promotes texture formation, also the high cooling rate and silicon content suppresses  $\gamma$ -phase formation from the phase diagram thus leaving no secondary phase to hinder ferritic grain development. The rapid solidification ( $10^3$ – $10^6$  K/s) in the SLM process resulted in this crystal texture. In addition to the high cooling rate, the direction of solidification



also plays an important role in the grain structure development during the SLM process. The vertical manufacturing direction from bottom to top makes the solidification preferred to form along the building direction. In cubic metals (such as the Bcc structure of Fe-Si), dendrite growth occurs most rapidly in the  $\langle 100 \rangle$  type crystallographic directions. According to the report of literature [24], the dendrite growth direction relative to the applied thermal gradient has a significant impact on the local undercooling and nucleation of misoriented grains. During the SLM process, partial remelting of the grains whose crystallographic directions of “easy growth” (the  $\langle 001 \rangle$  family in Bcc systems) orient along the BD provides a substrate for the next processed layer to solidify epitaxially [25]. In the Fe-3wt.%Si alloy, these also correspond to the easy magnetization directions.

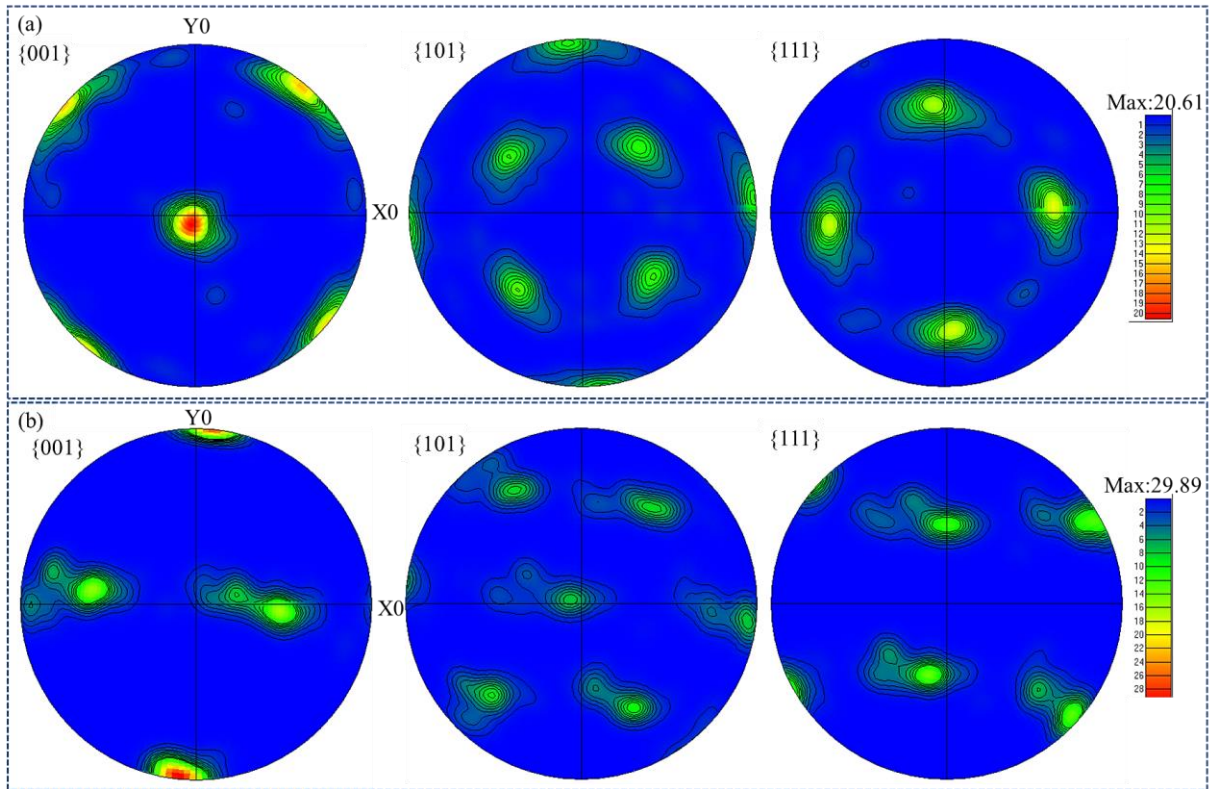


Figure 4.7 The pole figures (PF) of two different planes (a) XY plane, (b) XZ plane

Besides, a few grains with other orientations are also identified from the EBSD maps (Figure 4.8). During the building process, a series of certain or uncertain phenomena including powder spatter, melting/re-melting, selective elemental evaporation, and solidification might occur simultaneously when the powder is irradiated by the laser beam. Moreover, since heat transfer will also occur from the sides of the part being built and not just through the bottom via the substrate, columnar grains do not necessarily grow along the building direction [26]. These might appear in other textures.

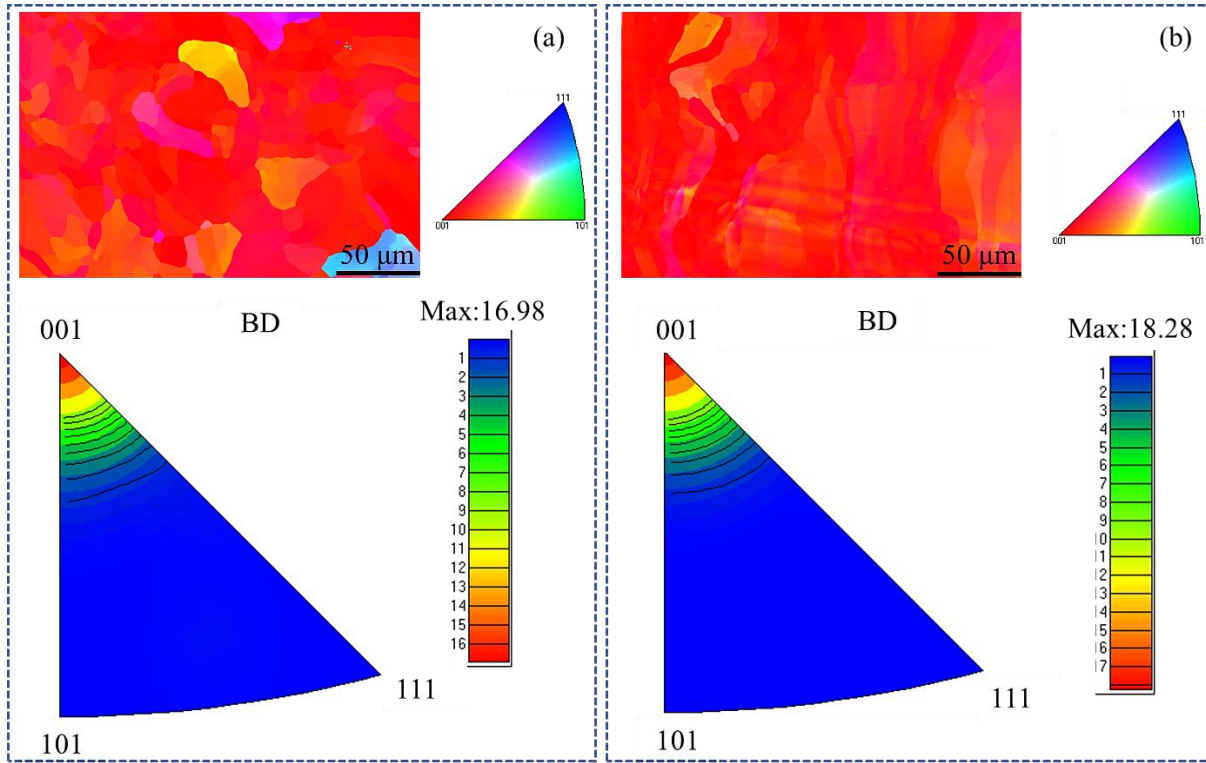


Figure 4.8 EBSD maps and IPFs (a) XY plane, (b) XZ plane

The magnetic anisotropy ( $F_k$ ) of a cubic system could be written below [27]:

$$F_k = K_0 K_1 (\alpha_1^2 \alpha_2^2 + \alpha_2^2 \alpha_3^2 + \alpha_3^2 \alpha_1^2) + K_2 \alpha_1^2 \alpha_2^2 \alpha_3^2 + \dots \quad \text{Equation 4.1}$$

where  $\alpha_1, \alpha_2, \alpha_3$  represent the direction cosines of magnetization,  $K_1, K_2$  are the anisotropy constants, while  $K_0$  is independent with the orientation. For Bcc-Iron,  $K_1$  is about  $4.8 \times 10^4 \text{ J/m}^3$  ( $4.8 \times 10^3 \text{ erg/cm}^3$ ) and  $K_2$  is  $-1 \times 10^4$  at room temperature [28]. The positive value of  $K_1$  indicates the [100] axis is the easy magnetic axis. Besides, it can be confirmed from the magnetization curves of a single Bcc-iron crystal shown in Figure 4.9. In addition to the [100] axis, [111] is the hard axis, i.e. [100] is the easy magnetization direction, [111] is the hard magnetization direction.

As shown in Figure 4.10, in cubic crystal, it is well known that the  $\langle 100 \rangle$  families include [100], [001] and [010] [29]. As mentioned previously, the SLM-produced Fe-3wt.%Si samples exhibit a strong  $\langle 001 \rangle$  texture along the building direction. Due to the strong texture, when a magnetic field was applied to the sample, the motion of the domain walls is easier to rotate along the [001] axis. It can increase the “softness” of the material by decreasing its coercivity field level [30]. Thus, strong  $\langle 001 \rangle$  texture along the building direction is beneficial significantly for the soft magnetic properties. Based on Figure 4.10 (a) and Figure 4.10 (b), for SLM produced Fe-3wt.%Si alloy with  $\{100\} \langle 001 \rangle$  cubic texture in this study, in the construction coordinate system, the three directions of X, Y, and Z are actually contained in the axis that is easy to be magnetized. Therefore, the SLM-produced Fe-3wt.%Si alloy exhibits isotropy soft magnetic properties in these three directions.

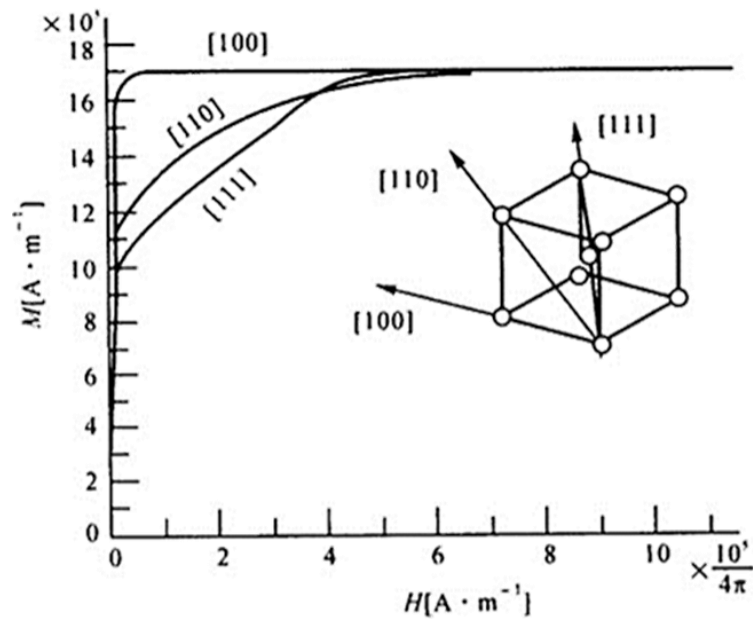


Figure 4.9 The magnetization curves of the single Bcc-iron crystal [28]

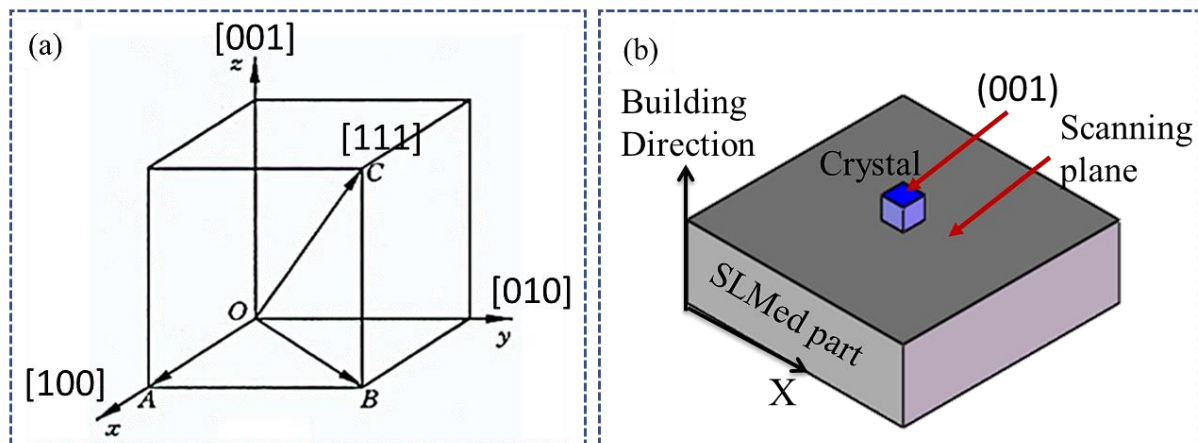


Figure 4.10 (a) A simple cubic crystal structure, (b) A simple schematic diagram of SLMed part with cubic texture

## 4.4 Mechanical properties

### 4.4.1 Microhardness and tensile properties

The Vickers microhardness of the SLMed sample in different measured planes is presented in Figure 4.11. Both average values of measurement microhardness are similar, which is about 235 HV<sub>0.1</sub>.

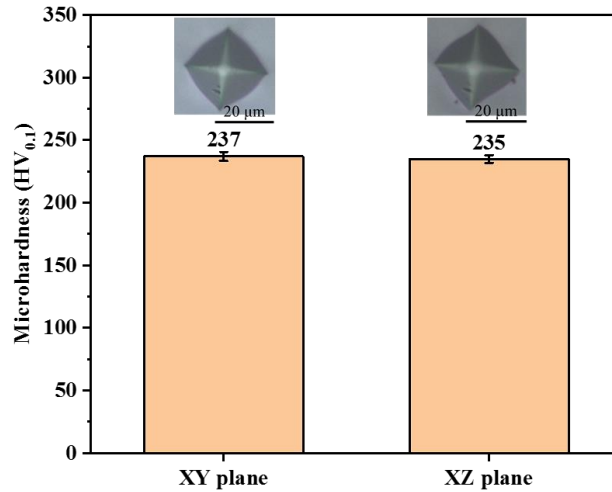


Figure 4.11 Vickers microhardness of SLMed sample

Figure 4.12 shows the stress-strain curve of the SLMed Fe-3wt.%Si alloy. The statistical mechanical properties data including ultimate tensile strength (UTS), yield strength (YS), and elongation at break (EL) are listed in Table 4.4. Due to the low microhardness, the elongation of the specimen reaches  $8.8\% \pm 0.3\%$ , and the UTS and YS are  $562 \pm 5.1$  MPa,  $445 \pm 5.3$  MPa, respectively. SEM photographs of the fracture morphologies of the Fe-3wt.%Si sample are displayed in Figure 4.13, to further investigate and understand the fracture mechanisms of the SLMed Fe-3wt.%Si alloy. In Figure 4.13 (a), it can be observed “necking” phenomenon in the SLMed specimen, which can suggest that the SLMed Fe-3wt.%Si alloy exhibit plasticity. As represented in Figure 4.13 (b), large and deep dimples generated due to plastic deformation were observed on the fracture surface of the SLMed sample at the enlarged region, indicating a ductile rupture mechanism [31]. Meanwhile, granular fracture with shallow dimples was identified on the fracture surface at some highly deformed regions. Hence, it can be considered a mixed-mode of ductile and brittle failure is the main rupture mechanism for SLMed Fe-3wt.%Si alloy.

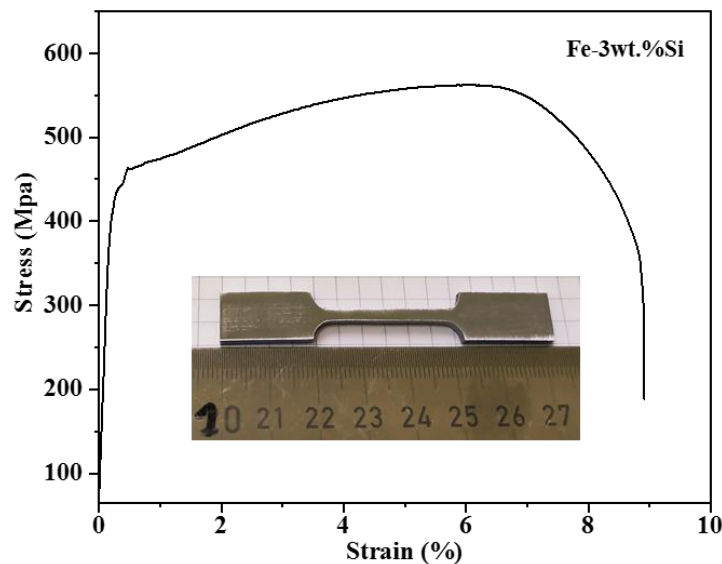


Figure 4.12 Tensile stress-strain curves for SLMed Fe-3wt.%Si part

Table 4.4 The statistical mechanical properties of SLMed Fe-3wt.%Si alloy

Sample	UTS (MPa)	YS (MPa)	EL(%)
SLMed Fe-3wt.%Si	$562 \pm 5.1$	$445 \pm 5.3$	$8.8 \pm 0.3$

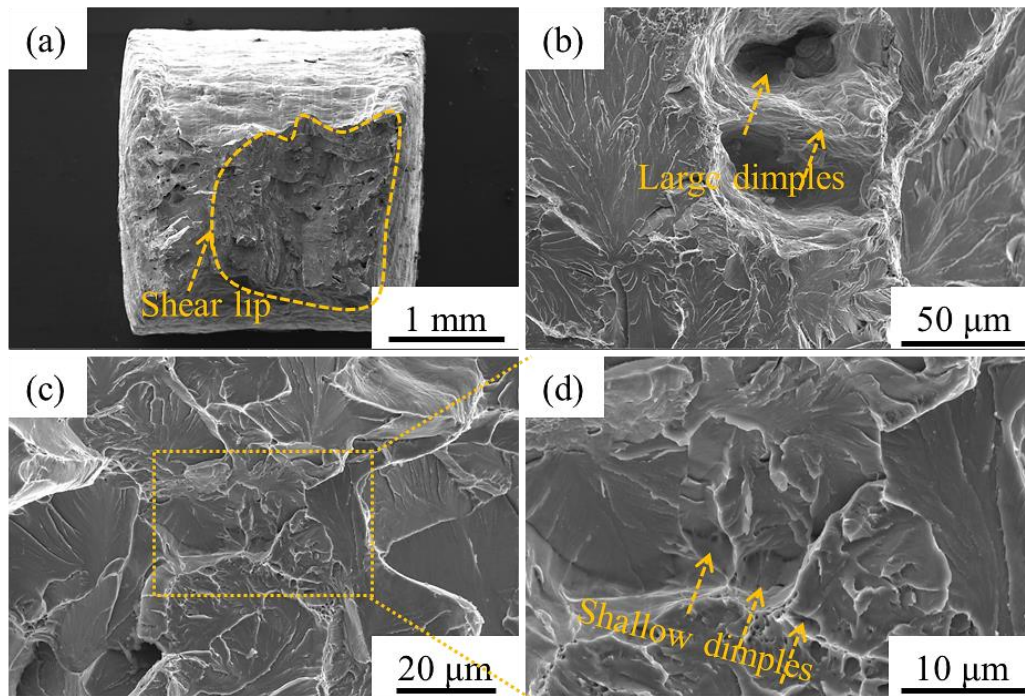


Figure 4.13 Fracture morphologies of the SLMed Fe-3wt.%Si part observed by SEM

## 4.5 Effect of heat treatment on the microstructures and magnetic properties

### 4.5.1 Microstructural evolution after heat treatment

For the as-built specimen, the SEM images of the XZ plane are depicted in Figure 4.14 (a) and Figure 4.14 (b), the typical microstructural features induced by SLM such as molten pool boundaries and cells could be observed. Although the boundaries of the molten pool are not significantly clear, they are still recognizable. The SEM images of the XZ plane for the heat-treated samples AT750/3h and AT850/3h are illustrated in Figure 4.14 (c-f). Through the comparison of the as-built samples, it can be noted that no grain growth occurred after annealing at 750 °C for 3 h, neither did the grains show any significant growth during the annealing at 850 °C for 3 h. The grain size in the vertical plane of the sample remains almost at the level of the as-built sample, which suggests that annealing the samples at 750 °C and 850 °C for 3 h does not affect the grain size, but the molten pool boundaries which have disappeared. The observed lack of grain enlargement agrees with the results previously reported in [19] for the SLMed high-Si steel annealed at 700 °C and 900 °C for 1 h. In this case, recrystallization and growth of equiaxial grains which is typical of annealing traditional deformed metals do not occur [19]. As represented in Figure 4.15, when the annealing temperature reached 1000 °C, although the dwell time was 1 h, the SEM graphs of the XZ plane still show that in addition to the disappearance of the molten pool boundaries, a low amount of grain grew to a large size. Annealing conducted at 1000 °C for 3 h, caused a marked grain growth as shown in Figure 4.15 (e) and Figure 4.15 (f). As the dwell time increased to 5h, through the comparison of the AT1000/3h sample, the grains almost did not grow further significantly. Similarly, no distinct microstructural differences are noted after annealing in this case. Nevertheless, as shown in Figure 4.16, after the heat treatment even at 1000 °C for 3 h, in addition to the grain growth, the grain size of no homogeneity is still observed.

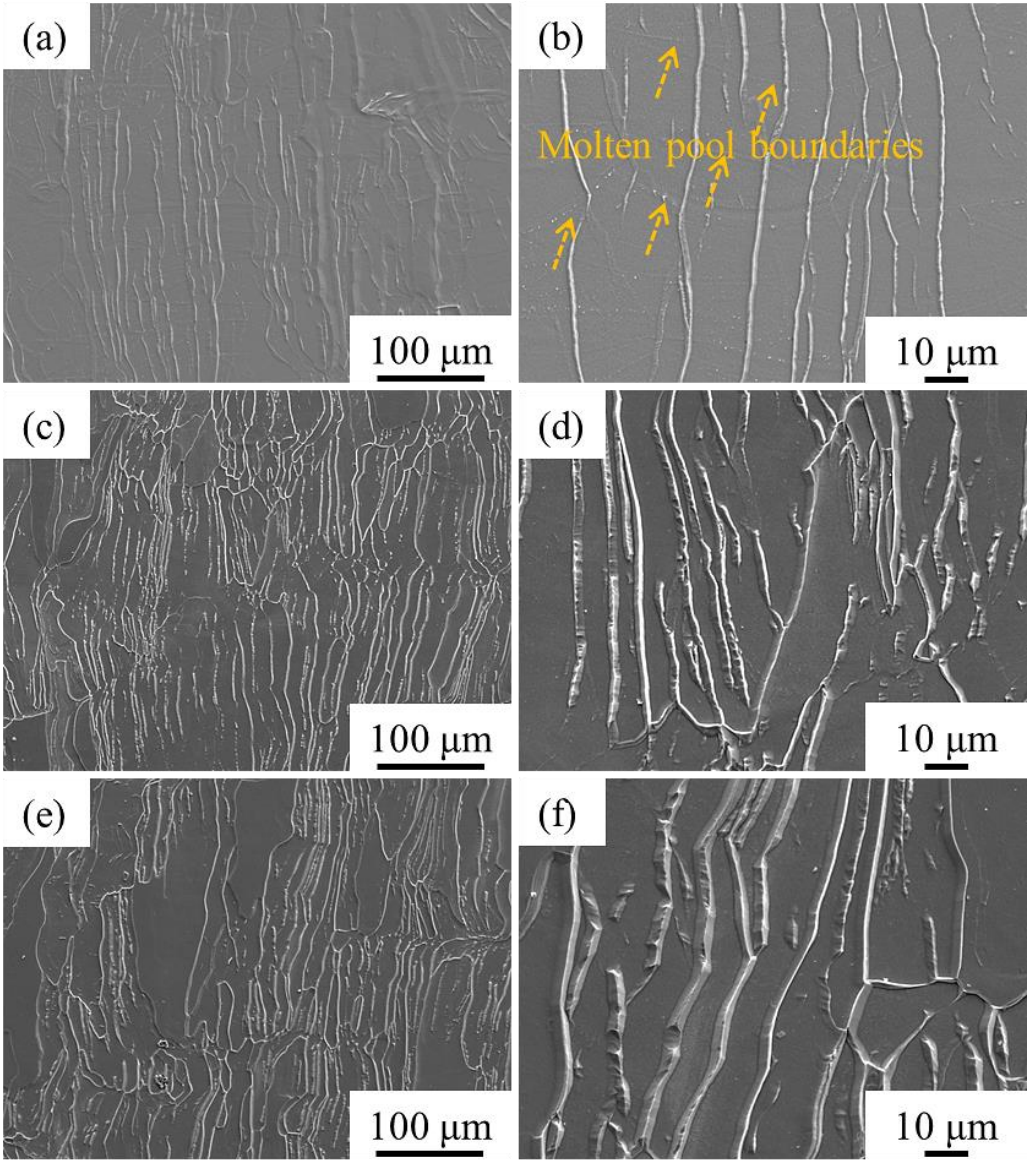


Figure 4.14 Microstructure of the SLMed Fe-3wt.%Si samples observed via SEM after etching: (a-b) SLMed as-built sample, (c-d) SLMed AT750/3h sample, (e-f) SLMed AT850/3h sample

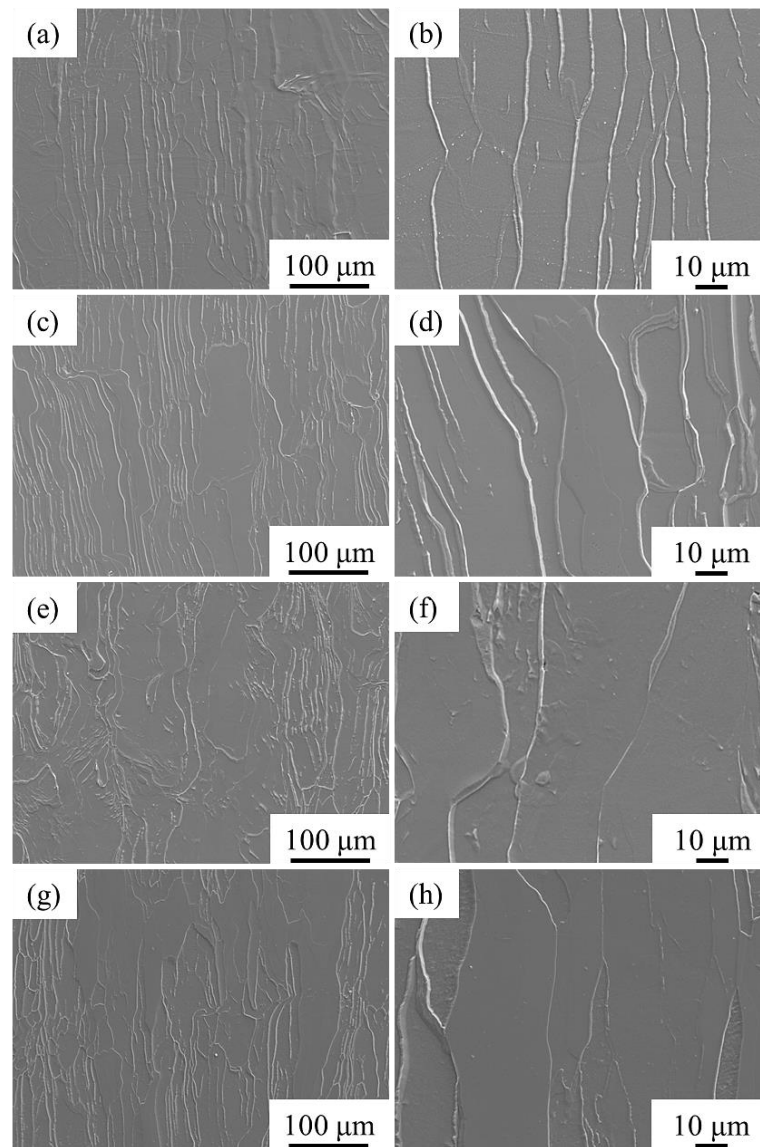


Figure 4.15 Microstructure of the SLMed Fe-3wt.%Si samples observed via SEM after etching: (a-b) SLMed as-built sample, (c-d) SLMed AT1000/1h sample, (e-f) SLMed AT1000/3h sample, (g-h) SLMed AT1000/5h sample

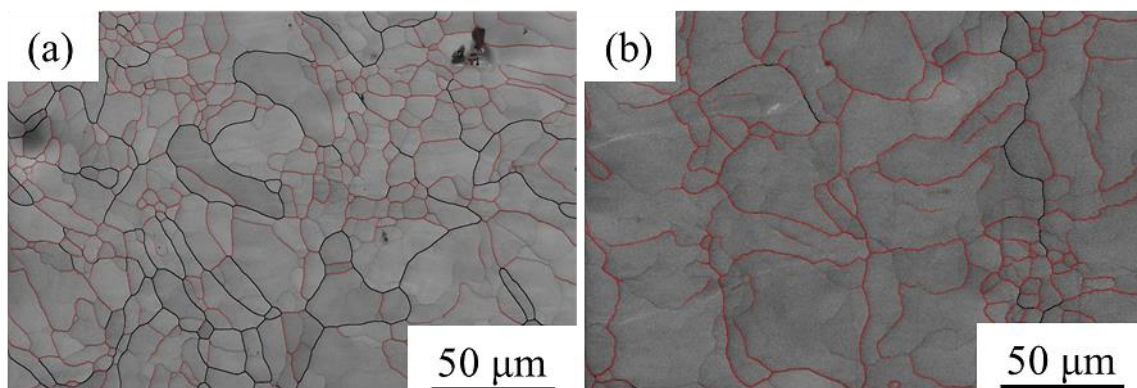


Figure 4.16 Microstructure of XY plane for SLMed Fe-3wt.%Si sample (a) as-built, (b) AT1000/3h

To further investigate the effect of annealing on the microstructures of SLMed Fe-3wt.%Si alloy, the XZ planes are observed at higher magnification. The solidification structures associated with the

micro-segregation, especially at the molten pool boundaries are clearly visible in the as-built microstructure of Figure 4.17 and Figure 4.18 displayed as small gray dots (as marked by orange arrows in Figure 4.18 (a-b)). The results of EDS in Figure 4.17 and Table 4.5 indicated that the micro-segregation is the micro-segregation of Si, since the silicon content of the small gray dots is higher than that of other regions without gray dots, resulting in a fine structure overlaying ferritic grains [19]. Figure 4.18 (c-f) presents the microstructure after annealing at 750 °C for 3 h and 850 °C for 3 h, it is worth noting the micro-segregation of Si is partly dissolved and appears discontinuous. It is believed that at those temperatures the diffusion rate is just sufficient to bring Si segregations into solid solution. But upon slow furnace cooling, some of the silicon segregated again, resulting in a discontinuous structure. The samples after heat treating at 1000 °C for 1 h, 3 h, and 5 h, no small gray dots are found in these SEM images of the XZ plane (Figure 4.19 (c-h)), suggesting the SLM induced structure have been dissolved completely, i.e., the micro-segregation of Si segregations entered solid solution. In this condition, grains grew and diffusion preceded so fast, that no segregations occurred again even after slow furnace cooling, silicon was kept in solid solution and the resulting in homogenous microstructure [14, 32]. As displayed in Figure 4.20 and Figure 4.21, the texture of the SLMed Fe-3wt.%Si magnet after annealing at 1000 °C for 3 h is the same as that as-built sample (as indicated in Figure 4.7 and Figure 4.8),  $\langle 001 \rangle$  is still along the BD. This is beneficial to improve the magnetic properties after heat treatment.

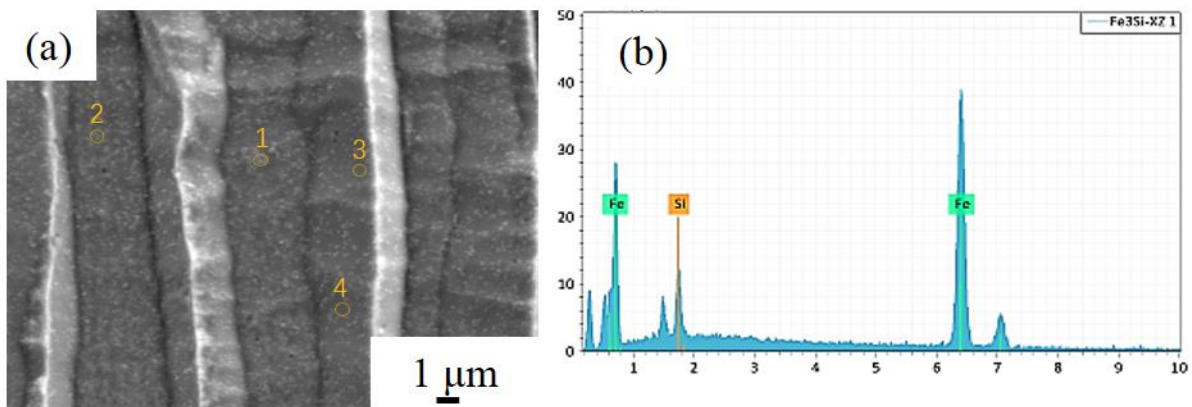


Figure 4.17 (a) SEM image of microstructure after etching, (b) EDS analysis of the SLMed Fe-3wt.%Si as-built sample

Table 4.5 Chemical composition in the five points under exam

Point	1	2	3	4
Fe (wt%)	95.23	95.31	97.10	97.22
Si (wt%)	4.77	4.69	2.90	2.78



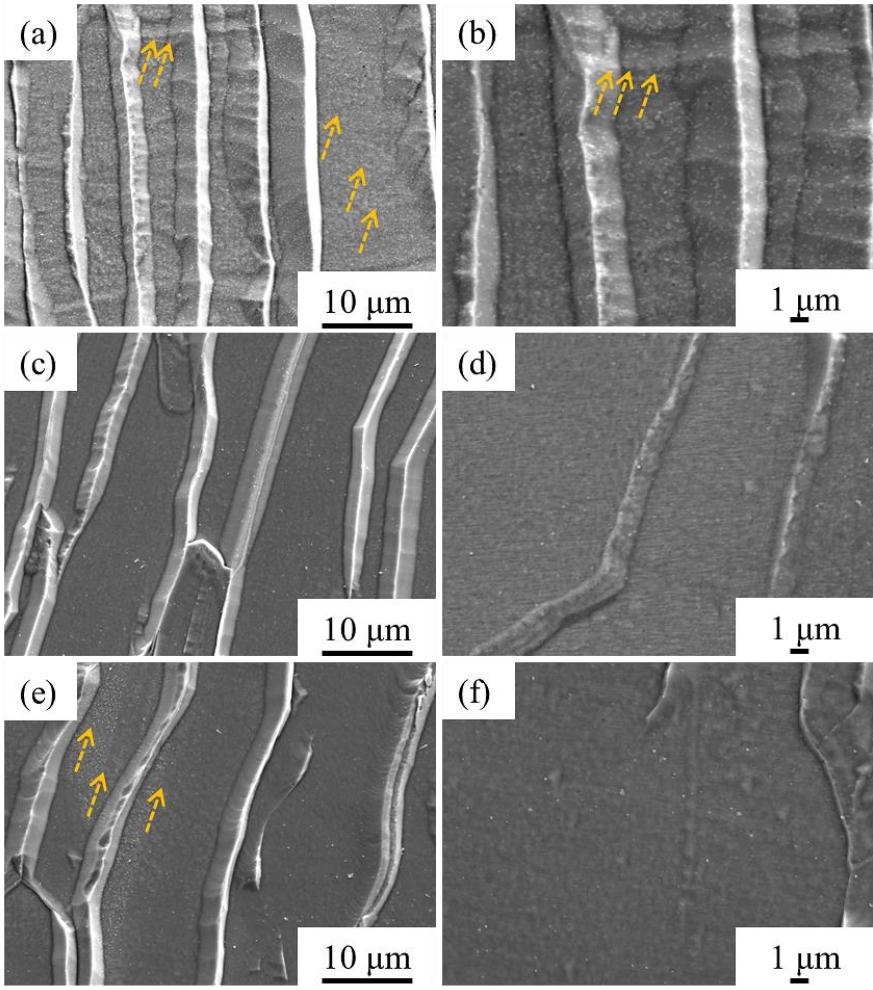


Figure 4.18 Microstructure under the high magnification of the SLMed Fe-3wt.%Si specimens observed via SEM after etching: (a-b) SLMed as-built specimen, (c-d) SLMed AT750/3hspecimen, (e-f) SLMed AT850/3h specimen

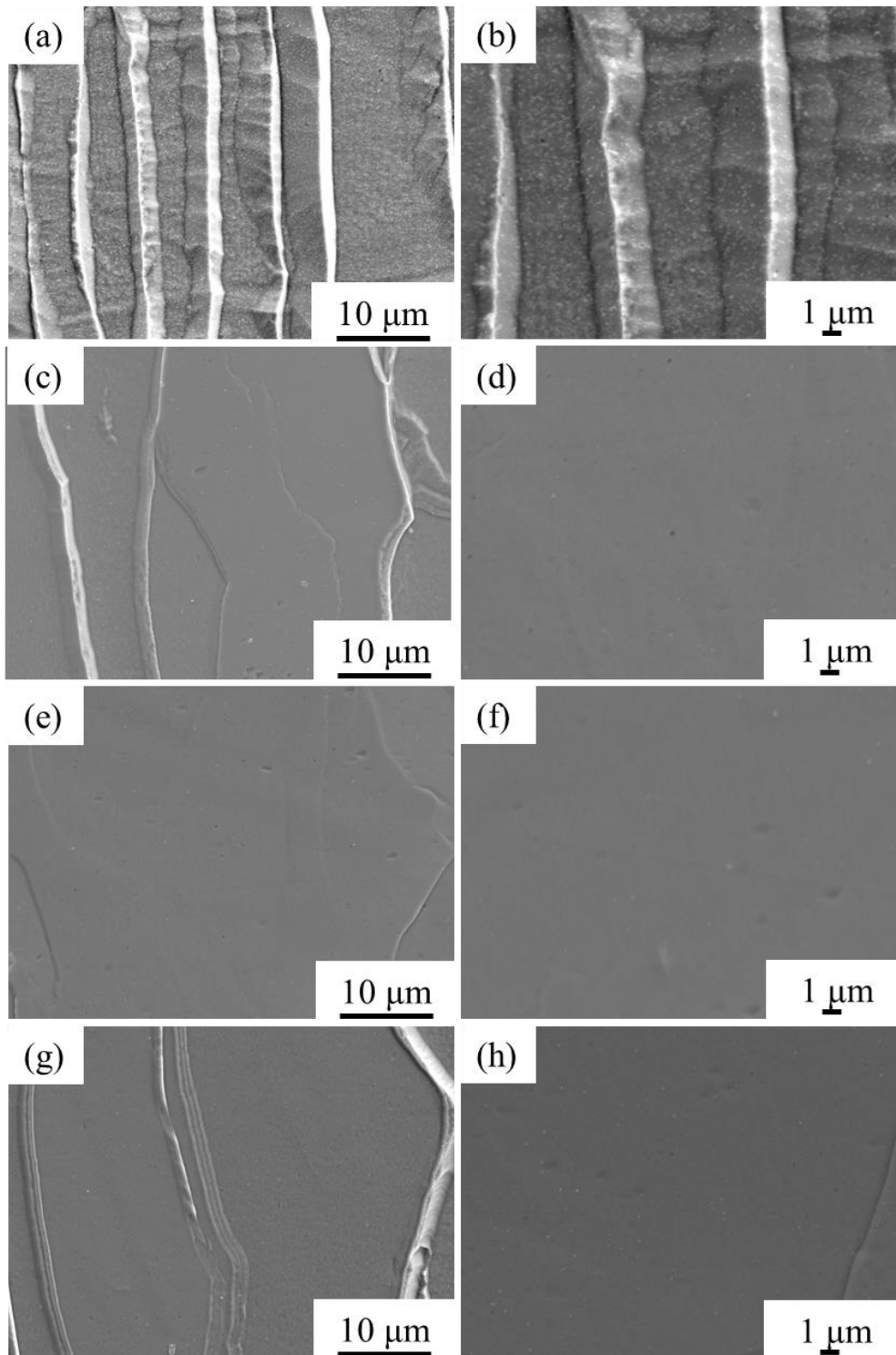


Figure 4.19 Microstructure under the magnification of the SLMed Fe-3wt.%Si specimens observed via SEM after etching: (a-b) SLMed as-built specimen, (c-d) SLMed AT1000/1h specimen, (e-f) SLMed AT1000/3h specimen, (g-h) SLMed AT1000/5h specimen

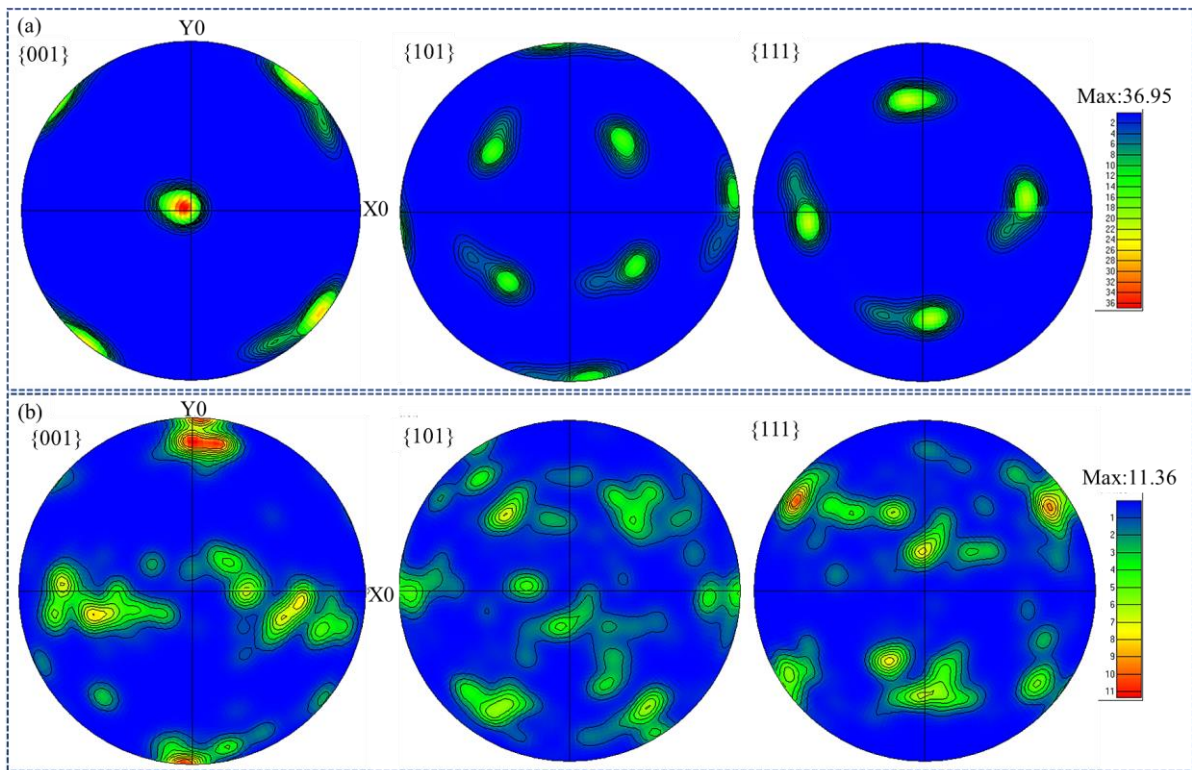


Figure 4.20 The pole figures (PF) after heat treatment of two different planes (a) XY plane, (b) XZ plane

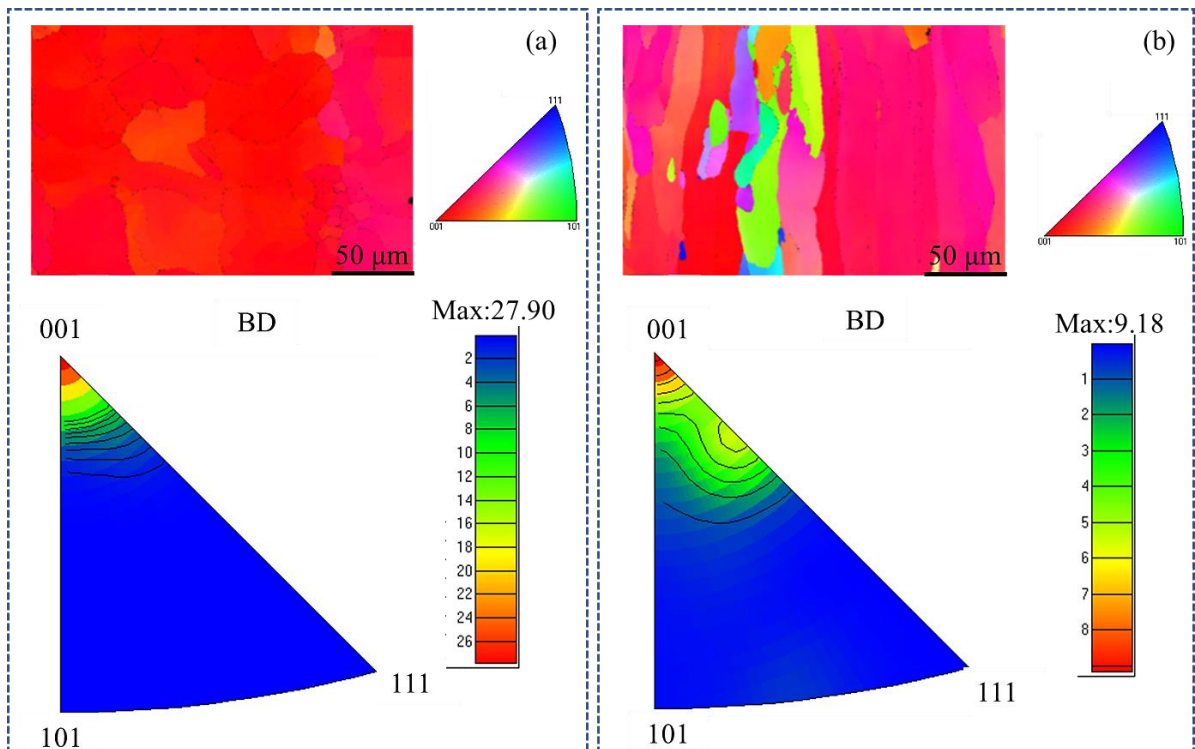


Figure 4.21 EBSD maps and IPFs after heat treatment (a) XY plane, (b) XZ plane

Generally, the residual stresses appear in the as-built sample due to rapid solidification of the melted alloy after laser scanning, also due to the thermal influence of the hot points of the track on colder

regions of the alloy. It led to temperature gradients and different local stresses between laser tracks and manufacturing layers and within one track or layer [33, 34]. Since without significant cracks in the SLMed Fe-3wt.%Si samples, there are no obvious macro stresses in these parts. Additionally, it can be known the SLMed Fe-3wt.%Si is a one-phase alloy according to the XRD analysis, so there are no interphase stresses. Therefore, it is reasonably considered that the stresses in the SLMed Fe-3wt.%Si samples are principally caused by the uneven heat distribution and lattice distortion during the SLM process. These internal stresses together with the wide distribution of the grain size may result in lower magnetic properties. The annealing heat treatments of the SLMed parts were submitted to relieve internal stresses to improve magnetic properties. The XRD spectrogram in Figure 4.22 suggests that the microstructures of the SLM processed samples before and after heat-treatment are characterized by a single bcc-phase. It can be observed that the peaks shift to bigger angles for the heat-treated sample in comparison to the as-built one which indicates partial stress relaxation [15]. The reference XRD patterns for the atomized powder, which is assumed to be stress-free, are also shown and used as a reference. Moreover, it can be observed from the magnified view that the offset angles of AT750/3h, AT850/3h, and AT1000/1h samples are almost the same. The peaks of AT1000/3h shifted more than those three cases, and the peaks of the AT1000/5h sample shifted the most. It is inferred, that within the cases of this work, the stress can be further released with the increase of annealing temperature or the extension of annealing time.

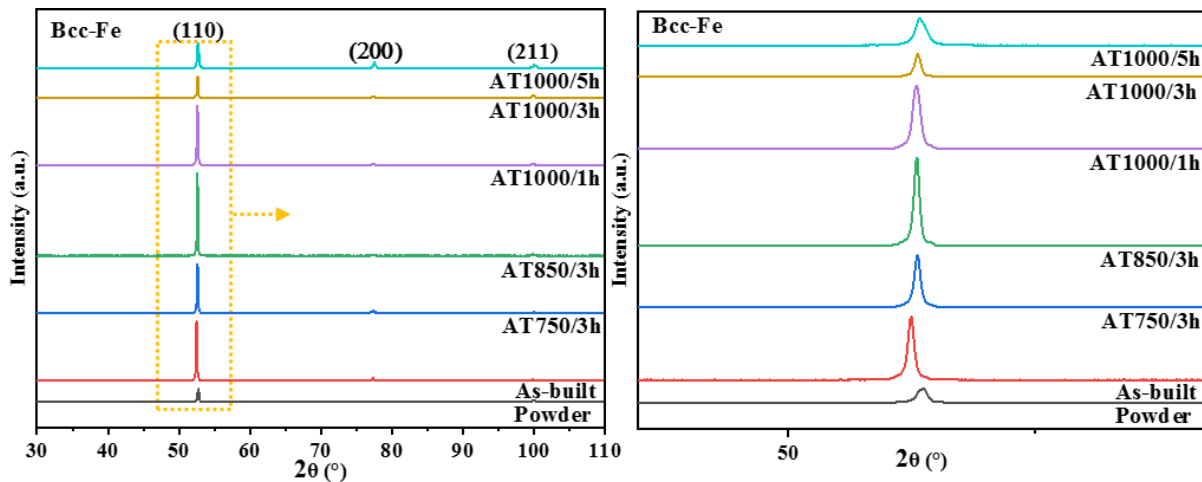


Figure 4.22 XRD analysis of SLMed Fe-3wt.%Si magnets

#### 4.5.2 Magnetic properties after heat treatment

The measured DC hysteresis loops of the SLMed ring specimens with varying heat treatments are presented in Figure 4.23. In addition to the differences in these curves before and after heat treatment, the differences in the curves between the samples that were submitted to different heat treatment conditions can also be identified. The difference of hysteresis loops can be explained in terms of different metallurgical interacting conditions during laser melting such as grain size, defects, and crystallographic texture and their combinations [22]. The evolution of the quasi-static magnetic properties for the as-built and annealed ring samples based on these hysteresis loops are shown in Figure 4.24 and Figure 4.25. The detailed values of these magnetic properties are listed in Table 4.6. In Figure 4.24 (a), for the samples upon annealing at 750 °C for 3 h, 850 °C for 3 h, and 1000 °C for 1 h, the maximum relative permeability ( $\mu_{\max}$ ) of the SLMed ring samples increases slightly. This can be explained by the partial stress relief in these annealing cases. Between AT1000/1h and AT1000/3h, the maximum relative permeability suddenly increases significantly, and this is attributed to both stress relief and grain growth which has been shown in Figure 4.15 (e-f) to occur within this temperature range. It is well known that both stress relief and grain growth reduce the density of lattice defects, having a detrimental effect on the

permeability by acting as pinning sites for the magnetic domain walls and therefore hindering their motion [35, 36]. The value of  $\mu_{\max}$  increases with increasing annealing temperature and dwell time from a value of approximately 1088 in the as-built condition to 2965 after annealing at 1000 °C for 5 h. Figure 4.24 (b) demonstrates that heat treatment decreases coercivity ( $H_c$ ). The decrease in coercivity is evidence of grain growth, as materials with larger grains tend to be easier to magnetize and demagnetize [37, 38]. As mentioned previously in the third chapter, in soft magnetic materials the coarser grain structure is beneficial to their magnetic properties. It can be explained due to higher concentration of grain boundaries for finer grain structure, which acts as pinning sites for the domain walls, and impedes their motion during the magnetization and demagnetization process. Due to the absence of a noticeable recrystallization process and a big number of grains boundaries that remain almost unchanged for the AT750/3h and AT850/3h parts while the partial stress relaxation still results in a comparatively lower coercivity as the as-built sample. Besides, when the annealing temperature was 1000 °C, with the increase in dwell time from 3 h to 5 h, the decrease in coercivity between AT1000/3h and AT1000/5h samples is slight.

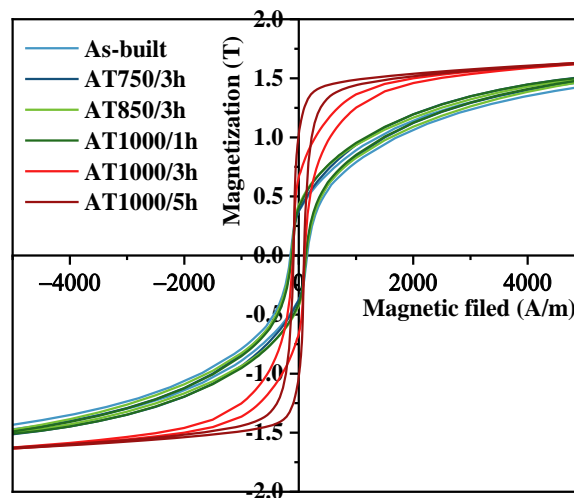


Figure 4.23 The evolution of measured DC hysteresis loops of the SLMed Fe-3wt.%Si ring specimens

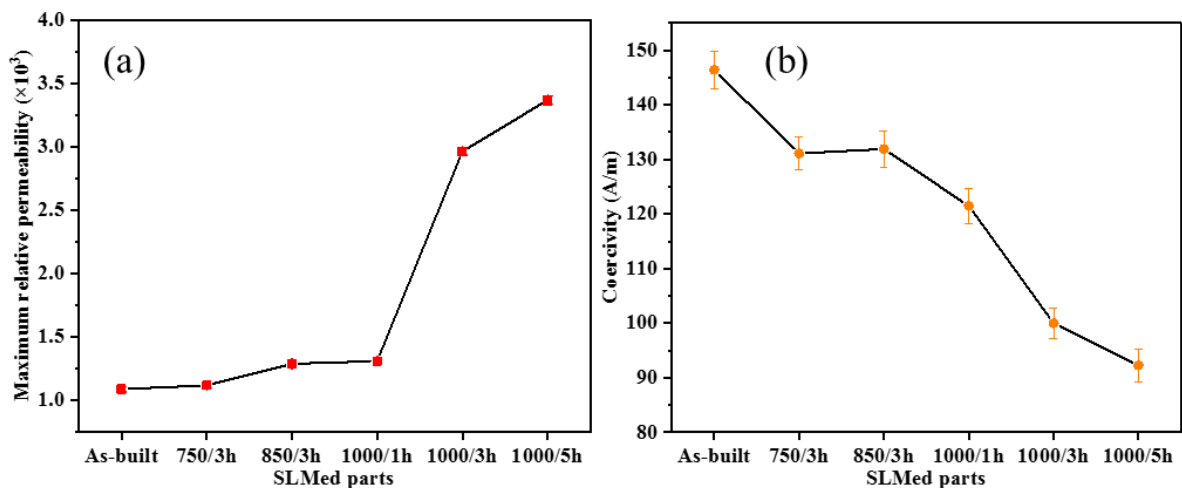


Figure 4.24 (a) The evolution of maximum relative permeability, and (b) the evolution of coercivity for SLMed Fe-3wt.%Si specimens before and after different annealed treatments

The plots in Figure 4.25 (b) show that saturation magnetic induction ( $B_s$ ) increases with annealing temperature and dwell time, from 1.46 T for the as-built sample to 1.64 T after annealing at 1000 °C for 5 h, although the increase in  $B_s$  between different heat-treated samples is slight. But it is also mentioned

that the remanence ( $B_r$ ) increases with the increase in annealing temperature or dwell time. However, considering the increase of  $B_s$ , the increase of  $B_r$  after annealing at 1000 °C for 5 h is acceptable. In fact, the probability of oxidation increases with the increase of annealing temperature or dwell time. It has been pointed out in the report [22] that oxides were found in SLMed Fe-6wt.%Si samples and they are comparatively small, generally <100 nm in diameter, which cannot be detected in XRD analysis or SEM observation results. The oxide particles that cannot be dissolved during annealing are insoluble and would be present during the grain growth process to act as pinning sites. Moreover, such defects would act as pinning sites as well and lead to lower magnetic properties by impeding magnetic domain motion to increase hysteresis loss, but also potentially by increasing electrical resistivity and reducing eddy current loss [39]. It can be also indicated that the appearance of these oxides will also damage the saturation magnetization  $B_s$ , but due to the existence of an external magnetic field in the magnetization process, the domain movement and magnetic moment rotation in the magnetization process can overcome this obstacle with greater potential. Hence, the saturation magnetization can be increased after annealing treatment, which is attributed to the grain growth. The considered applied field of 5000 A/m is strong enough to overcome most of the manufacturing-induced obstacles demagnetization for Fe-6.9wt.%Si, which could be used to further support the above explanation [14]. However, due to the lack of external magnetic field during demagnetization, the domain movement and magnetic moment rotation are strongly hindered, so lower remanence cannot be obtained. Therefore, although oxide particles have not been found in the relevant analysis results of this work due to nano-scale, the appearance is still considered to explain the increase of  $B_r$ .

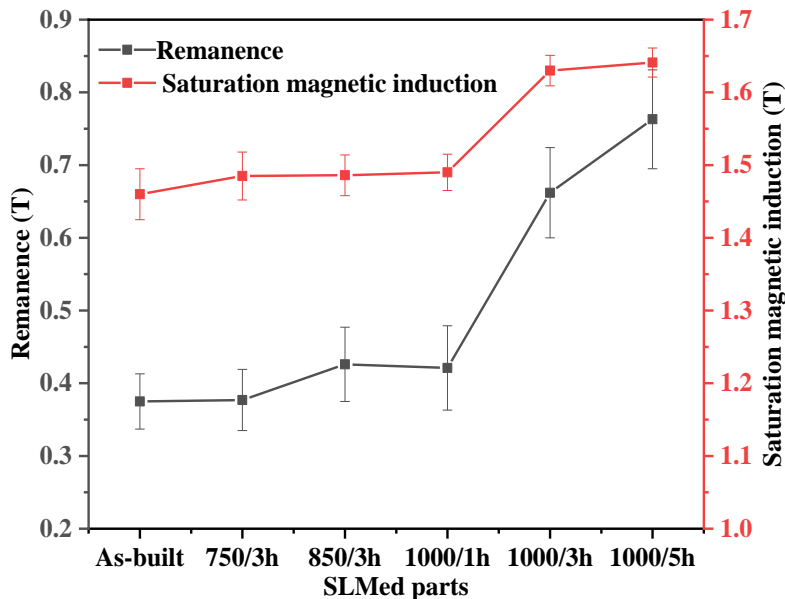


Figure 4.25 The evolution of saturation magnetic induction and remanence for SLMed Fe-3wt.%Si magnets before and after different annealed treatments

The evolution of the power losses ( $P_{50-1}$ ) in dynamic conditions with excitation frequency  $f=50$  Hz and maximum flux density  $B=1$  T for the as-built and annealed ring samples are shown in Figure 4.26. The trend of the total power loss is qualitatively like that of  $H_c$ , suggesting that the eddy current loss component does not increase significantly with grain growth. For those samples upon annealing at 750 °C for 3 h, 850 °C for 3 h, and 1000 °C for 1 h, the power losses of the SLMed samples increase slightly against the as-built sample, which also was related to the partial stress relief and the slight increase of coercivity in these annealing cases. For the AT1000/3h sample, the power losses decrease from 18.8 W/kg for the as-built sample to 13.7 W/kg, although the increase in dwell time from 3 h to 5 h does not further reduce significantly in power losses. It is contributed to both stress relief and

significant grain growth upon annealing at 1000 °C for 3 h. The submitted annealing temperature-time combination of 1000 °C for 3 h reduces the hysteresis loss component without inducing extra dynamic loss. This agrees with the finding that at the same dynamic condition, the grain size of high silicon steels can grow to a coarser size without prompting significant loss associated with increased domain wall displacement speed [14, 40].

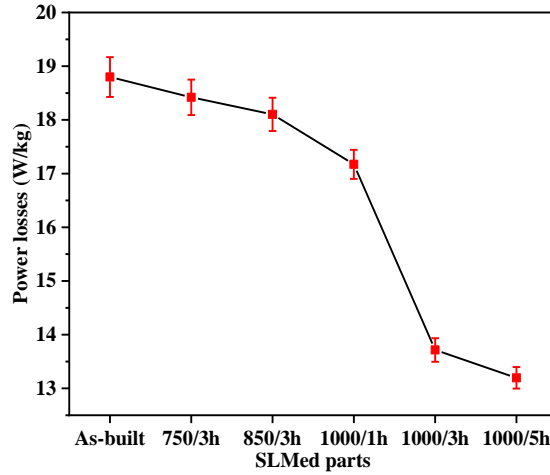


Figure 4.26 The evolution of the power losses in dynamic conditions of SLMed Fe-3wt.%Si magnets before and after different annealed treatments

The detailed average values of the magnetic properties for SLMed Fe-3wt.%Si magnets before and after different annealed treatments are listed in Table 4.6. The evolution of the magnetic properties is consistent with that mentioned previously, after annealing at 750 °C, 850 °C for 3 h, the  $\mu_{\max}$  of SLMed Fe-3wt.%Si magnet has a slight increase. After annealing at 1000 °C for 1 h, the  $\mu_{\max}$  of SLMed Fe-3wt.%Si magnet is about 20% higher than that of before annealing. While after annealing at 1000 °C for 3 h, the  $\mu_{\max}$  of SLMed Fe-3wt.%Si magnet increases from 1088 to 2965, i.e. the  $\mu_{\max}$  of SLMed Fe-3wt.%Si magnet after annealing is about 172.5% higher than that of before annealing. This is undoubtedly significant in promoting the pursuit of high permeability. The  $H_c$  of SLMed Fe-3wt.%Si magnet decreases from 146 A/m for the as-built sample to 100 A/m for AT1000/3h sample, i.e. the  $H_c$  of SLMed Fe-3wt.%Si magnet after annealing at 1000 °C for 3 h is about 31.5% lower than that of before annealing. Similarly, the  $P_{50-1}$  of SLMed Fe-3wt.%Si magnet decreases from 18.8 W/kg for the as-built sample to 13.7 W/kg for AT1000/3h sample, i.e. the  $P_{50-1}$  of SLMed Fe-3wt.%Si magnet after annealing at 1000 °C for 3 h is about 27.1% lower than that of before annealing. This is consistent with the goal of low coercivity and low power losses. Although  $B_s$  and  $B_r$  showed an increasing trend, in general, the comprehensive magnetic properties of SLMed Fe-3wt.%Si magnet have been enhanced by post heat treatment with annealing at 1000 °C for 3 h. It can be attributed to both stress relief and grain growth. When the annealing temperature was 1000 °C, with the increase in dwell time from 3 h to 5 h, the change of magnetic properties between AT1000/3h and AT1000/5h samples is slight. From the economic point of view, annealing at 1000 °C for 3 h is a better choice than annealing at 1000 °C for 5 h.

Table 4.6 The detailed values of magnetic properties for SLMed Fe-3wt.%Si magnets before and after different annealed treatments

SLMed parts	$\mu_{\max} (\times 10^3)$	$H_c$ (A/m)	$B_s$ (T)	$B_r$ (T)	$P_{50-1}$ (W/kg)
As-built	$1.088 \pm 0.02$	$146 \pm 3.5$	$1.460 \pm 0.035$	$0.375 \pm 0.038$	$18.80 \pm 0.37$
AT750/3h	$1.118 \pm 0.22$	$131 \pm 3.0$	$1.485 \pm 0.033$	$0.377 \pm 0.042$	$18.42 \pm 0.33$
AT850/3h	$1.288 \pm 0.23$	$132 \pm 3.3$	$1.486 \pm 0.028$	$0.426 \pm 0.051$	$18.10 \pm 0.31$
AT1000/1h	$1.310 \pm 0.25$	$121 \pm 3.2$	$1.490 \pm 0.025$	$0.421 \pm 0.058$	$17.17 \pm 0.27$

AT1000/3h	$2.965 \pm 0.28$	$100 \pm 2.8$	$1.630 \pm 0.021$	$0.662 \pm 0.062$	$13.72 \pm 0.22$
AT1000/5h	$3.370 \pm 0.32$	$92 \pm 3.1$	$1.641 \pm 0.02$	$0.763 \pm 0.068$	$13.20 \pm 0.20$

## 4.6 Summary

In this chapter, the crystalline texture, and oriented magnetic properties of the SLM produced Fe-3wt.%Si alloy were investigated, the relationship between the texture and magnetic characteristic and their theoretical elaboration was also summarized. The mechanical performances including microhardness, tensile properties were studied in detail. Besides, the effects of heat treatment on the microstructures and magnetic properties of SLM-processed Fe-3wt.%Si alloy samples were evaluated. The following conclusions can be drawn:

- (1) Dense SLMed Fe-3wt.%Si soft magnets with a very low porosity below 0.5% were obtained, it showed an inhomogeneous structure, the microstructure of the SLMed parts exhibited a typical columnar structure with an oriented growth of building direction.
- (2) Only peaks related to the Bcc-Fe phase were observed in the XRD pattern of the as-built samples. The analysis of phase composition from EBSD also confirmed that the Fe-3wt.%Si alloy was a one-phase alloy.
- (3) The SLM-produced Fe-3wt.%Si alloy presented a  $\{100\}\langle 001\rangle$  cubic texture in this study, i.e. a  $\langle 001\rangle$  texture along the BD. Hence, in the construction coordinate system, the three directions of X, Y, and Z are contained in the axis that are easy to be magnetized. Therefore, the SLMed Fe-3wt.%Si magnet had isotropy magnetic properties at these three measured directions (X, Y, and Z).
- (4) Due to the relatively low microhardness, the elongation of the specimen reached 8.8%, the UTS and YS are 562 MPa, 445 MPa, respectively. A mixed-mode of ductile and brittle failure was the dominant rupture mechanism for SLMed Fe-3wt.%Si alloy.
- (5) Annealing the samples at 750 °C and 850 °C for 3 h did not affect the grain size. The micro-segregation of Si was partly dissolved and appears discontinuous, indicating that at those temperatures the diffusion rate is just sufficient to bring Si segregations into solid solution. But upon slow furnace cooling, some of the silicon reseggregated.
- (6) When the annealing temperature reached 1000 °C, although the dwell time was 1 h, in addition to the disappearance of the molten pool boundaries and micro-segregations, a low amount of grain grew to a large size. Annealing conducted at 1000 °C for 3 h, caused instead marked grain growth. The texture of SLMed Fe-3wt.%Si magnet after annealing at 1000 °C for 3 h was the same as that as-built sample,  $\langle 001\rangle$  is still along the BD. This is beneficial to improve the magnetic properties after heat treatment. As the dwell time increased to 5h, by the comparison of the AT1000/3h sample, the grains almost did not grow further significantly.
- (7) Within the cases of this work, the internal stress of the SLMed parts could be relieved by annealing heat treatment, and it can be further released with the increase of annealing temperature or extension of annealing time.
- (8) The magnetic properties of the SLMed Fe-3wt.%Si magnet could be comprehensively enhanced, attributing to grain growth and stress release via submitted annealing appropriate temperature-time combination.

## References of Chapter 4

- [1] C. Coulais, E. Teomy, K. De Reus, Y. Shokef, M. Van Hecke, Combinatorial design of textured mechanical metamaterials, *Nature*, 535 (2016) 529-532.
- [2] H. Le Ferrand, F. Bouville, T.P. Niebel, A.R. Studart, Magnetically assisted slip casting of bioinspired heterogeneous composites, *Nat. Mater.*, 14 (2015) 1172-1179.



- [3] C. Gheorghies, A. Doniga, Evolution of texture in grain oriented silicon steels, *Journal of iron and steel research, international*, 16 (2009) 78-83.
- [4] J. Zou, Y. Gaber, G. Voulazeris, S. Li, L. Vazquez, L.-F. Liu, M.-Y. Yao, Y.-J. Wang, M. Holynski, K. Bongs, Controlling the grain orientation during laser powder bed fusion to tailor the magnetic characteristics in a Ni-Fe based soft magnet, *Acta Mater.*, 158 (2018) 230-238.
- [5] Y. Zhang, C. Esling, J.-S. Lecomte, C. He, X. Zhao, L. Zuo, Grain boundary characteristics and texture formation in a medium carbon steel during its austenitic decomposition in a high magnetic field, *Acta Mater.*, 53 (2005) 5213-5221.
- [6] L. Thijs, K. Kempen, J.-P. Kruth, J. Van Humbeeck, Fine-structured aluminium products with controllable texture by selective laser melting of pre-alloyed AlSi10Mg powder, *Acta Mater.*, 61 (2013) 1809-1819.
- [7] W. Li, Y. Yang, J. Liu, Y. Zhou, M. Li, S. Wen, Q. Wei, C. Yan, Y. Shi, Enhanced nanohardness and new insights into texture evolution and phase transformation of TiAl/TiB<sub>2</sub> in-situ metal matrix composites prepared via selective laser melting, *Acta Mater.*, 136 (2017) 90-104.
- [8] S. Dadbakhsh, B. Vrancken, J.-P. Kruth, J. Luyten, J. Van Humbeeck, Texture and anisotropy in selective laser melting of NiTi alloy, *Mater. Sci. Eng., A*, 650 (2016) 225-232.
- [9] A. Krings, A. Boglietti, A. Cavagnino, S. Sprague, Soft magnetic material status and trends in electric machines, *IEEE Trans. Ind. Electron.*, 64 (2016) 2405-2414.
- [10] A. Krings, M. Cossale, A. Tenconi, J. Soulard, A. Cavagnino, A. Boglietti, Magnetic materials used in electrical machines: A comparison and selection guide for early machine design, *IEEE Ind. Appl. Mag.*, 23 (2017) 21-28.
- [11] J.F. Gieras, *Advancements in electric machines*, Springer Science & Business Media, 2008.
- [12] B. Cheng, S. Shrestha, K. Chou, Stress and deformation evaluations of scanning strategy effect in selective laser melting, *Addit. Manuf.*, 12 (2016) 240-251.
- [13] L. Zhou, W. Tang, L. Ke, W. Guo, J.D. Poplawsky, I.E. Anderson, M.J. Kramer, Microstructural and magnetic property evolution with different heat-treatment conditions in an alnico alloy, *Acta Mater.*, 133 (2017) 73-80.
- [14] M. Garibaldi, I. Ashcroft, J. Lemke, M. Simonelli, R. Hague, Effect of annealing on the microstructure and magnetic properties of soft magnetic Fe-Si produced via laser additive manufacturing, *Scr. Mater.*, 142 (2018) 121-125.
- [15] A. Mazeeva, M. Staritsyn, V. Bobyr, S. Manninen, P. Kuznetsov, V. Klimov, Magnetic properties of Fe-Ni permalloy produced by selective laser melting, *J. Alloys Compd.*, 814 (2020) 152315.
- [16] E. Périgo, J. Jacimovic, F.G. Ferré, L. Scherf, Additive manufacturing of magnetic materials, *Addit. Manuf.*, 30 (2019) 100870.
- [17] D. Jiles, *Introduction to magnetism and magnetic materials*, CRC press, 2015.
- [18] H. Jiao, W. Qiu, W. Xiong, Y. Zhang, F. Fang, G. Cao, C. Li, Y. Yu, Y. Xu, Effect of recrystallization annealing temperature on microstructure, texture and magnetic properties of non-oriented silicon steel produced by strip casting, *Procedia Eng.*, 207 (2017) 2078-2082.
- [19] J. Lemke, M. Simonelli, M. Garibaldi, I. Ashcroft, R. Hague, M. Vedani, R. Wildman, C. Tuck, Calorimetric study and microstructure analysis of the order-disorder phase transformation in silicon steel built by SLM, *J. Alloys Compd.*, 722 (2017) 293-301.
- [20] Y.F. Liang, F. Ye, J. Lin, Y. Wang, G. Chen, Effect of annealing temperature on magnetic properties of cold rolled high silicon steel thin sheet, *J. Alloys Compd.*, 491 (2010) 268-270.
- [21] C. Bacaltchuk, G. Castello-Branco, M. Ebrahimi, H. Garmestani, A. Rollett, Effect of magnetic field applied during secondary annealing on texture and grain size of silicon steel, *Scr. Mater.*, 48 (2003) 1343-1347.
- [22] A. Plotkowski, K. Carver, F. List, J. Pries, Z. Li, A.M. Rossy, D. Leonard, Design and performance of an additively manufactured high-Si transformer core, *Mater. Des.*, 194 (2020) 108894.

- [23] K. Kunze, T. Etter, J. Grässlin, V. Shklover, Texture, anisotropy in microstructure and mechanical properties of IN738LC alloy processed by selective laser melting (SLM), *Mater. Sci. Eng., A*, 620 (2015) 213-222.
- [24] J.A. Dantzig, M. Rappaz, *Solidification: -Revised & Expanded*, EPFL press, 2016.
- [25] S. David, J. Vitek, Correlation between solidification parameters and weld microstructures, *Int. Mater. Rev.*, 34 (1989) 213-245.
- [26] M.M. Attallah, R. Jennings, X. Wang, L.N. Carter, Additive manufacturing of Ni-based superalloys: The outstanding issues, *MRS Bull.*, 41 (2016) 758-764.
- [27] R.C. O'handley, *Modern magnetic materials: principles and applications*, Wiley, 2000.
- [28] C. Robert, O. Handley, *Modern magnetic materials: principles and applications*, Ed. John Wiley & Sons, Inc., New York, (2000) 23.
- [29] H.L. Monaco, G. Artioli, D. Viterbo, G. Ferraris, G. Gilli, G. Zanotti, M. Catti, *Fundamentals of crystallography*, Oxford university press, USA, 2002.
- [30] F. Fiorillo, *Characterization and measurement of magnetic materials*, Academic Press, 2004.
- [31] J. Pan, Y. Wang, Y. Li, Ductile fracture in notched bulk metallic glasses, *Acta Mater.*, 136 (2017) 126-133.
- [32] S. Raghavan, B. Zhang, P. Wang, C.-N. Sun, M.L.S. Nai, T. Li, J. Wei, Effect of different heat treatments on the microstructure and mechanical properties in selective laser melted INCONEL 718 alloy, *Mater. Manuf. Processes*, 32 (2017) 1588-1595.
- [33] D. Gu, C. Ma, M. Xia, D. Dai, Q. Shi, A multiscale understanding of the thermodynamic and kinetic mechanisms of laser additive manufacturing, *Engineering*, 3 (2017) 675-684.
- [34] L. Van Belle, G. Vansteenkiste, J.C. Boyer, Investigation of residual stresses induced during the selective laser melting process, in: *Key Eng. Mater.*, Trans Tech Publ, 2013, pp. 1828-1834.
- [35] H. Hilzinger, The influence of planar defects on the coercive field of hard magnetic materials, *Applied physics*, 12 (1977) 253-260.
- [36] H.R. Hilzinger, Recent advances in rapidly solidified soft magnetic materials, *J. Magn. Magn. Mater.*, 83 (1990) 370-374.
- [37] C.-W. Chen, *Magnetism and metallurgy of soft magnetic materials*, Courier Corporation, 2013.
- [38] R.M. Bozorth, *Ferromagnetism*, 1993.
- [39] P. Jang, B. Lee, G. Choi, Effects of annealing on the magnetic properties of Fe-6.5% Si alloy powder cores, *J. Appl. Phys.*, 103 (2008) 07E743.
- [40] B.D. Cullity, C.D. Graham, *Introduction to magnetic materials*, John Wiley & Sons, 2011.



## Chapter 5 Effects of silicon content on the microstructures and properties of selective laser melted silicon steels

### 5.1 Introduction

The magnetic Fe–Si alloy is usually called silicon steel, which are iron alloys with silicon in different concentrations [1, 2]. The silicon steels represent the most widely used and most cost-effective core materials for devices used in electric power handling [3, 4]. Silicon is a very effective element to improve the soft magnetic properties and increase the electrical resistivity of iron, inspired by decreasing the saturation magnetization and Curie temperature [5-7]. The properties of silicon steels are affected by the silicon content. For Fe-Si alloy, during the SLM process, a complex solidification, grain growth, and phase transformation may occur. The degree of such interplay mainly depends on the silicon composition in the alloy and processing parameters [8, 9]. The effects of parameters have been discussed and described in the previous chapters. This chapter mainly focused on the effects of selected silicon contents.

### 5.2 Materials and methods

The raw material, manufacturing equipment, and partial parameters have been introduced in Chapter 2. In this chapter, silicon steels with silicon contents of 3.5wt.%, 4.5wt.%, 5.5wt.% were fabricated via SLM technique using the optimized parameters given in Chapter 4 in Table 4.1. As illustrated in Figure 3.1 (a) and Figure 3.7 (b), the zigzag scanning pattern with neighboring laser track rotation of 90 ° was utilized during the SLM process, other process parameters were also consistent with those described above. Cubic specimens with dimensions of 8 mm × 8 mm × 8 mm and ring samples of height  $h=4$  mm, external diameter  $d_1=26$  mm, internal diameter  $d_2=18$  mm were manufactured for microstructural observation and magnetic properties measurements respectively. These specimens were annealed at 1000 °C for 3 h in the Ar atmosphere. Besides, standard samples for the tensile test were also fabricated. The samples fabricated by SLM before treatment in the as-built condition are named ‘As-built’. The samples after annealing at 1000 °C for 3 h are referred to AT1000/3h.

As presented in Chapter 2, the OM and SEM devices were applied to observe the microstructures of the SLMed specimens. The phase composition was also performed by XRD equipment. The detailed mechanical tests of as-built specimens were also adopted as mentioned in chapter 2. The quasi-static magnetic properties for the as-built and annealed ring samples were measured by the method of DC magnetic property measurement, and the dynamic magnetic properties of  $P_{50-1}$  were characterized in AC conditions, which were described in detail in Chapter 2.

### 5.3 Evolution of microstructures

It is well known that the magnetic properties and mechanical performance are structurally sensitive properties, which depend on the porosity dramatically [10, 11]. The representative OM images of the microstructures of XZ planes for these three SLMed silicon steels are displayed in Figure 5.1. No obvious cracks are found, although small-sized circular pores are still observed in these SLMed parts. As indicated by the statistical average values in Figure 5.1 (a-c), the porosity after measurement and calculation of each SLMed silicon steel is lower than 0.5%. Figure 5.1 (a-c) reveals the corresponding OM graphs of the microstructures after etching for these different SLMed silicon steels. It can be noted that with the increase of silicon content, the boundary and morphology of the molten pool become more visible and clearer. This is related to the more concentrated micro segregation of silicon at the edge of the molten pool during solidification. Besides, the columnar structure along the BD direction also becomes discontinuous with the increase of silicon content.

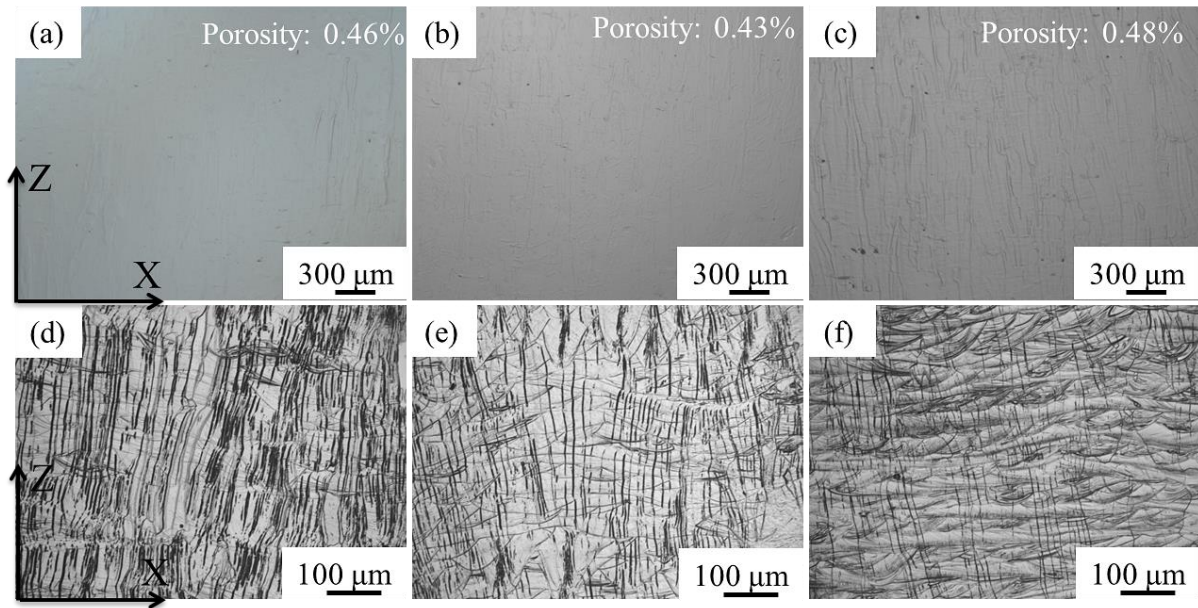


Figure 5.1 The representative OM images of the microstructures of XZ planes without etching for the SLMed silicon steels (a) Fe-3.5wt.%Si, (b) Fe-4.5wt.%Si, (c) Fe-5.5wt.%Si, and after etching (d) Fe-3.5wt.%Si, (e) Fe-4.5wt.%Si, (f) Fe-5.5wt.%Si

To further study the effect of Si content on microstructure, as demonstrated in Figure 5.2 (a-c), the microstructures of XZ planes for SLMed silicon steels under different Si content were observed via SEM. At high magnification, it is significant that the small gray dots as described in Chapter 3 become more concentrated with the increase of silicon content, their size also becomes larger, and the aggregation at the boundary of the molten pool becomes more visible. This indicates that with the increase of silicon content, the micro segregation of silicon in SLMed samples becomes more serious, especially at the boundary of the molten pool.

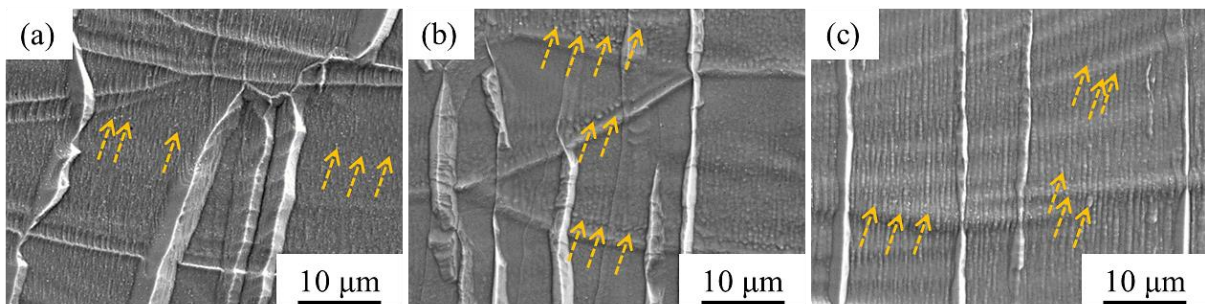


Figure 5.2 The representative SEM images of the microstructures of XZ planes after etching for the SLMed silicon steels (a) Fe-3.5wt.%Si, (b) Fe-4.5wt.%Si, (c) Fe-5.5wt.%Si

Figure 5.12 (a-c) displays the phase compositions of the SLMed silicon steel samples with different Si content. Basically, only the Fe-bcc phase could be detected in the XRD curves of the SLMed silicon steel as-built samples. According to the well-known binary phase diagram of Fe-Si, ordered phases of type DO<sub>3</sub> and B<sub>2</sub> are expected at Si-contents above 4wt.% [12, 13]. The amplified XRD spectra are shown in Figure 5.12 (d-f), which represent a zoom into regions of where super-lattice lines associated with the DO<sub>3</sub> and B<sub>2</sub> phases [14]. Although the amplitude diffraction spectrum of the Fe-4.5wt.%Si and Fe-5.5wt.%Si is almost comparable to the background noise, no significant diffraction peaks were detected in these curves, indicating that no fcc DO<sub>3</sub> and B<sub>2</sub> phases were formed in the SLMed silicon steel specimens. Hence, it also suggests that the very high cooling rate of solidification for the SLM process impedes the formation of these phases.

## 5.4 Evolution of magnetic properties

The measured DC hysteresis loops of three SLMed silicon steels under different Si content are revealed in Figure 5.3. The three hysteresis loops exhibit a typical soft magnetic characteristic with a narrow shape [7, 15]. The certain differences between these three loops should be noted, which can be implied that the differences in magnetic properties in the SLMed silicon steels. To further investigate and described the effects of Si content on the magnetic properties, the evolution of the quasi-static magnetic properties for the different SLMed silicon steel samples based on the hysteresis loops are revealed in Figure 5.4 (a-b). As exhibited in Figure 5.4 (a), it can be overserved that the maximum relative permeability ( $\mu_{\max}$ ) of the SLMed silicon steel increases with the increase of silicon content. The value of the  $\mu_{\max}$  for SLMed Fe-5.5wt.%Si is the highest. Contrary, it also can be noticed that the coercivity ( $H_c$ ) of the SLMed silicon steel decreases with the increase of silicon content. The value of the  $H_c$  for SLMed Fe-5.5wt.%Si is the lowest with 60 A/m. Normally, high anisotropy energy would suppress permeability in a nonoriented polycrystalline material [16]. Besides, high anisotropy increases the domain wall energy density, leading to harder movement of the walls. When the domain walls are harder to move, the coercivity increases, energy is lost in driving the material around a hysteresis loop [12]. More addition of silicon further degrades the magnetic anisotropy constant ( $K$ ) and magnetostriction constants ( $\lambda$ ), which can increase  $\mu_{\max}$  and reduce  $H_c$  of the silicon steel [17, 18]. The evolution of saturation magnetic induction ( $B_s$ ) and remanence ( $B_r$ ) of the different SLMed silicon steels are displayed in Figure 5.4 (b). It can be offered that the  $B_s$  exhibits a slightly decreasing trend while the  $B_r$  of the SLMed silicon steel show an increasing trend when the Si content increase from 3.5wt.% up to 5.5wt.%. With the increase of Si content, the magnetostriction decreases, leading to smaller dimensional changes with magnetization and demagnetization, and lower stress-sensitivity of magnetic properties [19]. Thus, the  $B_s$  decrease with the increase of Si content.

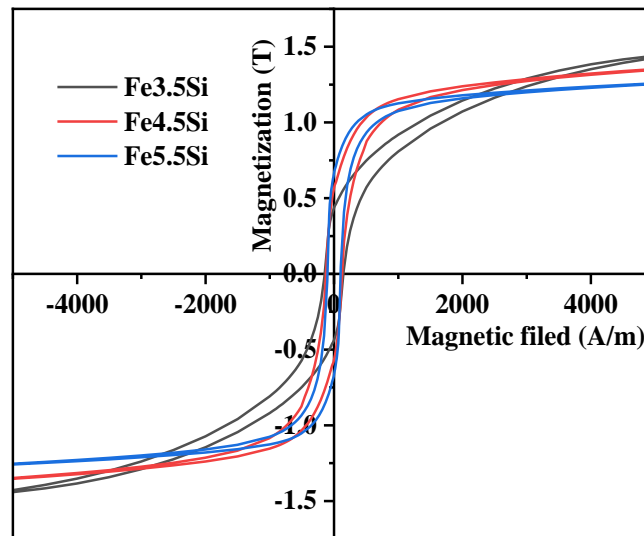


Figure 5.3 The DC hysteresis loops of three SLMed silicon steels under different Si content

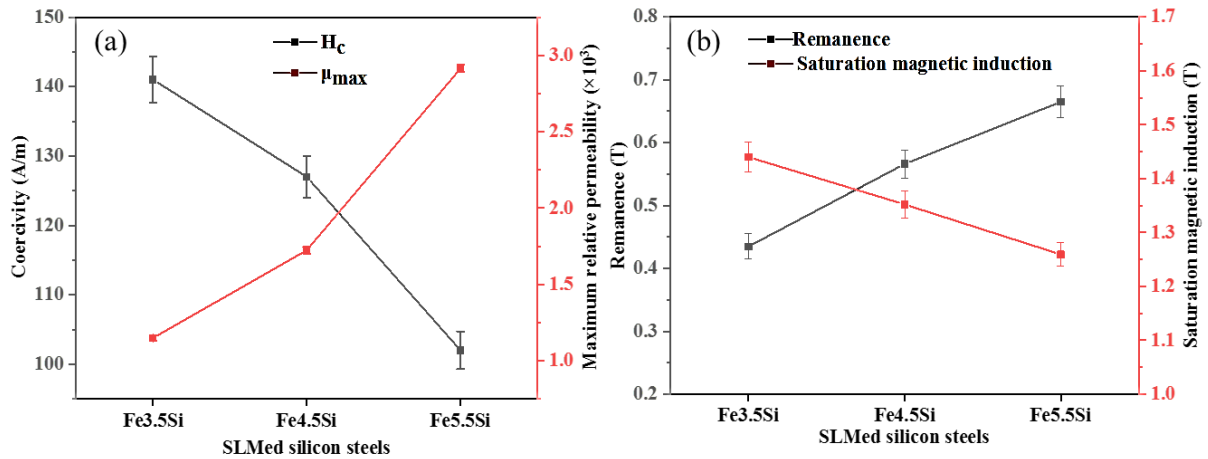


Figure 5.4 The evolution of DC magnetic properties for three SLMed silicon steels under different Si content

The evolution of the power losses ( $P_{50-1}$ ) in dynamic conditions is presented in Figure 5.5. Note that the  $P_{50-1}$  of the SLMed silicon steel decreases with the increase of Si content. Theoretically, since there is no free electron in the silicon crystal, its conductivity is lower than that of metal, the addition of silicon can reduce the conductivity and increase the electrical resistivity of the alloy [20, 21]. Also, the electrical resistivity and the magnetostriction constants  $\lambda$  decrease with the increase of silicon content, as a result, the eddy current loss also decreases with the increase of silicon content. The detailed corresponding average values of all measured DC magnetic properties and AC magnetic properties of the SLMed silicon steels are listed in Table 5.1. The changes of these average values in the table are consistent with those shown in the previous hysteresis loops.

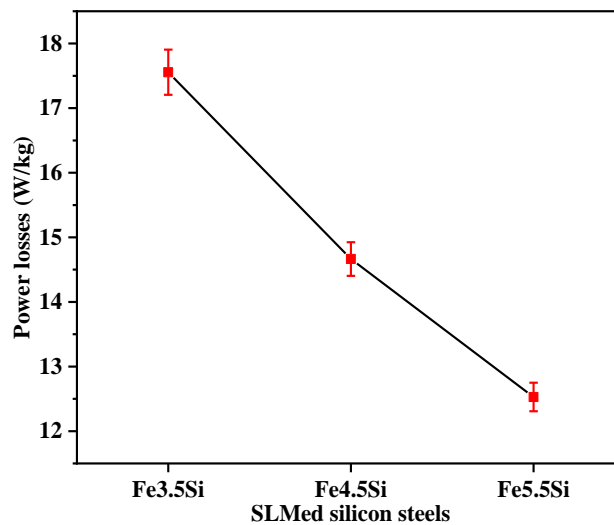


Figure 5.5 The evolution of AC power losses for three SLMed silicon steels under different Si content

The detailed average values of the magnetic properties for three types of SLMed silicon steels are listed in Table 5.1. The evolution of the magnetic properties is consistent with that mentioned previously, the  $\mu_{max}$  of SLMed Fe-4.5wt.%Si silicon steel is about 51.6% higher than that of SLMed Fe-3.5wt.%Si silicon steel, the  $\mu_{max}$  of SLMed Fe-5.5wt.%Si silicon steel is about 69.0% higher than that of SLMed Fe-4.5wt.%Si silicon steel. The  $H_c$  of SLMed Fe-4.5wt.%Si silicon is about 10.0% lower than that of SLMed Fe-3.5wt.%Si silicon steel, the  $H_c$  of SLMed Fe-5.5wt.%Si silicon steel is about 19.7% lower than that of SLMed Fe-4.5wt.%Si silicon steel. The evolution of  $\mu_{max}$  and  $H_c$  is related to more addition of silicon further degrades the magnetic anisotropy constant  $K$  and magnetostriction constants  $\lambda$ , which can increase  $\mu_{max}$  and reduce  $H_c$  of the silicon steel. Similarly, the  $P_{50-1}$  of decreases from 17.56 W/kg

for SLMed Fe-4.5wt.%Si silicon steel to 14.66 W/kg for Fe-5.5wt.%Si silicon steel, i.e. the  $P_{50-1}$  of SLMed Fe-4.5wt.%Si silicon steel is about 16.5% lower than that of SLMed Fe-3.5wt.%Si silicon steel. The  $P_{50-1}$  of SLMed Fe-5.5wt.%Si silicon steel is about 14.5% lower than that of SLMed Fe-4.5wt.%Si silicon steel. These are consistent with the goal of low coercivity and low power losses. However, due to the increase of Si content, the magnetostriction decreases, leading to smaller dimensional changes with magnetization and demagnetization, and lower stress-sensitivity of magnetic properties. Thus, it is noticed that the  $B_s$  showed a decreasing trend.

Table 5.1 The detailed average values of all measured DC magnetic properties and AC magnetic properties of the SLMed silicon steels

SLMed parts	$\mu_{\max}$ ( $\times 10^3$ )	$H_c$ (A/m)	$B_s$ (T)	$B_r$ (T)	$P_{50-1}$ (W/kg)
Fe-3.5wt.%Si	$1.149 \pm 0.02$	$141 \pm 3.3$	$1.440 \pm 0.028$	$0.435 \pm 0.025$	$17.56 \pm 0.35$
Fe-4.5wt.%Si	$1.724 \pm 0.22$	$127 \pm 3.0$	$1.352 \pm 0.025$	$0.377 \pm 0.020$	$14.66 \pm 0.26$
Fe-5.5wt.%Si	$2.914 \pm 0.25$	$102 \pm 2.7$	$1.259 \pm 0.025$	$0.426 \pm 0.022$	$12.53 \pm 0.31$

## 5.5 Mechanical properties

### 5.5.1 Microhardness

Hardness is one of the basic mechanical properties of metallic materials, which has a sensitive correlation with other mechanical properties [22]. To understand the impacts of Si content on the microhardness of SLMed silicon steel, Figure 5.6 displays the average values of microhardness including XY planes and XZ planes of the SLMed silicon steel parts with different Si content. It shows that the values of microhardness for these two planes are almost similar, both increase with the evolution of Si content. The average values of microhardness increase from  $275.5 \pm 3.5$  HV<sub>0.1</sub> to  $371.5 \pm 4.5$  HV<sub>0.1</sub>. Due to silicon having a strong solid solution strengthening effect on a-Fe (bcc), resulting in a higher microhardness and strength [23, 24].

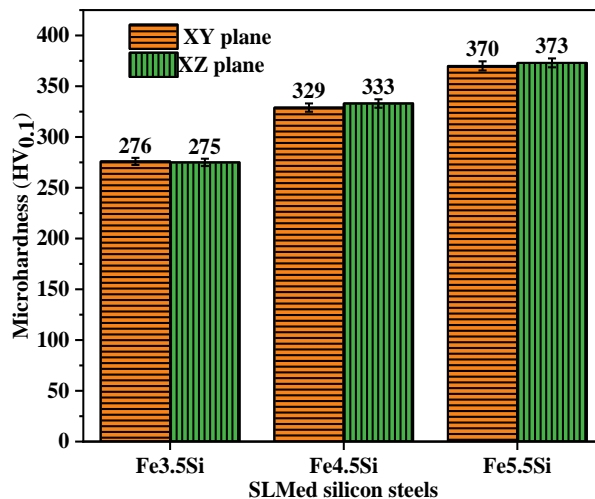


Figure 5.6 The average values of microhardness including XY planes and XZ planes of the SLMed silicon steel parts with different Si content

### 5.5.2 Tensile properties

Figure 5.7 shows the typical stress strain curves of the different SLMed silicon steels. The statistical data regarding the mechanical properties including ultimate tensile strength (UTS), yield strength (YS), and elongation at break (EL) of the SLMed silicon steels are listed in Table 5.2. It revealed that the SLMed Fe-5.5wt.%Si silicon steel was fractured at the earliest stages among these three SLMed parts, having the highest average UTS value of 684 MPa, and the lowest EL of 1.5%. The SLMed Fe-3.5wt.%Si was fractured at a later stage than that of Fe-4.5wt.%Si silicon steel, having a lower average



UTS value of 586 MPa, and the highest EL of 3.6%. These are also reflected in the D-value between their UTS and YS. The D-value between the UTS and YS of SLMed Fe-3.5wt.%Si is only 18MPa, while the D-value between the UTS and YS of Fe-5.5wt.%Si reaches 70MPa. The UTS and YS of the SLMed silicon steels increase with the increase of silicon content, but the elongation also decreases. It suggests that the increase of Si content has a positive effect on the strength while damaging the ductility of the SLMed silicon steel. These changes in tensile properties are associated with the evolution of the microhardness of the SLMed silicon steels, which is attributed to the stronger solid solution strengthening that is created by higher silicon content.

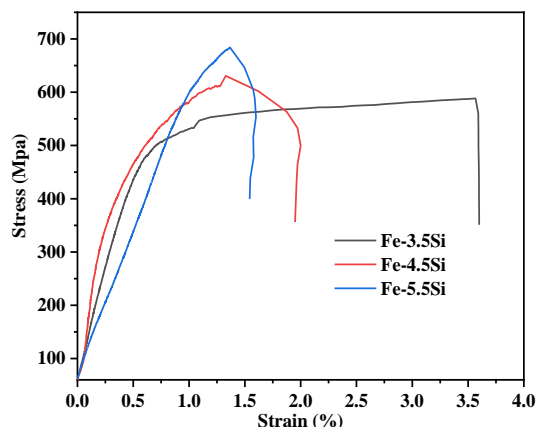


Figure 5.7 The stress strain curves of the different SLMed silicon steels

Table 5.2 The statistical values regarding the mechanical properties of the SLMed silicon steels

SLMed parts	UTS (MPa)	YS (MPa)	EL (%)
Fe-3.5wt.%Si silicon steel	586 ± 5.5	568 ± 5.3	3.6 ± 0.2
Fe-4.5wt.%Si silicon steel	630 ± 5.8	601 ± 5.5	2.0 ± 0.1
Fe-5.5wt.%Si silicon steel	684 ± 6.0	614 ± 5.8	1.5 ± 0.1

To further study and better understand the effects of Si silicon on fracture mechanisms of the SLMed silicon steels, the fracture surface morphologies were examined by an SEM system. As given in Figure 5.8 (a) and Figure 5.8 (b), in the representative fracture surface of the SLMed Fe-3.5wt.%Si and SLMed Fe-4.5wt.%Si specimen, only very slightly “necking phenomenon” which was indicated by yellow arrows can be observed, while no “necking phenomenon” can be found almost in the representative fracture surface of the SLMed Fe-5.5wt.%Si silicon steel as illustrated in Figure 5.8 (c). Stair-like and layered-cracks (as marked by red arrows) can be also observed. In the corresponding enlarged-view images Figure 5.8 (b-c), an intergranular rough (dimpled) fracture can be detected. Although this dimpled-like fracture suggests that slight ductile deformation occurs during the tensile process, brittle fracture still should be determined as the dominant fracture mechanism of the SLMed Fe-3.5wt.%Si silicon steel. Besides, in the fracture surfaces at enlarged-view of the SLMed Fe-4.5wt.%Si and SLMed Fe-5.5wt.%Si silicon steels as displayed in Figure 5.8 (e-f) and Figure 5.8 (h-i), respectively, the fractures appear faceted with “river patterns” of radiating lines (as indicated by orange arrows) under micro-scale. They are caused by a mechanism known as cleavage which is a typical characteristic of the brittle fracture mechanism [25], which can be believed reasonable that the brittle fracture mechanism is also the dominant fracture mechanism of the SLMed Fe-4.5wt.%Si and SLMed Fe-5.5wt.%Si silicon steels. In the SLMed Fe-4.5wt.%Si and SLMed Fe-5.5wt.%Si silicon steels with columnar crystal structure, the tensile direction in the present case is almost perpendicular to the grain boundaries of columnar crystals. The tensile force made the whole columnar crystals were fractured after slight deformation in the way of transgranular, as such, the fracture surface usually cut through the columnar grains in a transgranular manner, leading to a river pattern [26, 27]. Although the brittle

fracture surfaces of three SLMed silicon steels are exhibit characteristics with brittle fracture mechanisms. It can be noted that from Figure 5.8, the fracture surface becomes flattered without dimple with the increase of silicon content, which further indicates that the ductility of SLMed silicon steel becomes worse with the increase of silicon content in the present case.

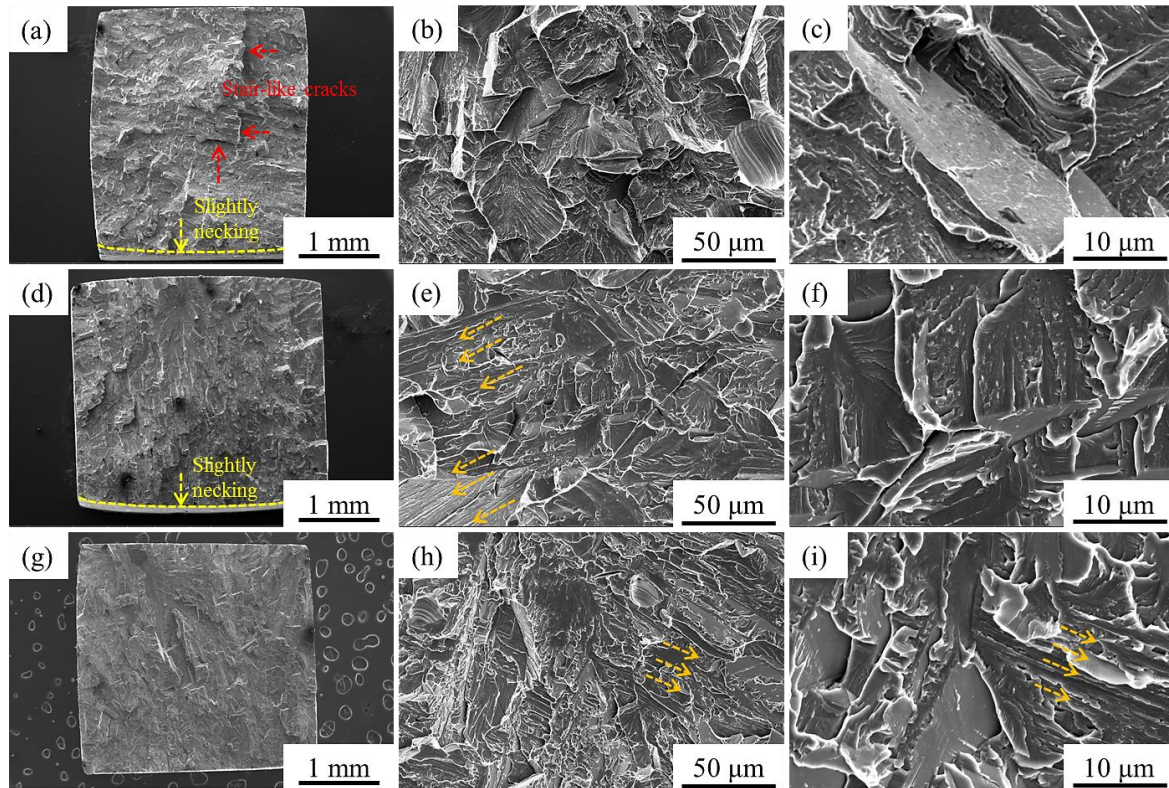


Figure 5.8 Fracture morphology of the SLMed silicon steel samples under different Si content observed using SEM: (a-c) SLMed Fe-3.5wt.%Si silicon steel, (d-f) SLMed Fe-4.5wt.%Si silicon steel, (g-i) SLMed Fe-5.5wt.%Si silicon steel

## 5.6 Effect of post-treatment on microstructure and magnetic properties

### 5.6.1 Microstructural evolution after heat treatment

To better understand the effects of the heat-treatment on the microstructures of the SLMed silicon steels under different Si content, the SEM images of the corresponding microstructures in XZ planes are displayed in Figure 5.9 to Figure 5.11 (the observed magnification enlarged from left to right). It can be observed that for the microstructures of all three types of the SLMed silicon steels before and after heat treatment, along the BD the grains are columnar and can span several hundred microns owing to the grain-remelting/epitaxial growth mechanism. At the same time, at lower magnification, it can be found that after annealing at 1000 for 3 h, the grain size of all the SLMed silicon steel samples increased noticeably due to the recrystallization. The microstructures are still characterized by non-uniform grain size, suggesting that the recrystallization process is not complete. The SEM micrographs also show that annealing at 1000 °C also for 3 h led to the complete dissolution of SLM-induced structure, i.e., the cells and molten pool segregations entered solid solution [28, 29]. The complete disappearance of the molten pool boundary lines is likely related to the dissolution of Si in the solid [30, 31]. The enlarged magnification observation indicates the micro-segregation and inhomogeneous distribution of Si are invisible, suggesting the dissolution of Si in the solid is almost complete.

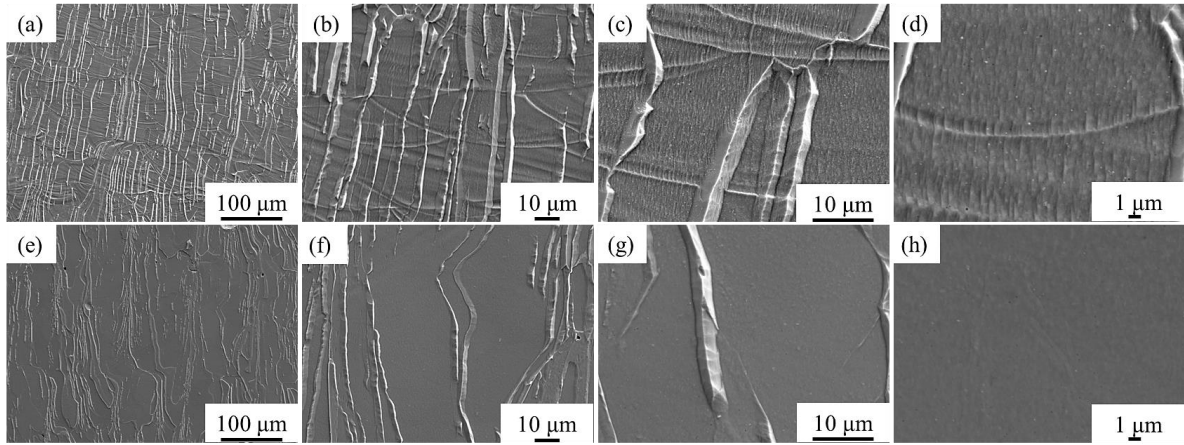


Figure 5.9 Microstructure of the SLMed Fe-3.5wt.%Si samples observed via SEM after etching: (a-d) as-built sample, (e-h) AT1000/3h sample

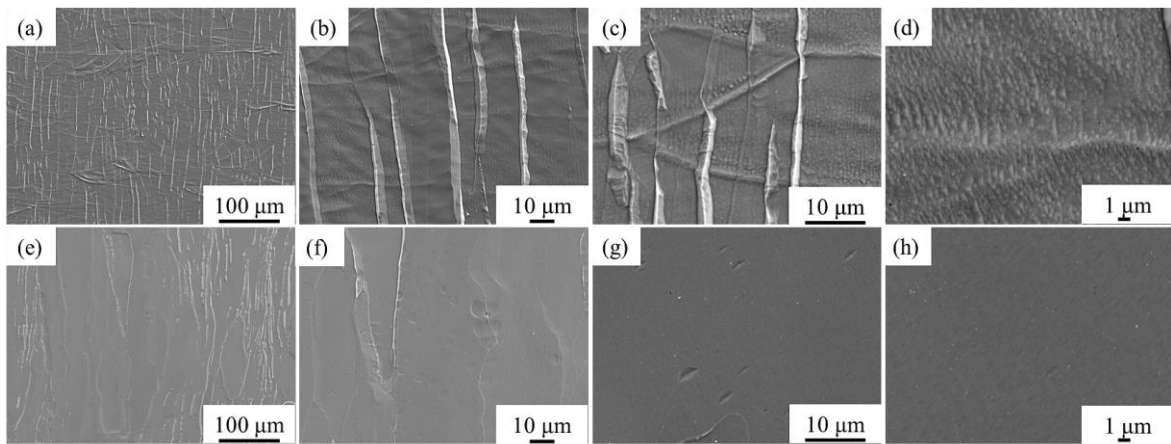


Figure 5.10 Microstructure of the SLMed Fe-4.5wt.%Si samples observed via SEM after etching: (a-d) as-built samples, (e-h) AT1000/3h samples

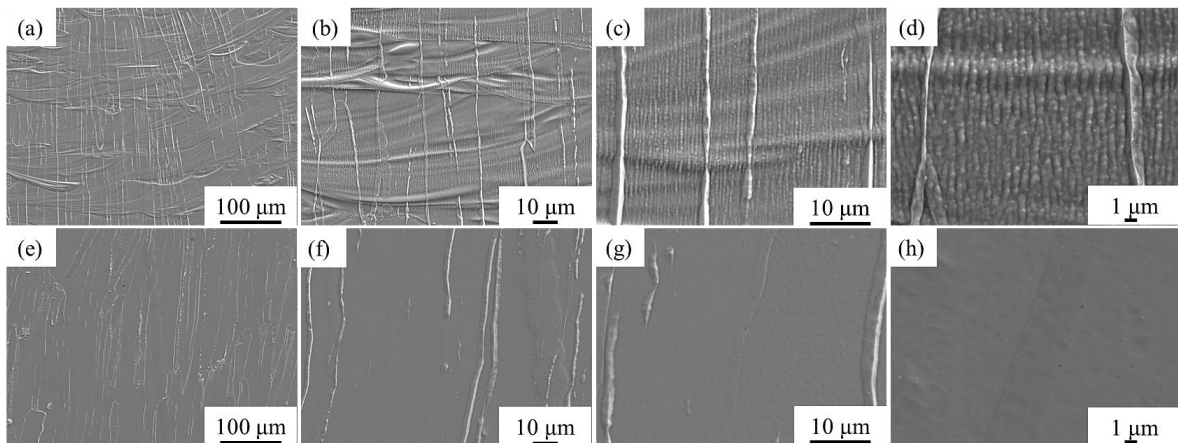


Figure 5.11 Microstructure of the SLMed Fe-5.5wt.%Si samples observed via SEM after etching: (a-d) as-built samples, (e-h) AT1000/3h samples

The XRD spectra in Figure 5.12 (a-c) suggests that the microstructures of both the SLMed as-built and annealed samples for three types of silicon steels are characterized by a single bcc-phase (Fe-bcc). From the binary phase diagram of Fe-Si, it is well-known that the ordered phases of type  $DO_3/B_2$  would be presented at Si-contents above about 4wt.% under general conditions are expected at Si-contents above. As the enlarged XRD spectra of the SLMed Fe-4.5wt.%Si and Fe-5.5wt.%Si in Figure 5.12 (e-

f), can be represented the regions of the diffraction spectrum where super-lattice lines associated with  $DO_3/B_2$  are expected [12, 14]. No significant super-lattice peaks corresponding to the phases ordering of type  $DO_3/B_2$  are detected in these XRD spectrums, which suggests that the disorder-ordered transformation from disorder phase  $A_2$  to short-range ordered  $B_2$  or  $DO_3$  phases did not occur or no significantly during the annealing. While it is not established how the ordered domains affect the electrical/magnetic properties of the alloy, it is well known that ordering increases the hardness and hence the brittleness of the material, reducing drastically its ductility and workability [1, 32, 33]. While more amplitude that is comparable to the background noise is found in the annealed AT1000/3h samples, which might be caused by the fine oxide and carbide particles that can be attributed to the leak of air into the argon furnace from the surrounding environment during heat-treatment. Besides, it can be observed that the peaks shift to the bigger angles for the annealed sample in comparison to the as-built one, which suggests micro-stress relief after annealing for three types of silicon steels [34, 35].

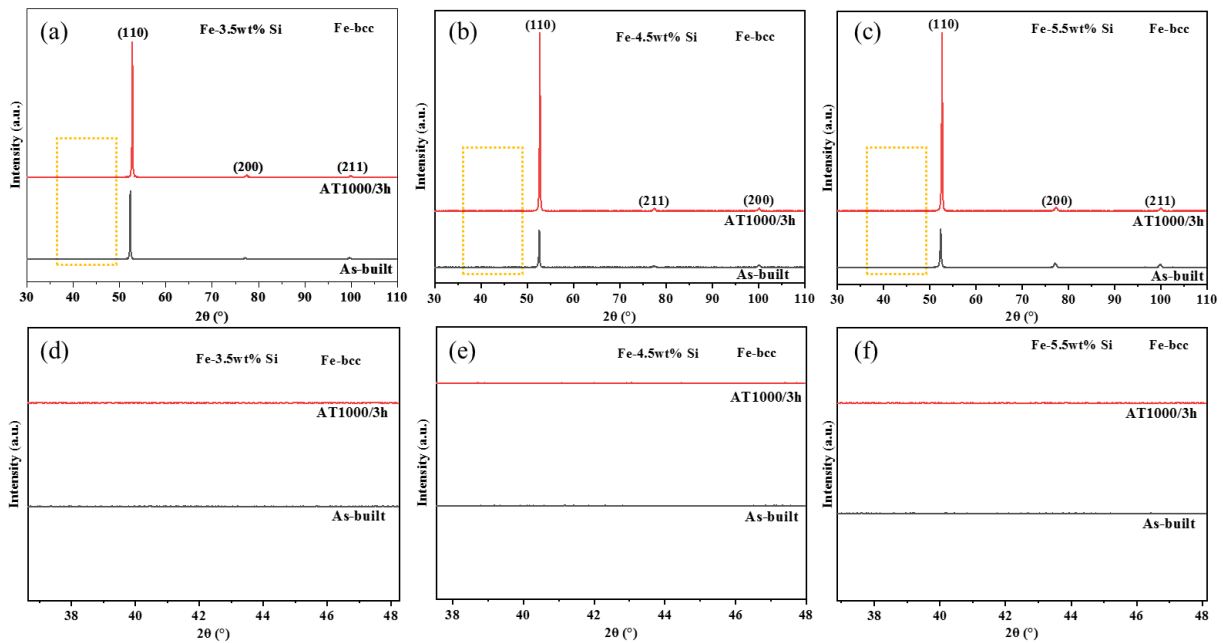


Figure 5.12 XRD spectra of the SLMed as-built samples and AT1000/3h samples

### 5.6.2 Magnetic properties after heat treatment

The measured DC hysteresis loops of three types of SLMed silicon steels before and after annealed heat treatment are plotted in Figure 5.13 (a-c). It can be found that the significant differences in the loop shape before and after annealed heat treatment are presented in all of the silicon steels, which indicates that the corresponding DC magnetic properties also change accordingly [36]. Obviously, annealed heat treatment has a positive effect on the DC magnetic properties of the silicon steels according to the hysteresis loops of the AT1000/3h samples are narrower than that of as-built samples. The change can be mainly attributed to the evolution of microstructures and stress relief after annealing.

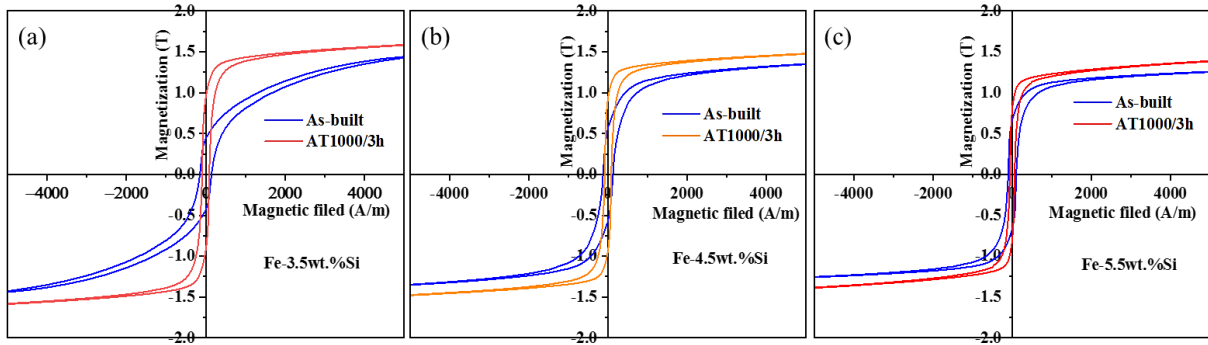


Figure 5.13 The measured DC hysteresis loops of three types of SLMed silicon steels (a) Fe-3.5wt.%Si, (b) Fe-4.5wt.%Si, (c) Fe-5.5wt.%Si

The evolution of the corresponding measured DC magnetic properties based on the DC hysteresis loops are displayed in Figure 5.14 (a-b) and Figure 5.15 (a-b). The detailed average values of these magnetic properties for the samples after annealing at 1000 °C for 3 h are also listed in Table 5.3, the evolution of the  $\mu_{\max}$  of the different SLMed silicon steel samples before and after annealing is demonstrated in Figure 5.14 (a). It shows the  $\mu_{\max}$  of all three SLMed silicon steels increase significantly after annealing. Especially, for SLMed Fe-3.5wt.%Si, the  $\mu_{\max}$  increase from  $1.149 \times 10^3$  to  $3.580 \times 10^3$ , it's more than tripled higher. For the coercivity  $H_c$ , a lower value is expected generally. As revealed in Figure 5.14 (b), the  $H_c$  of AT1000/3h samples is lower noticeably than that of as-built samples. After annealing at 1000 °C for 3 h, the  $H_c$  of these three SLMed silicon steels decreases from 141, 127, 102 m/A to 90, 78, 60 m/A, which are about 36.2%, 38.6%, 41.2% lower than that of before annealing, respectively. Besides, the  $B_s$  also increase as expected, which is presented in Figure 5.15 (a). The improvement of DC magnetic properties after annealed heat treatment as described above can be attributed to grain growth and micro stress relief. It is noted that the  $B_r$  also increases with the increase of  $B_s$  (Figure 5.15 (b)), which might be associated with the fine oxide and carbide particles produced due to the leak of air into the argon furnace from the surrounding environment during annealing.

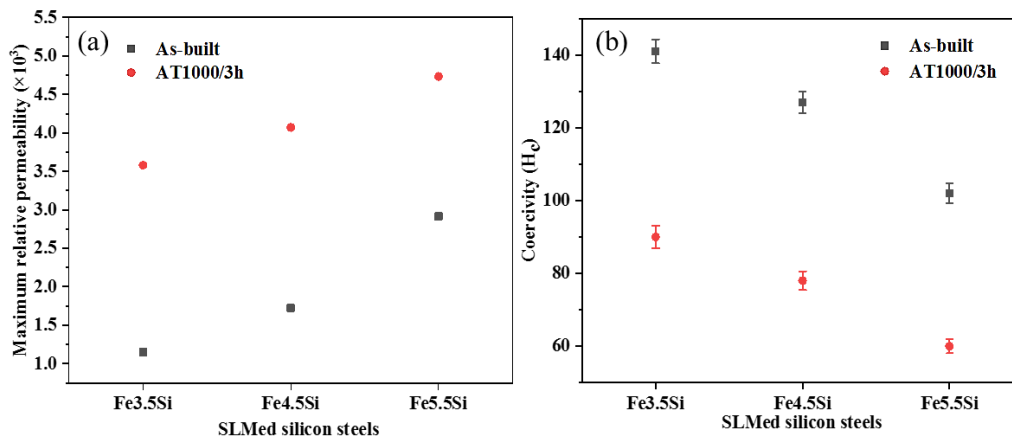


Figure 5.14 The evolution of the (a)  $\mu_{\max}$ , (b)  $H_c$  of the different SLMed silicon steel samples before and after annealing

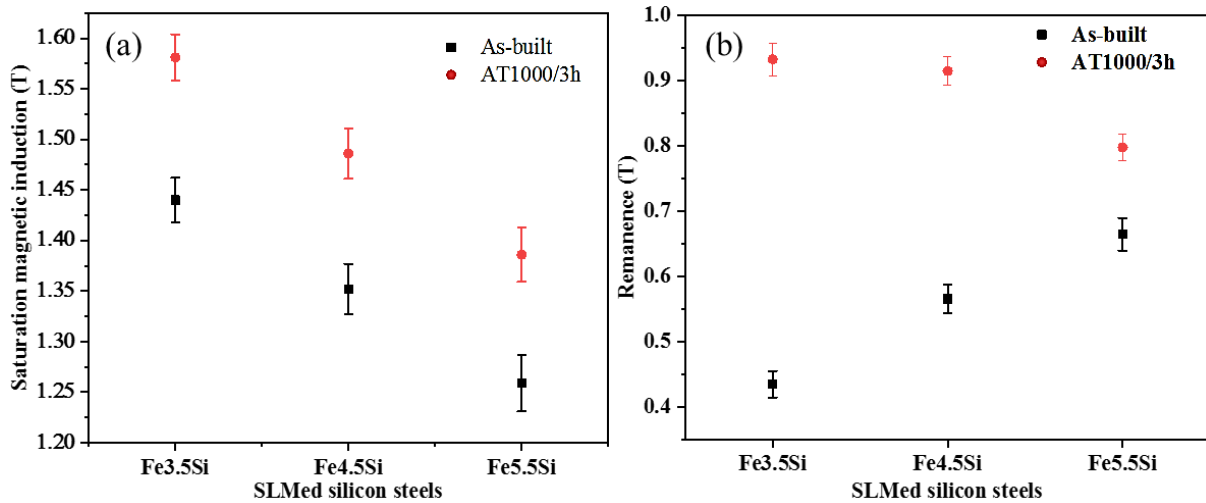


Figure 5.15 The evolution of the (a)  $B_s$ , (b)  $B_r$  of the different SLMed silicon steel samples before and after annealing

The evolution of the power losses  $P_{50-1}$  in dynamic conditions is summarized in Figure 5.16, the AT1000/3h samples show lower power losses than the as-built samples. Combined with the detailed average in Figure 5.1 and Table 5.3, the  $P_{50-1}$  decreases from 17.56, 14.66, 12.53 W/kg to 12.88, 10.03, 8.73 W/kg, respectively. The  $P_{50-1}$  of the Fe-3.5wt.%Si annealed sample is about 26.7% lower than that of the as-built sample. For Fe-4.5wt.%Si and Fe-5.5wt.%Si, the  $P_{50-1}$  of AT1000/3h samples are 31.6% and 30.3% lower than that of as-built samples, respectively. It is also contributed to both stress relief and significant grain growth upon annealing at 1000 °C for 3 h.

In conclusion, after annealing at 1000 °C for 3 h, the microstructures of three present SLMed silicon steels under different Si content exhibit similar evolution with grain growth and stress relief. Therefore, their comprehensive magnetic properties are also improved. It can be believed that the annealing behavior is not dramatically altered by variations in alloy chemistry of Si content.

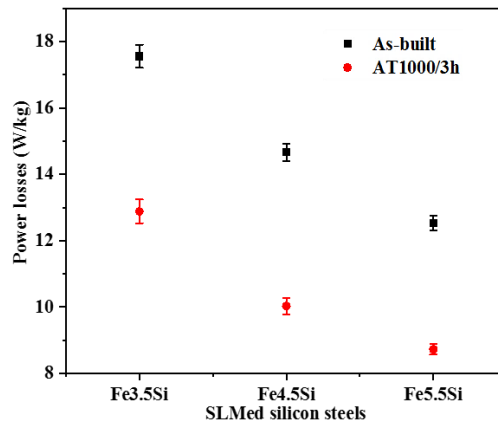


Figure 5.16 The evolution of the power losses  $P_{50-1}$  in dynamic conditions

Table 5.3 The detailed average values of these magnetic properties for the SLMed samples after annealing at 1000 for 3 h

SLMed parts	$\mu_{\max} (\times 10^3)$	$H_c$ (A/m)	$B_s$ (T)	$B_r$ (T)	$P_{50-1}$ (W/kg)
Fe-3.5wt.%Si	$3.580 \pm 0.03$	$90 \pm 3.1$	$1.581 \pm 0.027$	$0.933 \pm 0.051$	$12.88 \pm 0.36$
Fe-4.5wt.%Si	$4.072 \pm 0.03$	$78 \pm 2.6$	$1.486 \pm 0.025$	$0.915 \pm 0.042$	$10.03 \pm 0.24$
Fe-5.5wt.%Si	$4.732 \pm 0.35$	$60 \pm 2.0$	$1.386 \pm 0.023$	$0.798 \pm 0.038$	$8.73 \pm 0.16$

## 5.7 Summary

In this chapter, three pre-alloyed powders with different Si content were applied to fabricate the silicon steels using the SLM technique. The effects of Si content on the microstructure evolution, phase composition, mechanical properties, and magnetic properties of SLMed silicon steels were examined in terms of OM, SEM, XRD analysis, and magnetic properties testing. The influence of post-annealing treatment on the microstructures, and DC, AC magnetic properties were also investigated and summarized in detail. The main conclusions can be drawn and are described in the following:

- (1) The average porosity of each SLMed silicon steel was lower than 0.5% with a few small-sized circular pores but without obvious cracks. With the increase of silicon content, the microsegregation of silicon in SLMed samples became more serious, especially at the boundary of the molten pool.
- (2) The SLMed silicon steels exhibited typical soft magnetic characteristics. The  $\mu_{\max}$  of the SLMed silicon steel increased with the increase of silicon content. Both coercivity  $H_c$  and power losses  $P_{50-1}$  of the SLMed silicon steel decreased with the increase of silicon content. The value of the  $H_c$  and  $P_{50-1}$  for SLMed Fe-5.5wt.%Si are the lowest with 102 A/m and 12.53 W/kg, respectively. The  $B_s$  exhibited a slightly decreasing trend while the  $B_r$  of the SLMed silicon steel showed an increasing trend when the Si content increased from 3.5wt.% up to 5.5wt.%.
- (3) The microhardness increased with the evolution of Si content, increased from 275.5 HV<sub>0.1</sub> to 371.5 HV<sub>0.1</sub>, which is attributed to higher Si content having a stronger solid solution strengthening effect in the silicon steel.
- (4) The SLMed Fe-5.5wt.%Si silicon steel had the highest average UTS value of 684 MPa and the lowest EL of 1.5%. The SLMed Fe-3.5wt.%Si had a lower average UTS value of 586 MPa and the highest EL of 3.6%. The increase of Si content has a positive effect on the strength while damaging the ductility of the SLMed silicon steel. The brittle fracture was the dominant fracture mechanism for the present three types of SLMed silicon steels.
- (5) Both the SLMed as-built and annealed samples for three types of silicon steels were characterized by a single bcc-phase, with no obvious phase transformation presented during annealing treatment.
- (6) The annealing treatment resulted in grain growth and stress relief for three types of silicon steels, as such, their comprehensive magnetic properties were also improved. The annealing behavior is not dramatically altered by variations in alloy chemistry of Si content.

## References of Chapter 5

- [1] G. Ouyang, X. Chen, Y. Liang, C. Macziewski, J. Cui, Review of Fe-6.5 wt% Si high silicon steel—A promising soft magnetic material for sub-kHz application, *J. Magn. Magn. Mater.*, 481 (2019) 234-250.
- [2] M. Garibaldi, I. Ashcroft, M. Simonelli, R. Hague, Metallurgy of high-silicon steel parts produced using Selective Laser Melting, *Acta Mater.*, 110 (2016) 207-216.
- [3] O. Gutfleisch, M.A. Willard, E. Brück, C.H. Chen, S. Sankar, J.P. Liu, Magnetic materials and devices for the 21st century: stronger, lighter, and more energy efficient, *Adv. Mater.*, 23 (2011) 821-842.
- [4] S. Pokharel, A. Dimitrovski, Analytical modeling of a ferromagnetic core reactor, in: 2019 North American Power Symposium (NAPS), IEEE, 2019, pp. 1-6.
- [5] K. Arai, K. Ishiyama, Recent developments of new soft magnetic materials, *J. Magn. Magn. Mater.*, 133 (1994) 233-237.
- [6] J.M.D. Coey, Magnetic materials, *J. Alloys Compd.*, 326 (2001) 2-6.

- [7] H. Shokrollahi, K. Janghorban, Soft magnetic composite materials (SMCs), *J. Mater. Process. Technol.*, 189 (2007) 1-12.
- [8] A. Plotkowski, J. Pries, F. List, P. Nandwana, B. Stump, K. Carver, R. Dehoff, Influence of scan pattern and geometry on the microstructure and soft-magnetic performance of additively manufactured Fe-Si, *Addit. Manuf.*, 29 (2019) 100781.
- [9] G. Stornelli, A. Faba, A. Di Schino, P. Folgarait, M.R. Ridolfi, E. Cardelli, R. Montanari, Properties of additively manufactured electric steel powder cores with increased si content, *Materials*, 14 (2021) 1489.
- [10] A. Hajalilou, S.A. Mazlan, A review on preparation techniques for synthesis of nanocrystalline soft magnetic ferrites and investigation on the effects of microstructure features on magnetic properties, *Appl. Phys. A*, 122 (2016) 1-15.
- [11] M. Jafari, P. Desmond, M.C. van Loosdrecht, N. Derlon, E. Morgenroth, C. Picioreanu, Effect of biofilm structural deformation on hydraulic resistance during ultrafiltration: A numerical and experimental study, *Water Res.*, 145 (2018) 375-387.
- [12] R.C. O'handley, *Modern magnetic materials: principles and applications*, Wiley, 2000.
- [13] H. Baker, H. Okamoto, *ASM Handbook. Vol. 3. Alloy Phase Diagrams*, ASM International, Materials Park, Ohio 44073-0002, USA, 1992. 501, (1992).
- [14] T.-K. Lee, G.-H. Kim, G.-B. Choi, I.-B. Jeong, Magnetic properties and workability of Fe-Si alloy powder cores, *J. Magn.*, 13 (2008) 170-172.
- [15] J.M. Silveyra, E. Ferrara, D.L. Huber, T.C. Monson, Soft magnetic materials for a sustainable and electrified world, *Science*, 362 (2018).
- [16] M. Littmann, Iron and silicon-iron alloys, *IEEE Trans. Magn.*, 7 (1971) 48-60.
- [17] S. Blugel, *Magnetische Anisotropie und Magnetostriktion (Theorie)*, IFF FERIENKURS, 30 (1999) C1-C1.
- [18] M. Reis, *Fundamentals of magnetism*, Elsevier, 2013.
- [19] B.D. Cullity, C.D. Graham, *Introduction to magnetic materials*, John Wiley & Sons, 2011.
- [20] F.D. Stacey, O.L. Anderson, Electrical and thermal conductivities of Fe-Ni-Si alloy under core conditions, *Phys. Earth Planet. Inter.*, 124 (2001) 153-162.
- [21] Q. Zhao, Z. Qian, X. Cui, Y. Wu, X. Liu, Influences of Fe, Si and homogenization on electrical conductivity and mechanical properties of dilute Al-Mg-Si alloy, *J. Alloys Compd.*, 666 (2016) 50-57.
- [22] B. Shassere, A. Nycz, M.W. Noakes, C. Masuo, N. Sridharan, Correlation of microstructure and mechanical properties of metal big area additive manufacturing, *Applied Sciences*, 9 (2019) 787.
- [23] Q. Zhao, B. Holmedal, The effect of silicon on the strengthening and work hardening of aluminum at room temperature, *Mater. Sci. Eng., A*, 563 (2013) 147-151.
- [24] S. Rao, E. Antillon, C. Woodward, B. Akdim, T. Parthasarathy, O. Senkov, Solution hardening in body-centered cubic quaternary alloys interpreted using Suzuki's kink-solute interaction model, *Scr. Mater.*, 165 (2019) 103-106.
- [25] J. Chen, R. Cao, *Micromechanism of cleavage fracture of metals: a comprehensive microphysical model for cleavage cracking in metals*, Butterworth-Heinemann, 2014.
- [26] B. Miller, R. Shipley, R. Parrington, D. Dennies, *Mechanisms and Appearances of Ductile and Brittle Fracture in Metals*, (2021).
- [27] X. Yan, S. Yin, C. Chen, C. Huang, R. Bolot, R. Lupoi, M. Kuang, W. Ma, C. Coddet, H. Liao, Effect of heat treatment on the phase transformation and mechanical properties of Ti6Al4V fabricated by selective laser melting, *J. Alloys Compd.*, 764 (2018) 1056-1071.
- [28] C. Meier, R.W. Penny, Y. Zou, J.S. Gibbs, A.J. Hart, Thermophysical phenomena in metal additive manufacturing by selective laser melting: fundamentals, modeling, simulation, and experimentation, *Annual Review of Heat Transfer*, 20 (2017).



- [29] J. Lemke, M. Simonelli, M. Garibaldi, I. Ashcroft, R. Hague, M. Vedani, R. Wildman, C. Tuck, Calorimetric study and microstructure analysis of the order-disorder phase transformation in silicon steel built by SLM, *J. Alloys Compd.*, 722 (2017) 293-301.
- [30] M. Roudnická, O. Molnárová, D. Dvorský, L. Křivský, D. Vojtěch, Specific response of additively manufactured AlSi9Cu3Fe alloy to precipitation strengthening, *Met. Mater. Int.*, 26 (2020) 1168-1181.
- [31] M. Garibaldi, I. Ashcroft, J. Lemke, M. Simonelli, R. Hague, Effect of annealing on the microstructure and magnetic properties of soft magnetic Fe-Si produced via laser additive manufacturing, *Scr. Mater.*, 142 (2018) 121-125.
- [32] J. Yu, J. Shin, J. Bae, Z.-H. Lee, T.D. Lee, H. Lee, E. Lavernia, The effect of heat treatments and Si contents on B2 ordering reaction in high-silicon steels, *Mater. Sci. Eng., A*, 307 (2001) 29-34.
- [33] T.F. Babuska, M.A. Wilson, K.L. Johnson, S.R. Whetten, J.F. Curry, J.M. Rodelas, C. Atkinson, P. Lu, M. Chandross, B.A. Krick, Achieving high strength and ductility in traditionally brittle soft magnetic intermetallics via additive manufacturing, *Acta Mater.*, 180 (2019) 149-157.
- [34] A.B. Kustas, D.F. Susan, K.L. Johnson, S.R. Whetten, M.A. Rodriguez, D.J. Dagel, J.R. Michael, D.M. Keicher, N. Argibay, Characterization of the Fe-Co-1.5 V soft ferromagnetic alloy processed by Laser Engineered Net Shaping (LENS), *Addit. Manuf.*, 21 (2018) 41-52.
- [35] A. Mazeeva, M. Staritsyn, V. Bobyr, S. Manninen, P. Kuznetsov, V. Klimov, Magnetic properties of Fe-Ni permalloy produced by selective laser melting, *J. Alloys Compd.*, 814 (2020) 152315.
- [36] I. Petryshynets, F. Kováč, B. Petrov, L. Falat, V. Puchý, Improving the Magnetic Properties of Non-Oriented Electrical Steels by Secondary Recrystallization Using Dynamic Heating Conditions, *Materials*, 12 (2019) 1914.

## Conclusions and perspectives

### Conclusions

The increasing number of industries and the growing demand for electricity and electronic devices are driving the requirement growth of soft magnetic materials. The available range of magnetic properties of soft magnetic materials was expanding, iron and iron silicon (Fe-Si) alloy are the most widely used. To seek better-performing manufacturing technologies for soft magnetic materials, additive manufacturing (AM) has been attracted wide attention. However, the research about AM Fe-Si-based soft magnetic alloy is still insufficient, especially a systematic study on the microstructure and materials properties of Fe-Si soft magnetic alloy via the SLM technology is still lacking. To explore and develop this research, a thorough investigation of SLMed Fe-Si soft magnetic alloy was conducted in this thesis. The following three sections are mainly contained.

First, chapter 3 studied and described the effects of processing parameters on surface morphology, microstructure, and the magnetic properties of Fe-3wt.%Si alloy manufactured by SLM, and obtained the optimized SLM parameters for producing Fe-Si alloy. Then, to put forward an insight into the microstructure characteristics and material properties of the SLMed Fe-3wt.%Si alloy. Chapter 4 discussed the microstructures, DC and AC magnetic properties, and mechanical properties of SLMed Fe-3wt.%Si soft magnet. Especially investigated the crystalline texture and oriented magnetic properties of the SLMed Fe-3wt.%Si alloy firstly, then, summarized the relationship between the texture and magnetic characteristics, carried on the theoretical elaboration. Then, the mechanical performances including microhardness, tensile properties were evaluated. Besides, this chapter also evaluated the effect of heat treatments on the microstructures and magnetic properties of SLM-processed Fe-3wt.%Si alloy samples. Chapter 5 studied the effects of silicon content on the microstructures and properties of selective laser melted silicon steels with the selected silicon contents of 3.5wt.%, 4.5wt.%, and 5.5wt.%. Moreover, it discussed the influence of annealed treatment on the microstructures, DC and AC magnetic properties of these SLMed silicon steels. The details of the conclusions are listed below.

### **Effect of processing parameters on surface morphology, microstructure, and the magnetic properties of Fe-3wt.%Si alloys manufactured by selective laser melting**

- (1) The surface morphology of the corresponding SLM Fe-3wt.% Si alloy can be improved by higher LED, which resulted in a low value of surface roughness. The decrease of the porosity rate of corresponding specimens was related to the increase of LED.
- (2) The cross-sectional microstructure of SLM Fe-3wt.% Si parts was a typical columnar structure with an oriented growth of building direction. The columnar structure at high LED is coarser than that at low LED.
- (3) The microhardness value of each SLM part was higher than 200 HV<sub>0.1</sub>. The microhardness value of the corresponding samples when LED lower than 420 J/m increased accordingly. However, it decreased when LED=420 J/m up to LED=540 J/m due to the almost similar porosity, the burning phenomenon, and Marangoni effects in sample E540.
- (4) The coercivity of SLM specimens decreased first and then increased with the increase of LED, while the evolution of saturation magnetization and LED was opposite. The specimen with a LED at 300 J/m exhibited better comprehensive magnetic properties than other specimens. It can be concluded that the magnetic properties of coercivity and saturation magnetization of Fe-3wt.%Si alloy produced by SLM are affected by the LED, which can be attributed to the parameters such as the number of defects, grain size, etc.

### **Microstructures, magnetic properties, and mechanical properties of selective laser melted Fe-3wt.%Si soft magnet**

- (1) Dense SLMed Fe-3wt.%Si magnets with a very low porosity below 0.5% were obtained, it showed an inhomogeneous structure, the microstructure of the SLMed parts exhibited a typical columnar structure with an oriented growth of building direction.
- (2) Only peaks related to the Bcc-Fe phase were observed in the XRD pattern of the as-built samples. The analysis of phase composition from EBSD also confirmed that the Fe-3wt.%Si alloy was a one-phase alloy.
- (3) The SLM-produced Fe-3wt.%Si alloy presented a  $\{100\}\langle 001\rangle$  cubic texture in this study, i.e. a  $\langle 001\rangle$  texture along the BD. Hence, in the construction coordinate system, the three directions of X, Y, and Z are contained in the axis that is easy to be magnetized. Therefore, the SLMed Fe-3wt.%Si magnet had isotropy magnetic properties at these three measured directions (X, Y, and Z).
- (4) Due to the relatively low microhardness, the elongation of the specimen reached 8.8%, the UTS and YS were 562 MPa, 445 MPa, respectively. A mixed-mode of ductile and brittle failure was the dominant rupture mechanism for SLMed Fe-3wt.%Si alloy.
- (5) Annealing the samples at 750 °C and 850 °C for 3 h did not affect the grain size. The micro-segregation of Si was partly dissolved and appears discontinuous, indicating that at those temperatures the diffusion rate was just sufficient to bring Si segregations into solid solution. But upon slow furnace cooling, some of the silicon re-segregated.
- (6) When the annealing temperature reached 1000 °C, although the dwell time was 1 h, in addition to the disappearance of the molten pool boundaries and micro-segregations, a low amount of grain grew to a large size. Annealing conducted at 1000 °C for 3 h, caused instead marked grain growth. As the dwell time increased to 5 h, by the comparison of the AT1000/3h sample, the grains almost did not grow further significantly.
- (7) Within the cases of this work, the internal stress of the SLMed parts could be relieved by annealing heat treatment, it can be further released with the increase of annealing temperature or extension of annealing time.
- (8) The magnetic properties of the SLMed Fe-3wt.%Si magnet could be comprehensively enhanced, attributing to grain growth and stress release via submitted appropriate annealing temperature-time combination.

### **Effects of silicon content on the microstructures and properties of selective laser melted silicon steels**

- (1) The average porosity of each SLMed silicon steel was lower than 0.5% with a few small-sized circular pores but without obvious cracks. With the increase of silicon content, the micro segregation of silicon in SLMed samples becomes more serious, especially at the boundary of the molten pool.
- (2) The SLMed silicon steels exhibited typical soft magnetic characteristics. The  $\mu_{\max}$  of the SLMed silicon steel increased with the increase of silicon content. Both coercivity  $H_c$  and power losses  $P_{50-1}$  of the SLMed silicon steel decreased with the increase of silicon content. The value of the  $H_c$  and  $P_{50-1}$  for SLMed Fe-5.5wt.%Si are the lowest with 102 A/m and 12.53 W/kg, respectively. The  $B_s$  exhibited a slightly decreasing trend while the  $B_r$  of the SLMed silicon steel showed an increasing trend when the Si content increased from 3.5wt.% up to 5.5wt.%.
- (3) The microhardness increased with the evolution of Si content, increased from 275.5 HV<sub>0.1</sub> to 371.5 HV<sub>0.1</sub>, which is attributed to higher Si content having a stronger solid solution strengthening effect in the silicon steel.
- (4) The SLMed Fe-5.5wt.%Si silicon steel had the highest average UTS value of 684 MPa and the lowest EL of 1.5%. The SLMed Fe-3.5wt.%Si had a lower average UTS value of 586 MPa and the

highest EL of 3.6%. The increase of Si content has a positive effect on the strength while damaging the ductility of the SLMed silicon steel. Brittle fracture was the dominant fracture mechanism for the present three types of SLMed silicon steels.

- (5) Both the SLMed as-built and annealed samples for three types of silicon steels were characterized by a single bcc-phase, without obvious phase transformation presented during annealed treatment.
- (6) The annealed treatment resulted in grain growth and stress relief for three types of silicon steels, as such, their comprehensive magnetic properties are also improved. The annealing behavior is not dramatically altered by variations in alloy chemistry of Si content.

### **Prospects and perspectives**

In perspective, several potential ideas can be highlighted based on this work for improving future research, which are listed below.

It is quite interesting to study the relationship between heat transfer and microstructure formation during the SLM process.

The stress in SLMed Fe-Si soft magnetic alloy should be quantitatively detected and analyzed. Combined with the simulation, the specific effects on the magnetic properties are worthy of in-depth study, to further improve the manufacturing process and reduce the damage of stress to the magnetic properties.

The influence of oxides in SLMed Fe-Si soft magnetic alloy on magnetic properties, especially the comprehensive effects of physical and chemical properties of original powder or oxygen content in the manufacturing process on the microstructure and properties of SLMed Fe-Si soft magnetic alloy should be further investigated.

Develop more effective post-treatment to further improve the comprehensive magnetic and mechanical properties of SLMed Fe-Si soft magnetic alloy.

The structural design of Fe-Si soft magnetic alloy and the manufacturing of the components with this structure by SLM is worthy of considerable investigation. For example, the structural design of alternating stacking of oxidized layer and non-oxidized layer.

Based on current research results to explore and develop application products of SLMed Fe-Si soft magnetic alloy.



## List of publications

- **Gao S, Yan X, Chang C, et al.** Effect of Laser Energy Density on Surface Morphology, Microstructure, and Magnetic Properties of Selective Laser Melted Fe-3wt.% Si Alloys[J]. *Journal of Materials Engineering and Performance*, 2021: 1-11.
- **Gao S, Yan X, Chang C, et al.** Microstructure and magnetic properties of FeSiBCrC soft magnetic alloy manufactured by selective laser melting[J]. *Materials Letters*, 2021, 290: 129469.
- Gao, S., Yan, X., Chang, C., Xie, X., Chu, Q., Deng, Z., ... & Fenineche, N. (2022). Finished surface morphology, microstructure and magnetic properties of selective laser melted Fe-50wt% Ni permalloy. *Acta Metallurgica Sinica (English Letters)*, 1-14.



## Abstract

Iron silicon (Fe-Si) alloys, also named silicon steels, are the most widely used owing to their excellent soft magnetic properties and economic costs. As electronic devices become diversified and automated, it is urgent to develop high-performance soft magnetic alloys with good reliability. For functional soft magnetic alloys, the SLM technique showed the potential to manufacture soft magnetic components directly from raw materials, such as the rotor and stator of the motor. To explore and develop new routes for manufacturing Fe-Si alloys, the investigation into the microstructures and properties of SLMed Fe-Si alloys from pre-alloyed powders was presented in this work. The most important finding in this work is listed in the following.

After adopting a series of experiments and characterization, under optimal linear energy density, SLMed Fe-3 wt.%Si specimens with good surface roughness, low porosity, and without cracks can be obtained. The microstructure of the SLMed parts exhibited a typical columnar structure with an oriented growth of building direction. The SLM-produced Fe-3wt.%Si alloy presented a single Fe-bcc phase, a  $\{100\}\langle 001\rangle$  cubic texture in this study, i.e. a  $\langle 001\rangle$  texture along the building direction (BD). Hence, in the printing coordinate system, the three directions of X, Y, and Z are contained in the axis that is easy to be magnetized, the alloy had isotropy magnetic properties at these three measured directions (X, Y, and Z). The elongation at break (EL) of the specimen reached 8.8%, the average ultimate tensile strength (UTS) and Yield strength (YS) were 562 MPa, 445 MPa, respectively. A mixed-mode of ductile and brittle failure was the main rupture mechanism for SLMed Fe-3wt.%Si alloy. A series of annealed treatments with different dwell times and annealed temperatures were adopted. The results show that annealing conducted at 1000 °C for 3 h, caused instead marked grain growth. As the dwell time increased to 5h, by the comparison of the AT1000/3h sample, the grains almost did not grow further significantly. The magnetic properties of the SLMed Fe-3wt.%Si magnet could be comprehensively enhanced, attributing to grain growth and stress release via submitted annealing temperature-time combination appropriately.

To investigate the effects of silicon content on the microstructures and properties of SLMed silicon steels, the pre-alloyed with silicon contents of 3.5wt.%, 4.5wt.%, and 5.5wt.% were selected. Experimental results revealed that with the increase of silicon content, the microsegregation of silicon in SLMed samples becomes more serious, especially at the boundary of the molten pool. The relative maximum permeability increased with the increase of silicon content, both coercivity and power losses decreased with the increase of silicon content. The saturation magnetic induction exhibited a slightly decreasing trend while the remanence showed an increasing trend. The increase of Si content had a positive effect on the strength while damaging the ductility of the SLMed silicon steel, resulting in the highest microhardness and the highest average UTS while the lowest average within these three types of silicon steels. Brittle fracture is the dominant fracture mechanism for the present three types of SLMed silicon steels. Both the SLMed as-built and annealed samples for three types of silicon steels were characterized by a single bcc-phase, without obvious phase transformation presented during annealed treatment. The annealed treatment resulted in grain growth and stress relief for three types of silicon steels, as such, their comprehensive magnetic properties were also improved. The annealing behavior is not dramatically altered by variations in alloy chemistry of Si content.

**Key words:** Selective laser melting, Soft magnetic alloys, Oriented magnetic properties, Microstructural evolution, Soft magnetic properties, Mechanical properties





## Résumé

Les alliages fer-silicium (Fe-Si), également appelés aciers au silicium, sont les plus largement utilisés en raison de leurs excellentes propriétés magnétiques douces et de leurs coûts économiques. Alors que les appareils électroniques se diversifient et s'automatisent, il est urgent de développer des alliages magnétiques doux performants et fiables. Pour les alliages magnétiques doux fonctionnels, la technique SLM a montré le potentiel de fabriquer des composants magnétiques doux directement à partir de matières premières, telles que le rotor et le stator du moteur. Afin d'explorer et de développer de nouvelles voies pour la fabrication d'alliages Fe-Si, l'étude des microstructures et des propriétés des alliages Fe-Si SLMed à partir de poudres pré-alliées a été présentée dans ce travail. Les conclusions de ce travail sont énumérées ci-dessous.

Après avoir adopté une série d'expériences et de caractérisation, sous une densité d'énergie linéaire optimale, des spécimens SLMed Fe-3Si avec une bonne rugosité de surface, une faible porosité relative, et sans fissures peuvent être obtenus. La microstructure des pièces SLMed présentait une structure colonnaire typique avec une croissance orientée dans le sens de la construction. L'alliage Fe-3wt.%Si produit par SLM présentait une seule phase Fe-bcc, une texture cubique  $\{100\}\langle 001\rangle$ , c'est-à-dire une texture  $\langle 001\rangle$  le long de la direction de construction (BD). Par conséquent, dans le système de coordonnées d'impression, les trois directions X, Y et Z sont contenues dans l'axe qui est facile à magnétiser, l'alliage avait des propriétés magnétiques d'isotropie dans ces trois directions mesurées (X, Y et Z). L'allongement à la rupture (EL) de l'éprouvette a atteint 8,8%, la résistance à la traction moyenne (UTS) et la limite d'élasticité (YS) sont respectivement de 562 MPa, 445 MPa. Un mode mixte de rupture ductile et fragile est le principal mécanisme de rupture pour l'alliage SLMed Fe-3wt.%Si. Une série de traitements de recuit avec différents temps de séjour et températures de recuit ont été adoptées. Les résultats montrent qu'un recuit effectué à 1000 °C pendant 3 h, a provoqué à la place une croissance marquée des grains. Au fur et à mesure que le temps de séjour augmentait à 5h, par comparaison avec l'échantillon AT1000/3h, les grains n'ont pratiquement pas augmenté de manière significative. Les propriétés magnétiques de l'aimant SLMed Fe-3wt.%Si pourraient être considérablement améliorées, en attribuant de manière appropriée à la croissance du grain et à la libération des contraintes via la combinaison température-temps de recuit soumise.

Afin d'étudier les effets de la teneur en silicium sur les microstructures et les propriétés des aciers au silicium SLMed, les pré-alliés avec des teneurs en silicium de 3,5 % en poids, 4,5 % en poids et 5,5 % en poids ont été sélectionnés. Les résultats expérimentaux ont révélé qu'avec l'augmentation de la teneur en silicium, la microségrégation du silicium dans les échantillons SLMed devient plus grave, en particulier à la limite du bain en fusion. La perméabilité maximale relative augmente avec l'augmentation de la teneur en silicium, à la fois la coercivité et les pertes de puissance diminuent avec l'augmentation de la teneur en silicium. L'induction magnétique de saturation présente une tendance légèrement décroissante tandis que la rémanence présente une tendance croissante. L'augmentation de la teneur en Si a un effet positif sur la résistance tout en endommageant la ductilité de l'acier au silicium SLMed, ce qui se traduit par la microdureté la plus élevée et l'UTS moyen le plus élevé tout en étant la moyenne la plus basse au sein de ces trois types d'aciers au silicium. La rupture fragile est le mécanisme de rupture dominant pour les trois types actuels d'aciers au silicium SLMed. Les échantillons SLMed tels que construits et recuits pour trois types d'aciers au silicium sont caractérisés par une seule phase bcc, aucune transformation de phase évidente n'est présentée pendant le traitement recuit. Le traitement recuit entraînant une croissance des grains et un soulagement des contraintes pour trois types d'aciers au silicium, en tant que tels, leurs propriétés magnétiques complètes sont également améliorées. Le comportement de recuit n'est pas considérablement modifié par les variations de la chimie de l'alliage de la teneur en Si.

**Mots clés :** Fusion sélective par laser, Alliages magnétiques doux, Propriétés magnétiques orientées, Evolution microstructurale, Propriétés magnétiques douces, Propriétés mécaniques



SPIM

■ École doctorale SPIM - Université de Technologie Belfort-Montbéliard  
F - 90010 Belfort Cedex ■ tél. +33 (0)3 84 58 31 39  
■ [ed-spim@univ-fcomte.fr](mailto:ed-spim@univ-fcomte.fr) ■ [www.ed-spim.univ-fcomte.fr](http://www.ed-spim.univ-fcomte.fr)

